POLYTECHNIQUE MONTRÉAL

affiliée à l'Université de Montréal

Investigating the durability of Stellitte hardfacing components used in the power generation industry

YUXIAO WU

Département de génie mécanique

Thèse présentée en vue de l'obtention du diplôme de *Philosophiæ Doctor*

Génie mécanique

OCTOBRE 2019

POLYTECHNIQUE MONTRÉAL

affiliée à l'Université de Montréal

Cette thèse intitulée :

Investigating the durability of Stellitte hardfacing components used in the power generation industry

présentée par **Yuxiao WU**

en vue de l'obtention du diplôme de *Philosophiæ Doctor*

a été dûment acceptée par le jury d'examen constitué de :

Rachid BOUKHILI, président
Myriam BROCHU, membre et directrice de recherche
Jolanta-Ewa KLEMBERG-SAPIEHA, membre et codirectrice de recherche
Jean-Philippe HARVEY, membre
Tapasvi LOLLA, membre externe

ACKNOWLEDGEMENTS

First of all, I would like to thank my thesis directors, Professor Myriam Brochu and Professor Jolanta Sapieha for directing me during these years. Furthermore, I would also like to thank Professor Ludvik Martinu from the Functional Coating and Surface Engineering Laboratory (FCSEL) for his support. I wish to acknowledge the National Sciences and Engineering Research Council of Canada and Velan Inc. for the financial support.

Second, I am grateful for the fruitful discussion with Dr. Thomas Schmitt and Dr. Etienne Bousser. When I have difficulties, they are always there to help and encourage me. They have inspired me a lot throughout the PhD study. Their dedication and commitment to research has influenced me significantly.

I would like to thank the Canadian Neutron Beam Centre for providing me a student grant to perform neutron diffraction experiments. I sincerely thank Dr. Michael Gharghouri, Senior Research Scientist at Canadian Nuclear Laboratories, for the assistance in fully completing the experiments. I would like to thank Dr. Paul Provencher for proofreading the three articles.

At the FCSEL, it is a pleasure to work and collaborate with many people. I would like to express my gratitude to all the former and present colleagues. They are: Adéla Jagerová, Amaury Kilicaslan, Bill Baloukas, Duanji Li, Erika Herrera, Erwens Broustet, Etienne Bousser, Fabrice Pougoum, Francis Blanchard, Gabriel Taillon, Jacques Lengaigne, Jincheng Qian, Josephina Crespo, Julien Gagnon, Julien Schmitt, Julien Tétreault, Justin Duby, Louis Dubé Riopel, Martin Caron, Marwan Azzi, Médard Koshigan, Michael Laberge, Oleg Zabeida, Phillip Rumsby, Richard Vernhes, Rodrigue Beain, Sasha Woodward, Soroush Hafezian, Stephen Brown, Simon Loquai, Thomas Poirié, Thomas Schmitt, William Trottier, and so on.

I would like to thank all the co-authors of my papers, especially those from Velan Inc. They are Nabil Tarfa, Luc Vernhes, Gil Perez, and Réjean René, Vahe Najarian, and Fadila Khelfaoui. This PhD project could not be completed without the technical assistance of Sébastien Chenard, Francis Turcot, and Josée Laviolette from Polytechnique Montréal; and Pascal Coté, Jonathan Delarosbil, James Mehta, and Nicolas Lévesque from Velan Inc.

I cannot express enough my gratitude to my family members. Thank you for all your love, understanding, and support during all the years.

I sincerely thank to a meditation practice, Falun Dafa, which keeps me healthy and energetic during the PhD study. I benefit immeasurably from Falun Dafa master, Mr. Li Hongzhi, who helps me follow the principle of Truthfulness, Compassion, and Forbearance in the daily life.

Many people help me during this long journey. Last but not least, I would like to extend my heartfelt thanks to them though I cannot list all the names. I wish each of them a very bright future.

RÉSUMÉ

Dans le secteur de la production d'énergie, les valves jouent un rôle essentiel dans la gestion du flux de vapeur à haute température et à haute pression. Elles sont utilisées pour démarrer et arrêter le flux, réguler le flux ou contrôler le sens du flux. Le fonctionnement des valves telles que l'ouverture et la fermeture peut provoquer l'usure des matériaux de la valve. Les progrès de la technologie des matériaux et des techniques de fabrication permettent aux valves de fonctionner à haute température. Par exemple, en appliquant l'alliage de surfaçage dur S6 sur les surfaces d'étanchéité des valves, un faible frottement est garanti et la résistance à l'oxydation et à la corrosion est également améliorée. Cependant, la délamination des alliages de surfaçage dur des valves représente un défi majeur pour le monde de la production d'électricité. Dans ce contexte, nous cherchons en premier lieu les causes de la délamination ; d'autre part, nous proposons des solutions pour améliorer la durabilité des composants de surfaçage dur Stellite.

Afin d'accomplir ces objectifs, une étude de l'évolution de la microstructure et des propriétés méchaniques du surfaçage dur durant la fabrication et le service des composants. Un traitement thermique après soudage (PWHT) à 760 °C d'une durée de 2 h fût performé sur les composants de surfaçage dur durant le processus de fabrication. Les conditions de service du surfaçage dur furent étudiées par vieillissement à des températures variant entre 550 et 700 °C pour des durées variant entre 1008 et 8760 heures. La microstructure fût caractérisée par OM, SEM, EDS et EBSD. La caractérisation mécanique fût effectuée par micro et nano-indentation, tests d'impact Charpy et par test de tension. Les contraintes résiduelles ont été testées par diffraction de neutrons.

Premièrement nous avons exploré l'effet du PWHT sur la microstructure, la dureté et les contraintes résiduelles des composants de surfaçage dur. Il a été observé que le PWHT diminue significativement la dureté du HAZ dans l'acier dû à la formation d'une microstructure en martensite revenue. De plus, il peut réduire substantiellement les contraintes résiduelles dans l'acier et homogénéiser les contraintes dans les composants de surfaçant dur.

Après la fabrication, nous avons étudié l'évolution de la microstructure interfaciale F91/S21 des composants de surfaçage dur. Les résultats ont montré que l'interface F91/S21 est instable lors du vieillissement en raison de la formation d'une couche interfaciale dure. En étudiant sa cinétique de croissance, il a été constaté que cette couche interfaciale suit un taux de croissance parabolique. En appliquant des méthodes de caractérisation complémentaires, trois phases, à savoir une phase

Fe_xCo_y de type BCC, un carbure de type $M_{23}C_6$ riche en Cr et une phase σ de type (Fe,Co) (Cr,Mo) ont été identifiées dans cette couche interfaciale. D'après les cartographies de nano-indentation obtenues sur l'interface F91/S21, les carbures $M_{23}C_6$ et la phase σ sont nettement plus durs que les autres phases. De plus, il a été constaté que les carbures $M_{23}C_6$ grandissaient avec la température et la durée de vieillissement, alors que la quantité de phase σ diminuait avec la température.

Pour donner suite à l'exploration de l'évolution de la microstructure interfaciale F91/S21, nous avons étudié les effets de la microstructure interfaciale F91/21 sur les propriétés mécaniques des composants de surfaçage dur au moyen de tests d'impact Charpy. Une géométrie innovante de l'encoche en U Charpy a été conçue, c'est-à-dire que l'interface F91/S21 était centrée dans l'encoche. Une diminution considérable de l'énergie après le vieillissement est attribuée à la couche interfaciale formée, où les craques primaires se propagent. Les composants de surfaçage dur vieillis présentent des défaillances par fissures fragiles. Il a été trouvé que les carbures $M_{23}C_6$ jouent un rôle plus important que la phase σ dans la dégradation de la ténacité lors des tests d'impact. Il est proposé que les facteurs microstructuraux contribuant au délaminage des alliages de surfaçage dur des soupapes à haute température soient la formation de ces phases dures.

Ensuite, nous avons réalisé une étude comparative sur l'évolution de la microstructure et les propriétés mécaniques des composants de surfaçage dur en utilisant l'IN82 comme alternative à la couche tampon S21. Comparativement aux composant de surfaçage dur S21, aucune couche interfaciale nuisible fût observée à l'interface F91/S21 après le vieillissement. La diminution de la ténacité des composants de surfaçage dur IN82 s'est avérée beaucoup moins importante que celle de S21, et, de plus, serait reliée à la formation grossière et à la précipitation des carbures intergranulaires/interdendritiques dans le IN82 plutôt qu'à l'interface F91/IN82.

En plus du IN82, les composants de surfaçage dur IN625 furent étudiés en raison du bas prix. L'interface F91/IN625 et le matériel massif IN625 se sont démontrés comme moins stables que les composants de surfaçage dur IN82 dû aux précipités formés durant le vieillissement. Bien que l'interface F91/IN625 ne soit pas le lien le plus faible durant les tests de tension, certains spécimens Charpy présentent des défaillances le long de l'interface F91/IN625, résultant possiblement des précipités parallèles à l'interface. La perte d'énergie d'impact est significative (88%) après un vieillissement de 650 °C pour 8760 h. Il n'est pas recommandé d'utiliser la couche tampon IN625.

Finalement, l'étude d'un composant d'ex-service a validé notre étude en laboratoire sur les composants de surfaçage dur S21. La fissure de délamination s'est propagée dans les zones riches en phases σ de la couche de S21. Cela s'explique par le fait que la phase σ s'est formée loin de l'interface, profondément dans le S21 via le chemin de diffusion aux limites de grain après plusieurs années de service. Le temps de service réel et la température concorde avec le temps et la température équivalente attendue par extrapolation.

Lors du service des valves, il existe également d'autres facteurs tels que le cyclage thermique et les contraintes induites par le fonctionnement (ouverture et fermeture des valves), en plus du vieillissement. Ils n'ont pas été pris en compte pour l'expérimentation. Cependant, nous pensons que les objectifs de ce travail ont été atteints. À savoir, les causes des défaillances prématurées ont été identifiées et les solutions alternatives pour améliorer la durabilité des composants de surfaçage dur ont été validées.

Pour relever le défi du délaminage d'alliages de surfaçage dur provenant de valves haute température, la couche tampon IN82 constitue une bonne alternative pour remplacer la couche tampon problématique S21, qui peut améliorer la durabilité des composants de surfaçage dur. Néanmoins, en raison de la dilution plus élevée de Fe et de Ni, la dureté de la couche supérieure de S6 déposée sur la couche tampon IN82 est compromise par rapport au S6 déposé sur la couche tampon de S21. Par conséquent, il est proposé que davantage de couches de S6 puissent être déposées pour maintenir sa dureté en fonction des applications. De plus, les paramètres de soudure utilisés durant la fabrication peuvent être optimisés pour réduire la dilution et maintenir la dureté du S6.

Pendant le service des valves, il y a aussi d'autres facteurs comme le cycle thermique et le stress induit par les opérations (ouverture et fermeture des valves) qui s'additionnent au vieillissement. Ces paramètres n'ont pas été pris en compte durant les expérimentations. D'autre part, nous croyons fortement que les objectifs établis dans le Chapitre 1 ont été atteints. Notamment, les causes d'échecs prématurés ont été identifiées et les solutions alternatives pour améliorer la durabilité des composants de surfaçage dur ont été validées.

Afin de répondre au défi de la délamination des alliages de surfaçage dur dans les valves hautes-températures, la couche tampon de IN82 est une bonne alternative à celle problématique de S21, car elle peut améliorer la durabilité des composants de surfaçage dur. Néanmoins, due à une plus

grande dilution de Fe et de Ni, la dureté de la couche supérieure de S6 déposée sur la couche tampon de IN82 est compromise quand elle est comparée avec le S6 déposé sur la couche tampon de S21. Donc, il est proposé que plus de couches de S6 peuvent être déposées afin de maintenir la dureté dans les applications où la résistance à l'usure est critique.

ABSTRACT

In the power generation industry, valves play a vital role, which manage the flow of high-temperature and high-pressure steam. They are used to start and stop the flow, regulate the flow, or control the direction of the flow. Operation of valves such as opening and closing can cause wear of valve materials. Advances in material technology and manufacturing techniques enable valves to operate at high temperatures. For instance, by applying the hardfacing alloy S6 onto the sealing surfaces of valves, wear, oxidation and corrosion resistance are improved. However, delamination of hardfacing alloys from valves has presented a major challenge to the power generation world. In this context, we aim at investigating the causes of delamination failures. In addition, we target at proposing solutions to enhance the durability of Stellite hardfacing components.

To fulfill the objectives, we carried out a comprehensive study on the microstructure evolution and mechanical properties of three types of hardfacing components during manufacturing and service. A PWHT at 760 °C for 2 h was performed on the hardfacing components during the manufacturing process. Valves are usually used at elevated temperatures for long duration. Aging experiments at four temperatures ranging from 550 to 700 °C for three exposure times within a one-year period were conducted on the hardfacing components. The microstructure was characterized using OM, SEM, EDS, and EBSD. The mechanical characterization was undertaken using nano- and micro-indentation, Charpy impact, and tensile testing. The residual strains/stresses were measured using neutron diffraction.

First, we explored the effects of the PWHT on microstructure, hardness and residual stresses of the hardfacing components to reduce the risk of failures introduced in process. The PWHT was found to soften the high-hardness HAZ in the steel significantly due to the formation of the tempered-martensitic microstructure. Moreover, it can reduce the residual stresses in steel substantially and homogenize the strains across the hardfacing component.

After manufacturing, we studied the F91/S21 interfacial microstructure evolution of the problematic S21 hardfacing components. A layer was found to grow along the F91/S21 interface during aging, which follows a parabolic rate of growth. Three phases including an (Fe,Co)(Cr,Mo)-type σ phase and a Cr-rich $M_{23}C_6$-type carbide were identified in this interfacial layer through the complementary characterization methods. This interfacial layer is harder than the

S21 and the F91 materials due to the presence of the hard σ phase and $M_{23}C_6$ carbides. The $M_{23}C_6$ carbides were found to grow with aging temperature and time. However, lesser amount of the σ phase was observed at higher temperatures studied.

Following the exploration of the F91/S21 interfacial microstructure evolution, we investigated the effects of F91/S21 interfacial microstructure on the mechanical properties of S21 hardfacing components by means of Charpy impact testing. An innovative Charpy U-notch geometry was designed. That is, the F91/S21 interface was centered in the notch. The significant decrease in impact energy after aging is resulted from the interfacial layer formed, where the primary cracks propagate. The aged S21 hardfacing components were found to fail in a brittle fashion. Both the the σ phase and $M_{23}C_6$ carbides were found to contribute to the toughness degradation during the impact testing, though the $M_{23}C_6$ carbides play a more important role than the σ phase. It is proposed that these two hard phases are the microstructural causes for the delamination of Stellite hardfacing from valves.

Then, we performed a comparative study on the microstructure evolution and mechanical properties of hardfacing components using the IN82 alloy as an alternative to the problematic S21 buffer layer. Compared with the S21 hardfacing components, no deleterious interfacial layer was observed along the F91/IN82 interface after aging. The impact toughness degradation in the IN82 hardfacing components was found to be much less significant than that of the S21, and in addition, to be related to coarsening and precipitation of the intergranular/interdendritic carbides in the IN82 bulk material rather than the F91/IN82 interface.

In addition to the IN82 alloy, the IN625 hardfacing components were investigated due to low cost. Both the F91/IN625 interface and the IN625 bulk material were found to be not as stable as the IN82 hardfacing components because of the presence of precipitates during aging. Though the F91/IN625 interface is not the weakest link during the tensile testing, some Charpy specimens were found to fail along the F91/IN625 interface possibly resulted from the precipitates parallel to the interface. The impact energy loss is significant (88%) after aging at 650 °C for 8760 h. It is not recommended to use the IN625 buffer layer.

Finally, the examination of an ex-service wedge gate valve validates our laboratory study on the S21 hardfacing components. The delamination crack was observed in the zones enriched with the σ phase of the S21 bulk material. It is because large amounts of the σ phase precipitate deeply into

the S21 bulk material via the grain boundary diffusion path after years of service. The service time and temperature of this ex-service component fulfill the expected equivalent time and temperature by extrapolation.

During service of valves, in addition to aging, there are other factors such as thermal cycling and operation induced stresses (opening and closing of valves). They were not taken into account by our experimentation. However, we do believe that the objectives of this work have been fulfilled. Namely, the causes of the premature failures have been identified and the alternative solutions to enhance the durability of the hardfacing components have been validated.

To meet the challenge of delamination of hardfacing alloys from high-temperature valves, the IN82 buffer layer is a good alternative to replace the problematic S21 buffer layer, which can enhance the durability of the hardfacing components. However, due to higher dilution of Fe and Ni, the hardness of S6 top layer deposited on the IN82 buffer layer is compromised compared with the S6 deposited over the S21 buffer layer. To mitigate this downside, it is proposed that more S6 layers can be deposited to maintain its hardness according to the applications. Moreover, the welding parameters used during manufacturing can be optimized to reduce the dilution, and thus to maintain the S6 hardness.

TABLE OF CONTENTS

LIST OF TABLES

LIST OF FIGURES

LIST OF SYMBOLS AND ABBREVIATIONS

Symbols

ε	Residual strain
θ	Incidence angle
λ	Wavelength
ν	Poisson's Ratio
σ	Residual stress
A	Projected area
C	Material constant
E	Young’s modulus
$E_{\max}$	Maximum impact energy
$E_{\min}$	Minimum impact energy
ΔE_{avg}	Uncertainty in the mean value of impact energy
H	Hardness
$H_{\max}$	Maximum hardness
$H_{\min}$	Minimum hardness
HP	Hollomon-Jaffe parameter
ΔH_{avg}	Uncertainty in the mean value of hardness
k	Growth rate constant
k_0	Pre-exponential coefficient
N	Number of measurements
P	Applied load
Q	Activation energy
R	Gas constant

T	Temperature
t	Time
x	Thickness of the interfacial layer

Abbreviations

ASTM	American Society for Testing and Materials
AT	As tempered
BCC	Body-centered cubic
BSE	Backscattered electron
DIC	Digital image correlation
EBSD	Electron backscattered diffraction
EDS	Energy dispersive spectroscopy
EPRI	Electric Power Research Institute
HAZ	Heat-affected zone
HRH	Hot reheat section of a boiler
HRSG	Heat recovery steam generator
HV	Vickers hardness
IN625	Inconel 625
IN82	Inconel 82
NSERC	Natural Science and Engineering Research Council
OM	Optical microscopy
PMZ	Partially mixed zone
PSGV	Parallel sliding gate valve
PSGVC	Parallel sliding gate valve
PTA	Plasma transferred arc

PWHT	Post-weld heat treatment
S21	Stellite 21
S6	Stellite 6
SE	Secondary electron
SEM	Scanning electron microscopy
XRD	X-ray diffraction

LIST OF APPENDICES

CHAPTER 1 INTRODUCTION

1.1 Context

In power plants, electric power is generated through the conversion of other energy sources. For example, fossil fuels such as coal and oil are burnt to produce electricity in most power plants in the world. However, the produced carbon dioxide emissions into the atmosphere absorb solar energy and trap heat close to the surface of Earth, which is known as the greenhouse effect. Greenhouse gases including carbon dioxide drive global warming and global climate change. Reducing greenhouse gas emissions has been agreed by many countries. According to United States Environmental Protection Agency, the second largest share of greenhouse gas emissions comes from burning fossil fuels for electricity, as shown in Figure 1.1 [1]. Material scientists have made every endeavor to advance material technology to improve the thermal power generation efficiency. That is, steam temperature and pressure are increased to reduce use of fossil fuels, and thus to reduce carbon dioxide and other environmentally hazardous gas emissions.

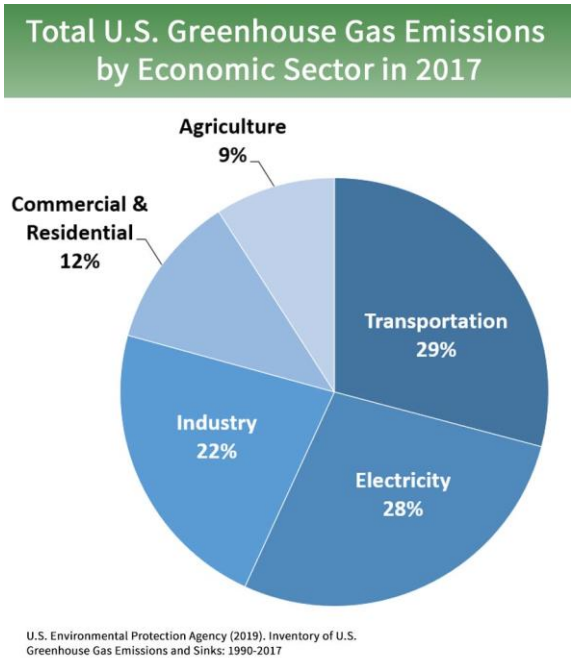

Figure 1.1: A pie chart illustrating numerical proportions of U.S. greenhouse gas emissions by economic sector in 2017 [1].

The steam created in the power generation industry operates a steam turbine and generator that then generates electricity. Accordingly, the steam needs to be controlled. Thus, steam control valves, essential components of a piping system, play an important part in controlling the flow and pressure of steam within a system or process. Valves are used to start and stop the steam flow, to regulate the flow or the process pressure, and to control the direction of the flow. Valve designs, models and types are many. A parallel slide gate valve manufactured by Velan is illustrated in Figure 1.2. Valve seats and disks are shown on the right side of Figure 1.2, which are removable and replaceable internal parts that are in contact with the steam flow. The disk is able to start, stop, or throttle the steam flow depending on its position (fully or partially opening or closing). Disks are usually forged and hardfacing alloys are often deposited on their surfaces to provide wear, oxidation and corrosion resistance. The seat provides the seating surface for the disk and they together form a seal to stop the steam flow. As shown in Figure 1.2, there are two seats in this parallel slide gate valve. Hardfacing alloys are also often deposited on the seating surfaces, which are then machined to reach a fine surface finish for tight sealing.

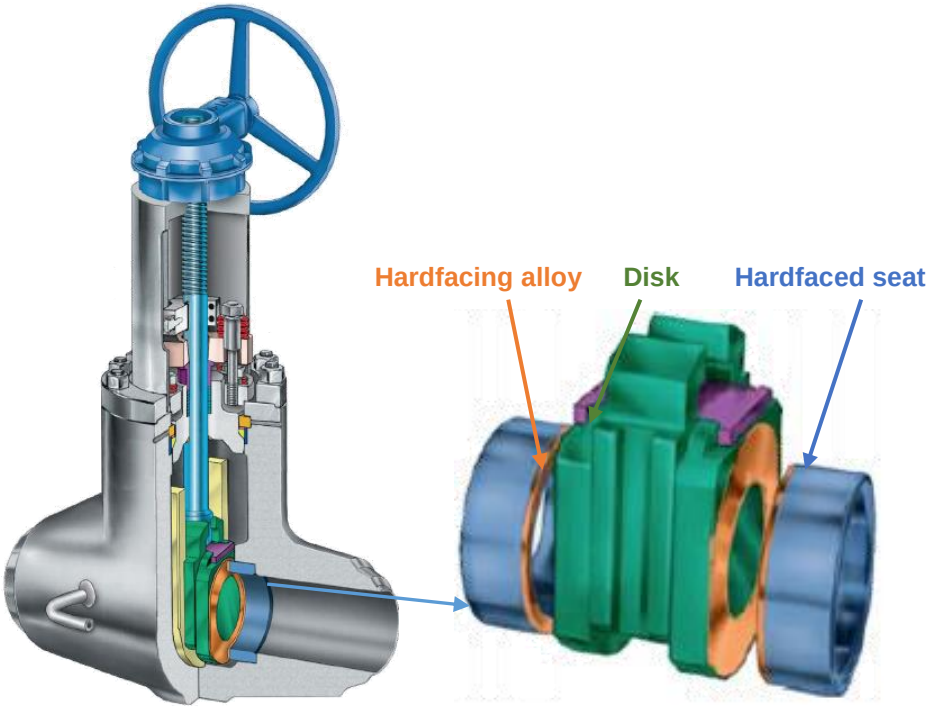

Figure 1.2: A Velan parallel slide gate valve (courtesy of Velan Inc.).

Hardfacing alloys are normally classified as iron-, nickel- and cobalt-based alloys. With regard to the hardfacing alloys used in the conventional power generation industry, a cobalt-based alloy

Stellite 6 (S6) has gained popularity for decades. Stolof concluded that the S6 alloy exhibited high hot hardness through the formation of complex carbides and good oxidation resistance provided by its high chromium content (about 30%) [2]. For some applications, the S6 alloy is applied directly on the steel substrate; for other applications, Stellite 21 (S21) alloy is used as a buffer layer (also referred to as a butter layer) between the steel substrate and the S6 top layer. One reason to use the S21 (alloy 21) is to bridge the thermal expansion gap between the steel substrate (grade 91) and the S6 (alloy 6) due to its intermediate thermal expansion, as shown in Figure 1.3 [3]. The S21 is also a cobalt-based alloy but less resistant to wear than S6.

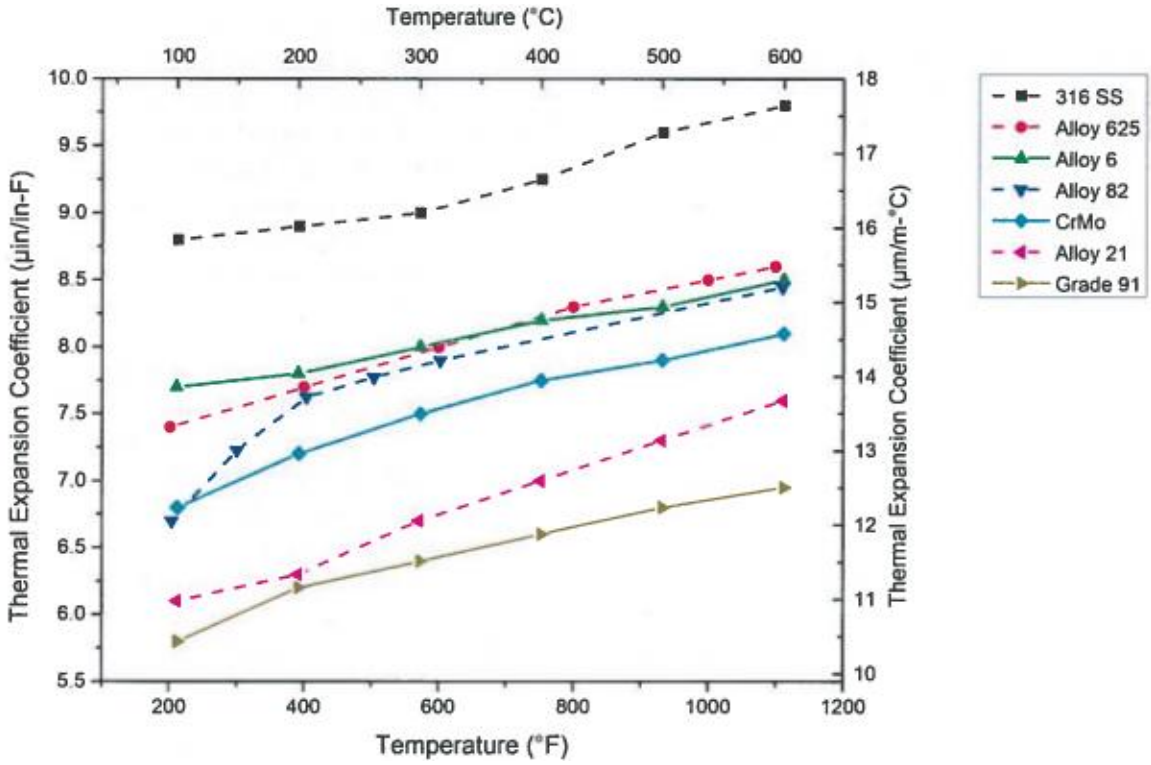

Figure 1.3: Coefficient of thermal expansion of several alloys [3].

Valves used in the conventional power generation industry are usually made of creep-resistant steels due to the elevated-temperature application. For example, valve components are manufactured using grade 91 steel, a tempered-martensitic steel. When the valve components need to be wear resistant, hardfacing alloys such as the S21 and the S6 alloys are applied on the component surfaces by hardfacing processes. Among the processes, plasma-transferred arc (PTA) welding is often used due to its advantages such as automation. When the Stellite alloys are

deposited on the steel substrate during welding, alloy mixing occurs due to melting of part of the steel substrate. Therefore, phase transformation may take place during manufacturing or service.

A major industry challenge in the form of delamination of cobalt-based hardfacing alloys from valve seats or disks during service has presented itself to the power generation industry. One such failure is illustrated in Figure 1.4 [4], where a delamination crack is growing between the S21 buffer layer and the grade 91 steel. These failures were documented by the Electric Power Research Institute (EPRI) in a technical update report in 2015 [3]. In 2011 and 2012, a leading valve services company repaired more than 25 valves due to the Stellite delamination failures [5]. These failures may cause steam leakage. Consequently, thermal efficiency of power plants is reduced, more fossil fuels are burnt to produce electricity, and thus more carbon dioxide is emitted into the atmosphere. In addition, the free hardfacing debris could damage other components within the system [6]. In response to this challenge, this PhD project was defined within the program of the Multisectorial Industrial Research Chair in Coatings and Surface Engineering, partnered by Montreal-based valve manufacturing company Velan Inc.

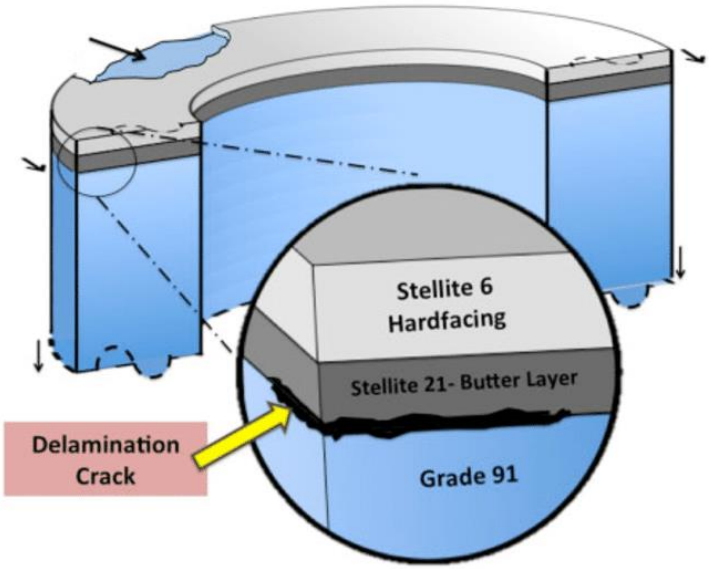

Figure 1.4: A schematic showing the delamination between the S21 and the grade 91 [4].

1.2 Objectives

In the context of this PhD project and of the needs of our industrial partner, we focus on comprehending the causes of the premature failures and investigating the alternative solutions to enhance the durability of the hardfacing components. This requires a thorough characterization of

the microstructure and mechanical properties of the hardfacing components during manufacturing and service, and an exploration of alternative materials to develop optimized Stellite hardfacing components using the existing state-of-the-art. In order to accomplish the main goals of this project, the specific objectives are set as follows:

- To explore the effects of the post-weld heat treatment (PWHT) on the microstructure and properties of the hardfacing components;
- To investigate the effects of long-term aging on the microstructure evolution of the hardfacing components;
- To study the effects of the microstructure evolution on the mechanical properties of the hardfacing components;
- To evaluate the effects of the alternative buffer layers on the durability of the hardfacing components.

CHAPTER 2 GENERAL ORGANIZATION OF THE THESIS

This thesis comprises twelve chapters including the introduction and general organization of the thesis. Chapter 3 presents the background information about hardfacing processes, hardfacing materials, and 9–12% Cr martensitic/ferritic steels. At the end of chapter 3, the premature failures of Stellite hardfacing in the steam power generation industry and the relevant studies are detailed. The experimental methods including the hardfacing deposition, and microstructural and mechanical characterization are described in chapter 4. The thesis body includes chapters 5 to 10 where the mains results were compiled in three journal papers (chapters 6, 7 and 8) and 3 complementary topics. A general discussion linking the results together and explaining the limitations of the work precedes the conclusions and perspectives.

To reduce the failures induced during the manufacturing process, the effects of the PWHT on microstructure, hardness and residual stresses of the hardfacing components were studied in chapter 5. It will be shown that the PWHT effectively tempers the microstructure of heat-affected zone (HAZ) in the steel, and thus significantly softens the high-hardness HAZ. In addition, the PWHT not only reduces the residual stresses in steel significantly, but also homogenizes the strains across the hardfacing component.

After the PWHT study, the effects of long-term aging on the F91/S21 interfacial microstructure were explored in chapter 6 (Article 1). It will be shown that three phases including an (Fe,Co)(Cr,Mo)-type σ phase and a Cr-rich $M_{23}C_6$-type carbide are formed in the F91/S21 interfacial layer after aging. It will also be shown that the σ phase and the $M_{23}C_6$ carbides are the hardest among the studied phases. The deleterious phases in the interfacial layer may cause the delamination of valves in service due to their high hardness.

To validate the above hypothesis, the F91/S21 interfacial microstructure is correlated with its toughness using Charpy impact testing in chapter 7 (Article 2). It will be shown that this interfacial layer formed during aging provides a brittle crack propagation pathway under the high-strain rate impact. The impact energy loss is mainly associated with the brittle $M_{23}C_6$ carbides and σ phase in the interfacial layer. Therefore, it will be concluded that the microstructural causes of the delamination of valve components are the σ phase and the $M_{23}C_6$ carbides formed along the F91/S21 interface during the high-temperature exposure.

Since the damage mechanism is clear, an Inconel 82 (IN82) buffer layer was evaluated to replace the problematic S21 buffer layer in chapter 8 (Article 3). A comparative study on the microstructure and mechanical properties of IN82 and S21 hardfacing components was performed. It will be shown that the F91/IN82 interface is much more stable than the F91/S21 interface after aging at 650 °C for 8760 h. The impact energy loss of the IN82 components is much less significant than that of the S21 after aging. Thus, the IN82 buffer layer is recommended to replace the problematic S21 to enhance the durability of the hardfacing components.

Following the evaluation of the IN82 buffer layer, another nickel-base alloy Inconel 625 (IN625) was also investigated due to its low cost in chapter 9. However, it will be shown that the IN625 is not recommended to be used as a buffer layer due to its unstable microstructure and mechanical properties.

To transfer our obtained laboratory knowledge to the industry, the case study of an ex-service wedge gate valve was undertaken in chapter 10. It will be shown that the results and discussion obtained from the laboratory experiments in chapter 6 and 7 provide a solid explanation for the delamination crack observed in the zones enriched with the σ phase of this ex-service wedge gate valve.

Finally, in the last two chapters, the general discussion linking the results together is presented and the limitations of this work are addressed as well. The main results of this work accomplished are summarized, followed by the relevant ideas, interests and recommendations with respect to the hardfacing components.

This research work resulted in the three publications, as listed in Table 2.1. In addition, some results of this work were presented at conferences, as summarized in Table 2.2.

Table 2.1 Peer reviewed publications related to this work.

Y. Wu, E. Bousser, T. Schmitt, N. Tarfa, F. Khelfaoui, R. René, J. Klemberg-Sapieha, and M. Brochu, "Thermal stability of a Stellite/steel hardfacing interface during long-term aging," *Materials Characterization*, vol. 154, pp. 181-192, 2019.
Y. Wu, T. Schmitt, E. Bousser, F. Khelfaoui, V. Najarian, J. Klemberg-Sapieha, and M. Brochu, "Effect of interfacial microstructure on mechanical properties of cobalt-based hardfacing during long-term aging," *Submitted*.
Y. Wu, T. Schmitt, E. Bousser, N. Tarfa, L. Vernhes, F. Khelfaoui, G. Perez, J. Klemberg-Sapieha, and M. Brochu, "Microstructural and mechanical characterization of Stellite hardfacing with two types of buffer layers," *Submitted*.

Table 2.2: Contributions to conferences.

Y. Wu, T. Schmitt, E. Bousser, F. Khelfaoui, R. René , N. Tarfa, J. Klemberg-Sapieha and M. Brochu, " Microstructural and mechanical characterization of Stellite hardfacing with different buffer layers". Poster, CMSC, 2017, Ottawa, ON, Canada.
Y. Wu, T. Schmitt, E. Bousser, F. Khelfaoui, R. René , N. Tarfa, J. Klemberg-Sapieha and M. Brochu, " Microstructural and mechanical characterization of Stellite hardfacing with different buffer layers". Poster, FCSE, 2017, Montreal, QC, Canada.

CHAPTER 3 LITERATURE REVIEW

This chapter offers an overview of the background knowledge with respect to hardfacing processes, hardfacing materials, and creep-resistant steels used in the power generation industry. The premature failures of hardfacing components are well described and the gaps in the present knowledge are addressed.

3.1 Hardfacing

3.1.1 Introduction

Hardfacing is a surface engineering process, which involves applying a wear-resistant material on the surface of a base material. During hardfacing, the coating material is melted on the surface of the substrate. One advantage it offers over other surface engineering processes is that it provides a metallurgical bond between the coated hardfacing material and the substrate. Thus, it is not susceptible to spallation. Hardfacing can also enhance oxidation and corrosion resistance in elevated-temperature applications.

Hardfacing layers are generally applied using welding processes. This process can be carried out easily even on site. Hardfacing can be applied on new components during the production or on worn-down and damaged surfaces. Consequently, it reduces machine downtime and cost of replacement. Over the recent years, hardfacing has been adopted in industries such as power generation, mining, petrochemical, construction and railroad.

3.1.2 Hardfacing process

Most welding processes can be used for hardfacing, which include:

- oxyfuel welding,
- oxyacetylene welding,
- shielded-metal arc welding,
- flux-cored arc welding,
- submerged arc welding,

- gas metal arc welding,
- electroslag welding,
- gas tungsten arc welding,
- plasma-transferred arc welding,
- and laser cladding.

Among the various processes, the principal differences lie in the welding efficiency, the manufacturing cost, and the dilution rate. They can be grouped as gas welding, arc welding and high-energy beam welding. Several processes will be described in the following sections.

3.1.2.1 Gas tungsten arc welding

Gas tungsten arc welding is also known as tungsten inert gas welding. The heat is produced by an electric arc between a non-consumable tungsten electrode and the workpiece during the process and then the hardfacing material is melted. As illustrated in Figure 3.1, an inert shielding gas would protect the electrode, the arc, the workpiece and the molten hardfacing alloy [7].

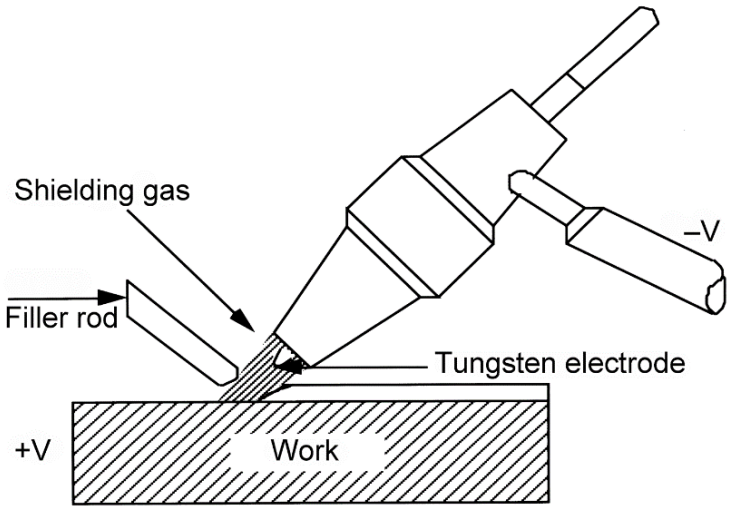

Figure 3.1: Schematic representation of a gas tungsten arc welding process [7].

Shanmugam and Murugan used a gas tungsten arc welding process to deposit the S6 alloy on the valve components made of low-carbon steel [8]. They studied the effects of processing parameters on dilution, bead width, and penetration of the hardfacing components using mathematical models. The prediction of geometry and controlling weld bead quality were presented in the graphical form, where the feed rate and current were found to play an important role among the studied parameters.

3.1.2.2 Plasma-transferred arc welding

PTA welding is quite similar to the gas tungsten arc hardfacing process. That is, an electric arc between a tungsten electrode and the workpiece is also used. However, the filler material is melted by the plasma formed when an inert gas such as argon flows through the electric arc. As shown in Figure 3.2, the deposited material, usually in the form of powder, is fed into the plasma area where it is fused and bonded to the workpiece.

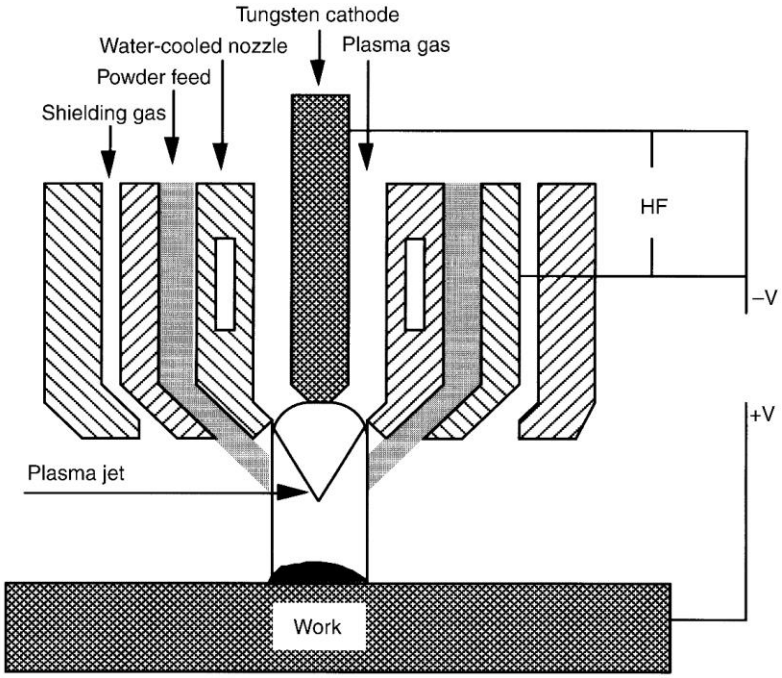

Figure 3.2: Schematic illustration of PTA welding process [9].

The PTA welding process is often used to weld hardfacing alloys on disks and seats of valves due to its advantages such as automation and precise control of welding parameters. However, it also has some disadvantages such as the expensive equipment and higher argon consumption than using the gas tungsten arc welding process.

Studies on the PTA hardfacing process are mainly focused on the processing parameters such as plasma gas flow rate, current, voltage, feed rate, preheat temperature, and welding speed. Mathematical models have been used to predict the weld bead geometry. For example, mathematical models developed by Marimuthu and Murugan could be applied to study the effects of processing parameters on the bead geometry [10]. They also used the mathematical models to optimize the processing parameters of S6 hardfacing alloy on valve seat rings made of carbon steel [11]. The results showed that the mechanical properties of the hardfacing components were

improved after the optimization. Tu et al. used the Taguchi-regression method to develop the optimal PTA hardfacing process to obtain high-quality hardfacing deposition [12]. They found that the two most significant processing parameters were hardfacing alloy and voltage, which agreed well with the experimental results.

In addition to the mathematical modelling, other researchers performed experiments to explore the influence of processing parameters on the microstructural and mechanical properties of the hardfacing components. By studying the surface finish, dilution, hardness, and wettability of an S6 weld bead, Takano et al. found that the two most significant processing parameters were current and the nozzle constriction [13]. Bharath et al. investigated the effects of the PTA welding processing parameters on the microstructure and mechanical properties of a Stellite F hardfacing onto X45CrSi93 steel used in the automotive industry [14]. They found that current levels played a significant part in dilution levels and further in hardness values. The above studies used a constant direct current. The pulsed current processing was found to result in finer and more homogeneous microstructure and lower dilution, and thus, the hardfacing component exhibited higher mechanical properties, as demonstrated by D'Oliveira et al. [15].

3.1.2.3 Laser hardfacing

Laser hardfacing is commonly referred to as laser cladding. Compared with the traditional welding processes, the main difference is that this process uses a high-energy laser beam as the heat source rather than an electric arc or a gas flame. As illustrated in Figure 3.3, the hardfacing alloy in the powder form is melted by a laser beam and bonded to the substrate.

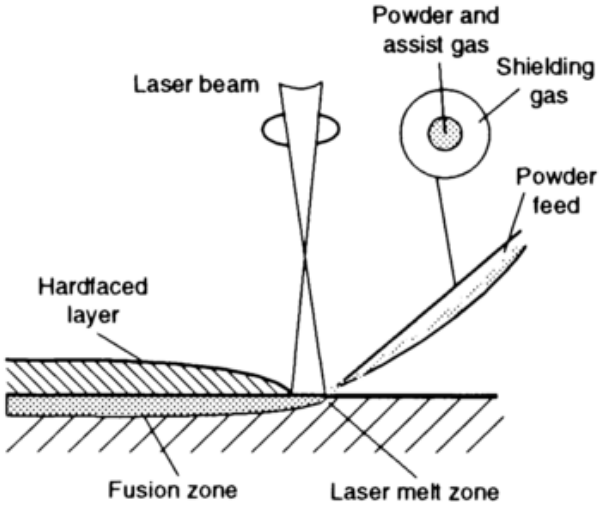

Figure 3.3: Schematic illustration of a laser hardfacing process [16].

The laser hardfacing process has several advantages. Due to its fast cooling rate, the heat input is low. Therefore, the HAZ and fused zones are small. The dilution level is also low. It is reported that laser hardfacing layer exhibited finer microstructure than that produced by the PTA welding process. Chang et al. deposited S6 on the seat surface of control valves using a laser hardfacing process and a PTA hardfacing process for comparison [24]. The laser hardfacing valve seats exhibited higher hardness, impact toughness, and impact wear resistance than the PTA hardfacing layers. However, as reported by D'Oliveira et al., the PTA hardfacing layers showed higher hardness and better microstructural stability after high-temperature exposure because of change in carbides morphology of the laser hardfacing layers [24].

The previous mentioned welding processes are all fusion welding. The solid-state welding process such as friction surfacing is also developed recently. During the friction hardfacing process, a metallic consumable rod is pressed against the workpiece under an applied load while moving parallel to the surface. The pressure and the heat generated through mechanical friction lead to an inter-diffusion process, and thereby a metallic bond between the plasticized material and the substrate is formed. Because no melting takes place, friction hardfacing is not a fusion hardfacing process. Therefore, no dilution of the substrate into the deposit occurs and the composition of the deposit is the same as that of the consumable. In addition, the low-heat input results in a small HAZ. Another advantage of friction hardfacing is that it is possible to join dissimilar materials that would be difficult to deposit by traditional fusion hardfacing processes.

We described the hardfacing processes above. For a given application, the suitable process can be selected according to the factors such as the form of the hardfacing alloy, cost, deposition rate, thickness, dilution rate and so on [17].

3.1.3 Hardfacing materials [18]

Hardfacing materials consist of a wide variety of alloys. From a metallurgical viewpoint, hardfacing materials can be classified into several types such as cobalt-, nickel-, and iron-based alloys.

3.1.3.1 Cobalt-based hardfacing alloys

Cobalt-based hardfacing alloys have been used for decades. In addition to the wear resistance, they also show corrosion and oxidation resistance at elevated temperatures. There are two types of

commercially available cobalt-based hardfacing alloys: carbide-containing Stellite alloys and Laves phase-containing Tribaloy alloys. Stellite and Tribaloy are both registered trademarks.

As seen in Table 3.1, the Stellite alloys are characterized by considerably high chromium contents, which give good oxidation and corrosion resistance at elevated temperatures. Chromium also participates in the formation of carbides. Elements such as tungsten and molybdenum are added to strengthen the cobalt matrix and to form the carbides. The microstructure of these alloys is composed of dendrites and carbides located in the interdendritic/intergranular regions (Figure 3.4). The common types of carbides are $M_{23}C_6$, M_7C_3, and M_6C. The S6 alloy is one of the most common cobalt hardfacing alloys. It contains higher contents of carbon and tungsten than S21 to promote carbide formation and enhance solid solution, respectively. The S21 alloy is rich in chromium and molybdenum and often used as a buffer layer between the substrate and the S6 alloy. The S6 and S21 are commonly selected as hardfacing materials for valve components.

Table 3.1: Nominal chemical compositions of three Co-based alloys (wt%) [19].

Alloy	**Co**	**Cr**	**W**	**C**	**Ni**	**Mo**	**Fe**	**Si**	**others**
S6	Bal.	28.5	4.6	1.2	<2.0	<1.0	<2.0	<2.0	<1.0
S21	Bal.	27.5	0.0	0.25	2.6	5.4	<2.0	<2.0	<1.0
Tribaloy T-400	Bal.	8.5	0.0	<0.08	<1.5	29	<1.5	2.8	<1.0

Tribaloy alloys are not strengthened by carbides but by Laves phase. Laves phase is an intermetallic compound having a stoichiometry of AB_2. As listed in Table 3.1, the contents of molybdenum and silicon are considerably high in these alloys. The microstructure of Tribaloy alloys is composed of a large volume fraction of hard Laves phase and cobalt matrix. Tribaloy alloys are recommended for the components requiring extreme wear and corrosion resistance at high temperatures [20].

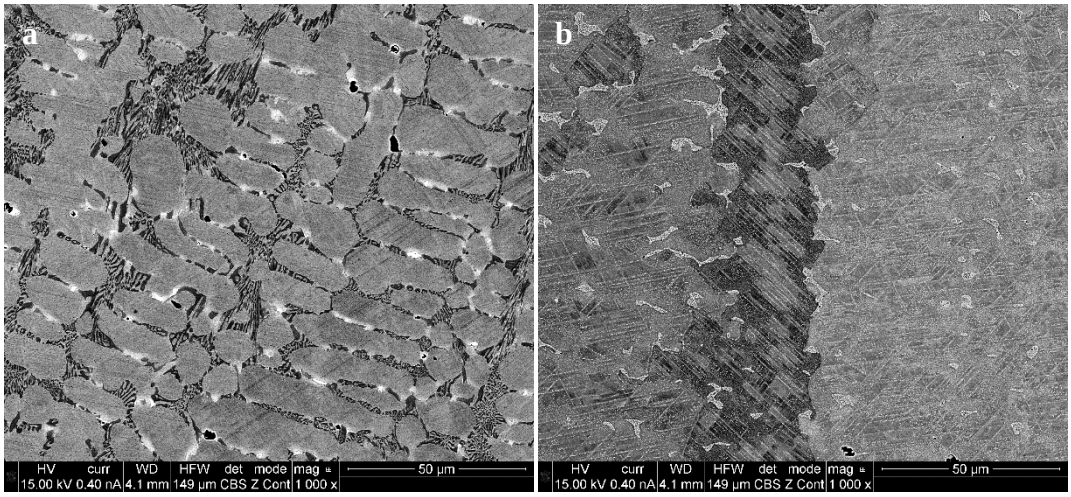

Figure 3.4: SEM micrographs of (a) S6 and (b) S21 showing the dendrite structure.

3.1.3.2 Nickel-based hardfacing alloys

Nickel-based hardfacing alloys are less expensive than the cobalt-based hardfacing alloys. There are three types of nickel-based hardfacing alloys available: carbide-containing, boride-containing, and Laves-phase-containing alloys. They are hardened by carbides, borides, and Laves phase respectively. Typical trade names of nickel-based hardfacing alloys are Deloro, Inconel and Colmonoy.

Table 3.2: Nominal chemical compositions of two Ni-based alloys (wt%) [21].

Alloy	Ni+Co	Cr	Mo	Nb+Ta	C	Mn	Fe	Cu	Si	others
IN82	Bal.	18.0-22.0	0.0	2.0-3.0	<0.1	2.5-3.5	<3.0	<0.5	<0.5	<1.3
IN625	Bal.	20.0-23.0	8.0-10.0	3.15-4.15	<0.1	<0.5	<1.0	<0.5	<0.5	<1.5

The chemical compositions of two Ni-based hardfacing alloys are shown in Table 3.2. High chromium contents in these alloys not only improve oxidation and corrosion resistance at elevated temperatures, but also act as carbide formers. Other elements such as niobium and molybdenum play dual roles as strengthening solutes and carbide formers. The dendrite microstructure of the two alloys is shown in Figure 3.5. It is composed of the nickel matrix and precipitates such as $M_{23}C_6$, MC, and M_6C carbides.

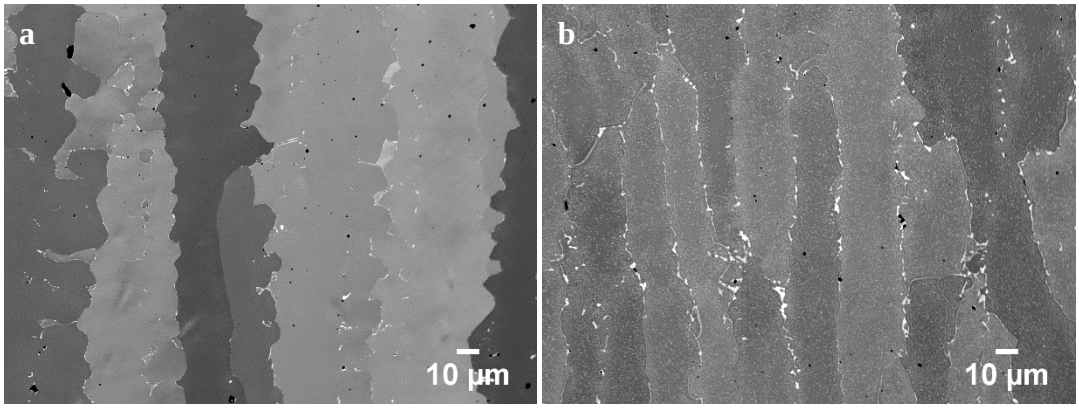

Figure 3.5: SEM micrographs of (a) IN82 [22] and (b) IN625 showing the dendrite structure.

3.1.3.3 Iron-based hardfacing alloys

Iron-based hardfacing alloys are more widely used than the previous mentioned cobalt- and nickel-based hardfacing alloys due to their low cost. They can be classified based on their microstructure such as pearlitic, austenitic, and martensitic steels. Typical trade names of iron-based hardfacing alloys are Delcrome, Incoloy and NOREM.

In addition to the above three types of hardfacing alloys. There are also copper-based hardfacing alloys and composite materials. For a given application, the suitable hardfacing alloy can be selected according to the factors such as wear resistance, cost, base material, oxidation resistance, corrosion resistance, hardfacing process, and so on.

3.1.4 Preheat treatment and post-weld heat treatment

During the hardfacing process, the microstructure and properties of the substrate are altered due to the high temperatures, which are higher than the melting temperature of the substrate. The properties of the hardfacing layer strongly depend on the thermal history. Preheating is necessary to reduce residual stresses accompanied during the hardfacing process. The PWHT is also necessary either to release residual stresses or to adjust mechanical properties such as to temper the hard martensite in the HAZ.

A few researchers studied the effects of preheating and PWHT on the properties of the hardfacing components. Alimardani et al. used modelling to investigate the thermal stresses of an Stellite hardfacing component [23]. They obtained a crack-free hardfacing component by preheating the substrate in a dynamic fashion. Deng et al. performed a PWHT of 710 °C for 3.5 h to Stellite 12 deposited on the heat-resistant steel X45CrSi9-3 using the PTA hardfacing process [24]. They

compared the hardfacing microstructure, the hardness and the residual stresses before and after the PWHT. The results showed that a more regular structure was obtained and the secondary $Cr_{23}C_6$ carbides were formed after the PWHT, leading to higher hardness. In addition, the residual stress measurement using XRD showed that the tensile residual stress was eliminated significantly after the PWHT.

3.2 Creep-resistant steels

Hardfacing alloys are many and various. There is also a broad range of base metals to be hardfaced. Creep-resistant steels are a type of alloys used at elevated temperatures for long duration. The application of creep-resistant steels includes the power generation, petroleum, and chemical industries. They have been developed for the purpose of improving the thermal power generation efficiency. Consequently, the cost and amount of fuels would be decreased and further CO_2 emissions would be reduced, which in turn reduces global warming.

3.2.1 Development of 9–12% Cr martensitic steels

Among the creep-resistant steels, 9–12% Cr martensitic steels are widely used in the power generation industry. Specifically, they find their applications in components such as turbines, valves, tubes, boilers, and steam pipes. They are high Cr-Mo steels. The Cr-Mo steels were firstly used in steam power generation plants in the 1920s [25]. In the 1940s, the 2.25% Cr-1% Mo steel was progressively developed and is still widely in use today [25]. Designated by ASTM as grade 22, this steel is further classified as T22 for tubing, P22 for piping, and F22 for forging. By adding the additional Cr to improve corrosion and oxidation resistance, grade 9 (9% Cr-1% Mo) was developed. Retrospectively, both these steels belong to the zeroth generation of martensitic/ferritic steels.

The development of all the 9–12% Cr martensitic/ferritic steel generations is summarized in Table 3.3. New alloying elements such as vanadium and niobium were introduced as carbide formers to improve precipitate strengthening in the first generation. Optimization of carbon, niobium and vanadium, and the addition of nitrogen constitute the second generation including grade 91 (modified grade 9) steel. In this work, the grade 91 steel was used as the substrate material to be hardfaced. For the third generation, some of the molybdenum was substituted by tungsten, and copper and boron were added. One of the representative steels is NF616 developed in Japan and

designated by ASTM as grade 92. The fourth generation represents all the efforts from late 1990s to today.

Table 3.3: Evolution of martensitic steels used in the power generation industry [25].

Generation	Period	Steel Modification	10^5 Rupture Strength, 600 °C (MPa)	Steel grades	Max use temperature (°C)
0	1940-60		40	T22, T9	520-538
1	1960-70	Addition of Mo, Nb, V	60	EM12, HT9, HT91	565
2	1970-85	Optimization of C, Nb, V, N	100	T91, HCM12	593
3	1985-95	Partial substitution of W for Mo and addition of Cu, B, N	140	NF616, E911, HCM12A	620
4	Present	Increase of W and addition of Co	180	NF12, SAVE12	650

3.2.2 Background on grade 91 and 92 steels

Grade 91 steel, a modified form of grade 9 steel, was originally studied at the Oak Ridge National Laboratory in the late 1970s [26]. It was selected as a structural material for reactor applications to replace grade 304 austenitic stainless steel and grade 22 martensitic steel [27]. Since the grade 91 steel offers higher creep-rupture strength and higher corrosion and oxidation resistance than the grade 22 steel, it was preferred to be used for high-temperature applications (>538 °C) in power plants in the 1990s [28].

However, the application of grade 91 is limited at temperatures above 593 °C in supercritical and ultra-supercritical power plants [28]. Later, a Nippon Steel's program led to develop the grade 92 steel (NF616) [29]. The chemical compositions of P91 and P92 steels in accordance with ASTM standard are shown in Table 3.4 [30]. Generally, grade 91 steel is composed of 9% chromium and 1% molybdenum, while grade 92 steel consists of 9% chromium, 1.8% tungsten and 0.5% molybdenum. The addition of tungsten contributed to the increase in stress rupture strengthening. Also, the addition of boron reduced the coarsening rate of $M_{23}C_6$ carbides and therefore improved its creep resistance, as reported by Abe [31].

Table 3.4: chemical compositions of P91 and P92 steels [30].

Grade		C	Mn	P	S	Si	Cr	Mo	V	N	Ni	Al	Nb	Ti	Zr	W	B	Fe
P91	min	0.08	0.3			0.2	8.0	0.85	0.18	0.03			0.06					Bal.
	max	0.12	0.6	0.02	0.01	0.5	9.5	1.05	0.25	0.07	0.4	0.02	0.10	0.01	0.01			
P92	min	0.07	0.3				8.5	0.3	0.15	0.03			0.04			1.5	0.001	Bal.
	max	0.13	0.6	0.02	0.01	0.5	9.5	0.6	0.25	0.07	0.4	0.02	0.09	0.01	0.01	2.0	0.006	

3.2.3 Microstructure of 9–12% Cr martensitic steels

The illustration of as-tempered microstructure of 9–12% Cr steels is shown in Figure 3.6. They have a complex microstructure composed of prior austenite grains that consists of original martensitic packets. These martensitic packets are further divided into martensitic blocks that are composed of several martensitic laths. Finally, as shown in Figure 3.6b, each martensitic lath is divided into sub-grains. $M_{23}C_6$ carbides (M represents Cr, Fe or other metallic elements) are found next to or at grain boundaries and MX carbonitrides (M represents V or Nb and X represents C or N) are dispersed homogeneously within the sub-grains as well as on sub-grain boundaries. These precipitates can pin dislocations and boundaries, resulting in an increase in creep strength.

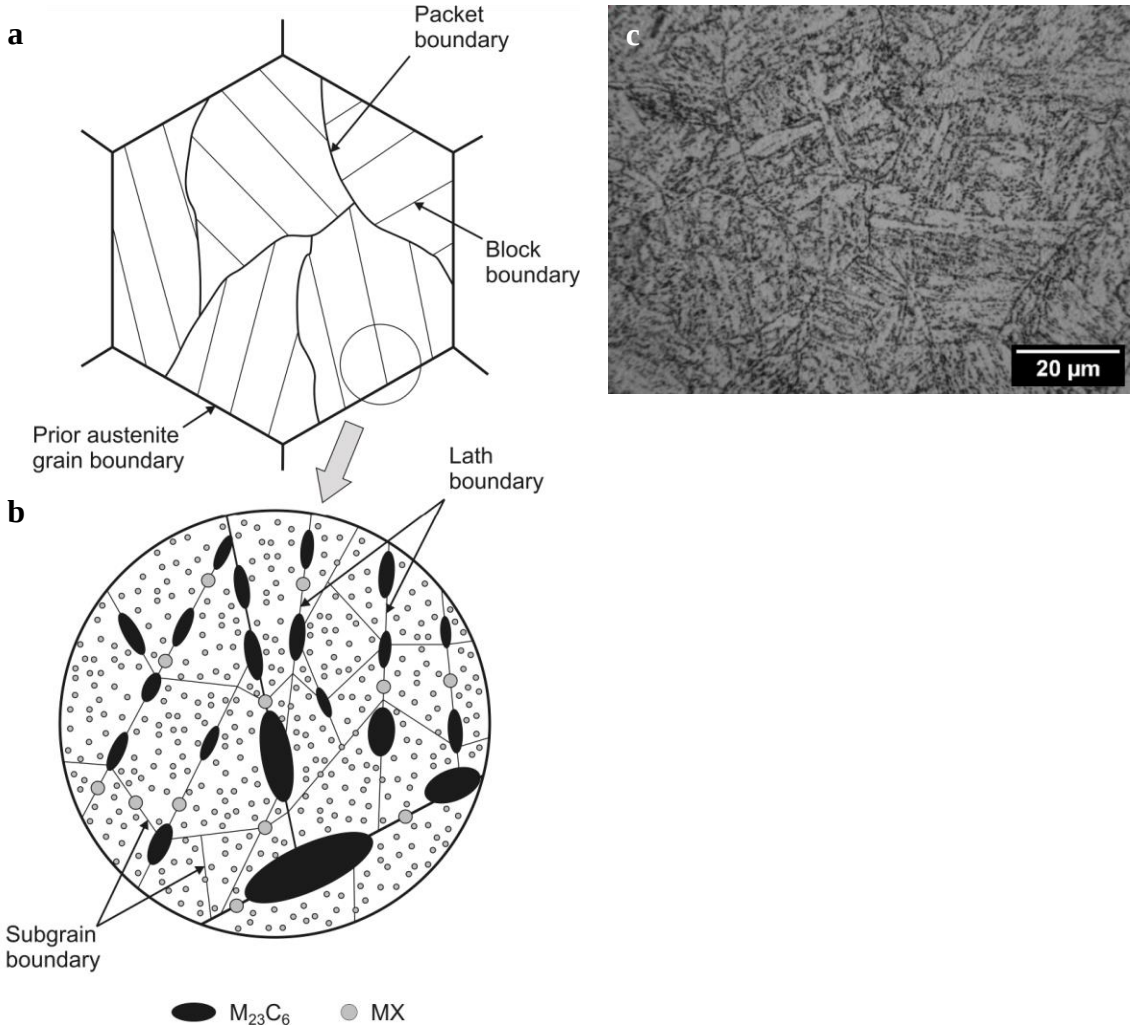

Figure 3.6: As-tempered microstructure of 9–12% Cr steels: (a) and (b) schematic illustration [32], and (c) optical micrograph.

In addition to the $M_{23}C_6$ carbides and MX carbonitrides found in the as-tempered microstructure, there are other phases precipitated during high-temperature exposure. Laves phase of the type $(Fe,Cr)_2Mo$ precipitated in a 12% Cr martensitic steel during long-term creep, as reported by Aghajani et al. [33]. W-rich Laves phase particles are reported to precipitate in grade 92 at temperatures up to approximately 750 °C [34]. Laves phase is known to remove Mo and W from the matrix and consequently the effect of solid solution strengthening by Mo and W is reduced. Therefore, Laves phase is considered to be detrimental to the strength of 9–12% Cr steels. However, Laves phase is reported to provide additional precipitation strengthening within the matrix especially at short times when the particles are small [35]. Z phase of the type CrXN (X represents Nb, V or Ta) is reported to precipitate in high-Cr (11–12%) steels much faster than that in 9% Cr steels [36]. Its precipitation causes the dissolution of MX carbonitrides and thus the creep strength of 9–12% Cr steels is reduced.

The 9–12% Cr steels are strengthened via the ways such as solid-solution hardening, dislocation hardening, precipitation hardening, and boundary hardening. However, microstructural degradation occurred during the long-term service, as illustrated in Figure 3.7. The degradation mechanisms include coarsening of precipitates such as the $M_{23}C_6$ carbides, formation of the Z phase and Laves phase, and so on.

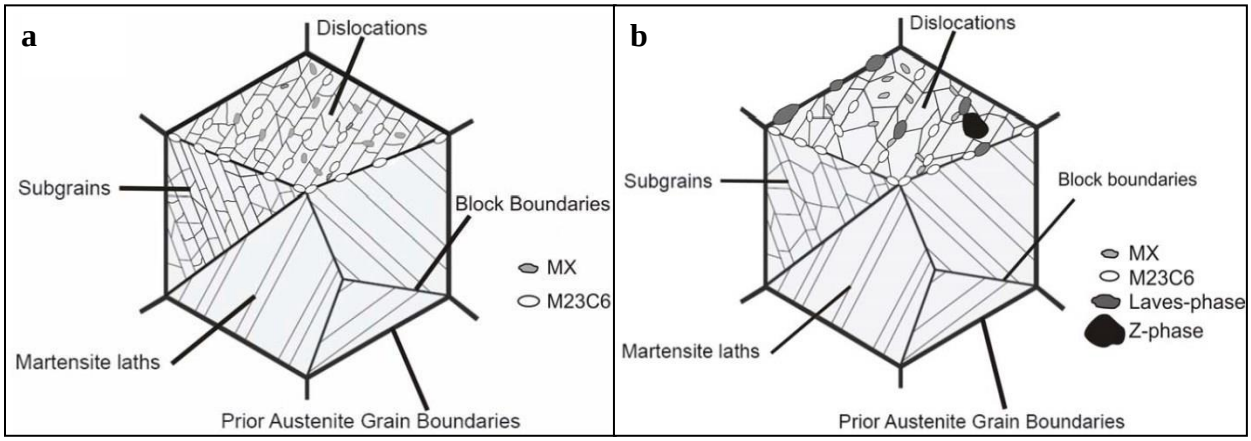

Figure 3.7: Schematic illustration of microstructure of 9–12% Cr steel (a) as tempered and (b) after creep exposure [37].

3.3 Failures of Stellite hardfacing in the power generation industry

As stated above, creep-resistant steels are widely used in the steam power generation industry. For example, grade 91 and 92 steels are used to manufacture valve components such as seats and disks. Although these steels offer creep strength over a range of temperatures, they do not provide wear resistance at elevated temperatures. To ensure durable valve function during operation, hardfacing alloys such as S6 and S21 are commonly deposited on the seats and disks of high-temperature valves.

However, the premature delamination failure of Stellite hardfacing layers in service has been regarded as a challenge in power plants. The failures usually take the form of disbonding and delamination of hardfacing layers from valves. One such example is shown in Figure 3.8, where it is seen that the delamination of an upstream seat ring was in progress. Due to these failures, valve function degenerated. The hardfacing debris shown in Figure 3.8b might damage other components and steam leakage might occur.

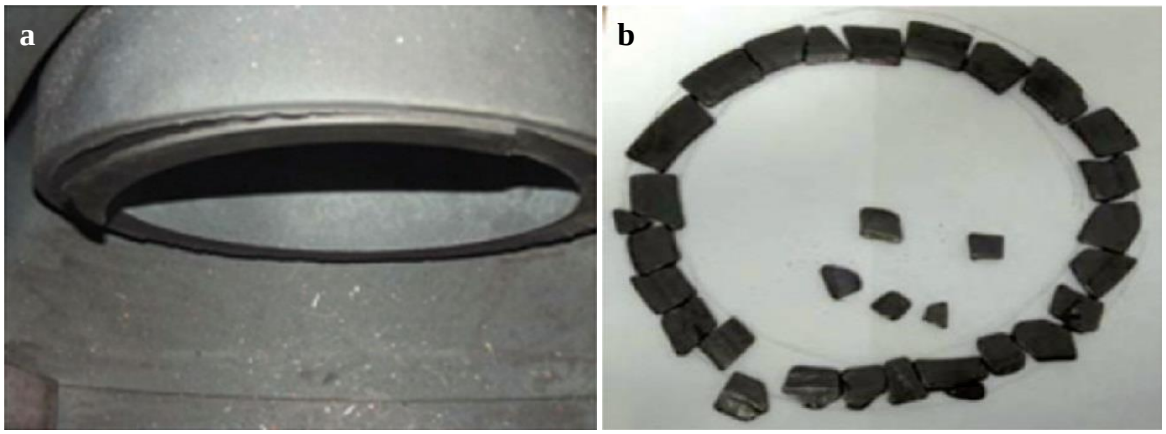

Figure 3.8: (a) Delamination of an upstream seat ring and (b) hardfacing debris from a combined stop and control valve [6].

EPRI established a committee on “Cracking and Disbonding of Hardfacing Alloys in Combined-Cycle Plant Valves” to investigate these failures. In 2015, they reviewed and summarized the failure events and their relevant information in a technical update report [3]. Table 3.5 shows the details of a few such failures, such as operation history, material combinations, and field experience.

Table 3.5: Summary of field experience in hardfacing disbonding from EPRI database [3].

	#1	#2	#3	#4	#5	#6	#7	#8
Opertation								
Plant type	HRSG	Coal-fired	HRSG	HRSG	HRSG	HRSG	Coal-fired	HRSG
Temperature (°F)	Unknown	Unknown	1070	1050	1050	1050	1083	1065
Service life	~10 years	~10 years	41,000 h	35,000 h	60,000 h	20,000 h	63,000 h	Unknown
Valve type								
Function	Stop	Stop	Stop and isolation	Isolation	Unknown	Isolation	Stop	Unknown
Location	Hot reheat	Main steam	Main steam and HRH	Main steam	Hot reheat	Hot reheat	Main steam	Unknown
Design	PSGV	Globe	Gate valve	PSGV	PSGV	PSGV	Unknown	PSGV
Material								
Seat/disc	Grade 22	Grade 11	Garde 91	Grade 22	Garde 91	Grade 22	Garde 91	Garde 91
Buffer layer		Unknown	S21		S21			
Top layer	S6	S6	S6	S6	S6	S6	S21	S6
Analysis notes								
Interfacial cracking	Yes	Yes	Yes	Yes	Yes	Yes	Yes	Yes
Observed bonding	Yes	Yes	Complete	Yes	Yes	Yes	Yes	No

Notes: Service life describes when disbonding was discovered, generally during inspection. Failures may have occurred earlier in life.

PSGV=Parallel sliding gate valve, HRH=Hot reheat section of a boiler, HRSG=heat recovery steam generator

A few studies were carried out to comprehend this specific failure mechanism. Hattel observed a crack at the interface between the S6 and P91 steel and the entire S6 hardfacing layer could be removed with light tools [38]. Later, he used the commercial software package DICTRA to simulate carbon migration across the fusion line in process and service. He found that a 10 μm decarburized zone in the P91 steel was formed close to the fusion line. Thus, the strength of this decarburized zone was reduced. In addition, the residual stresses were present at the fusion line. Therefore, the two factors caused the delamination.

Nevertheless, Leinenbach et al. reported the formation of a hard layer between the steel and the S6 alloy after aging at 600 and 625 °C [39]. They found that this layer consisted of a $M_{23}C_6$-type carbide, a BCC α phase, and a Cr-rich α' phase. Lolla et al. studied an ex-service component after approximately 60000 h of operation in steam conditions of 566 °C and 3.66 MPa [4]. In addition to the α phase and the $M_{23}C_6$ carbides, they found a Cr-enriched σ phase at the fusion line. This σ phase was characterized to be the hardest among the studied phases, 11.7 GPa. They believed that the σ phase was responsible for the delamination. EPRI also agreed with this conclusion in their technical update report [3].

After the detailed documentation of ex-service components, EPRI performed thermodynamic simulations to predict the possible phases at high-temperature exposure over a range of alloy combinations [40]. The deleterious σ phase was predicted not to precipitate when applying nickel-based filler materials as a buffer layer between the martensitic steels and the cobalt-based hardfacing alloys. Three nickel-based filler materials including IN82, Inco Weld A and EPRI P87 were recommended by EPRI [41]. However, the nickel-based hardfacing components should be validated experimentally.

The application of IN625 filler material between alloy Deloro 50 and the modified 9Cr-1Mo steel was observed to facilitate crack-free deposition due to bridging the thermal gap during the hardfacing process, as reported by Chakraborty et al. [42]. They also found that the ductile IN625 buffer layer prevented the increase in the Fe dilution in the top layer.

In the present work, we would further investigate the causes of delamination of high-temperature valves. In addition, we would evaluate the nickel-based IN82 and IN625 buffer layers to increase the durability of Stellite hardfacing components.

CHAPTER 4 EXPERIMENTAL METHODOLOGY

This chapter describes the experimental procedures and tools that have been used to obtain the information presented in this work. First, sample preparation for stress measurements and for mechanical testing are introduced. Then, the mechanical characterization approaches including indentation testing, Charpy impact testing, and tensile testing coupled with digital image correction are presented. Following the mechanical testing, the microstructural characterization techniques, including the fundamentals of their uses, are addressed. Finally, measurements of residual strains/stresses using neutron diffraction are described.

4.1 Materials and hardfacing deposition

Grade 91 steel was used as the substrate. There were three buffer layers: S21, IN82 and IN625. Two layers of S6 were applied on the buffer layers. Their combinations and deposition are listed in Table 4.1. The main PTA welding conditions are presented in Table 6.2 of article 1—chapter 6.

Table 4.1: Three types of hardfacing configurations.

Base material	Welding method	Buffer layer	Top layer
Grade 91	PTA	S21	S6
Grade 91	PTA	IN82	S6
Grade 91	PTA	IN625	S6

4.2 Sample preparation for strain/stress measurements

A hardfacing component is shown in Figure 4.1. After hardfacing deposition, these hardfacing components were in the as-welded condition. A PWHT of 760 °C for 2 h was performed on these hardfacing components to release residual stresses. After the PWHT, they were in the as-tempered (AT) condition. Further aging was conducted on these components in accordance with the information provided in Table 4.2. As shown in Appendix A, these components were machined

into the geometry suitable for neutron diffraction measurements. In addition, reference samples were machined from these components in accordance with Appendix B.

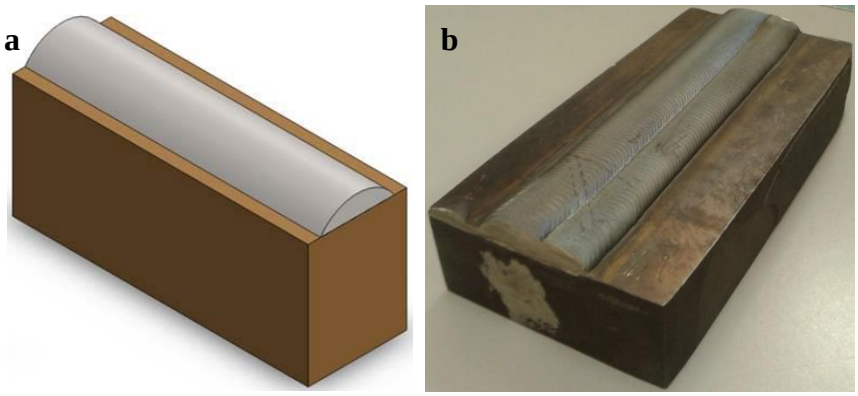

Figure 4.1: Hardfacing component: (a) illustration and (b) manufactured.

Table 4.2: Sample conditions used for neutron diffraction measurements.

Number	1	2	3	4	5
Condition	As welded	760 °C for 2 h (AT)	550 °C for 1008 h	650 °C for 1008 h	700 °C for 1008 h

4.3 Manufacturing of the hardfacing assembly

As shown in Figure 4.1a, the thickness of the hardfacing was limited, approximately 6 mm. It is a challenge to evaluate the hardfacing interface using mechanical testing. Three assemblies were manufactured to meet this challenge. The assembly manufacturing process for mechanical testing of the three types of interfaces is presented in Figure 7.1 of article 2—chapter 7. The drawings of these assemblies are given in Appendix C. The three produced assemblies were cooled in air to room temperature, followed by a PWHT of 760 °C for 2 h to temper the HAZ of the grade 91 steel and release residual stresses. The cross-section of an etched hardfacing assembly is shown in Figure 4.2.

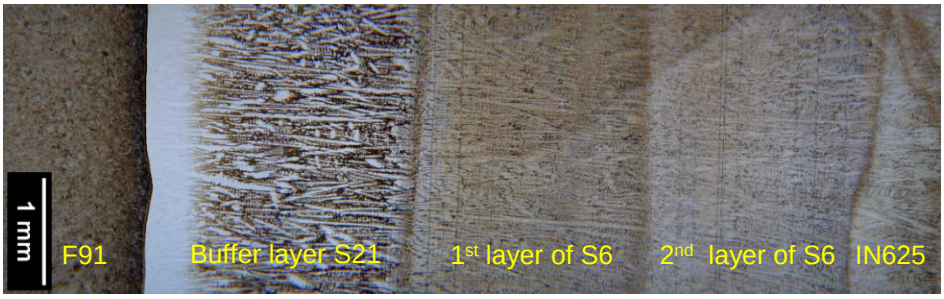

Figure 4.2: A montage of 5× optical images showing the cross-section of a hardfaing component: F91 base material, buffer layer S21, 1st and 2nd layers of S6, and filler material IN625.

4.4 Aging

The bars (Figure 7.1d) cut from the assemblies were aged under ambient atmosphere according to the temperatures and times given in Table 4.3. The four temperatures were selected to simulate service temperatures (550 °C), to accelerate the aging process, or to represent conditions that are more demanding (600, 650 and 700 °C). Grade 91 is tempered at temperature ranging from 730 to 800 °C [43]. The PWHT of 760 °C for 2 h is generally used in field after welding. Thus, it is hypothesized that the selected aging temperatures did not significantly influence the base material microstructure and properties. Characterization of the samples aged for 30000 h is not within the scope of this PhD project.

Table 4.3: Aging conditions of the three types of hardfacing components.

Temperature (°C)	550	600	650	700
Duration (h)	1008	1008	1008	1008
	3600	3600	3600	
	8760	8760	8760	
	30000	30000	30000	

4.5 Machining

Charpy U-notch specimens were machined from the aged bars and the as-tempered bars. The drawing of the Charpy U-notch specimen is provided in Appendix D. The interface between the grade 91 steel and the buffer layer were centered in the notch, as shown in Figure 4.3. The dimensions of Charpy U-notch specimens were 55 mm × 10 mm × 10 mm with a 5 mm deep notch having a 1 mm tip radius which is in accordance with ASTM E23 standard [44].

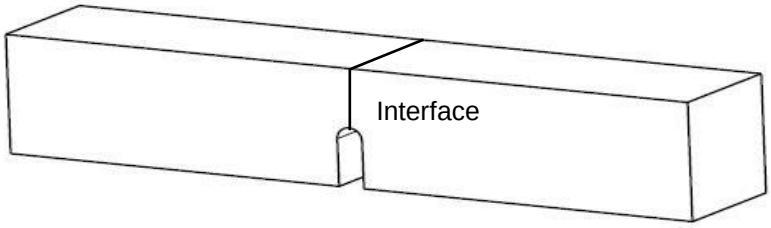

Figure 4.3: The three-dimensional illustration of a Charpy U-notch specimen.

Tensile specimens were also machined from these bars. The drawings of tensile specimens are provided in Appendix E. As shown in Figure 4.4a, there are two types of specimens. One type was notched and the other type was straight shank. The interface between the grade 91 steel and the buffer layer were centered in the straight shank. The dimensions of straight-shank tensile specimen were in accordance with ASTM E8 standard [45]. Similar as the Charpy U-notch specimen, the interface between the grade 91 steel and the buffer layer were also centered in the notched tensile specimens.

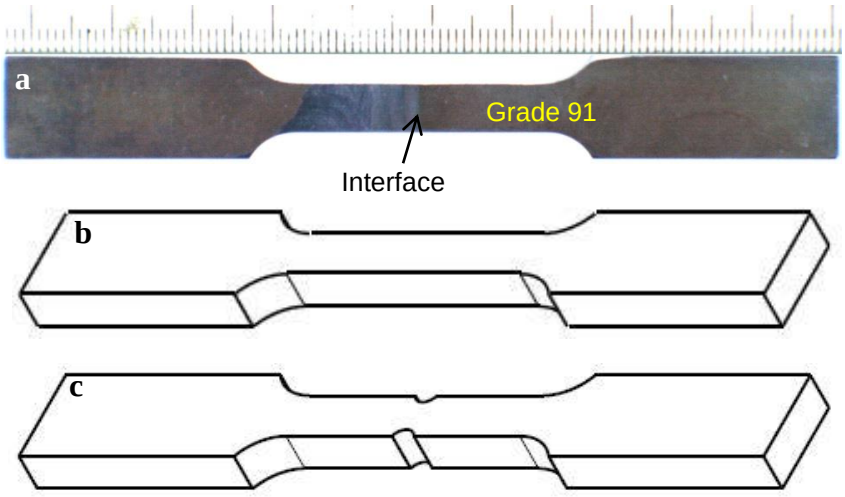

Figure 4.4: (a) A machined straight-shank tensile specimen, (b) its three-dimensional illustration, and (c) three-dimensional illustration of the notched tensile specimen.

4.6 Metallographic techniques

The hardfacing components in the as-tempered condition and the aged conditions listed in Table 4.3 were cut and mounted in conductive resin. The cross-sections of hardfacing components were mechanically ground up to 1200 grade silicon carbide paper, and then followed by mechanical polishing using 6, 3 and 1µm diamond suspensions. For optical microscopy observation, the cross-sections were etched with Kalling's No. 2 reagent (5 grams $CuCl_2$, 100 ml Hydrochloric acid and 100ml Ethanol) at room temperature. When preparing for SEM and EBSD observation, the cross-sections were further polished with a 0.04 µm mixed colloidal silica suspension (150 ml distilled water, 150 ml standard colloidal silica suspension and 30 ml H_2O_2). After polishing, the mounted samples were ultrasonically cleaned in acetone and isopropanol. To observe the crack propagation of Charpy specimens, the cross-sections were etched with Kalling's No. 2 reagent to reveal the material sections. The fractured Charpy specimens were mounted in conductive resin, and their cross-sections were ground and polished for SEM observation. For the base material grade 91, samples were etched using Vilella's reagent (1g picric acid, 5ml hydrochloric acid and 100ml ethanol) for around 30 s at room temperature.

4.7 Mechanical characterization

4.7.1 Indentation testing

Indentation testing is a method used for decades to characterize the mechanical properties of materials. During the testing, an indenter of known geometry is pressed into the surface of a material and then a permanent indentation is left in the material. In depth-sensing indentation, the load and the displacement of the tip are continuously monitored and recorded during loading and unloading cycles. Thus, a load-displacement curve is obtained, as shown in Figure 4.5. Both elastic and plastic deformation of the tested material occur during loading while the unloading part only involves elastic deformation. Consequently, the hardness and Young's modulus can be extracted from this load-displacement curve using the methodology proposed by Oliver and Pharr [46].

Hardness measures the resistance of a material to deformation due to a compression load. It is used for comparison and cannot be considered a fundamental property of a material. There are a few classic standard indentation tests, such as Brinell, Rockwell and Vickers hardness tests. They differ

from one another in the geometry of the indenter, the load used, and so on. As for the depth-sensing indentation, hardness can be expressed as:

$$H = P/A \qquad \text{Equation 4.1}$$

where P is the applied load and A is the projected contact area. It is essentially the contact pressure and is commonly expressed in GPa.

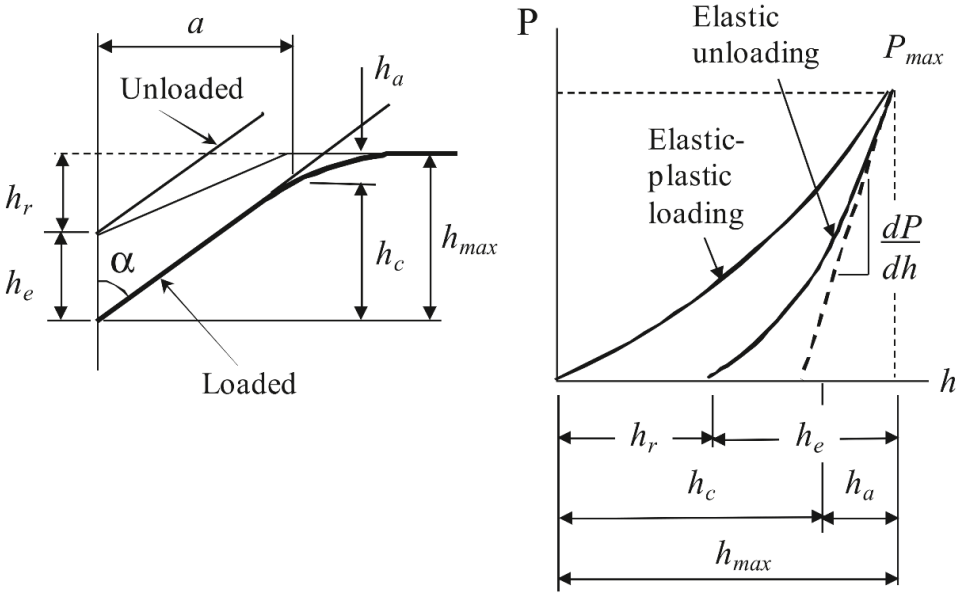

Figure 4.5: Depth-sensing indentation: (a) schematic representation of the cross-section of an indentation at full load and unload and (b) typical load-displacement curve for elastic–plastic loading followed by elastic unloading [47].

In this project, both Vickers and Berkovich indenters were used to evaluate the hardness of the samples on different scales. Micro-indentation measurements on the cross-sections of the hardfacing components were employed using an Anton-Paar (formerly CSM Instruments) Micro-Combi Tester equipped with a diamond pyramidal tip with a Vickers geometry. To measure the hardness of individual phases at the interfaces, nanoindentation was performed on the cross-sections of the hardfacing components by a Bruker Triboindenter 950 (formerly Hysitron Inc.) equipped with a Berkovich diamond tip. The testing procedure followed the standard ISO14577-1 [48]. Prior to testing, the area function of each tips were calibrated using fused quartz as a reference. For micro-indentation measurements on the cross-sections, the load function was composed of a 30 s linearly increased loading segment, a 15 s constant period at a maximum load 5 N, and a 30 s linearly decreased unloading segment. For micro-indentation measurements on the

F91/S21 interfacial layer, the load function was composed of a 30 s linearly increased loading segment, a 15 s constant period at a maximum load 200 mN, and a 30 s linearly decreased unloading segment. For nanoindentation measurements, the load function was composed of a 5 s linearly increased loading segment, a 2 s constant period at a maximum load 2 mN, and a 5 s linearly decreased unloading segment.

4.7.2 Charpy impact testing

Charpy impact testing is commonly used to evaluate the fracture toughness of materials at a very high-strain rate. A standard notched specimen is supported horizontally and then received an impact from a pendulum on the side opposite that of the notch. The energy absorbed by the specimen is measured and recorded, which is equal to the difference between the potential energies of the pendulum before and after the impact. The results obtained are qualitative and used to make comparisons between different materials or conditions on a material's toughness. This test is defined by the ASTM standard E23 [44]. As shown in Figure 4.6, there are three types of notched specimen geometry. The notch, on the side away from the pendulum, is used to cause a stress concentration to force the failure at this location in the specimen.

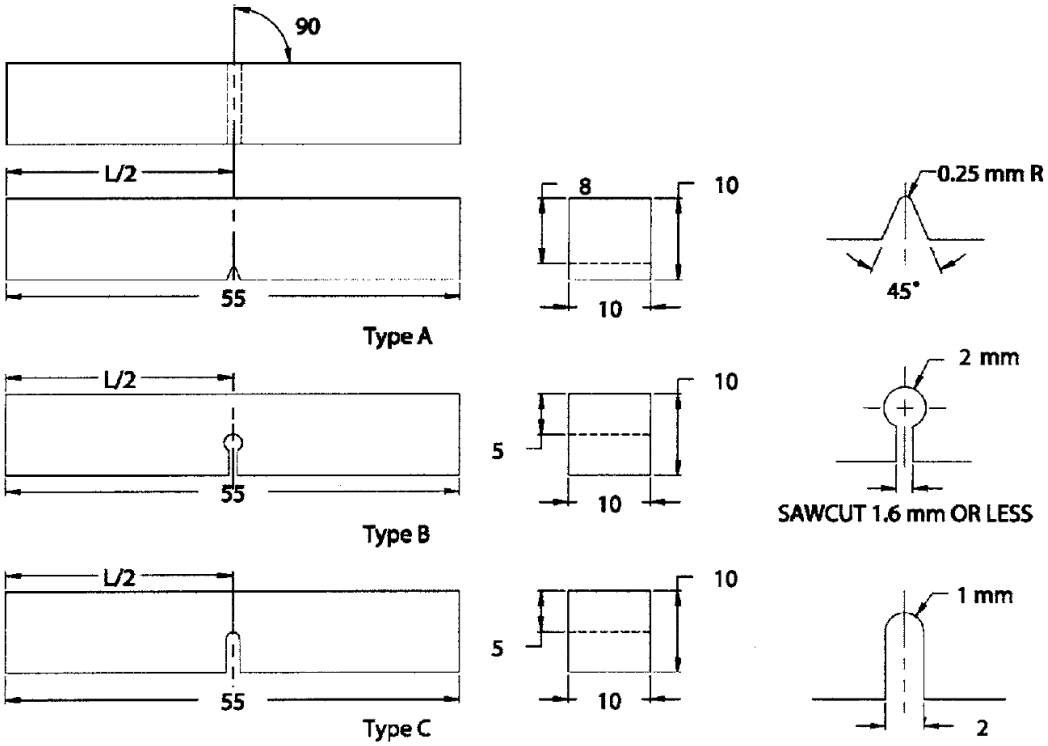

Figure 4.6: There types of Charpy (simple-beam) specimens [44].

U-notch (Type C) was selected over V-notch for the purpose of increasing the probability of positioning the interface in the highly stressed area in this project. According to the ASTM E23 procedure [44], an Instron pendulum impact testing machine in Velan was used to perform Charpy impact tests at room temperature. Fracta Software connected with the Charpy machine was used to calculate and record the energy absorbed by the specimen.

4.7.3 Tensile testing coupled with digital image correlation

Tensile testing is a test method to characterize the strength of materials in which a specimen is subjected to a uniaxial tensile load until failure. The tensile load changes while the specimen length increases during the testing. Compared with the Charpy impact testing, it is a slow-strain rate testing. In this project, tensile tests were conducted at room temperature using an Insight electromechanical machine equipped with a 50 kN load cell with a displacement rate of 0.8 mm/min. During tesing, an axial extensometer with a gage length of 25 mm was directly attached to the straight-shank specimens.

The tensile specimens were machined from the assemblies by welding several materials. Thus, the specimen is heterogeneous and the properties of materials vary from each other. To extract local properties of the hardfacing components, digital image correlation (DIC) is widely used during a global tensile test. DIC is an image analysis method using grey value patterns in digital images taken during the deformation process. It can be used to determine the strain field of an object under load after processing the digital images.

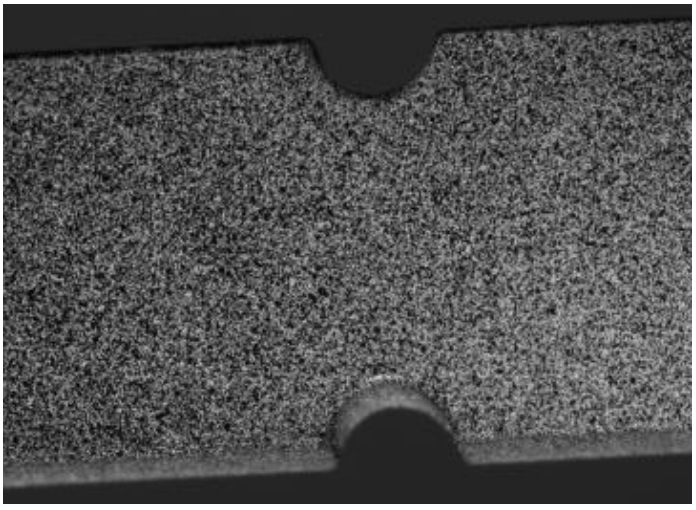

Figure 4.7: The speckle pattern on the surface of a tensile specimen.

The specimen used for DIC is speckle patterned. First, the surface of one side of a specimen was cleaned with methanol and dried. Then, a thin coating of white paint was applied on the surface of one side of the specimen. Finally, a random black paint was sprayed on the surface using an airbrush pen. The speckle pattern is shown in Figure 4.7. Measurements that are more accurate usually result from smaller particle size.

Two cameras were set to take pictures during the tensile testing. Before the testing, the system was calibrated with the help of calibration objects. Images were captured during different steps of deformation. VIC-3D software from Correlated Solutions was used to post-process the images to obtain local strain distributions. Local stress-strain curves can also be extracted.

Figure 4.8: Tensile testing setup combined with the DIC.

4.8 Microstructural characterization

4.8.1 Optical microscopy

Optical microscopy (OM) is a conventional method to reveal the microstructure. In this project, the microstructure of the etched samples was examined using a Zeiss optical microscope Axio Scope A1 equipped with a Lumenera's INFINITY3-6UR camera. This camera was connected to a computer acquisition software, Lumenera Infinity Analyze software. Therefore, the images were

clearly reviewed, captured, recorded, and stored in digital form. Two objective magnifications were used. That is, for overall images it was 5× while for detailed images it was 100×. The macro-examination of the Charpy specimens was undertaken using an Olympus stereo-microscope SZ2-STU1 equipped with a Clemex camera.

4.8.2 Scanning electron microscopy

Scanning electron microscopy (SEM) is also commonly used to analyze material's surface. For detailed microstructural observation, it has great advantages over OM due to higher spatial resolution. Instead of using photons, SEM uses a focused electron beam to scan over the surface of the studied sample. When the beam hits the sample, the accelerated electrons interact with the atoms at the surface. Thus, the interaction generates several signals including inelastically scattered electrons, elastically scattered electrons and characteristic X-rays. These emissions produced are collected by three different detectors. Each of them can be used to obtain different information about the sample.

The inelastically scattered electrons are primarily collected by a secondary electron (SE) detector. Due to the small volume of interaction, they are much more sensitive to surface topography. This SE mode is very similar to conventional optical microscopy, where contrast mainly comes from surface topography. To use this mode, the sample's cross-section has to be chemically etched. The fracture surfaces of Charpy specimens were examined using the SE mode as well. The elastically scattered electrons are detected in backscattered electron (BSE) mode. They are sensitive to the atomic number of the surface atoms. In the project, this BSE mode has been mainly used on polished samples to show the microstructure and distribution of the precipitates. Characteristic X-rays are also sensitive to the atomic number and can be used to identify the elements in the sample. This technique is known as energy-dispersive x-ray spectroscopy (EDS). However, the resolution of EDS is limited by the large interaction volume at high voltages. Thus, the voltage should be reduced when analyzing the small precipitate.

In this project, the microstructure and chemical compositions of the samples were characterized from the polished cross-sections using a JEOL JSM-7600F field emission SEM equipped with an Oxford Instruments X-Max EDS in high-current mode. The EDS mapping, line scans and spot measurements were analyzed using AZtec software with the built-in EDS quant standardizations. SEM and EDS were also both used to examine the fracture surfaces of Charpy specimens.

4.8.3 Electron backscatter diffraction

Electron backscattered diffraction (EBSD) is a characterization technique to obtain local crystallographic information from polycrystalline materials in an SEM. It is based on Kikuchi diffraction. When an electron beam hits the crystallographic planes, diffraction occurs if the angle 2θ between the incident electrons and the backscattered electrons satisfies Bragg's law:

$$2dsin\theta = n\lambda \qquad \text{Equation 4.2}$$

where n is a positive integer, d is the interplanar spacing and λ is the wavelength of the electron beam.

In three dimensional space, the diffracted backscattered electron beam is actually a cone as shown in Figure 4.9. When the cones intersect the flat phosphor screen, bands are observed. These bands observed on the phosphor screen are referred to as Kikuchi bands. These bands are directly associated with the crystal lattice structure in the sampled region. During an EBSD measurement, the polished sample is highly tilted in the chamber, approximately 70° from the horizontal, which increases the contrast in the diffraction pattern. At the same time, EDS mapping is also collected allowing simultaneously detection of chemical composition and crystallographic patterns. Consequently, the crystalline phases in the sampled region can be identified through automated EBSD indexing and simultaneous EDS acquisition.

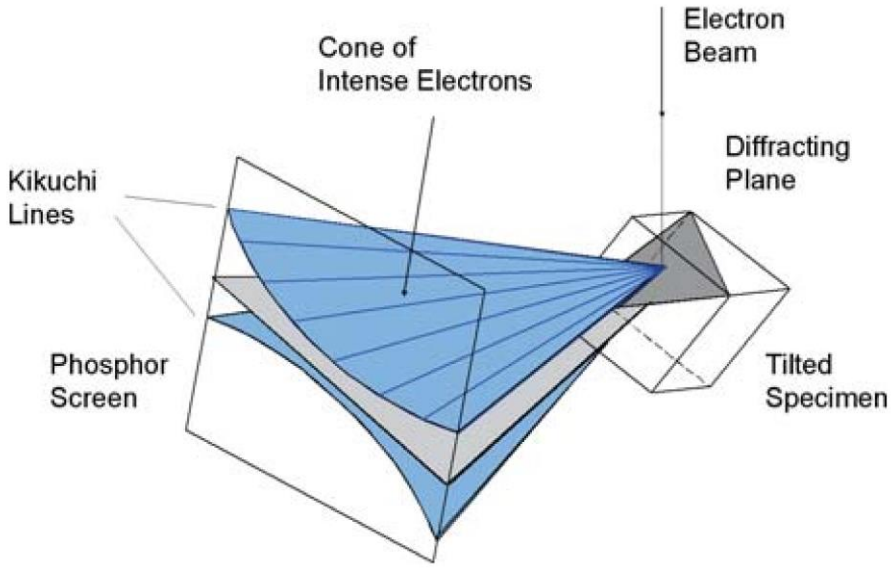

Figure 4.9: Schematic of the diffracting cones with respect to the diffracting plane, the sample, and the phosphor screen in three dimensional space [49].

In this project, the EBSD measurements was carried out on the polished cross-sections using an Oxford Instruments Nordlys Max2 detector. This detector was installed on a Zeiss Sigma field emission SEM in high-current mode at 20 kV. AZtec software was used to collect and index Kikuchi patterns. HKL Channel 5 software was used to post process the EBSD maps to identify the phases in the interfaces.

4.8.4 X-ray diffraction

X-ray diffraction (XRD) is usually used to determine the crystallographic characteristics of materials. When an incident X-ray beam hits the crystallographic planes at an angle θ, diffraction occurs according to Bragg's law:

$$2dsin\theta = n\lambda \qquad \text{Equation 4.3}$$

where n is a positive integer, d is the interplanar spacing and λ is the wavelength of the incident X-ray beam. From this equation, one can see that with the wavelength of the incident beam λ and the incident angle θ, the interplanar spacing d can be estimated. Consequently, the crystalline phases in the material can be identified through comparison with material databases.

In the context of this project, the three types of interfaces were characterized using a Rigaku SmartLab XRD equipped with a Cu 3 kW X-ray source.

4.9 Residual strain/stress measurements

During welding, residual stresses can be generated due to phase transformation and thermal contraction when the weld metal cools and solidifies. They may affect the performance of the hardfacing components and contribute to failures. Neutron diffraction can be used to measure the residual stresses, whose distinctive advantage over XRD lies in higher depth of penetration.

In this project, neutron diffraction measurements were performed using the L3 diffractometer of the Canadian Neutron Beam Centre, located at Canadian Nuclear Laboratories, in Ontario, Canada. The experimental setup and its schematic layout are shown in Figure 4.10 and Figure 4.11, respectively. A continuous/white thermal neutron beam is generated from the neutron source. Subsequently, a monochromatic neutron beam is obtained by inserting a large single-crystal monochromator in the continuous beam according to Bragg's law. The monochromatic beam passes through an aperture and then is diffracted by the polycrystalline sample; then the diffracted

beam passes through the other aperture and arrives at the detector. The gauge volume is defined by the two apertures. The measured lattice strain is the average value over the diffracting grains (satisfying Bragg's law) inside the gauge volume.

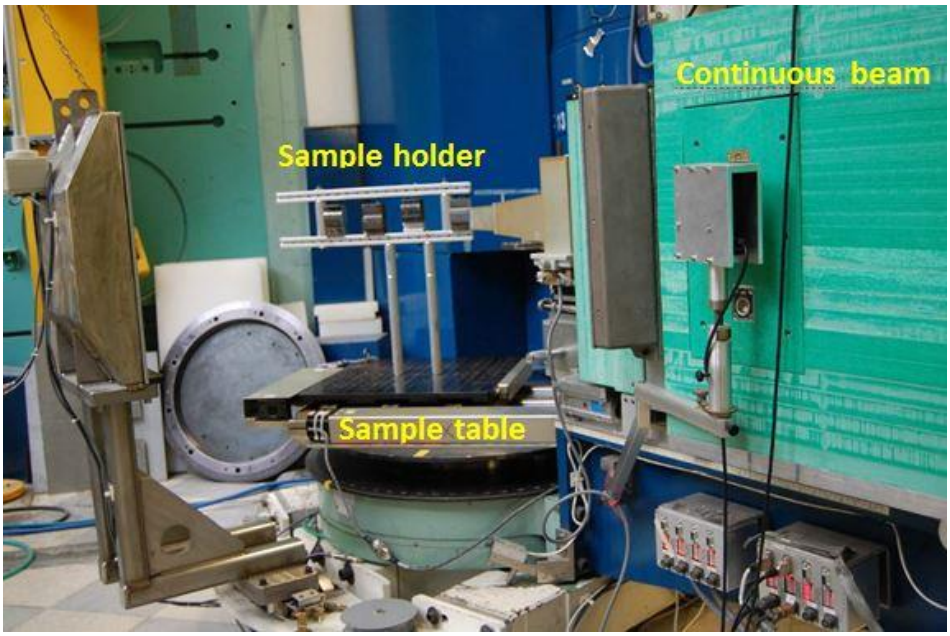

Figure 4.10: L3 Diffractometer in Chalk River.

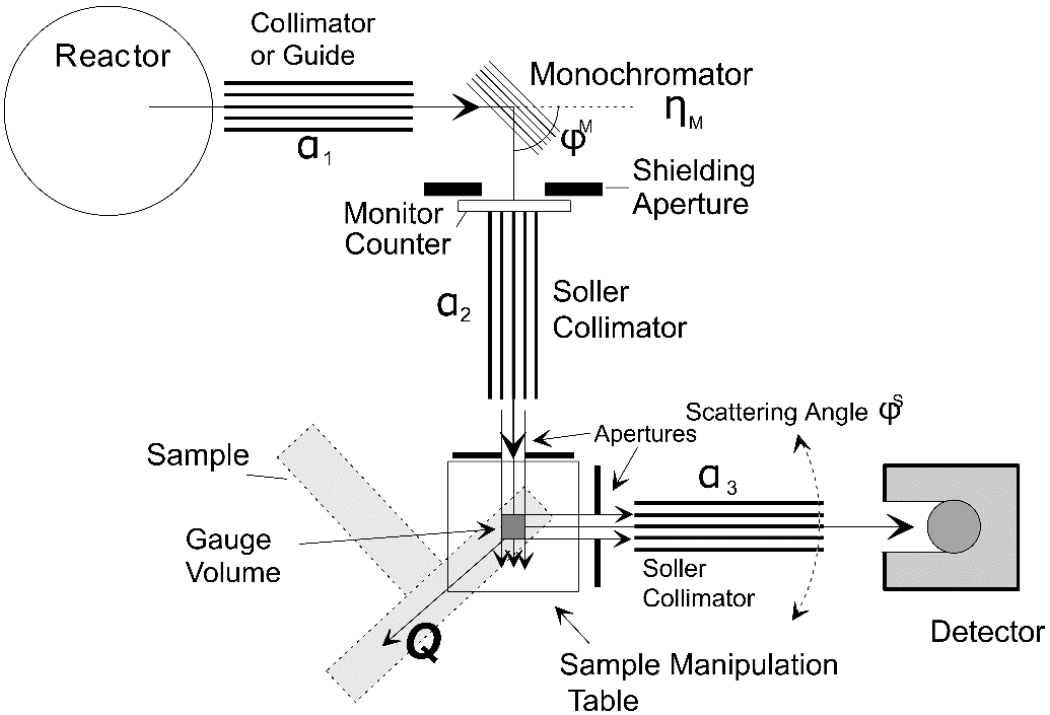

Figure 4.11: Schematic layout of the L3 Diffractometer for strain measurement [50].

After obtaining the lattice spacing of the strained sample, the strain-free lattice spacing is also measured and then the residual strain is determined:

$$\varepsilon = \frac{d-d_0}{d_0} \qquad \text{Equation 4.4}$$

where ε is the residual strain, d is the lattice spacing of the strained sample, and d_0 is the lattice spacing of the strain-free sample (reference sample). To avoid the changes in the lattice spacing that are not caused by stresses but by other factors such as chemical compositions, matchstick-like reference samples were machined using wire electrical discharge machining. It is assumed that the residual strains/stresses are relieved after machining. One example is shown in Figure 4.12, where the two matchsticks are parallel to the welding direction. The size of the cross-section of the matchstick was 1 × 1 mm^2. Due to the variation in chemical composition in the sample, the individual reference strain-free lattice spacings for each location were measured at exactly the same locations as the strained points.

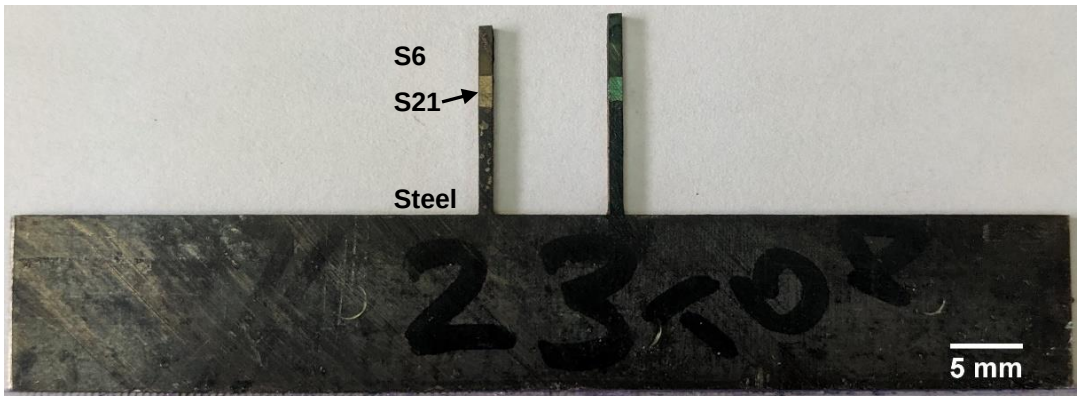

Figure 4.12: Matchstick-like reference samples.

The samples are mounted accurately on an automated-translation table. To measure the strains along three directions, the mounted samples are shown in Figure 4.13. For strains along the transverse and normal directions, a sampling volume of 0.75 × 0.75 × 30 mm^3 was used; for strains along the longitudinal direction, a sampling volume of 0.75 × 0.75 × 4 mm^3 was used. The blue diamonds in Figure 4.14 represented the sections of the sampling volumes for transverse and normal strains. For S21 hardfacing components in as-welded condition and after PWHT, two line measurements shown in Figure 4.14 were made at middle and a quarter location of the weld bead. For other hardfacing components, one line measurements were made at middle location of the weld bead. The wavelength of the incident beam was calibrated using a standard nickel powder reference

sample, which has accurately known lattice spacing. The wavelength was found to be 0.153 nm. Reflections of {311}, {211} and {311} were used for Stellite, grade 91 and Inconel, respectively. The diffraction peaks were fitted using a Gaussian function.

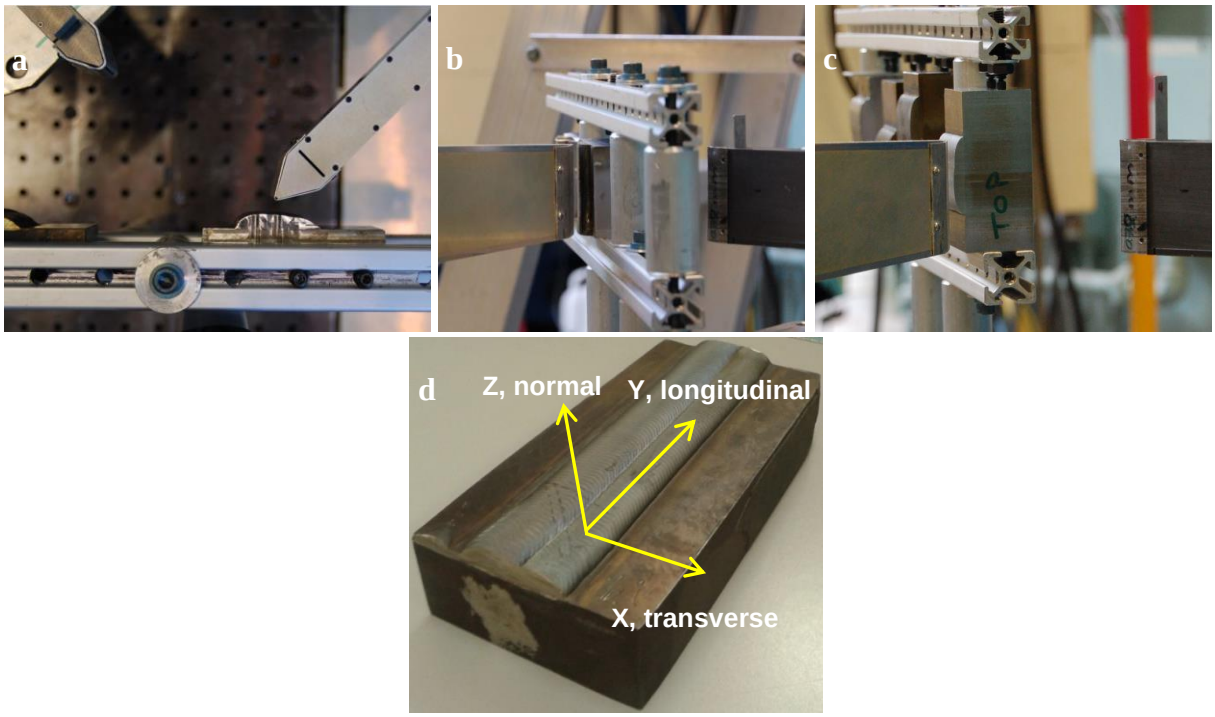

Figure 4.13: Mounted samples showing strain measurements along (a) normal, (b) transverse and (c) longitudinal directions; (d) a hardfacing component showing the three directions.

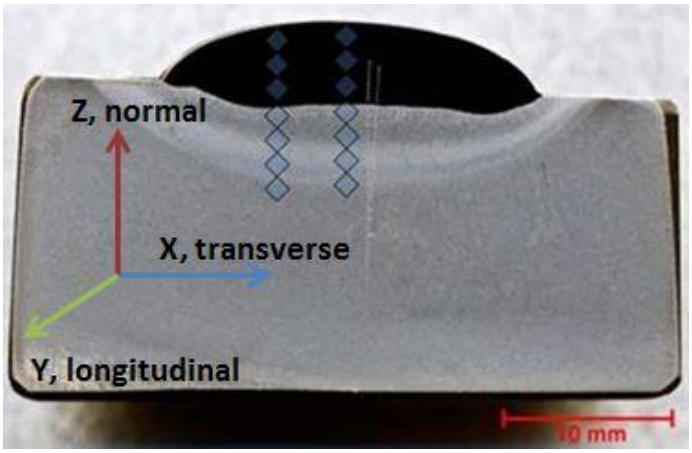

Figure 4.14: Cross-section of a hardfacing component with neutron diffraction measurement locations indicated.

From the obtained residual strains along the transverse (X), longitudinal (Y) and normal (Z) directions, the residual stresses are estimated using the generalized Hooke's law (the shear stresses are assumed to be zero):

$$\sigma_i = \frac{E}{1+\nu}\left[\varepsilon_i + \frac{\nu}{1-2\nu}(\varepsilon_X + \varepsilon_Y + \varepsilon_Z)\right] \quad i = (X, Y, Z) \qquad \text{Equation 4.5}$$

where σ_i is the stress along the transverse (X), longitudinal (Y) and normal (Z) directions, ν is Poisson's ratio, E is Young's modulus, and ε is the residual strain.

CHAPTER 5 EFFECTS OF THE PWHT ON MICROSTRUCTURE AND PROPERTIES OF THE HARDFACING COMPONENTS

During the manufacturing process, PWHT is usually considered as an important step because it can temper the microstructure and change the properties of hardfacing components. A common heat treatment practice at 760 °C for 2 h is employed for the deposited components after welding. How the PWHT would affect the microstructure and properties of the hardfacing components is presented in this chapter.

5.1 Effect of the PWHT on hardness

The hardness profiles of an S21 hardfacing component in the as-welded condition and after the PWHT are shown in Figure 5.1. The most notable observation was the significant decrease in hardness of HAZ in the steel after the PWHT. The peak hardness reduction reached as high as 49% after the PWHT. The PWHT tempered the HAZ of steel. In addition, S6 and S21 were hardened after the PWHT, which may be caused by precipitation of the carbides [24].

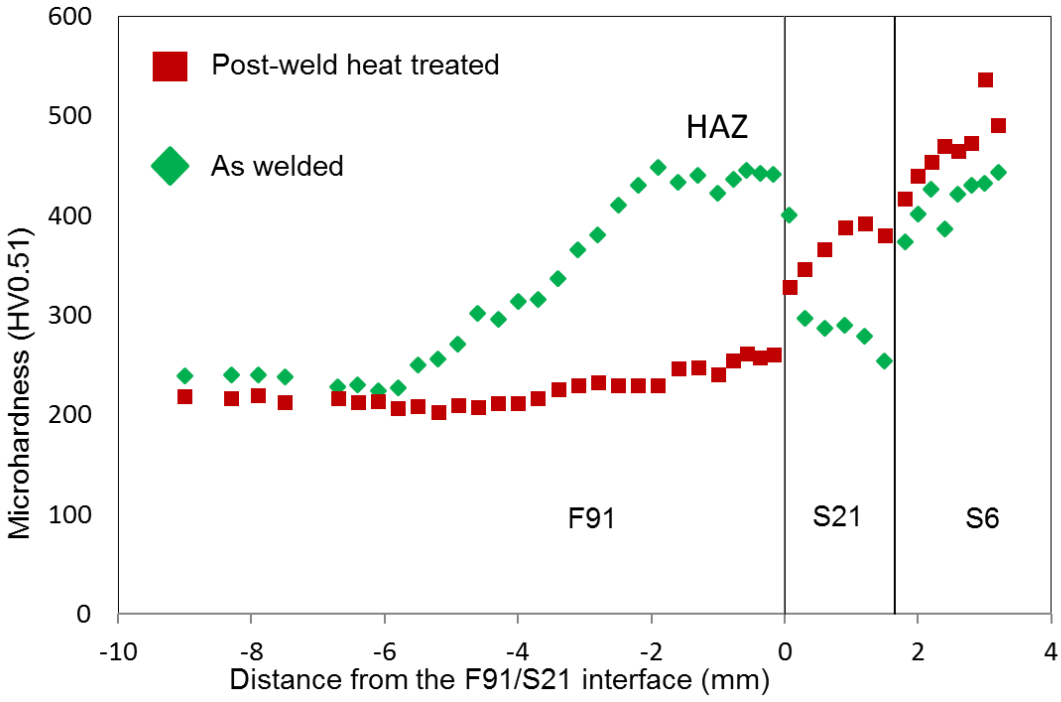

Figure 5.1: Hardness profiles of the S21 samples in the as-welded condition and after the PWHT.

5.2 Effect of the PWHT on steel microstructure

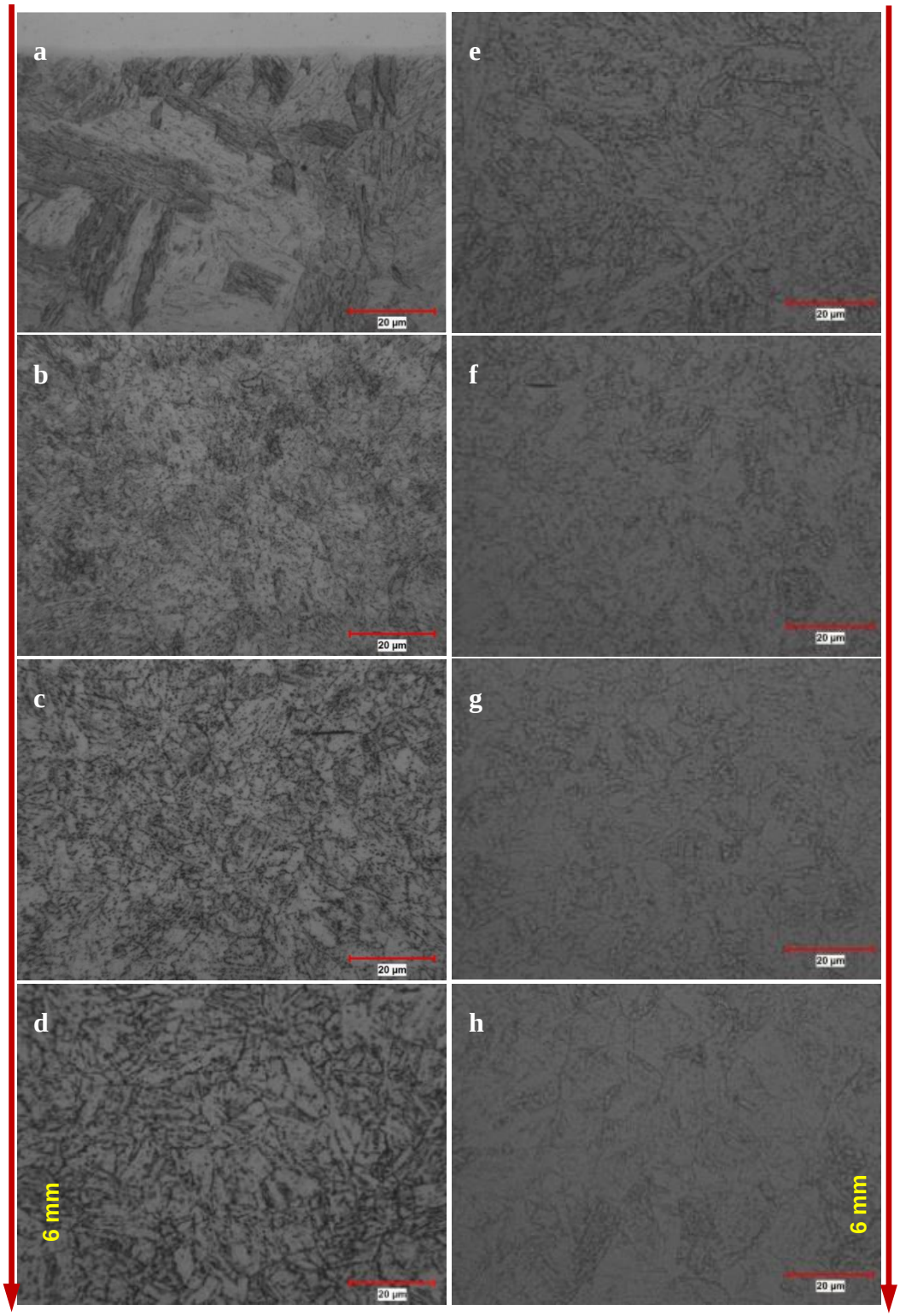

Figure 5.2: Microstructure change of the HAZ in the steel from the interface to the unaffected steel: (a), (b), (c), and (d) in the as-welded condition; (e), (f), (g), and (h) after the PWHT.

To comprehend the hardness reduction of HAZ in steel after the PWHT, its microstructure in the as-welded condition and after the PWHT is shown in Figure 5.2 (Figure 5.2e was taken close to the interface). During the hardfacing process, the heat input generated by welding leads to the formation of a HAZ in the steel next to the fusion line/interface. Phase transformations, dissolution of strengthening precipitates and re-precipitation of particles in HAZ occur in the thermal cycle [51]. As a result, the HAZ after welding can be divided into grain growth zone (close to the interface), grain-refined zone (in the middle of HAZ) and intercritical zone.

As shown in Figure 5.2a, the grain growth zone is adjacent to the interface and characterized by coarse grains. It is because this zone experiences the highest temperatures during welding and all the precipitates obstructing the growth of austenite grains would dissolve, leading to coarse grains of austenite. During cooling, the martensitic microstructure is formed and thus this zone is characterized by the highest hardness.

As shown in Figure 5.2b, the grain-refined zone is characterized by small prior austenite grains. It is a zone where the transformation into austenite is completed [52]. However, the grain growth is limited due to the pinning of the undissolved precipitates. During cooling, the martensitic microstructure is also formed.

The intercritical zone is shown in Figure 5.2c. It is a zone where the transformation into austenite partially occurred under the peak temperatures. The untransformed tempered-martensitic microstructure is tempered again. After cooling, the microstructure is composed of newly formed martensite and the original microstructure.

The unaffected microstructure is shown in Figure 5.2d. The zones in Figure 5.2e, f, g, and h after the PWHT are corresponding to the as-welded zones in Figure 5.2a, b, c, and d, respectively. Seemingly, not like the variation observed among the zones in Figure 5.2a, b, c, and d, zones in Figure 5.2e, f, g, and h were found to be quite uniform. The hardness of HAZ in the steel after the PWHT is comparable to that of the unaffected zone, as shown in Figure 5.1. Therefore, the reduction in hardness after the PWHT may be caused by the microstructure change.

5.3 Effect of the PWHT on residual strains/stresses

The results of residual strain/stress measurements are presented in this section. It should be mentioned that Dr. Michael Gharghouri, Senior Research Scientist at Canadian Nuclear Laboratories, assisted in completing the experiments and result analysis.

Figure 5.3 shows the distribution of residual stresses along three directions of the samples in the as-welded condition and after the PWHT. It should be noted that these stresses were distributed in the steel. Residual strains/stresses in the hardfacing layers were difficult to obtain. It might be due to the fact that the deposited hardfacing alloys are composed of large columnar grains, and thus it is hard to obtain high-quality diffraction peaks. As seen in Figure 5.3, residual stresses in the steel were significantly reduced after the PWHT. For the location 0.5 mm from the interface, the reduction in stresses after the PWHT ranged from 47% to 72%. All the stresses decreased as a function of distance from interface. They reached approximately 0 MPa at 6 mm from the interface. Transverse and longitudinal stresses were compressive and normal stress was tensile.

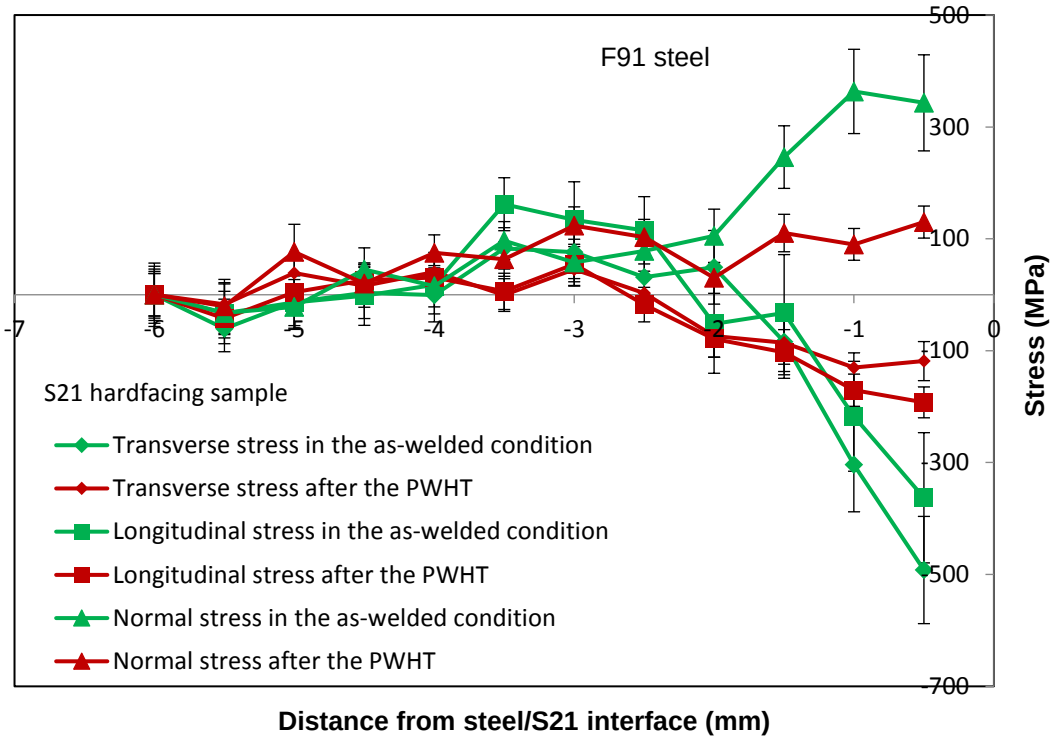

Figure 5.3: Residual stresses along three directions of the S21 samples in the as-welded condition and after the PWHT.

As shown in Figure 5.4a, the above measurements were obtained at the middle line of the weld bead. The measurements at a quarter line of the weld bead were also obtained. Figure 5.4b shows the transverse lattice strains at the middle and a quarter of the weld bead in the as-welded condition and after the PWHT. It is found that transverse lattice strains were reduced and changed into negative after the PWHT. Moreover, the PWHT homogenized the lattice strains across the hardfacing components. That is, the strain difference values observed between the points at the middle and a quarter of the weld bead were significantly reduced. Again, it is strongly recommended to conduct the PWHT to the as-welded components right away after the hardfacing process. Otherwise, distortion of components may occur.

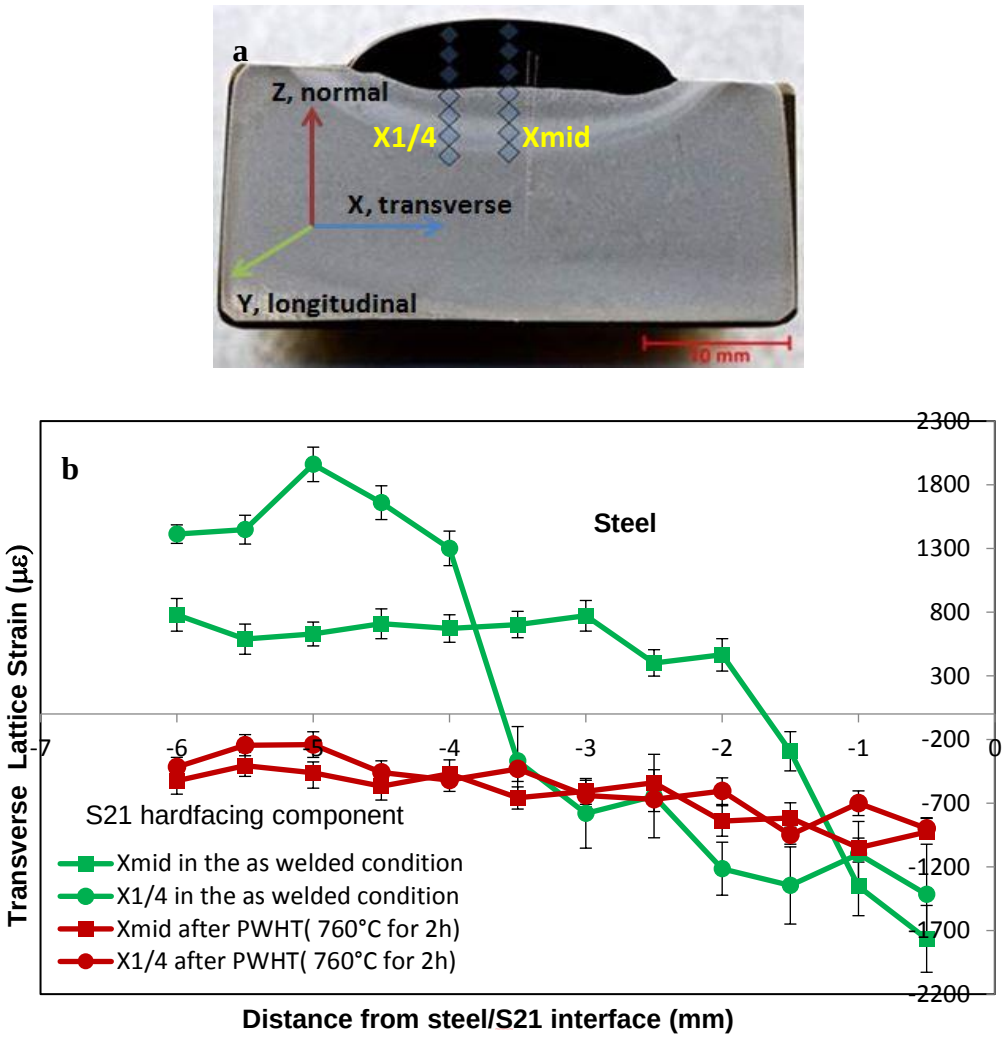

Figure 5.4: (a) A graph showing the measurements performed at the middle and a quarter of the weld bead and (b) transverse lattice strains across the weld in the as-welded condition and after the PWHT.

The stress distributions of the IN82 hardfacing components in the as-welded condition and after the PWHT are shown in Figure 5.5. Before the PWHT, the longitudinal stresses in steel were positive at greater depths, and getting increasingly more negative as the steel/Inconel interface was approached; after the PWHT, they almost fell in the negative region. For some locations in the IN82 layer, stresses were obtained. The tensile longitudinal stress in the IN82 hardfacing layer may be detrimental which help promote the crack propagation.

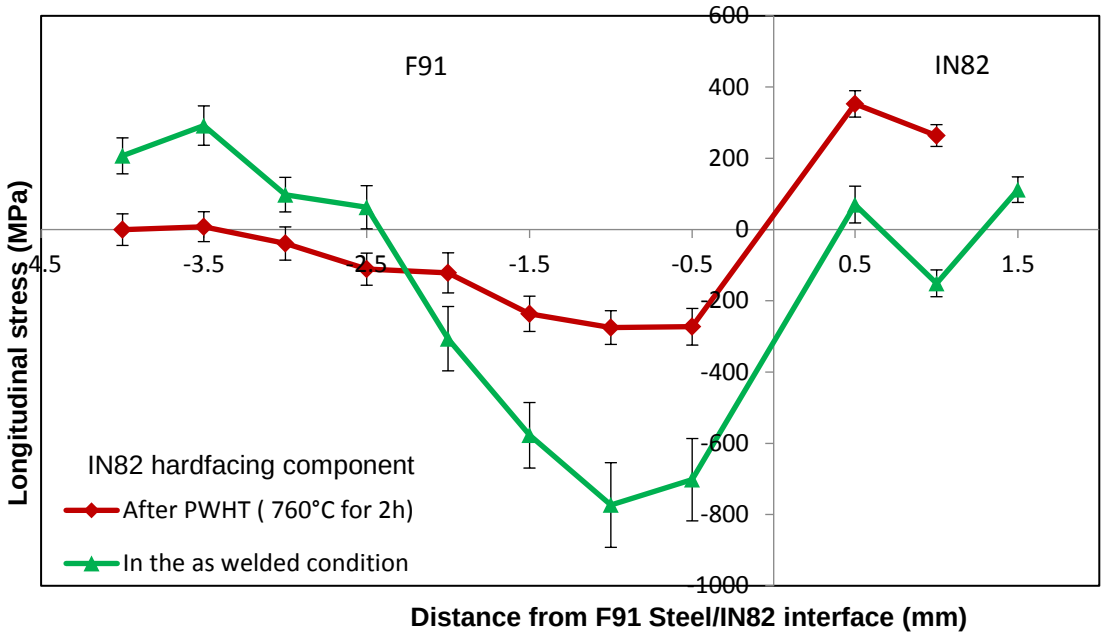

Figure 5.5: Longitudinal stress distribution of the IN82 samples in the as-welded condition and after the PWHT.

According to Figure 1.3, the thermal expansion mismatch values between the steel and the three types of buffer layers are different. Thus, it is expected that the three types of hardfacing components show different stress levels. However, the conclusive results could not be obtained, which may be due to the measurements, the instrument, the fabrication of samples and so on. More strain/stress distributions are provided in Appendix F.

CHAPTER 6 ARTICLE 1: THERMAL STABILITY OF A STELLITE/STEEL HARDFACING INTERFACE DURING LONG-TERM AGING

Yuxiao Wu[a], Etienne Bousser[a, b], Thomas Schmitt[a], Nabil Tarfa[c], Fadila Khelfaoui[c], Réjean René[c], Jolanta-Ewa Klemberg-Sapieha[a], and Myriam Brochu[a]

[a]Polytechnique Montréal, 2900 Boulevard Edouard-Montpetit, Montreal, Quebec H3T 1J4, Canada

[b]The University of Manchester, School of Materials, Manchester M13 9PY, United Kingdom

[c]Velan Inc., 7007 Côte-de-Liesse, Montreal, Quebec H4T 1G2, Ca nada

Published in the Journal of Materials Characterization

Abstract: Disbonding and delamination of Stellite hardfacing used in high-temperature valves have caused serious challenges in the power generation industry in recent years. To determine the microstructural factors that may contribute to the failures, Stellite 21 and Stellite 6 hardfacing alloys were deposited onto an F91 steel substrate using plasma-transferred arc welding. A series of aging experiments simulating service temperatures were conducted at temperatures between 550 and 650 °C for exposure times ranging from 1008 to 8760 h. The F91/S21 interface was found to be unstable during aging; a hard layer was formed, consisting mainly of three phases. This layer follows a parabolic rate of growth; its thickness increases as the square root of aging time. The activation energy was determined, which might be associated with carbon diffusion. Complementary characterization methods showed that the three phases in the hard layer are: a BCC-like intermetallic compound, Fe_xCo_y; a Cr-rich $M_{23}C_6$-type carbide; and an (Fe,Co)(Cr,Mo)-type σ phase. The area fraction and the equivalent diameter of the $M_{23}C_6$ carbides increase with aging temperature and time, while the area fraction of the σ phase decreases with temperature. Nanoindentation maps showed that both the $M_{23}C_6$ carbides and the σ phase in the interfacial layer are significantly harder than the other phases. The σ phase contributes more in the increase of the interfacial layer's hardness at lower temperatures than that at higher temperatures. These hard phases may affect high-temperature valve integrity.

Keywords: Stellite hardfacing; Delamination; Interfacial microstructure; $M_{23}C_6$ carbides; σ phase; Nanoindentation.

6.1 Introduction

Creep-resistant 9-12% Cr martensitic steels are used in elevated-temperature applications. These steels are widely used in the fossil fuel power generation industry in components such as valves, boilers, tubes, steam pipes, and turbines. They are also candidates for nuclear applications, as reviewed by Klueh in 2005 [53] and by Klueh and Nelson in 2007 [54]. Grade 91, a modified 9% Cr steel, is used to manufacture valve components such as discs, seats, slides, and bodies. In order to ensure durable valve sealing quality and actuation efficiency, hardfacing alloys are often applied onto the sealing surfaces of high-temperature valves to provide low friction and improve oxidation and corrosion resistance under sliding contact conditions.

Hardfacing alloys are usually deposited by welding processes, such as plasma-transferred arc (PTA) welding, laser cladding, oxyfuel gas welding, gas tungsten arc welding, and gas metal arc welding. According to an ASM handbook, the following factors should be considered to select the most suitable process for a given application: physical characteristics of the workpiece; the form of the hardfacing alloy such as rods, wires, or powder; the welder's skills; cost; minimum deposition thickness; deposition rate; and dilution rate [17]. In hardfacing, dilution refers to chemical dilution, that is, change in the chemical composition of a filler material due to the admixture of the base material or of the previously deposited weld material. Among the previously named processes, PTA welding has gained popularity due to several significant advantages when compared with other processes: automation; high productivity; and precise control of important welding parameters such as voltage, current, powder feed rate, gas flow rate, and travel speed. Therefore, this process is the preferred method with which to weld hardfacing alloys.

Stellite 6 (S6, Stellite^{RT}), a cobalt-based alloy, has been used as a hardfacing alloy for decades due to its high-temperature wear resistance and good oxidation resistance, according to an ASM handbook [2]. In a study performed by Birol, the Cr_2O_3 on S6 alloy sustained the sliding wear action without spalling and was claimed to be responsible for the wear resistance observed at 750 °C [55]. S6 can be deposited directly onto the steel substrate. However, residual stresses are induced because of thermal expansion differences across the welded joint in a dissimilar metal welding process. Stellite 21 (S21) is commonly deposited as a buffer layer between S6 and the steel substrate, providing an intermediate thermal expansion, thus reducing thermal mismatch [3]. S21

is another cobalt-based alloy rich in Cr and Mo but less resistant to wear than S6; S6 has more W to enhance solid solution and higher C to promote carbide formation.

Even when this S21 buffer layer is applied, disbonding or delamination of Stellite hardfacing from valve seats or discs has been recognized as a major industry challenge. The Electric Power Research Institute reviewed and summarized the information on field experience; data on valve manufacturing, design and operating parameters; and the failure events in a technical update report [3]. A leading valve services company reported that in 2011 and 2012 it had repaired 50 valves, more than half of which involved Stellite delamination [5]. These failures led to steam leakage, and in addition, also produced hardfacing debris that damaged other components, as mentioned by Bezzant [6].

Efforts have been made better to understand this specific failure mechanism. Hattel analyzed the failure of an S6 weld overlay on P91 (piping) steel and found that a crack had grown at the fusion line between the two materials [38]. By simulating carbon migration across the interface during heat treatment and in service, the P91 steel was predicted to become completely decarburized in a zone 10 μm wide near the interface, resulting in decreased strength. The delamination took place in the P91 material very close to or at the interface, which was explained by the loss of material strength combined with the presence of residual stresses. However, Leinenbach et al. reported that an interfacial layer sensitive to delamination was formed between the steel and S6 during long-term exposure at 600 and 625 °C [39]. They measured that this layer exhibited a high hardness value, 720 HV0.1, which is equivalent to an indentation hardness H_{IT} value of 7.6 GPa.[1] This team also proposed that this layer was composed of a body-centered cubic (BCC) Fe-Co-enriched α phase, a Cr-enriched α' phase, and a $M_{23}C_6$-type carbide. Moreover, they found that some additional intermetallic phases could be stable in the layer, based on the thermodynamic simulations. Lolla et al. investigated the interfacial microstructure of hardfacing overlays on grade 91 steel after

[1] Vickers hardness HV can be correlated to indentation hardness H_{IT} by the formula $HV = 0.0945 * H_{IT}$, according to the ISO 14577-1 standard [48] "ISO 14577-1:2002 Metallic materials -- Instrumented indentation test for hardness and materials parameters -- Part 1: Test method," Geneva: International Organization for Standardization, 2002.

approximately 60,000 h service exposure at temperatures up to 566 °C [4]. In addition to the BCC phase rich in Fe and Co and the carbides, a Cr-rich σ phase was found at the interface between grade 91and S21. The σ phase showed the highest hardness among the phases studied, 11.7 GPa. It was believed to be the primary contributor to hardness increase at the interface, where cracks propagated. The Electric Power Research Institute also agreed with Lolla et al. on the formation of brittle σ phase in the hard layer in a technical update report [3]. Nonetheless, the hardness of the $M_{23}C_6$ carbides was not explored.

The objective of the present study is further to understand the thermal stability of the interface between Stellite and the steel substrate. Therefore, S21 and S6 hardfacing alloys were deposited onto an F91 steel substrate using PTA welding. A series of aging experiments simulating service temperatures were conducted between 550 and 650 °C over durations ranging from 1008 to 8760 h (1 year), as is explained in the experimental section. The interfacial microstructure evolution and growth kinetics were thoroughly studied. The hardness of the main phases observed at the interface was fully characterized. The presence of the hard $M_{23}C_6$ carbides and σ phase result in the increase of the interfacial layer's hardness, which may affect high-temperature valve integrity.

6.2 Experimental details

6.2.1 Materials, deposition and aging

The substrate material used in this work was F91 (forging) steel with dimensions 356 mm × 57 mm × 38 mm. S21 and S6 powders were successively used as hardfacing materials. The chemical compositions of F91, S21, and S6, provided by the material suppliers, are listed in Table 6.1. The deposition process was PTA welding with the conditions given in Table 6.2. Pure argon (100%) was used as the shielding, plasma and powder gas. One layer of S21 and two layers of S6 were deposited on the F91. The thickness of each layer was approximately 2 mm. After deposition, this hardfacing sample was cooled in air to room temperature. Following cooling, a post-weld heat treatment (PWHT) was performed to temper the heat-affected zone of the F91 steel and release residual stresses.

Table 6.1: Chemical compositions of F91, S21 and S6 (wt%).

	Cr	Mo	Fe	Co	C	Mn	Si	Ni	W	Others
F91	8.39	0.90	Bal.	0.015	0.11	0.48	0.30	0.18	0.00	<1.00
S21	27.45	5.37	1.44	Bal.	0.26	0.60	1.69	2.76	0.00	<0.50
S6	27.34	0.17	0.33	Bal.	1.63	0.33	1.09	1.78	4.22	<0.50

Table 6.2: Welding conditions used for S21 and S6 deposition.

Parameter	Value
Feed rate of S21 (g/min)	18
Feed rate of S6 (g/min)	25
Particle size (mesh)	80/325
Current (A)	170 - 200
Voltage (V)	21.5 - 25.0
Preheat (°C for 1 h)	204
Interpass temperature (°C)	316 max
PWHT (°C for 2 h)	760

The as-tempered sample was cut into bars using wire electrical discharge machining. Some of these bars were then aged under ambient atmosphere to simulate service temperatures. The detailed aging temperatures and times are given in Table 6.3. As indicated by Dobson, grade 91 steel is used in high-temperature steam systems working at temperatures ranging from 538 to 593 °C (1000-1100 °F) [28]. Thus, aging at 550 °C was chosen to represent typical service temperature, while other higher temperatures were also chosen either to study the equilibria and stability of the observed phases or to be representative of more demanding applications. The highest aging temperature, 650 °C, is lower than the tempering temperature of F91, which is in the range of 730 to 800 °C according to an ASTM standard [43].

Table 6.3: Aging conditions.

Temperature (°C)	550	600	650
Time (h)	1008	1008	1008
	3600	3600	3600
	8760	8760	8760

6.2.2 Microstructural analysis

The bars in the as-tempered and other aging conditions were cross-sectioned, mounted, ground, and polished. The microstructure and local chemical compositions of the samples were characterized on cross-sectional surfaces using optical microscopy (OM) and scanning electron microscopy (SEM, JEOL JSM-7600F) equipped with energy dispersive X-ray spectroscopy (EDS) operating at 15 kV (image) or 5 kV (EDS). An acceleration voltage of 15 kV was chosen to improve backscattered electron (BSE) imaging resolution. On the other hand, 5 kV was chosen to reduce the size of the interaction volume when measuring chemical compositions of individual phases, which were analyzed using the built-in EDS quant standardizations (5 kV set).

The interfacial microstructure was further characterized by electron backscatter diffraction (EBSD) phase mapping using an Oxford Instruments Nordlys Max2 detector installed on a Zeiss Sigma FEG-SEM operating at 20 kV in high-current mode. The maps were collected using step sizes of 0.05 μm (sample aged at 650 °C) or 0.1 μm (sample aged at 550 °C) with total sizes of 30 μm × 40 μm (sample aged at 550 °C) and 30 μm × 30 μm (sample aged at 650 °C). Kikuchi patterns, taken at 4 × 4 binning, were collected and indexed using AZtec software at about 40 Hz and maps were processed using HKL Channel 5.

The interfacial layer thickness was measured from OM and SEM micrographs at magnifications of 1000× and 5000×, respectively. At least 10 OM or SEM micrographs were analyzed for a total length of at least 854 μm per aging condition. In each micrograph, five measurements were evenly performed using ImageJ software. The uncertainties of each interfacial layer thickness were estimated using the standard deviation of the mean.

In order to show the relative proportion of a specific feature, such as the σ-phase-rich zones or the reactive zones along grain boundaries, over the whole interfacial layer, the length of the whole

interfacial layer was measured using a ruler and the lengths of the σ-phase-rich zones and the reactive zones along grain boundaries were measured using OM (Figure 6.1). Finally, the length fractions of the σ-phase-rich zones and the reactive zones along grain boundaries were obtained.

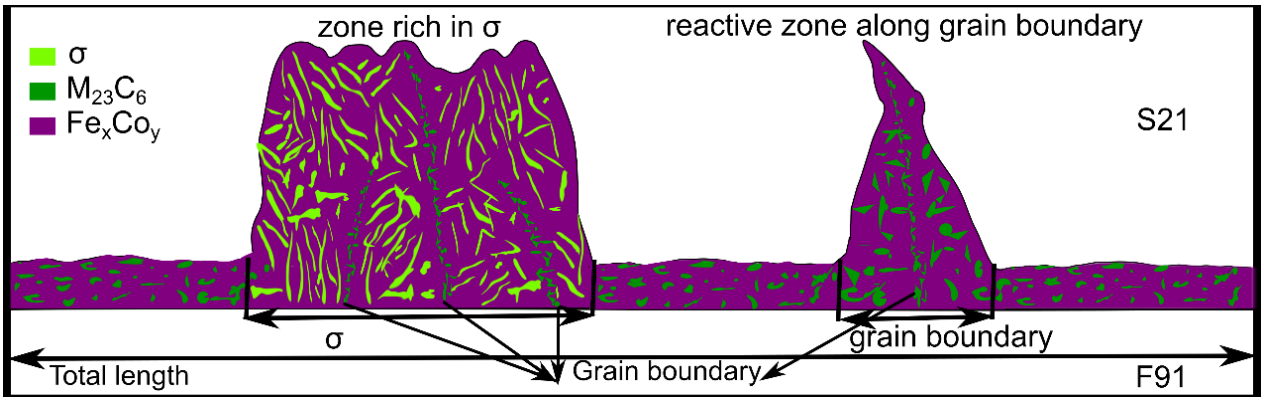

Figure 6.1: Schematic illustration of the methodology used to obtain the length fractions of the σ-phase-rich zones and the reactive zones along grain boundaries, at the interface between the S21 hardfacing and the F91 substrate.

The area fractions of the $M_{23}C_6$ carbides and the σ phase were determined from the SEM micrographs using ImageJ and Photoshop or Clemex softwares. Four to six SEM micrographs having an area of 411 μm^2 were analyzed to evaluate the area fractions of the $M_{23}C_6$ carbides per aging condition. Also, four to six SEM micrographs having an area of 411 μm^2 were analyzed to evaluate the area fractions of the σ phase when aged at 550, 600 and 650 °C for 8760 h. It is worth mentioning that the area fraction of the σ phase only applied to the σ-phase-rich zones, because the σ phase was distributed heterogeneously in the interfacial layer. If one would like to know the proportion of the σ phase over the whole interfacial layer, please refer to its length fraction, as described previously. The average equivalent diameter of the $M_{23}C_6$ carbides was determined from the SEM micrographs containing 28 to 94 carbides using Clemex software. The uncertainty of each equivalent diameter was estimated using the standard deviation of the mean.

A Rigaku SmartLab X-ray diffraction (XRD) equipped with a Cu 3 kW X-ray source and a 100 μm (sample aged at 650 °C) or 200 μm (sample aged at 550 and 600 °C) collimator was used for phase identification in the interfacial microstructure region. A Hypix-3000 2D hybrid semiconductor detector was employed, allowing for integration of the diffracted signal over part of the diffraction cone. This detector also has fluorescence suppression to allow for the testing of samples containing elements such as Cr, Fe and Co when using Cu radiation.

6.2.3 Indentation

In order to compare the hardness of the interfacial layer, of the F91, and of the S21, depth-sensing micro-indentation measurements on the cross-section of a hardfacing sample aged at 650 °C for 8760 h were performed using an Anton-Paar (formerly CSM Instruments) Micro-Combi Tester equipped with a pyramidal-diamond tip with a Vickers geometry. For each indentation, the load was linearly increased over 30 s up to a maximum of 200 mN, kept constant for 15 s, and then linearly decreased over 30 s. The maximum of 200 mN was chosen to make indentations that could be entirely located in the interfacial layer. One line of measurements spaced by an interval ranging from 41 to 91 μm was carried out perpendicular to the interface, covering the F91, the interfacial layer and the S21. To get more indentations in the interfacial layer, the other line, spaced by an interval ranging from 28 to 35 μm, was carried out in the interfacial layer. The microhardness from each indentation was obtained using the Oliver and Pharr method [46]. The average microhardness values of the F91, the interfacial layer and the S21 were obtained over seven measurements, respectively. Because the number of the repeated measurements was small, the uncertainties were obtained from the formula:

$$\Delta H_{\mathrm{avg}} = \frac{H_{\mathrm{max}} - H_{\mathrm{min}}}{2\sqrt{N}} \qquad \text{Equation 6.1}$$

where ΔH_{avg} is the uncertainty in the mean value of the microhardness, H_{max} is the maximum microhardness, H_{min} is the minimum microhardness, and N is the number of measurements, seven.

In order to measure the mechanical properties of individual phases within the interfacial layer, depth-sensing nanoindentation was employed on the cross-sections of the hardfacing samples using a Bruker Triboindenter (formerly Hysitron Inc.) equipped with a Berkovich diamond tip. The tip area function was calibrated with a fused silica standard. Matrices of 16 × 16 and 25 × 25 indentations evenly spaced by 2 μm were carried out with a load function consisting of a 5 s linearly increased loading segment, a 2 s constant period at maximum load (2 mN), and a 5 s linearly decreased unloading segment. The Oliver and Pharr method [46] was used to estimate the hardness and the elastic modulus of each indentation from the individual load-displacement curve.

6.3 Results

6.3.1 F91/S21 interfacial microstructure

The F91/S21 interfacial microstructure after 8760 h of exposure at 550, 600 and 650 °C is shown in Figure 6.2, where S21 and F91 are located at the image top and bottom, respectively. A sample in the as-tempered condition (Figure 6.2a) is also shown for comparison purposes. After aging, an interfacial layer was observed between the F91 substrate and the S21 buffer layer, as seen in Figure 6.2b, c and d. Figure 6.2e shows that this layer also grew preferentially along the grain boundaries of the S21. Indeed, grain boundaries are generally known to be a fast diffusion path. In some zones, the interfacial layer grew much thicker, leaving islands of S21, as shown in Figure 6.2f. These features observed in Figure 6.2e and f indicated that this interfacial layer grew from the fusion line into the S21.

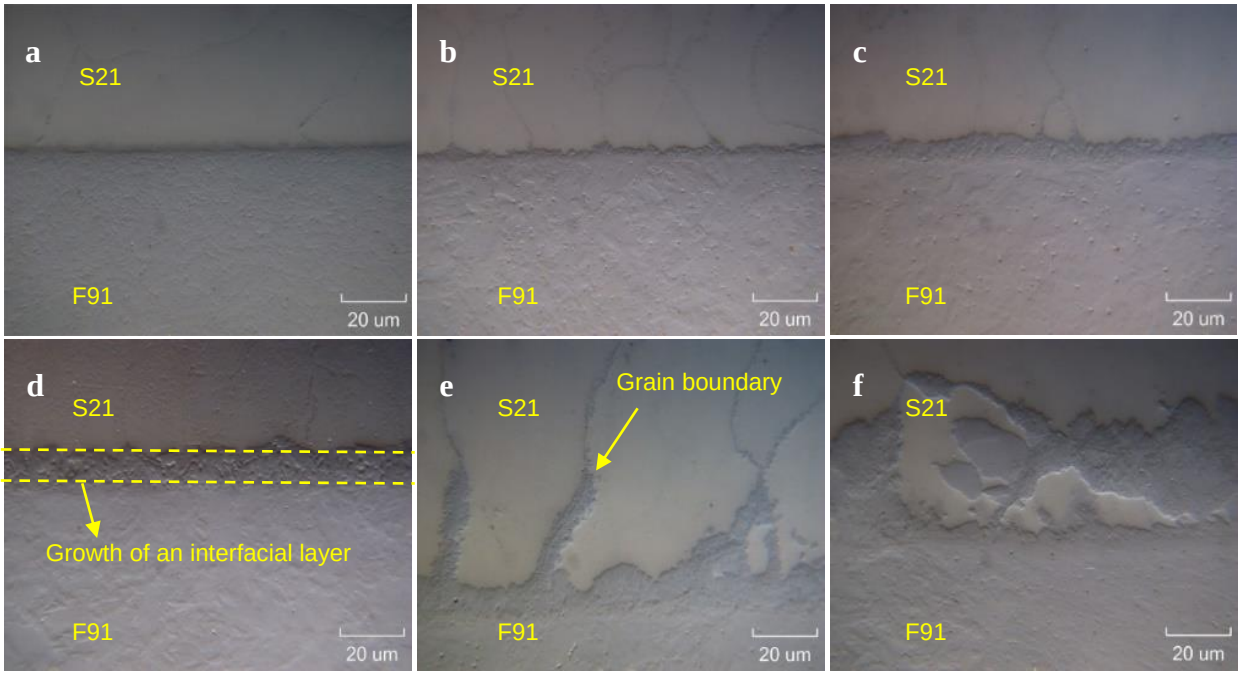

Figure 6.2: Optical micrographs of the F91/S21 interfacial microstructure under different conditions: (a) as-tempered condition; (b) 550 °C, (c) 600 °C and (d) 650 °C for 8760 h; (e) 600 °C for 8760 h showing the growth along grain boundaries, and (f) 550 °C for 8760 h showing a thicker zone.

After exposure at 550 °C for 8760 h, zones with the two aforementioned features covered less than 12% (length fraction) of the observed length (i.e., 1.5 cm, sample's overall length), from which

zones with the feature in Figure 6.2f covered less than 4% (length fraction). No such local features were observed in the sample aged at 650 °C for 8760 h. When measuring the thickness of the interfacial layer, these special features were excluded.

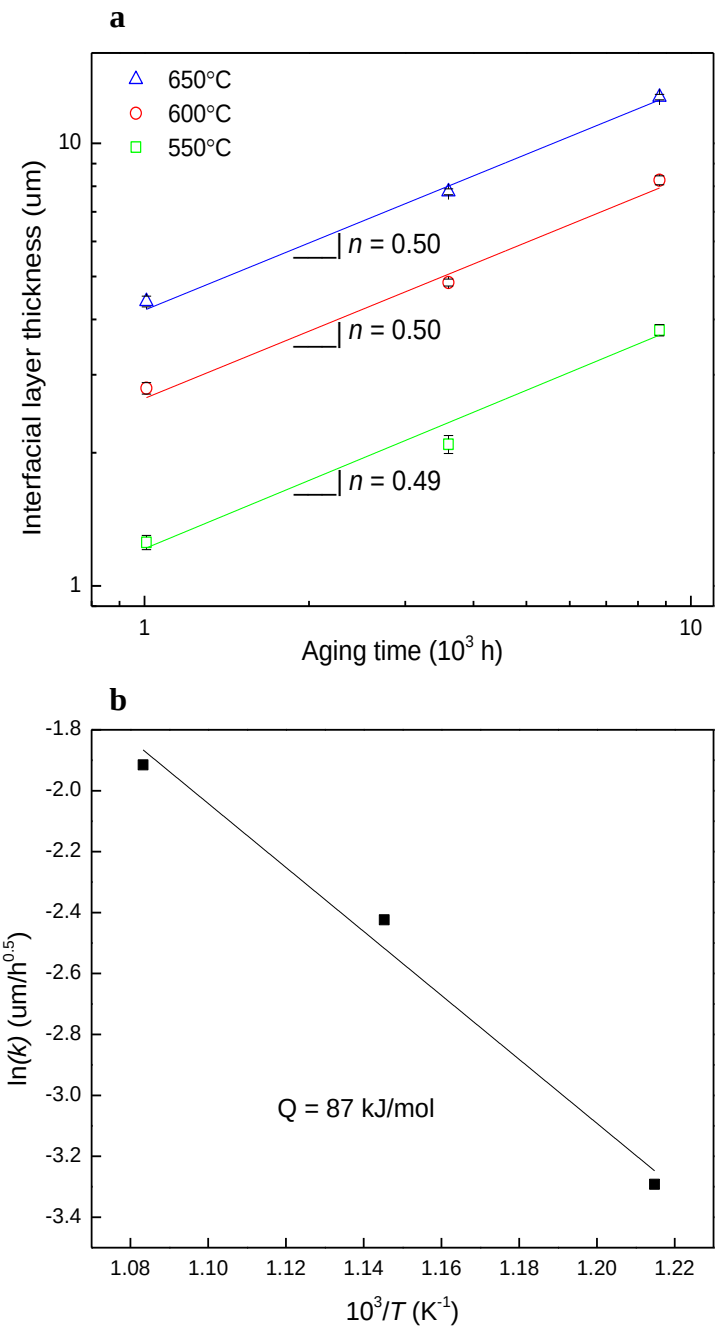

Figure 6.3: (a) Growth kinetics of the interfacial layer with a double logarithmic scale and (b) Arrhenius plot of ln(k) versus $10^3/T$.

The average thickness of the interfacial layer is presented as a function of time in Figure 6.3a, where a logarithmic scale was used. An empirical power law equation was used to investigate the growth kinetics of the interfacial layer [56]:

$$x = kt^n \quad \text{Equation 6.2}$$

where x is the thickness of the interfacial layer, k is the growth rate constant at a given temperature, t is the aging time, and n is the time exponent. The time exponent n was determined from the slopes shown in Figure 6.3a. At all the studied temperatures, the exponent n is close to or equal to 0.50. It appears that the interfacial layer follows a parabolic rate of growth, which suggests a diffusion-controlled growth phenomenon.

The growth rate constant k was determined for each of the three temperatures from the y-intercepts of Figure 6.3a, allowing for the estimation of the activation energy characterizing the interfacial layer growth during the solid-state reaction, via the Arrhenius equation:

$$k = k_0 \exp\left(\frac{-Q}{RT}\right) \quad \text{Equation 6.3}$$

where k_0 is pre-exponential coefficient, Q denotes the activation energy, R is the gas constant and T is the temperature measured in kelvin. The activation energy characterizing the interfacial layer growth, 87 kJ/mol, was obtained from the slope of the Arrhenius plot (Figure 6.3b) by a linear regression approach.

The F91/S21 interfacial microstructure was further investigated using BSE imaging to validate that the thickness of the interfacial layer increased with temperature and time (Figure 6.4). Three phases having different morphology and BSE contrast were observed. They are identified by letters A, B and C (see for example Figure 6.4i). The interfacial microstructure was mainly composed of phase A, followed in proportion by B and C. The B phase had an irregular shape and was embedded in the A phase. The A and B phases were present along most of the interface at all temperatures. From Figure 6.4j, the B embedded in A microstructure grew along grain boundaries as well, corresponding to the zone in the optical micrograph of Figure 6.2e. On the other hand, the C phase was distributed sparsely, especially after aging at 650 °C; the proportion of the C phase decreased with temperature. At 550 °C, shown in Figure 6.4k, a large amount of C phase was observed and it presented a lamellar structure. It should be noted that the zone in Figure 6.4k was much thicker than the average thickness under the same aging condition, corresponding to the zone in the optical

micrograph of Figure 6.2f. The morphology and amount of C phase seemed to be influenced by temperature.

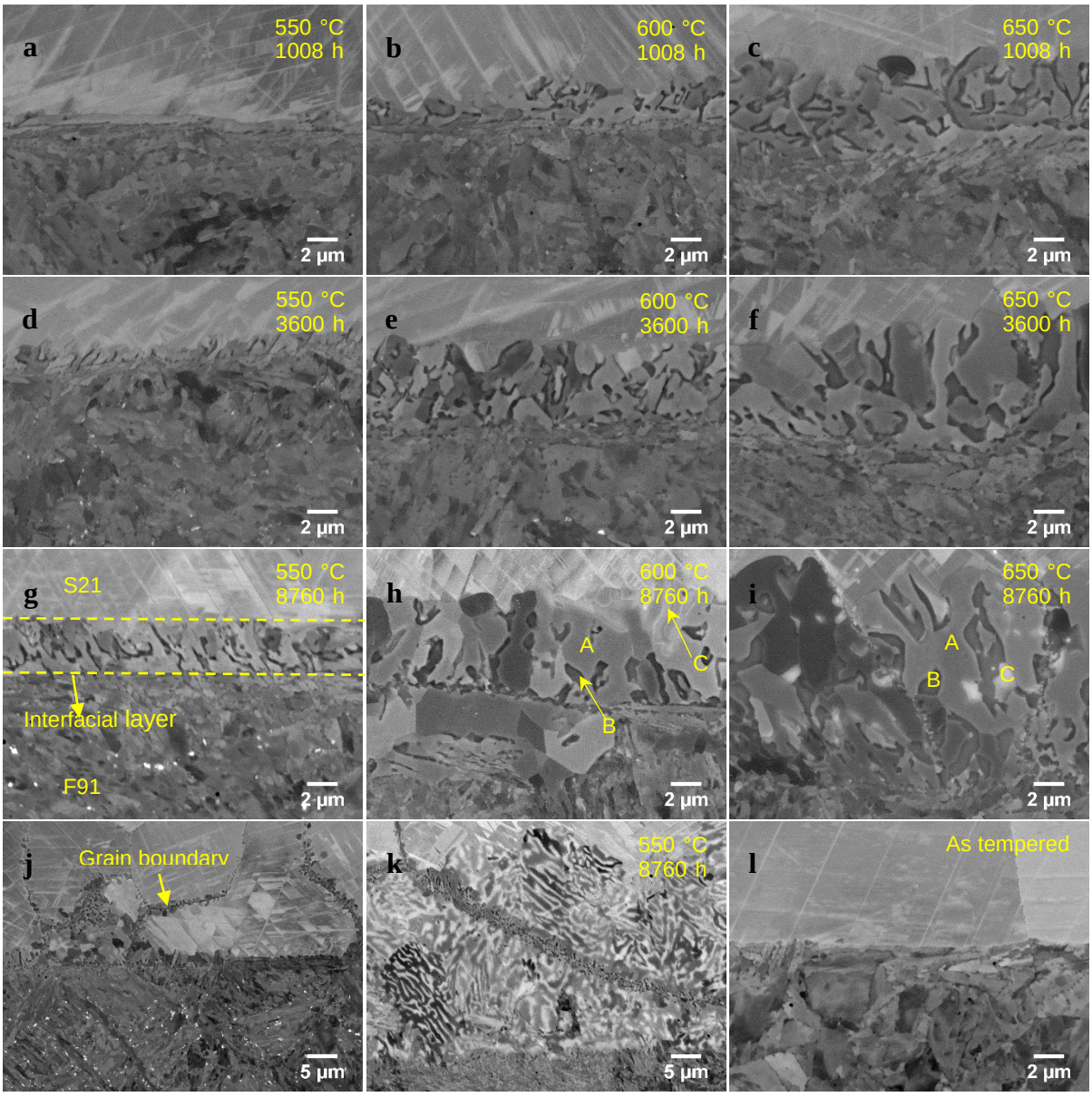

Figure 6.4: BSE images showing the interfacial microstructure: (a) 550 °C, (b) 600 °C and (c) 650 °C for 1008 h; (d) 550 °C, (e) 600°C and (f) 650°C for 3600 h; (g) 550 °C, (h) 600 °C and (i) 650 °C for 8760 h; (j) 550 °C for 8760 h showing the growth along grain boundaries observed in Figure 6.2e; (k) 550 °C for 8760 h showing the lamellar structure observed in Figure 6.2f; and (l) in the as-tempered condition.

The EDS chemical elemental mapping carried out on the interface at 600 °C for 8760 h (Figure 6.5) shows that the A phase (purple) was rich in Fe and Co, the B phase (green) was rich in carbon and Cr, and the C phase (light green) was rich in Fe and Cr but depleted in C. The B phase was darker green than the C phase because it contained more Cr. The C phase was close to the S21 side. The same color codes representing different chemical elements in the EDS map were also used in the following Figure 6.6 and Figure 6.8.

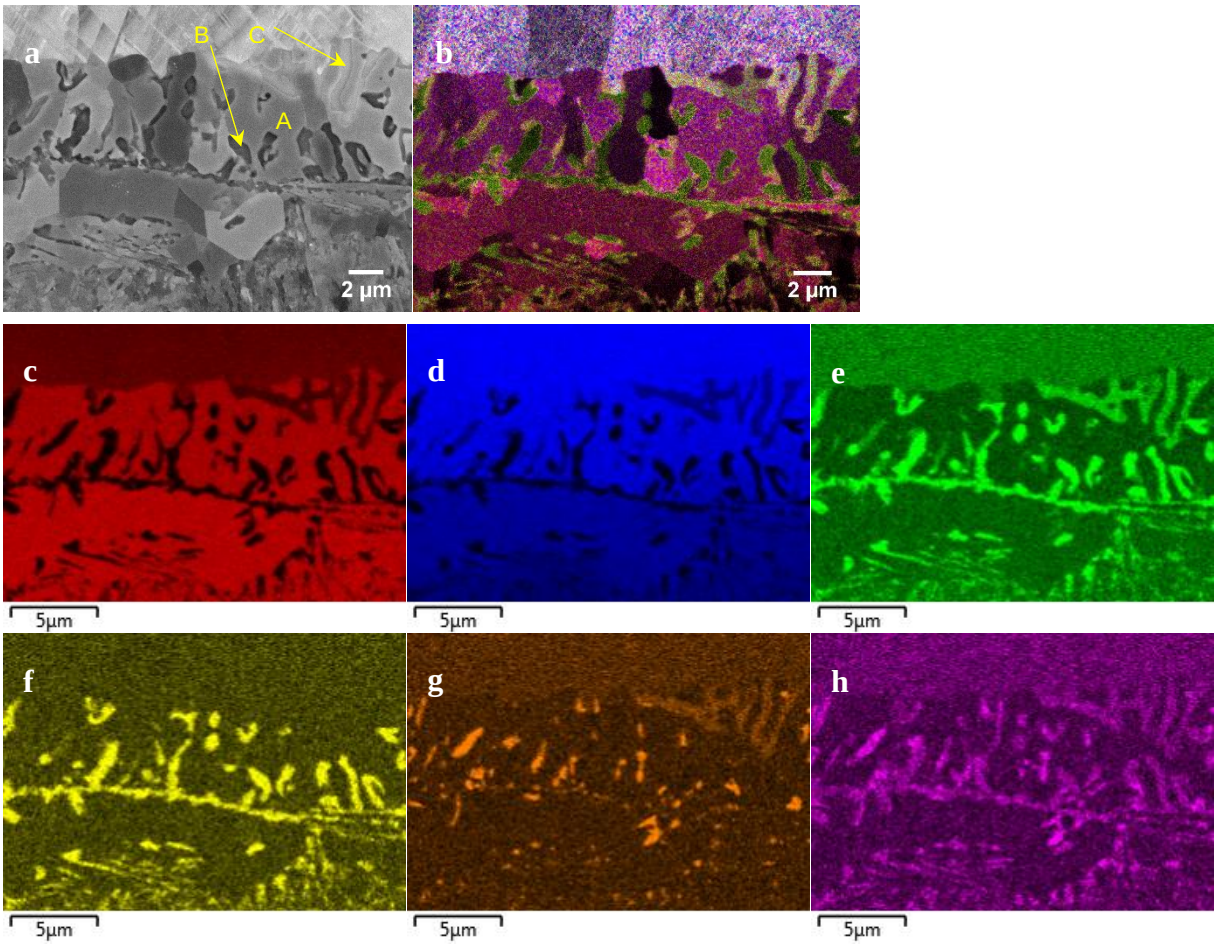

Figure 6.5: EDS elemental mapping on the interface of the sample aged at 600 °C for 8760 h: (a) BSE image; (b) EDS composite map; (c) Fe, (d) Co, (e) Cr, (f) C, (g) Si and (h) Mo elemental maps.

To appreciate better the difference in chemistry between the phases, Table 6.4 provides the relative proportions of 8 elements obtained from the EDS spot measurements performed on the phases A, B and C identified from samples aged at 550, 600 and 650 °C for 8760 h. The averaged values were obtained over 10 to 36 measurements. The uncertainties of each element represented the

standard deviation of the mean values. EDS measurements on the F91 and S21 regions close to the interfacial layer from a sample aged at 600 °C for 8760 h are also listed in Table 6.4 for comparison. The uncertainty of each element represented the error of this individual EDS analysis. Based on the chemical compositions, the A phase was expected to be an intermetallic compound, BCC-like Fe_xCo_y (possibily α_2-Fe_9Co_7). The Si and C elements may be interstial atoms in Fe_xCo_y. The B phase was expected to be a Cr-rich $M_{23}C_6$-type carbide, where the letter M represents Cr, Fe, Co, and Mo. The C phase was expected to be an (Fe,Co)(Cr,Mo)-type σ phase.

Table 6.4: Chemical compositions of phases A, B, C, F91, and S21 (wt%).

Element	A	B	C	F91	S21
Cr	0.0 ± 0.0	72.3 ± 1.0	40.5 ± 1.7	12.4 ± 0.0	22.4 ± 0.0
Fe	54.1 ± 0.9	8.9 ± 0.7	32.8 ± 4.1	71.8 ± 0.0	22.1 ± 0.0
Co	44.9 ± 1.0	4.3 ± 0.4	18.6 ± 3.2	11.7 ± 0.0	49.4 ± 0.0
Mo	0.0 ± 0.0	8.2 ± 0.6	5.5 ± 0.9	1.2 ± 0.0	2.9 ± 0.0
C	0.7 ± 0.4	6.1 ± 1.7	1.2 ± 1.2	2.6 ± 0.0	2.1 ± 0.0
Si	0.3 ± 0.1	0.1 ± 0.2	1.3 ± 0.6	0.3 ± 0.0	1.0 ± 0.0
Ni	0.0 ± 0.0	0.0 ± 0.0	0.0 ± 0.2	0.0 ± 0.0	0.0 ± 0.0
Mn	0.0 ± 0.0	0.0 ± 0.0	0.0 ± 0.0	0.0 ± 0.0	0.0 ± 0.0

EBSD was further applied to characterize the interfacial layer. As shown in Figure 6.6, there were three zones (from top to bottom): the S21, the interfacial microstructure and the F91. In the interfacial microstructure, the red phase (Figure 6.6b) was the σ phase. In addition to the σ phase, Cr-rich $M_{23}C_6$ carbides were observed in the interfacial layer (Figure 6.6b and e). From the EDS measurements, the A phase was expected to be Fe_xCo_y. However, as seen in Figure 6.6b and e, EBSD could not be used to differentiate Fe_xCo_y and α-Fe in the F91 substrate. Herein, it is indexed as Fe_xCo_y according to the EDS measurements. γ-Co and ε-Co coexisted in S21, as shown in Figure 6.6b and e. Thus, it was reasonable to observe the lines in S21 from Figure 6.4, which indicated different allotropes of Co. Even in the interfacial microstructure, there were some yellow γ-Co areas corroborating that the interfacial layer grew from the fusion line into the S21. It is worth

noting that, although the EBSD band contrast maps showed fairly good data quality, the indexing of the phases was far from perfect. Indeed, one can see many differences with the EDS map, most notably many regions of small green carbides dispersed in the Fe_xCo_y. We believe that in many cases these are errors in indexing most probably due to grain distortion because of the large strains typically found in weldments. They may also come from lattice distortion due to solid solutions, defects, and so on.

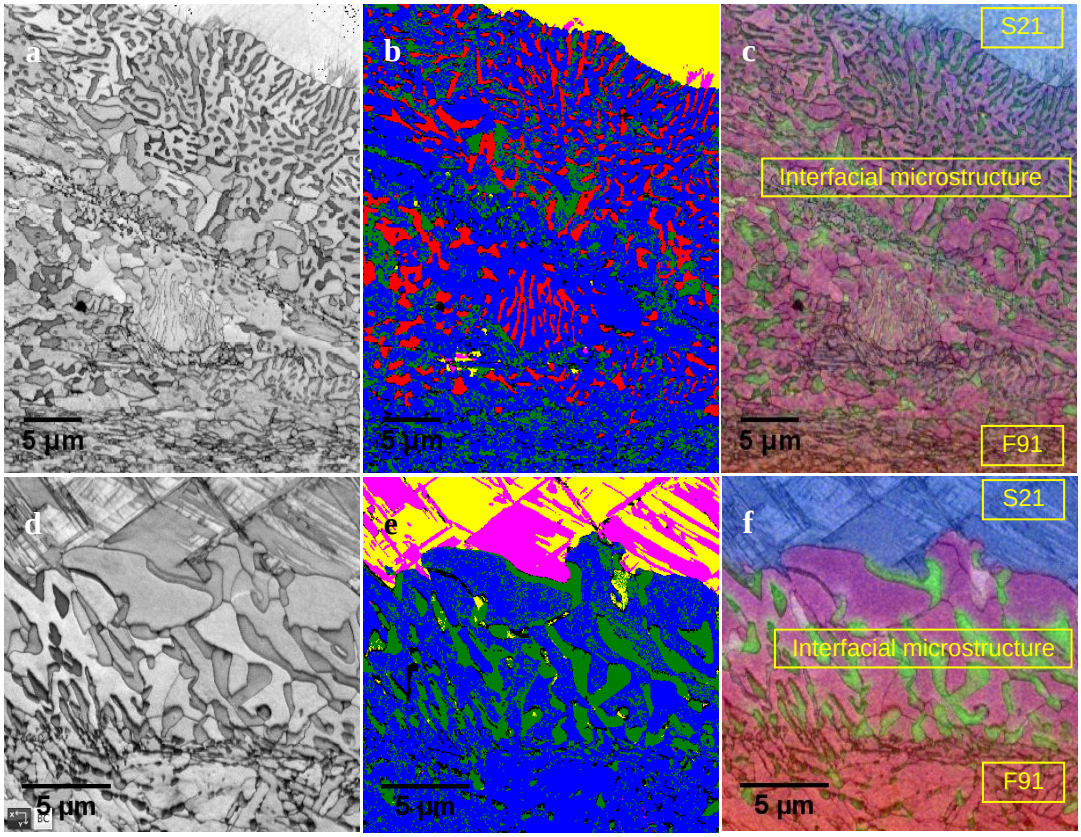

Figure 6.6: The interface of a sample aged at 550 °C for 8760 h (a) band contrast map, (b) the corresponding EBSD phase map (γ-Co in yellow, ε-Co in pink, α-Fe and Fe_xCo_y in blue, $M_{23}C_6$ in green, σ in red, and black no signal), and (c) the corresponding EDS composite map (Fe, Co, Cr, C, Si, and Mo); the interface of a sample aged at 650 °C for 8760 h (d) band contrast map, (e) the corresponding EBSD phase map, and (f) the corresponding EDS composite map (Fe, Co, Cr, C, Si, and Mo).

XRD patterns of the F91/S21 interface collected from samples aged at 550, 600 and 650 °C for 8760 h are presented in Figure 6.7. The XRD pattern from the sample aged at 650 °C for 8760 h confirmed that S21 was a mixture of γ-Co and ε-Co. However, the peaks of ε-Co from the samples

aged at 550 and 600 °C for 8760 h were not observed, which may be due to the low volume fraction. The Co peaks shifted from their theoretical positions (for pure Co) towards lower angles. This could be attributed to alloying elements, like large amount of Cr and Mo substitutional solutions with larger atomic radii than Co, expanding the lattice parameters. Again, the XRD patterns could not be used to identify the presence of α-Fe (BCC) and Fe_xCo_y individually. Fe_xCo_y was labled in Figure 6.7 only according to the EDS measurements. Weak peaks originating from the $M_{23}C_6$ carbides were also observed. However, the presence of the σ phase could not be detected even in the zones rich in the σ phase for the samples aged at 550 and 600 °C for 8760 h, possibly due to its low volume fraction.

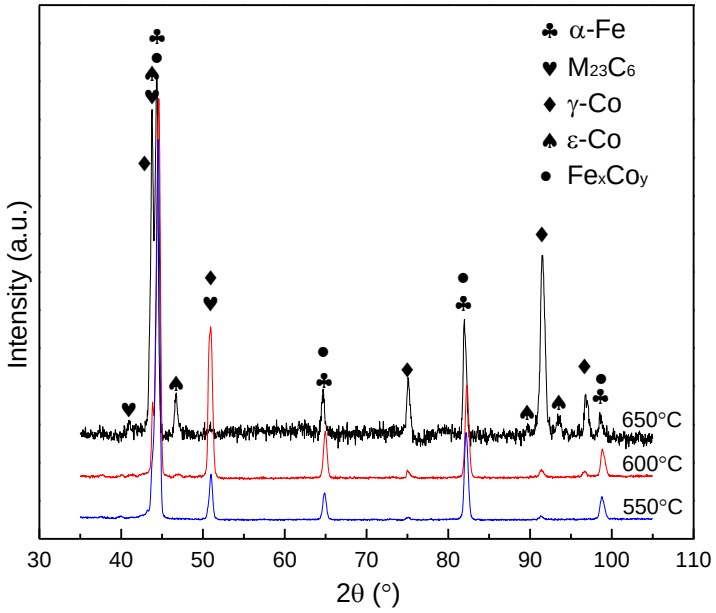

Figure 6.7: XRD patterns of the F91/S21interfaces at 550, 600 and 650 °C for 8760 h.

6.3.2 Indentation on the F91/S21interface

In order to show the hardness of the interfacial layer, the F91 and the S21, micro-indentation measurements on the cross-section of the hardfacing sample were carried out. Considering the load, 200 mN, and the interfacial layer's thickness, only one sample having the maximum thickness was tested, which was aged at 650 °C for 8760 h. Table 6.5 shows the average microhardness values of

the interfacial layer, the F91 and the S21. It is seen that the interfacial layer was harder than the F91 and the S21.

Table 6.5: Microhardness values of the interfacial layer, the F91 and the S21 (200 mN).

Location	Interfacial layer	F91	S21
Hardness (GPa)	7.7 ± 0.3	3.36 ± 0.04	6.5 ± 0.3

In order to show which phase(s) contributed to the increase in the interfacial layer's hardness, laterally resolved nanoindentation tests were performed. BSE images and EDS composite maps were obtained from the zones covered by the indentations to match the mechanical results with specific phases. One example is illustrated in Figure 6.8 for a sample aged at 600 °C for 8760 h. Two indents (1) fully within the $M_{23}C_6$ carbides exhibited the highest hardness, in the range of 19 GPa. Another two indents (2) fully within the σ phase exhibited the second highest hardness, in the range of 16 GPa. Ohmura et al. used nanoindentation to determine the hardness of the σ phase to be of the order of 17 GPa at the peak load of 500 μN [57]; whereas Lolla et al. found that it was of the order of 11 GPa [4]. The S21 exhibited a hardness value in the range of 6 GPa. The F91 hardness ranged from 4 to 6 GPa, decreasing with distance from the interfacial layer. This section of F91 was in the heat affected zone, generated by the heat input during welding.

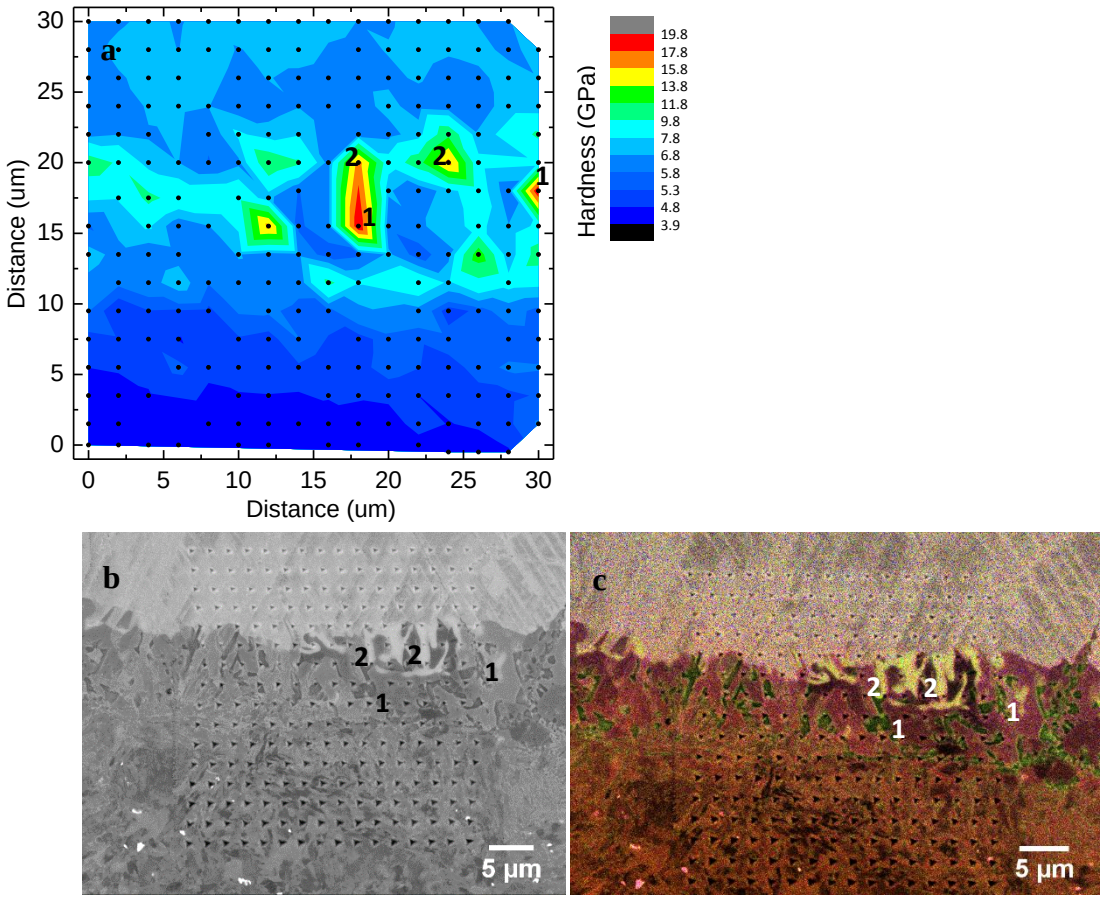

Figure 6.8: A sample aged at 600 °C for 8760 h (a) hardness map, (b) the corresponding BSE image and (c) the corresponding EDS composite map (the σ phase in light green 2, the $M_{23}C_6$ carbides in green 1 and the Fe_xCo_y in purple).

Nanoindentation maps were also obtained from samples aged at 650 °C for 8760 h to ease the sampling in the $M_{23}C_6$ carbides, and at 550 °C for 8760 h to ease the sampling in the σ phase. At these aging conditions, large areas of the $M_{23}C_6$ carbides and the σ phase were observed. Consequently, hardness and elastic moduli of the three main phases were obtained from the samples aged at 550, 600 and 650 °C for 8760 h. The averaged values over at least 10 measurements are presented in Table 6.6. The hardness of the $M_{23}C_6$ carbides was 3.3 times higher than the surrounding Fe_xCo_y and the hardness of the σ phase was 2.7 times higher than the surrounding Fe_xCo_y. The uncertainties represented the standard deviation of the mean values.

Table 6.6: mechanical properties of the three phases observed in the interfacial layer.

Precipitate	$M_{23}C_6$	(Fe,Co)(Cr,Mo)	Fe_xCo_y
Hardness (GPa)	19.8 ± 0.4	16.0 ± 0.2	5.97 ± 0.04
Elastic modulus (GPa)	271 ± 3	242 ± 2	236 ± 3

6.4 Discussion

Based on the above results obtained from the complementary characterization methods, an interfacial layer, formed between F91and S21 after aging, was composed of three main phases: the Fe_xCo_y, the $M_{23}C_6$ carbides and the σ phase. The $M_{23}C_6$ carbides were present along most of the interface at all temperatures. They grew with temperature and time, while the proportion of the observed σ phase decreased with temperature. As shown in Figure 6.2b and f, the zone rich in the σ phase was much thicker than the average thickness of the interfacial layer. It covered less than 4% (length fraction) of the observed sample's length (1.5 cm) when aged at 550 °C for 8760 h. It did not account for the interfacial layer thickness measurement. Thus, the previously presented interfacial layer growth kinetics mainly described the homogeneous layer including the $M_{23}C_6$ carbides and the Fe_xCo_y phase.

In dissimilar metal welding, there is a transition zone near the fusion line (interface) where composition gradients take place, different from the bulk weld metal. This zone is often referred to as the partially mixed zone (PMZ). Phase transformations might occur to achieve thermodynamic stability in this zone when aging at high temperatures for long durations. The composition gradients across the interface between F91 and S21 of the hardfacing sample in the as-tempered condition were measured using an EDS line scan. The variation in alloying elements across the interface is shown in Figure 6.9, where it is seen that the width of the PMZ was around 17 μm, enriched with Fe, Co and Cr. However, we believe that the growth of this layer would not stop after 17 μm. As shown in Figure 2e and f, the thickness of the reactive zones along grain boundaries and the σ-phase-rich zones is larger than 17 μm. It might be due to the grain boundary diffusion mechanism.

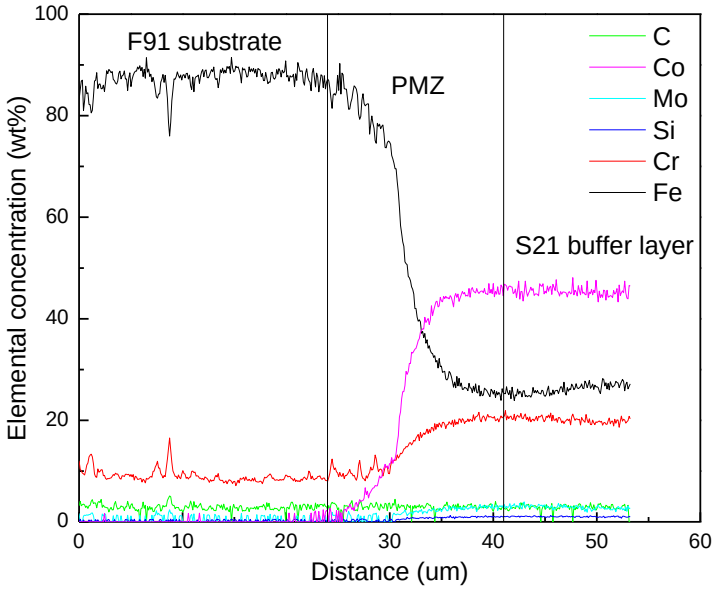

Figure 6.9: EDS line scan measurements showing composition profiles across the interface between F91 and S21 of the hardfacing sample in the as-tempered condition.

The obtained activation energy characterizing the homogeneous interfacial layer growth was 87 kJ/mol. The activation energies of some elements for diffusion in Co are listed in Table 6.7, where it is seen that the activation energies of substitutional elements such as Cr, Fe and Mo for inter-diffusion in Co were higher than 200 kJ/mol. The activation energy for self-diffusion in Co was also higher than 200 kJ/mol. On the other hand, the activation energy of C for diffusion in Co was lower than the other elements and comparable to the present calculation of 87 kJ/mol, which might suggest that the growth of the homogeneous interfacial layer was controlled by carbon diffusion. Table 6.8 shows the activation energies of some phases. As validated by Xu et al., the activation energy of the $M_{23}C_6$ precipitation in a creep-resistant steel (72 kJ/mol) was nearly equal to the activation energy of carbon diffusion in martensite, suggesting that it was controlled by carbon diffusion [58]. Carbon can diffuse as interstitial solutes and the activation energies for interstitial diffusion are considerably lower than self-diffusion and substitutional diffusion. For the same species, grain boundary diffusion usually requires lower activation energy than the bulk diffusion [59].

Table 6.7: Activation energies of some elements for diffusion in Co.

Element	Activation energy (kJ/mol)	Reference
Cr	255±19	[60]
Fe	219	[61]
Fe	254±9	[60]
Mo	262±10	[60]
Co	283	(Mead, 1955, as cited in Brown, 1980) [62]
C	140±15	[63]
C	91	[64]

Table 6.8: Activation energies of some phases.

Phase	Activation energy (kJ/mol)	Reference
$M_{23}C_6$	72	[58]
$M_{23}C_6$+Fe_xCo_y	87	The present study
FeCo family	270-365	[65]
FeCo family	240 (growth)	[66]
σ	357-482 (nucleation)	[67]
σ	185	[68]
σ	200-283	[69]

From the previous study of the interfacial layer growth kinetics, it is obtained that the time exponent n is equal to 0.50. However, it cannot be determined that this process is controlled by bulk diffusion or by grain boundary diffusion from the parabolic relationship. As stated in a book, parabolic growth occurred both in bulk diffusion and grain boundary diffusion from the analytical models of layer growth kinetics of bronze-processed Nb_3Sn and V_3Ga [56]. Yamada et al. [70] and Sasaki et al. [71] also agreed that parabolic relationship was valid both for bulk diffusion and grain boundary

diffusion when investigating reactive diffusion kinetics between Au and Sn and between Ag-5Pt alloy and Sn at solid-state temperatures, respectively.

As shown in Figure 6.2e and 4j, reactive zones along grain boundaries penetrating the S21 were observed in the samples aged at 550 and 600 °C for 8760 h. It might suggest that grain boundary diffusion occurred in these zones. Grain boundaries in the zones rich in the lamellar σ phase were also often observed. One example is shown in Figure 6.4k, where a grain boundary was present, which might also suggest the grain boundary diffusion mechanism. Nevertheless, the two types of zone in Figure 6.4j and k were not observed in the sample aged at 650 °C for 8760 h. It might be due to the fact that the bulk diffusion becomes more predominant as temperature increases.

The most widely used classification of diffusion kinetics in a polycrystal with parallel grain boundaries was proposed by Harrison [72].There are three regimes called type A, B, and C in his classification, shown in Figure 6.10. A planar front diffusion is observed in type A kinetics at high temperatures, or/and after very long durations, or/and when the grain size is small. In the present study, the interfacial layer in the sample aged at 650 °C for 8760 h fell into Type A regime, where bulk diffusion fields of neighboring grain boundaries overlap very extensively. As shown in Figure 6.2e, the interfacial layer in the sample aged at 600 °C for 8760 h fell into Type B regime, where grain boundary diffusion is accompanied by bulk diffusion around grain boundaries but bulk diffusion fields of neighboring grain boundaries do not overlap.

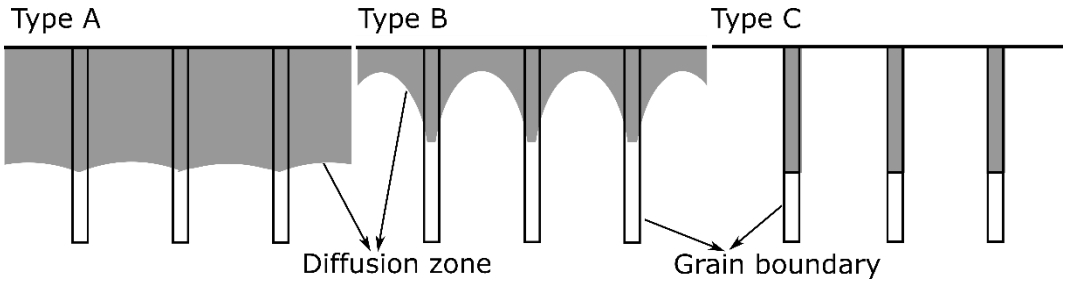

Figure 6.10: Schematic illustration of three diffusion regimes in Harrison's classification.

In the present study, the activation energy of the σ phase formation was not obtained. As shown in Table 6.8, the activation energies of the σ phase and the FeCo family phases found in the literature were all much higher than that of the $M_{23}C_6$ carbides. As stated previously, the σ phase covered less than 4% (length fraction) of the observed sample's length when aged at 550 °C for 8760 h. No σ phase was observed when aged at 550 °C for 1008 h, while the $M_{23}C_6$ carbides were found under the same aging condition. It may be due to the fact that the activation energy required for the σ

phase is higher than that of the $M_{23}C_6$ carbides. The activation energies of the substitutional elements such as Fe, Cr and Mo for inter-diffusion in Co were higher than 200 kJ/mol, as listed in Table 6.7. From Table 6.4, one can see that Fe, Cr, Mo and Co were main elements to form the σ phase. Since grain boundary diffusion requires lower activation energy than the bulk diffusion, it is easier for Fe, Cr and Mo to diffuse along the grain boundary. This well explains the phenomenon that grain boundaries were often observed in the σ-phase-rich zones.

In order to comprehend how temperature affected the proportion of the σ phase, a graph showing the relationship between the area fraction of the σ phase and the aging temperature is plotted in Figure 6.11, where the area fraction of the σ phase decreased considerably with temperature. This may be due to the fact that the $M_{23}C_6$ carbides are more thermodynamically stable than the σ phase with temperature, as demonstrated by Leinenbach et al. [39]. The authors' thermodynamic simulations showed a decrease of the σ phase proportion with temperature during long-term aging of S6 hardfacing on a 12% Cr steel. They calculated the molar fractions of the phases at equilibrium as a function of the temperature for the boundary chemical compositions of the interfacial layer, i.e. Fe-20Co-15Cr-2.5W-2.5Ni-0.2C (wt%) and Fe-40Co-20Cr-4W-2.5Ni-1C (wt%), for which the σ phase would disappear when the temperature was higher than 650 and 600 °C, respectively.

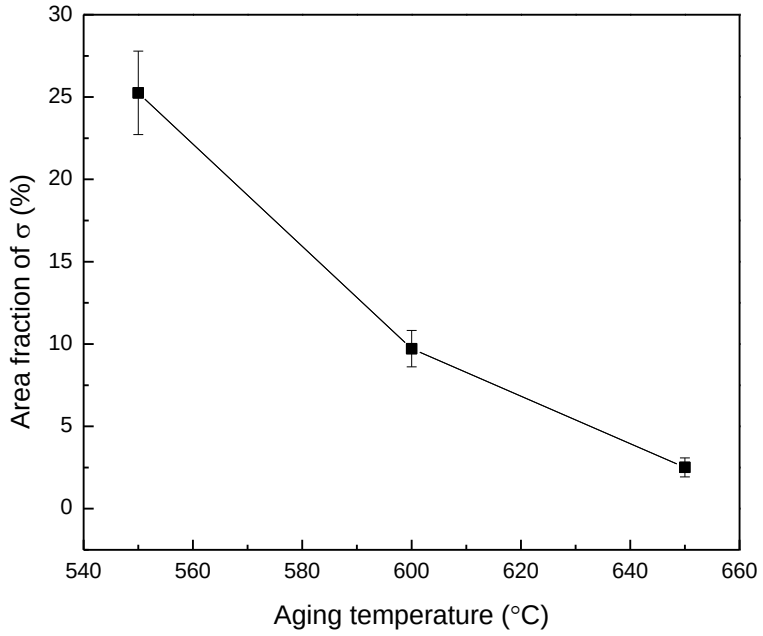

Figure 6.11: Area fraction of the σ phase aged at 550, 600 and 650 °C for 8760 h.

The area fraction of the σ phase decreased with temperature. To show the proportion, distribution and morphology of the σ phase with temperature distinctly, a schematic illustration of the σ-phase-rich zones at the three temperatures is presented in Figure 6.12. This zone exhibited a lamellar-type microstructure when aged at 550 °C for 8760 h. However, this lamellar microstructure only remained in the upper part of the interfacial layer, close to the S21, when aged at 600 °C for 8760 h. In the lower part of the interfacial layer, the $M_{23}C_6$ carbides were formed, close to the fusion line. As shown in Figure 6.9, the weight percentage of Fe and Co ranges from 69 to 91% in the PMZ zone, whereas that of Cr and Mo ranges from 7 to 25%. There were more Cr and Mo close to the S21 side. Higher σ-phase-forming elements such as Cr and Mo content could promote the precipitation of the σ phase. Gray et al. detected the transformation of the δ-ferrite to the σ phase in type 308 and 304 austenitic stainless steels; the δ-ferrite contained more Cr than the austenite from their chemical analysis [73]. Villanueva et al. observed that the σ phase precipitated in the ferrite rather than the austenite of a duplex stainless steel, which was attributed to the fact that the ferrite contained more Cr and Mo than the austenite [74]. The addition of Mo accelerated the rate of the σ-phase formation dramatically in Fe-Cr alloys containing different amounts of Mo [75]. Sasikala et al. pointed out that diffusion of Mo could also lead to the formation of the σ phase [76]. By adding Si, the fraction and size of the σ phase showed a significant increase in super austenitic stainless steel welds [77]. There was also more Si close to the S21 side in Figure 6.9. Therefore, the σ phase precipitated close to the S21. When aged at 650 °C for 8760 h, this lamellar microstructure disappeared and only some spotted σ phase could be observed.

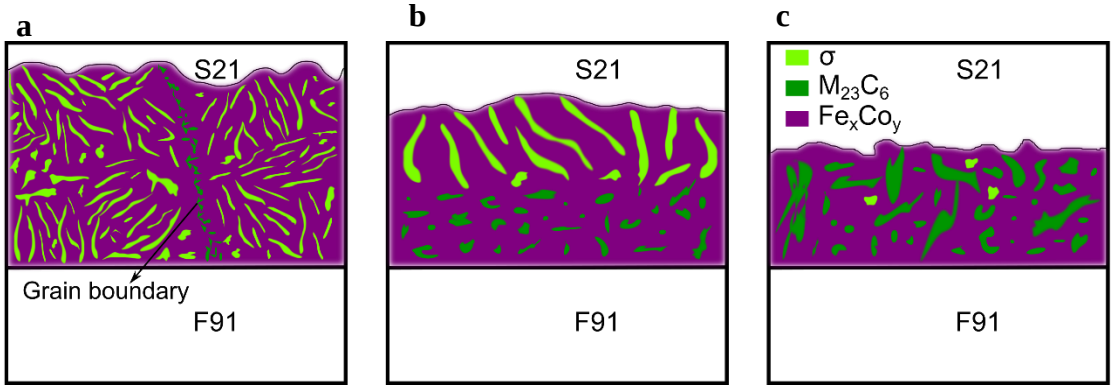

Figure 6.12: Schematic illustration of the σ-phase-rich zones aged at (a) 550, (b) 600 and (c) 650 °C for 8760 h (colored zone: interfacial layer).

The σ phase usually precipitates in stainless steels and is known for causing embrittlement [78]. It is reported that the area fraction (2–8%) of brittle σ phase affected the ductile to brittle transition behavior of a stainless steel [79]. When it reached about 8%, no transition could be determined due to the significant embrittlement for all the studied temperatures. Pohl et al. found that the σ phase showed first cracks during in-situ tensile tests in a stainless steel [80]. The ductility of two duplex stainless steels also decreased by precipitation of the σ phase [81].

The presence of $M_{23}C_6$ carbides has been reported in S21 [82] and S6 [83]. They are also the most common precipitates in the 9% Cr steels as they are used to strengthen the steels. The strengthening effect of $M_{23}C_6$ carbides, located at grain boundaries and martensite lath boundaries, was attributed to the stabilization of sub-grain boundaries, as reviewed by Maruyama et al. in 2001 [84] and by Abe in 2008 [85]. Further, Abe investigated the creep rates of 9% Cr steels with different carbon and boron concentrations and validated that sub-boundary hardening enhanced by fine dispersions of precipitates was the most important strengthening mechanism in 2009 [86]. However, during high-temperature exposure, the precipitates tended to coarsen and the strengthening effect decreased with exposure time [87].

The effects of $M_{23}C_6$ carbides on mechanical properties depend on their size and distribution. It is reported that the tensile strength of a novel austenitic stainless steel decreased due to the evolution of $M_{23}C_6$ carbides in morphology and amount [88]. The cracks preferentially initiated and propagated along the $M_{23}C_6$/austenite interfaces. It was also found that the coarsening of the $M_{23}C_6$ carbides decreased the tensile strength and elongation of an aged Inconel 690 tube [89]. In addition, the $M_{23}C_6$ carbides along grain boundaries were found to be responsible for the embrittlement of an austenitic stainless steel [90]. Nevertheless, fine $M_{23}C_6$ carbides the size of which was of the order of tens of nm could strengthen grain boundaries, as reported by He et al. in a study performed on a Ni-based superalloy M963 [91].

In the present study, the interfacial layer thickness increased with time and temperature, as shown in Figure 6.13a. From equations (2) and (3), discussed previously, the interfacial layer thickness can be expressed as:

$$x = k_0 \left(\exp\left(\frac{-Q}{RT}\right) t^{0.5}\right) \qquad \text{Equation 6.4}$$

This implied that the interfacial layer thickness *x* was linear with $\exp\left(\frac{-Q}{RT}\right) t^{0.5}$, as shown in Figure

6.13. The area fraction of the $M_{23}C_6$ carbides is plotted in the same graph. The slopes of the two linear fits were almost identical, indicating that the growth of the $M_{23}C_6$ carbides followed the same trend as the growth of the interfacial layer.

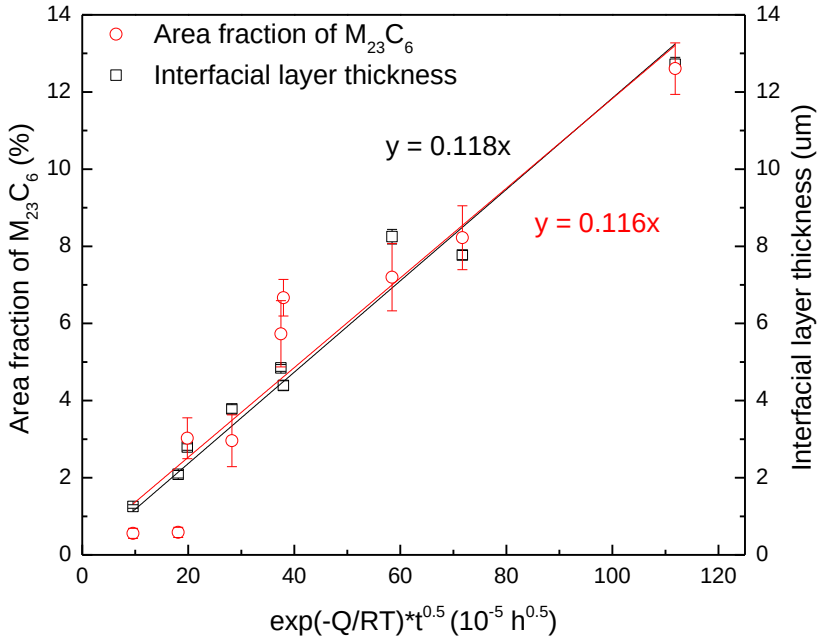

Figure 6.13: Area fraction of the $M_{23}C_6$ carbides.

The equivalent diameter of the $M_{23}C_6$ carbides is shown in Figure 6.14. It increased with time and temperature and was of the order of hundreds to thousands of nm. The equivalent diameter of the $M_{23}C_6$ carbides in P92 (a modification of grade 91 by adding W and reducing the content of Mo) was of the order of tens to hundreds of nm aged at 600 or 650 °C for up to 26,000 h, as investigated by Gustafson and Hättestrand [92]. As mentioned earlier, the strengthening effect of the $M_{23}C_6$ carbides in the 9% Cr steels would decrease during high-temperature exposure because of coarsening. The size of the newly formed $M_{23}C_6$ carbides in the interfacial layer after aging was around an order of magnitude larger than those in P92. In addition, due to the significant difference in hardness between the $M_{23}C_6$ carbides and the surrounding Fe_xCo_y, they wouldn't deform compatibly. Therefore, the large $M_{23}C_6$ carbides in the interfacial layer could be vulnerable to crack initiation.

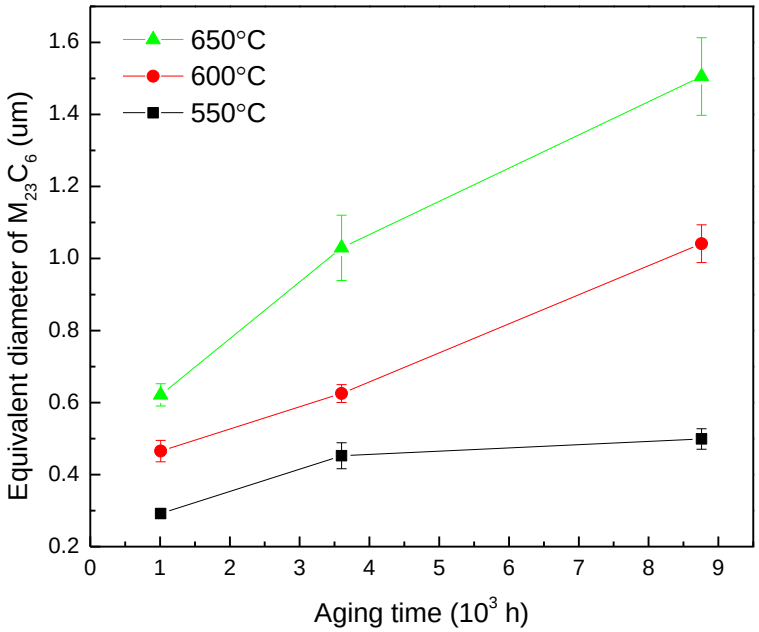

Figure 6.14: Equivalent diameter of the $M_{23}C_6$ carbides (The straight lines in the right-side plot, connecting each individual data point, have no physical significance.).

Both the $M_{23}C_6$ carbides and the σ phase in the interfacial layer were significantly harder than the Fe_xCo_y, the F91 and the S21. It is proposed that the increase of the interfacial layer's hardness was mainly caused by the presence of the $M_{23}C_6$ carbides and the σ phase. However, Lolla et al. concluded that the σ phase contributed to the increase of the interfacial layer's hardness [4], which agreed with the Electric Power Research Institute in their report [3]. The hardness of the $M_{23}C_6$ carbides was not investigated by them. Within the studied aging conditions, the area fraction of the σ phase decreased with temperature, while the $M_{23}C_6$ carbides grew with temperature and time. Therefore, it is proposed that the σ phase might contribute more in the increase of the interfacial layer's hardness at lower temperatures than that at higher temperatures, namely, the σ phase might contribute more at services temperatures. This well explained that a delamination crack propagated in the lamellar-σ-phase-rich zone of a hardfacing component after approximately 60,000 h service exposure at temperatures up to 566 °C, as reported by Lolla et al. [4]. The $M_{23}C_6$ carbides and the σ phase would eventually affect the mechanical properties of the hardfacing components.

6.5 Conclusions

The present work explored the F91/S21 interfacial microstructure of S6 and S21 hardfacing on a F91 steel. The F91/S21 interface is thermodynamically unstable during aging, leading to the formation of an interfacial layer. This interfacial layer is composed of three main phases: a BCC-like intermetallic compound, Fe_xCo_y; a Cr-rich $M_{23}C_6$-type carbide; and an (Fe,Co)(Cr,Mo)-type σ phase. This layer follows a parabolic rate of growth. Namely, its thickness (mainly including Fe_xCo_y and $M_{23}C_6$) increases as the square root of aging time, suggesting a diffusion-controlled growth phenomenon. The activation energy estimated for the growth of this interfacial layer is 87 kJ/mol, which might be related to carbon diffusion.

The area fraction of the $M_{23}C_6$ carbides increases with aging temperature and time, while the area fraction of the σ phase decreases with aging temperature. The equivalent diameter of the $M_{23}C_6$ carbides increases with aging temperature and time. It is of the order of hundreds to thousands of nm. The $M_{23}C_6$ carbides and the σ phase were found to be significantly harder than the other phases. The increase of the interfacial layer's hardness is mainly caused by the $M_{23}C_6$ carbides and the σ phase. It is proposed that the σ phase contributes more in the increase of the interfacial layer's hardness at lower temperatures than that at higher temperatures.

The presence of the continuous interfacial layer containing hard and large $M_{23}C_6$ carbides and the σ phase after aging may affect high-temperature valve integrity. It may provide a brittle crack propagation pathway, leading to the delamination of valves in service. Hence, mechanical testing will be presented to validate this hypothesis in our future article.

6.6 Acknowledgments

The authors wish to acknowledge the Natural Sciences and Engineering Research Council (NSERC) of Canada and Velan Inc. for their financial support through the NSERC Multisectorial Industrial Research Chair in Coatings and Surface Engineering (IRC 433808–11). The authors also wish to thank Gil Perez, Luc Vernhes, and Vahe Najarian for providing their expertise to define the aging experiments and Nicolas Lévesque, Jonathan Delarosbil, and Pascal Coté from Velan for their help and assistance in the welding process and machining of samples. Dr. Etienne Bousser would like to acknowledge the NSERC's support through the postdoctoral fellowship program.

CHAPTER 7 ARTICLE 2: EFFECT OF INTERFACIAL MICROSTRUCTURE ON MECHANICAL PROPERTIES OF COBALT-BASED HARDFACING DURING LONG-TERM AGING

Yuxiao Wu[a], Thomas Schmitt[a], Etienne Bousser[a, b], Fadila Khelfaoui[c], Vahe Najarian[c], Jolanta-Ewa Klemberg-Sapieha[a], and Myriam Brochu[a]
[a]Polytechnique Montréal, 2900 Boulevard Edouard-Montpetit, Montreal, Quebec H3T 1J4, Canada
[b]The University of Manchester, School of Materials, Manchester M13 9PY, United Kingdom
[c]Velan Inc., 7007 Côte-de-Liesse, Montreal, Quebec H4T 1G2, Canada
Submitted to the Journal of Materials Science & Engineering A

Abstract: Disbonding and delamination of Stellite-hardfaced coating from high-temperature valves have presented a major challenge to the power generation industry. In order to study how the interfacial microstructure of Stellite-hardfaced coating might damage valve integrity during service, a series of aging experiments were conducted at temperatures ranging from 550 to 650 °C over three durations within a one-year period. After high-temperature exposure, the hardfacing interface was evaluated using innovative Charpy U-notch specimens. It was observed that the impact energy decreased significantly (by at least 92%) after aging. The fractographic analysis revealed that the fractures of the aged hardfacing specimens were brittle. It is proposed that an interfacial layer formed during aging provides a brittle crack propagation pathway. The impact energy loss is mainly associated with the formation of hard and brittle $M_{23}C_6$ carbides in the interfacial layer. The larger the $M_{23}C_6$ carbides grow, the smaller the impact energy becomes. The presence of the σ phase would also contribute to the decrease of the impact energy. It is concluded that the microstructural factors contributing to the delamination of Stellite-hardfaced coating in service are the formation of hard and brittle $M_{23}C_6$ carbides and σ phase.

Keywords: Stellite hardfacing; Interface; $M_{23}C_6$; σ phase; Impact; Delamination.

7.1 Introduction

Hardfacing, a surface engineering process, is employed to apply a wear-resistant material on the surface of a base material. According to an ASM handbook, hardfacing can reduce wear or material loss from abrasion, impact, erosion, galling, and cavitation [93] . Hardfacing can also enhance oxidation and corrosion resistance in elevated-temperature applications. Stellite 6 (S6), a cobalt-based hardfacing alloy, has been used in the fossil fuel power generation industry for

decades. Stellite 21 (S21) is commonly used as a buffer layer between the substrate and S6. One reason to use an S21 buffer layer is to reduce the thermal mismatch between the steel substrate and the S6 because of its intermediate thermal expansion, as demonstrated in a report [3]. These hardfacing alloys are generally applied to the sealing surfaces of valves which control the flow of high-temperature and high-pressure steam in power plants. Consequently, durable valve function is ensured by reducing friction and wear under sliding contact conditions during operation. However, when Stellite alloys are deposited on the valve materials during welding, such as the creep-resistant grade 91steel, part of the steel is inevitably melted and thus alloy mixing is unavoidable. Accordingly, unexpected deleterious phases may form during welding or service.

An industry challenge in the form of delamination of Stellite-hardfaced coating from valve seats or disks during service has been faced by the power generation world. The failure events and their relevant information were reviewed and summarized by the Electric Power Research Institute in a technical update report [3]. The damage mechanisms explaining these failures have been studied by several research teams. Hattel believed that the main cause was the presence of a decarburized zone in the steel near the interface and the residual stresses at the interface between P91 (piping) and S6 [38]. This decarburized zone was characterized by a loss of material strength. Nevertheless, some deleterious phases have been reported by some authors, such as the σ phase and the $M_{23}C_6$ carbides formed in the interfacial microstructure between the steel and Stellite. Leinenbach et al. observed an interfacial layer containing a $M_{23}C_6$-type carbide between the steel and S6 during long-term exposure at 600 and 625 °C [39]. In addition to the carbides, Lolla et al. also found a Cr-rich σ phase at the interface between grade 91 and S21 which showed the highest hardness among the phases studied, 11.7 GPa [4]. This team investigated the interfacial microstructure of naturally aged hardfacing, that is, approximately 60000 h of operation in steam conditions of 566 °C and 3.66 MPa. They believed that the σ phase was the main cause for hardness increase of the interfacial layer. The Electric Power Research Institute agreed with this conclusion in their technical update report [3].

In a previous study, we determined that the $M_{23}C_6$ carbides showed the highest hardness, 19.8 GPa, and the σ phase showed the second highest hardness, 16.0 GPa [94]. They were both significantly harder than F91 (forging) and S21. The F91/S21 interfacial microstructure was investigated after artificial aging between 550 and 650 °C over durations ranging from 1008 to 8760 h. The $M_{23}C_6$ carbides were present along most of the interface at all the studied temperatures, while the σ phase

was distributed heterogeneously. Thus, we concluded that both the $M_{23}C_6$ carbides and the σ phase, primarily the $M_{23}C_6$ carbides, contributed to the local hardening measured at the interface between F91 and S21.

The $M_{23}C_6$ carbides and the σ phase were reported to deteriorate toughness. Hong et al. reported the precipitation of grain boundary carbides ($M_{23}C_6$) at 850 °C in a high-nitrogen austenitic steel [95]. This team further studied the carbides' influence on the steel's mechanical properties [90]. The impact toughness of the specimen with grain boundary carbides was 53% lower than that of the specimen without the precipitation of carbides, performed at –40 °C. Liu et al. studied the microstructure evolution and toughness of the 25Cr2Ni2MoV steel weldments treated at 550 °C for 5, 10 and 20 h [96]. The results showed that the precipitated $M_{23}C_6$ carbides during the heat treatment led to the dramatic decrease in the toughness of the weld metal. Wei et al. reported that the presence of the $M_{23}C_6$ precipitates during aging was the dominant factor for the toughness reduction of an Fe-22Cr-25Ni alloy aged at 650, 700 and 750 °C [97]. Ibrahim et al. evaluated the effect of aging on the impact toughness of 2205 duplex stainless steel weldments using a tungsten inert gas welding process [98]. They determined that the degradation in impact toughness was related to the precipitation of the σ phase.

It is worth noting that the $M_{23}C_6$ carbides and the σ phase precipitated in the bulk materials in the reported studies above. Concerning this major industry challenge, it is clear that a hard interfacial layer containing the $M_{23}C_6$ carbides and the σ phase was formed between the steel and the cobalt-based hardfacing when exposed at temperatures ranging from 550 to 650 °C. Nevertheless, the $M_{23}C_6$ carbides and the σ phase did not precipitate in the bulk material, but in the local interfacial layer. The thickness of this hard interfacial layer was approximately 13 µm after aging at 650 °C for 8760 h [94]. In addition, the thickness of the Stellite-hardfaced coating layer was limited. The challenge lies in how to evaluate the toughness of such a local hard interface using mechanical testing. As defined by the ASTM C633 standard, the bonding strength of a coating to a substrate can be determined using tensile testing applied on the coated system composed of a coated sample glued to another sample [99]. This method is adapted particularly for testing thermal spray coatings. However, the hardfaced coating is generally deposited by welding, and thus a metallurgical bond is provided between the hardfaced coating and the substrate. Therefore, to determine the toughness of such a local hard interface, innovative Charpy U-notch specimens consisting of a hardfaced coating sample welded to another sample with the F91/S21 interface

centered in the notch were designed for the present study. We probe the effects of the interfacial microstructure on mechanical properties of hardfaced coating by means of impact testing.

7.2 Experimental details

7.2.1 Sample preparation

An F91 steel part with dimensions 356 mm × 57 mm × 38 mm was used as the substrate material. S21 and S6 powders were used as buffer and top hardfacing materials, respectively. The chemical compositions of F91, S21 and S6, as provided by the material suppliers, are listed in Table 7.1. The PTA welding conditions are given in Table 7.2. The shielding, plasma and powder gas were pure argon (100%). Only one layer of S21 was deposited on the F91 steel, while two layers of S6 were applied thereafter. Each layer was approximately 2 mm thick.

Table 7.1: Chemical compositions of F91, S21 and S6 (wt%).

	Cr	Mo	Fe	Co	Mn	Ni	W	C	Si	others
F91	8.39	0.90	Bal.	0.015	0.48	0.18	0.00	0.11	0.30	<1.00
S6	27.34	0.17	0.33	Bal.	0.33	1.78	4.22	1.63	1.09	<0.50
S21	27.45	5.37	1.44	Bal.	0.60	2.76	0.00	0.26	1.69	<0.50

Table 7.2: Welding conditions used for S21 and S6 deposition.

Parameter	Value
Particle size (mesh)	80/325
Feed rate of S6 (g/min)	25
Feed rate of S21 (g/min)	18
Current (A)	170 – 200
Voltage (V)	21.5 – 25.0
Preheat (°C for 1 h)	204
Interpass temperature (°C)	316 max

In order to manufacture specimens allowing mechanical testing of the F91/S21interface, another block of F91 steel was cut into V-shape (Figure 7.1a) and then welded to the hardfacing sample (Figure 7.1b) using Inconel 625 (IN625) as the filler material. This new assembly (Figure 7.1c) was cooled in air to room temperature after welding. To temper the heat-affected zone of the F91 steel and release residual stresses, a post-weld heat treatment (PWHT) was then conducted at 760 °C for 2 h. Subsequently, the assembly was cut into bars using wire electrical discharge machining. Each bar was then cut into two halves (Figure 7.1d).

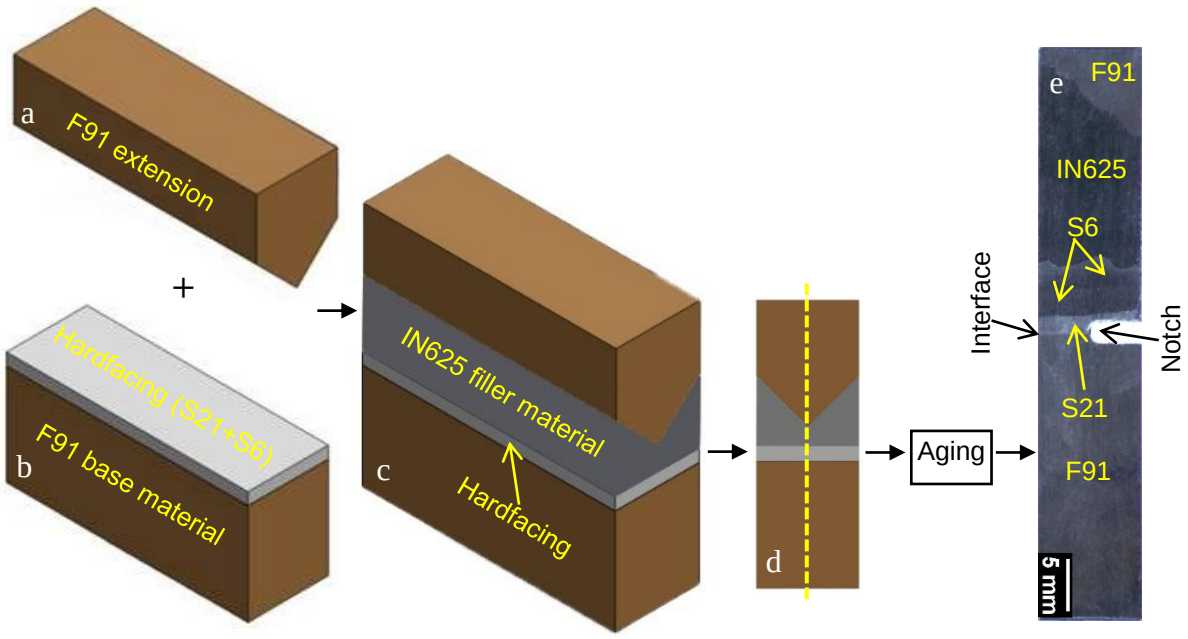

Figure 7.1: Charpy specimen manufacturing: (a) F91 extension, (b) Stellite-hardfaced coating with buffer layer of S21 and top layer of S6, (c) assembly made by welding an F91 extension to the Stellite-hardfaced coating sample using IN625 as the filler material, (d) bars cut from the assembly, and (e) Charpy U-notch specimen machined from the half bars (cross-section).

Some of these bars were aged under ambient atmosphere according to the aging information given in Table 7.3. The operating temperature range of grade 91 steel used for high-temperature steam systems is 538–593 °C (1000–1100 °F), according to Dobson [28]. Hence, one aging temperature was set at 550 °C for the purpose of representing typical service temperature. Higher temperatures were also chosen to be representative of more demanding applications. As F91 is tempered at temperatures ranging from 730 to 800 °C according to the ASTM A182 standard specification [43],

a hypothesis was made that the chosen aging temperatures did not significantly influence the base material microstructure.

Table 7.3: Aging conditions.

Temperature (°C)	550	600	650
Duration (h)	1008	1008	1008
	3600	3600	3600
	8760	8760	8760

After aging, the bars were machined into Charpy U-notch specimens with the F91/S21 interface centered in the notch, as shown in Figure 7.1e. In accordance with ASTM E23 requirements, the Charpy U-notch specimens were 55 × 10 × 10 mm with a notch 5 mm deep having a 1 mm tip radius [44]. A U-notch geometry was chosen to increase the probability of positioning the interface in the highly stressed area. In addition, Charpy U-notch specimens made of the F91 base material aged at 650 °C for 0, 1008, 3600 and 8760 h were also prepared for comparison purposes.

7.2.2 Microstructural analysis

The surfaces and cross-sections of fractured Charpy specimens were first examined using stereomicroscopy. Prior to observation, the cross-sections of fractured specimens were etched using Kalling's No. 2 reagent (5 g $CuCl_2$, 100 ml Hydrochloric acid and 100ml Ethanol) at room temperature to observe the main crack propagation. Following the stereomicroscopy observation, the specimens were cut and mounted in conductive resin. Subsequently, the cross-sections of the specimens were mechanically ground using silicon carbide abrasive papers up to 1200 grade, then polished using diamond suspensions up to 1 µm, and finally polished using a 0.04 µm mixed colloidal silica suspension (150 ml distilled water, 150 ml standard colloidal silica suspension and 30 ml H_2O_2). After polishing, the cross-sections were ultrasonically cleaned in acetone and isopropanol, and stored under vacuum at room temperature.

The microstructure was characterized using a JEOL JSM-7600F field-emission scanning electron microscopy (SEM) equipped with an Oxford Instruments X-Max energy dispersive X-ray spectroscopy (EDS) detector operating at an accelerating voltage of 15 kV. The EDS analysis was

performed using AZtec software with the built-in extended-quant standardizations (15 kV set). Measurements of the interfacial layer thickness, the area fractions of the $M_{23}C_6$ carbides and the σ phase, and the equivalent diameter of the $M_{23}C_6$ carbides were detailed in our previous article [94].

7.2.3 Mechanical testing

To measure the hardness of individual phases at the F91/S21 interface, nanoindentation was carried out on the cross-section of a hardfacing specimen aged at 650 °C for 8760 h using a Bruker Triboindenter 950 equipped with a Berkovich diamond tip following the standard ISO14577-1 [48]. Prior to testing, the area function of the tip was calibrated using a fused quartz reference. A matrix of 16 × 16 indentations evenly spaced by 2 μm was performed. The applied load increased linearly over 5 s, kept constant at 2 mN for 2 s, and then decreased linearly over 5 s. The Oliver and Pharr method [46] was used to calculate the hardness of each indentation.

Charpy impact tests were carried out on an Instron pendulum impact testing machine (model SI-1C3) at room temperature following the ASTM E23 procedure [44]. An 8 mm radius striker was used. The Charpy machine verification program administered by the National Institute of Standards and Technology was used to calibrate this Charpy impact testing machine, in accordance with the ASTM E23 standard. Fracta Software connected to the Charpy machine was used to calculate and record the energy absorbed by specimens during testing. The averaged impact energy for each aging condition was obtained over two to four measurements. Because the repeated number was small, the uncertainties were obtained from the formula:

$$\Delta E_{\mathrm{avg}} = \frac{E_{\max} - E_{\min}}{2\sqrt{N}} \qquad \text{Equation 7.1}$$

where ΔE_{avg} is the uncertainty in the mean value of the impact energy, $E_{\max}$ is the maximum impact energy, $E_{\min}$ is the minimum impact energy, and N is the number of measurements.

7.3 Results

7.3.1 F91/S21 interfacial microstructure

The F91/S21 interfacial microstructure is shown in Figure 7.2. Compared with the sample in the as-tempered condition (Figure 7.2a), an interfacial layer (Figure 7.2b) was observed between the F91 substrate and the S21 buffer layer after aging at 650 °C for 8760 h. There were thee main

phases having different morphologies and BSE contrasts in this interfacial layer, as shown in Figure 7.2b. They were identified in our previous article: a BCC-like Fe_xCo_y phase, a Cr-rich $M_{23}C_6$-type carbide, and an (Fe,Co)(Cr,Mo)-type σ phase [94]. The $M_{23}C_6$ carbides were embedded in the Fe_xCo_y phase and they were present along most of the interface, while the σ phase was distributed heterogeneously and in smaller amounts. In the EDS composite maps, the σ phase was in color white or light green, the $M_{23}C_6$ carbides were in color green, and the Fe_xCo_y was in color purple. The color codes representing the thee phases were used in the following Figures 7.3, 7.7 and 7.9.

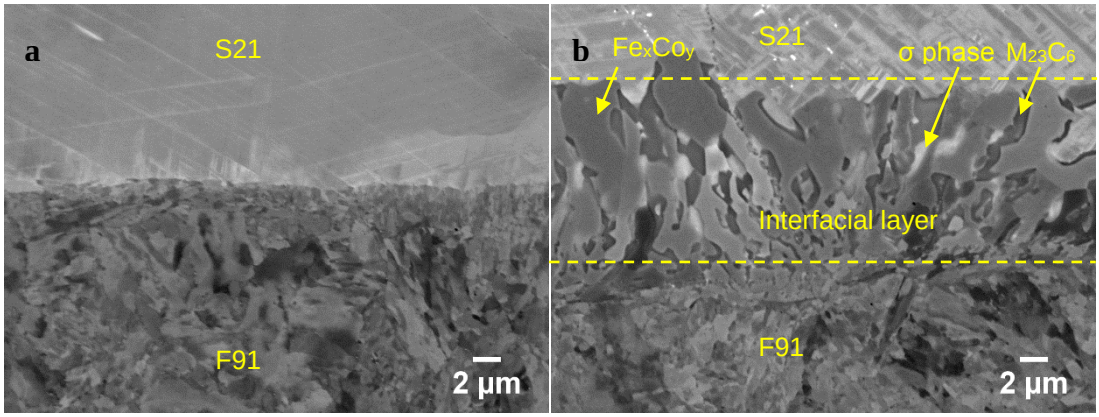

Figure 7.2: BSE images showing the F91/S21 interfacial microstructure: (a) in the as-tempered condition and (b) after aging at 650 °C for 8760 h.

7.3.2 Nanoindentation on the F91/S21 interface

Nanoindentation was performed on the cross-section of a sample aged at 650 °C for 8760 h. The hardness map, the corresponding BSE image and the corresponding EDS composite map are shown in Figure 7.3. As seen from the hardness map, the interfacial layer exhibited higher hardness than the F91 and the S21. The hardness of the individual phases in this interfacial layer was reported in our previous article [94]. The $M_{23}C_6$ carbides and the σ phase were significantly harder than other phases. As shown in Figure 7.3, one indent on the $M_{23}C_6$ carbides outlined by a circle exhibited the highest hardness, in the range of 19 GPa. Another indent on the σ phase outlined by a triangle exhibited the second highest hardness, in the range of 18 GPa.

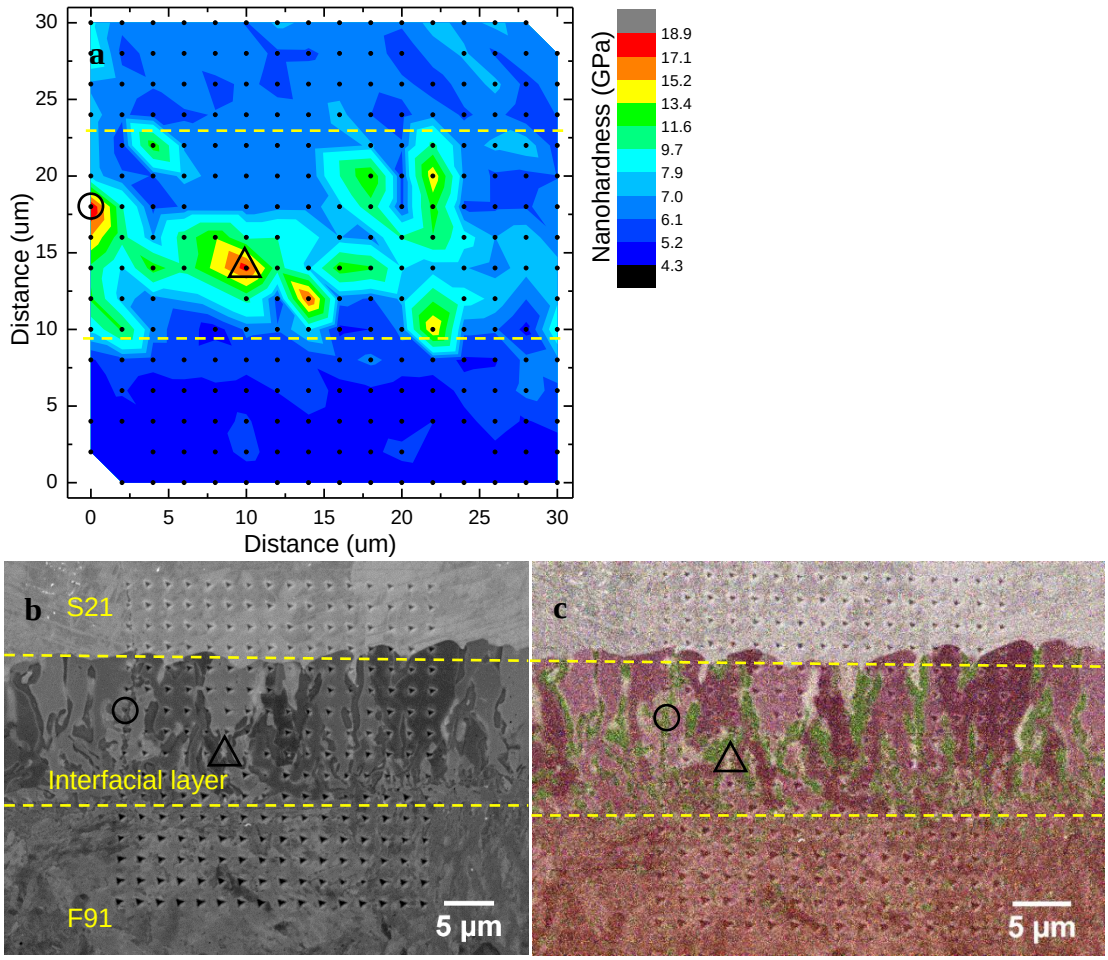

Figure 7.3: A sample aged at 650 °C for 8760 h (a) hardness map, (b) the corresponding BSE image and (c) the corresponding EDS composite map.

7.3.3 Charpy impact testing

The Charpy impact energy measurements are shown in Figure 7.4a for all the aging durations and temperatures studied. The “down” triangles represent the Charpy impact energy evolution of the F91 steel aged at 650 °C for durations ranging from 0 to 8760 h. The other symbols represent the Charpy impact energy evolution of the hardfacing specimens aged at temperatures between 550 and 650 °C for durations ranging from 0 to 8760 h. As expected, the impact energy of the F91substrate material did not evolve significantly with time at 650 °C and was always greater than that of the hardfacing specimens. Compared with the specimens in the as-tempered condition (aged for 0 h), the impact energy of the hardfacing specimens decreased significantly after aging

for 1008 h. At least 92% of the impact energy was lost (92%/1008 h). The impact energy continued to decrease with aging time up to 8760 h, but to a lesser extent than that from 0 to 1008 h, as may be seen in Figure 7.4b. The total energy loss reached up to 97% after aging at 650 °C for 8760 h. For a given aging time, the impact energy also decreased with temperature, as seen in Figure 7.4b.

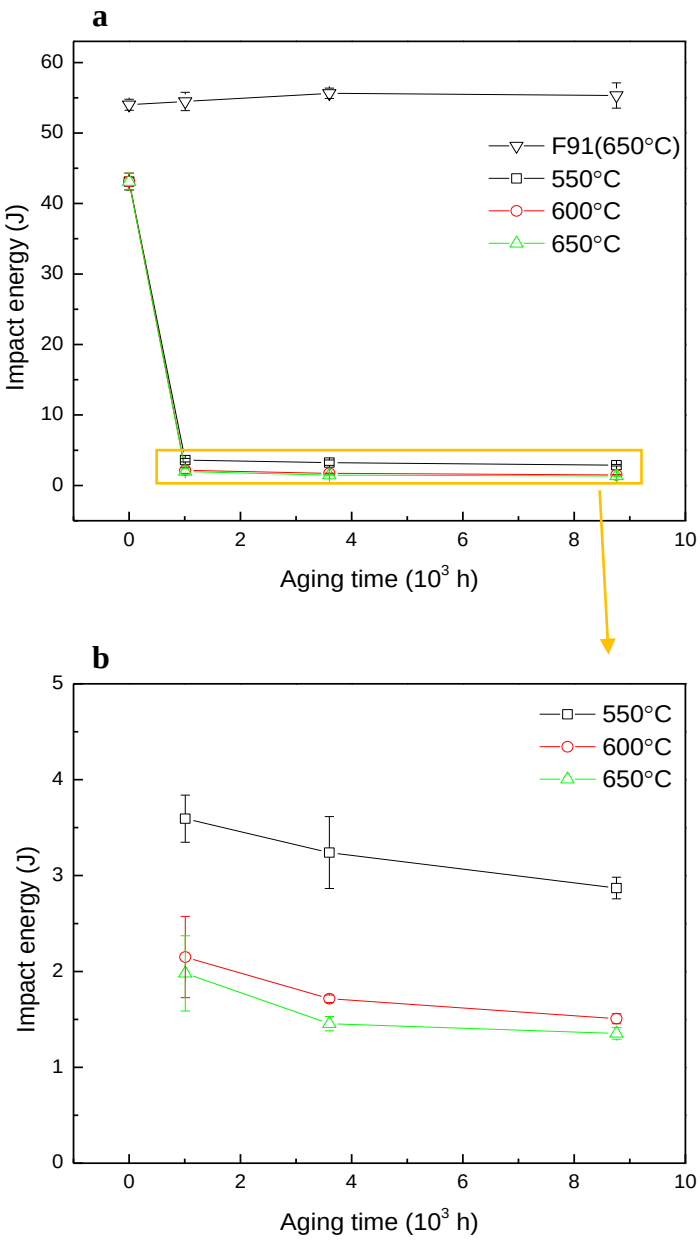

Figure 7.4: (a) Charpy impact energy evolution of F91 and hardfacing specimens and (b) magnification of (a) for the hardfacing specimens after aging. The straight lines, connecting each individual data point, have no physical significance.

In order to explain the sharp decrease of the impact energy affecting the hardfacing specimens after aging, an examination of the fractured specimens was carried out using stereomicroscopy. As seen in Figure 7.5a and b, the fracture occurred in the F91 steel for the as-tempered Charpy specimens while the fracture occurred along the F91/S21 interface for all the aged Charpy specimens. The fracture surfaces also exhibited completely distinct morphology, as may be seen in Figure 7.5c and d. Pronounced plastic deformation and lateral expansion took place for the as-tempered specimens, as is demonstrated by the impact energy above 40 J. In contrast, reasonably smooth fracture surfaces and no significant lateral expansion were observed for the aged specimens, as is evidenced by the impact energy below 4 J. Based on the aforementioned results, the fracture of the specimens in the as-tempered condition was mainly ductile, while the aged specimens showed brittle fracture along the F91/S21 interface. Nevertheless, further investigation was necessary.

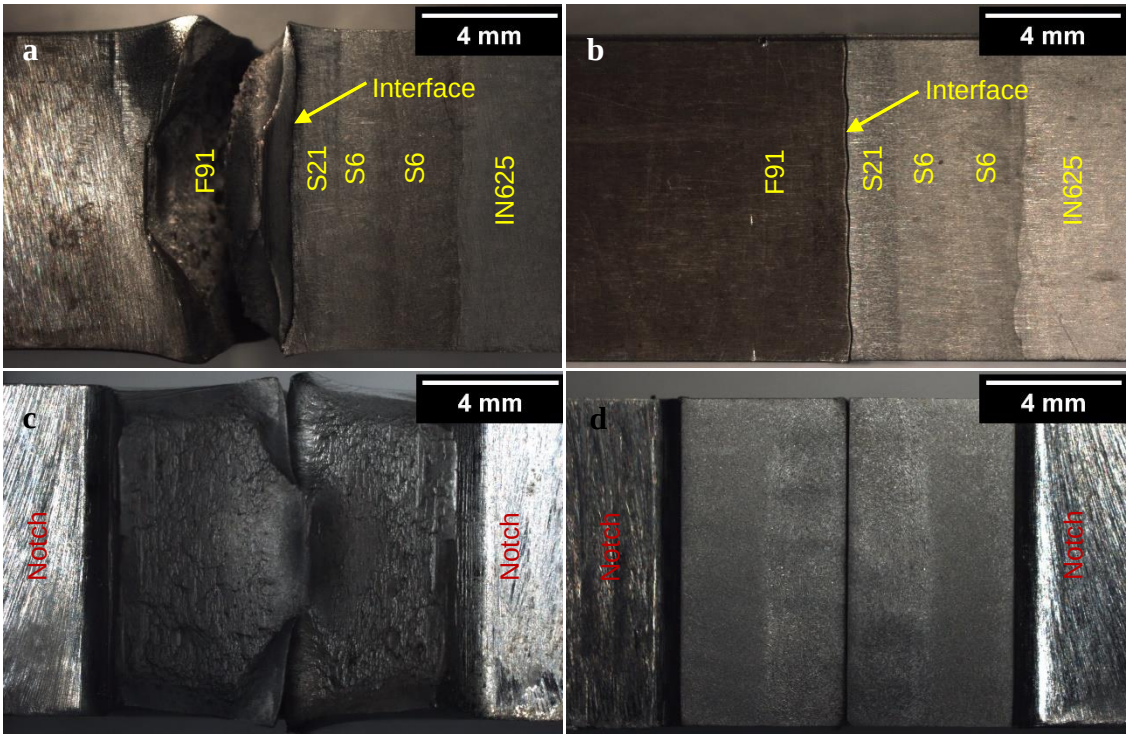

Figure 7.5: Representative back-faces of the fractured Charpy specimens (a) in the as-tempered condition and (b) after aging; representative macro-fracture surfaces of Charpy specimens (c) in the as-tempered condition and (d) after aging.

7.3.4 SEM observation on cross-sections of fractured specimens

The cross-sections of the fractured specimens aged at 550, 600 and 650 °C for 8760 h were analyzed by backscattered electron (BSE) imaging, shown in Figure 7.6, where the fracture was along the interfacial layer. This interfacial layer grew thicker with temperature, as may be appreciated in Figure 7.6. The $M_{23}C_6$ carbides and the σ phase, were significantly harder than other phases, such as the Fe_xCo_y, the F91 and the S21. Herein it is corroborated that this layer provided a crack propagation pathway under high-strain rate impact, which is the favored explanation for the decrease of the impact energy.

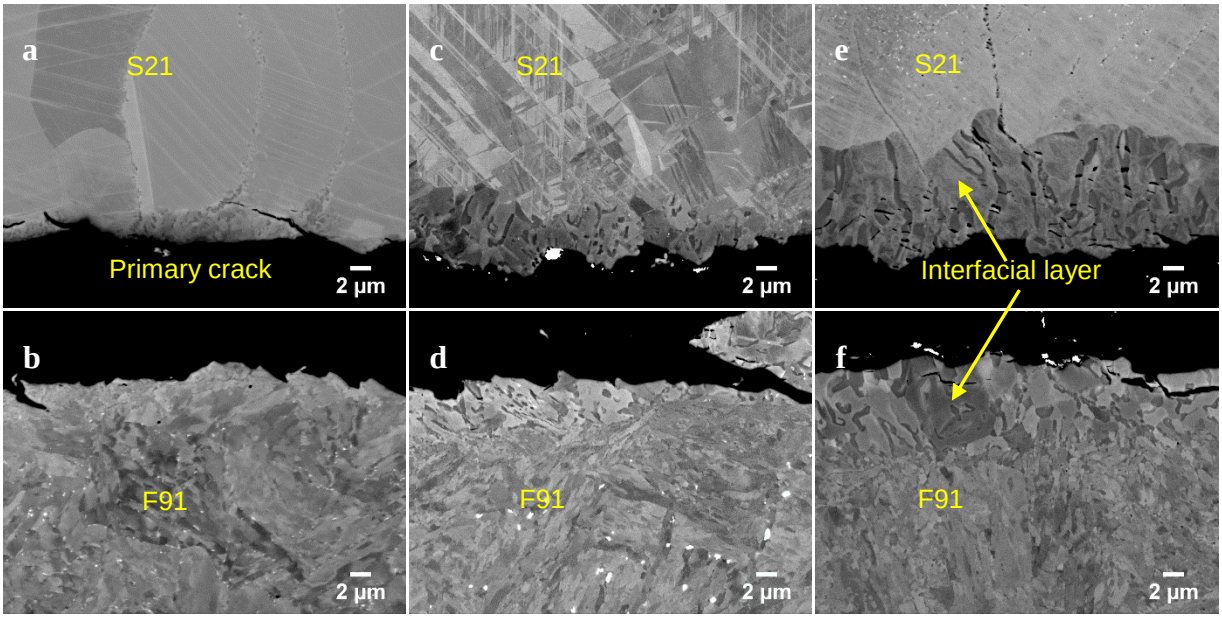

Figure 7.6: Cross-sections showing the fracture along the interfacial layer (a) and (b) at 550 °C 8760 h, (c) and (d) at 600 °C 8760 h, and (e) and (f) at 650 °C for 8760 h (the crack propagation direction was perpendicular to the cross-section).

In order further to study the behaviors of individual phases in the interfacial layer under the impact force, secondary cracks were more closely observed using BSE imaging and EDS mapping. As shown in Figure 7.7a and b, a large secondary crack propagated along grain boundaries, which are rich in the green $M_{23}C_6$ carbides. As seen in Figure 7.7c and d, another large secondary crack first propagated along grain boundaries and then branched off into the zone rich in the lamellar σ phase (light green color in Figure 7.7d). In addition, more small cracks were observed in the $M_{23}C_6$ carbides and the σ phase some distance away from the main crack, as indicated by the yellow

arrows in Figure 7.7f and h. These secondary cracks indicated that the $M_{23}C_6$ carbides and the σ phase were both brittle phases. In addition, some small secondary cracks were arrested at $M_{23}C_6/Fe_xCo_y$ and σ/Fe_xCo_y boundaries, or in Fe_xCo_y because the surrounding Fe_xCo_y is expected to be more ductile than both the $M_{23}C_6$ carbides and the σ phase.

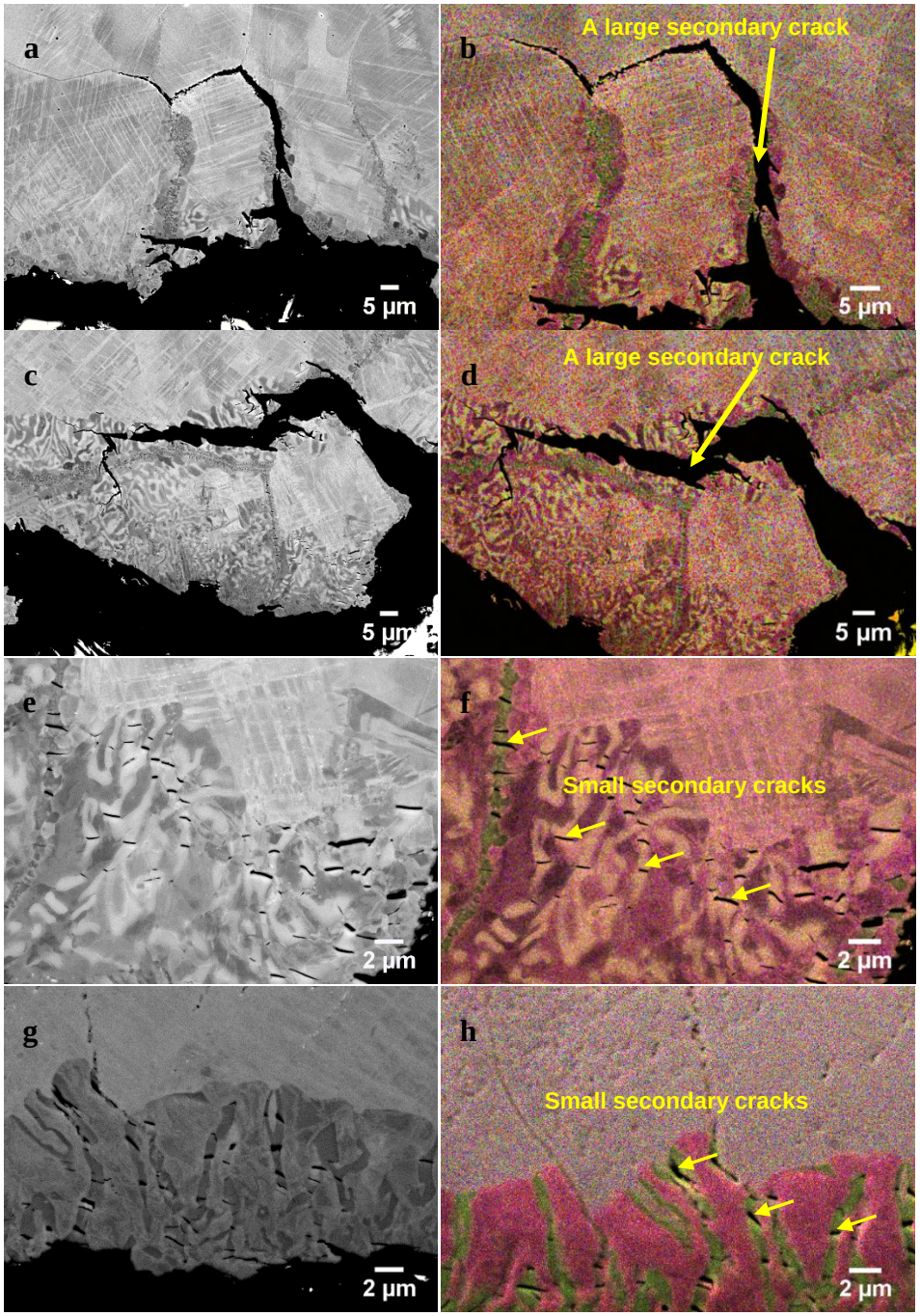

Figure 7.7: BSE images and EDS layered maps showing the secondary cracks at 600 °C for 8760 h (a), (b), (c) (d), (e), and (f); and at 650 °C for 8760 h (g) and (h).

7.3.5 SEM Fractographic observation

SEM fractographs of a hardfacing specimen in the as-tempered condition are shown in Figure 7.8. Figure 7.8a presents a full section from the back-face edge at the image top to the notch edge at the image bottom (fracture initiation). Along with the fracture propagation, the appearance became smoother toward the back-face edge. Higher-magnification views of zones 1 and 2 outlined by the yellow rectangles in Figure 7.8a are shown in Figure 7.8b and c, respectively. Zone 2 was quite steep. Although the two zones demonstrated different macro-morphology in Figure 7.8a, they exhibited the similar dimple rupture mechanism. The dimples in Figure 7.8b were shallower and smaller than those in Figure 7.8c. The failure of the as-tempered hardfacing specimens was found to be ductile.

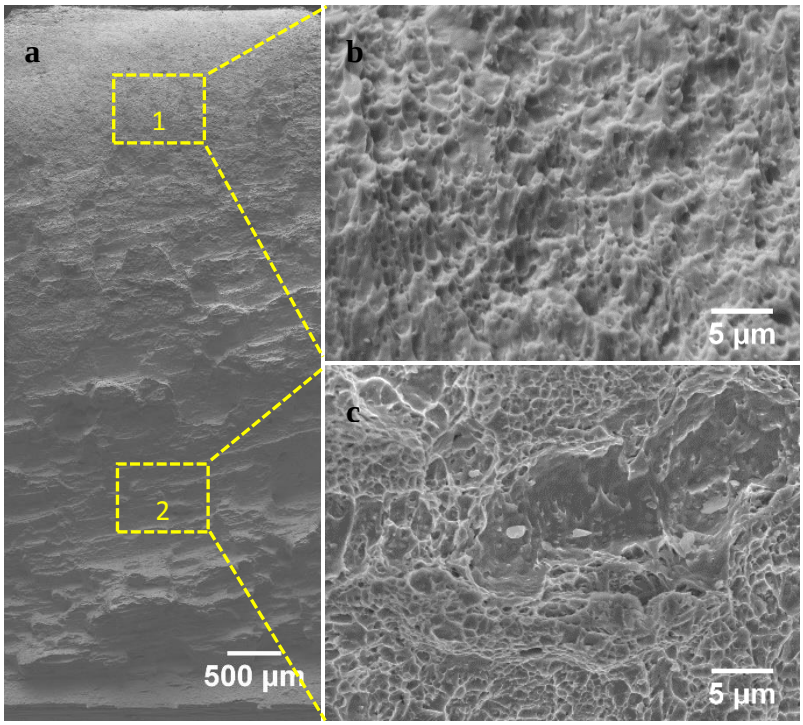

Figure 7.8: Representative fractographs of a hardfacing specimen in the as-tempered condition: (a) macro-fractograph, (b) higher magnification view of zone 1, and (c) higher magnification view of zone 2.

A fractograph of a hardfacing specimen aged at 600 °C for 8760 h is shown in Figure 7.9a. Zone 1 in Figure 7.9a exhibited quite different morphology from the rest of the fracture surface. The quasi-cleavage feature indicated by the yellow arrow was observed in Figure 7.9b. As seen in its EDS map, Figure 7.9c, the upper left corner exhibited a mixture of green $M_{23}C_6$ and purple Fe_xCo_y,

while the quasi-cleavage area was reddish. From the EDS spot measurement on the reddish area, it is inferred that the quasi-cleavage area was located in the F91 due to high Fe content. This indicated that the fracture path penetrated into the base material in some regions which explained the curved-line morphology in zone 1 of Figure 7.9a. As for zone 2 in Figure 7.9a, its higher-magnification area presented cleavage fracture, as indicated by the arrow in Figure 9d. Its corresponding EDS map, Figure 7.9e, exhibited a mixture of green $M_{23}C_6$ and purple Fe_xCo_y, precipitated in the interfacial layer. Therefore, the fracture was mainly located in the interfacial layer; it also penetrated into the base material in some regions, as appreciated in zone 1. The above quasi-cleavage and cleavage features indicated the brittle failure of the aged hardfacing specimen.

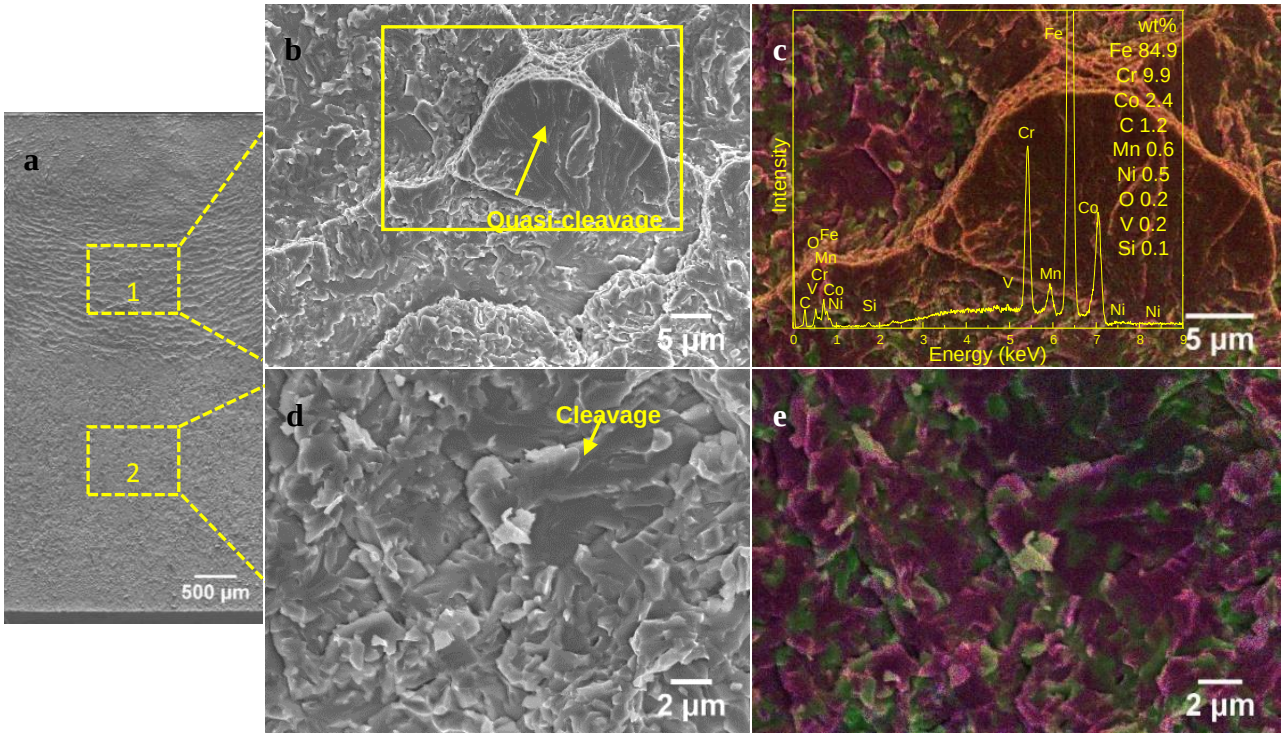

Figure 7.9: A hardfacing specimen aged at 600 °C for 8760 h: (a) macro-fractograph, (b) SEM fractograph from zone 1, (c) EDS map of the zone outlined by the rectangle in (b) and EDS spot measurement on the reddish zone, (d) SEM fractograph from zone 2, and (e) EDS map of (d).

7.4 Discussion

Since the fracture mainly occurred along the interfacial layer, a graph showing the relationship between the impact energy loss percentage and the interfacial layer thickness or the equivalent

diameter of the $M_{23}C_6$ carbides is proposed in Figure 7.10. There was a trend showing that a thicker interfacial layer resulted in lower impact energy. The more the equivalent diameter of the $M_{23}C_6$ carbides grew, the greater the impact energy loss was. The interfacial layer thickness and the equivalent diameter of the $M_{23}C_6$ carbides grew as $\exp\left(\frac{-Q}{RT}\right)t^{0.5}$, while the impact energy loss increased rapidly at the beginning, but became asymptotical when the thickness reached about 10 µm. Therefore, the impact energy loss was associated with the interfacial layer and the $M_{23}C_6$ carbides.

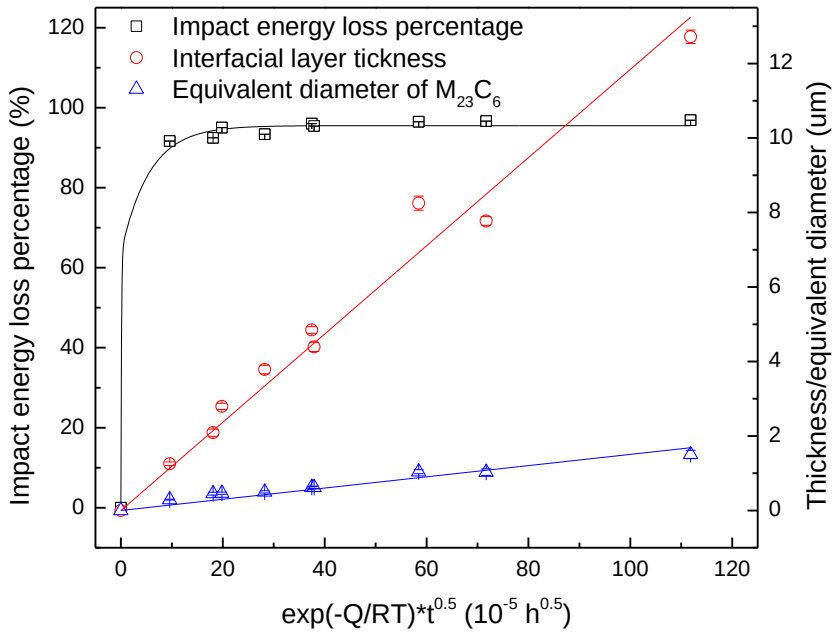

Figure 7.10: Relationship between the impact energy loss percentage and the interfacial layer thickness or the equivalent diameter of the $M_{23}C_6$ carbides for the specimens aged at 550, 600 and 650 °C for 1008, 3600 and 8760 h, with exponential and linear best-fit regressions.

In addition to the hard $M_{23}C_6$ carbides, there was also the hard σ phase in this layer. As a further step to identify the phases that could drastically decrease the impact energy, the relationship between the impact energy loss and area fractions of the $M_{23}C_6$ carbides and the σ phase is plotted in Figure 7.11. The results were obtained from the specimens aged at 550, 600 and 650 °C for 8760 h. Both the impact energy loss percentage and the area fraction of the $M_{23}C_6$ carbides were

observed to increase with temperature, while the area fraction of the σ phase decreased with temperature. Therefore, the loss of impact energy was mainly associated with the $M_{23}C_6$ carbides.

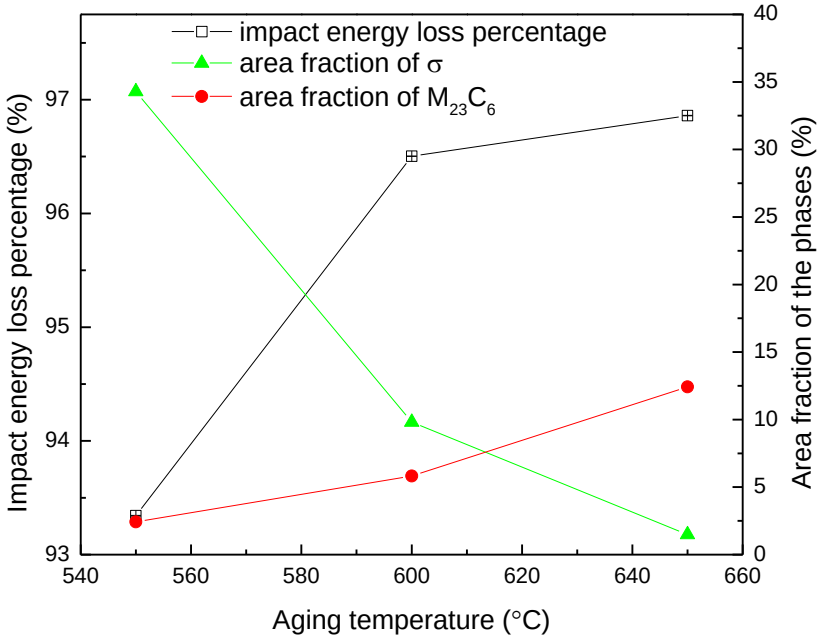

Figure 7.11: Relationship between the impact energy loss percentage and area fractions of the $M_{23}C_6$ carbides and the σ phase for the specimens aged at 550, 600 and 650 °C for 8760 h. The straight lines, connecting each individual data point, have no physical significance.

In our present study, the $M_{23}C_6$ carbides in the interfacial layer were the principal cause of the impact energy loss. These carbides exhibited the highest hardness in the interfacial layer and they were present along most of the interface. The poor deformability of these carbides made the $M_{23}C_6/Fe_xCo_y$ interface quite weak. As the $M_{23}C_6$ carbides grew, the area of the $M_{23}C_6/Fe_xCo_y$ interface also increased. Consequently, the impact energy decreased. The $M_{23}C_6$ carbides precipitated in the bulk materials were also reported to be the cause of toughness loss. Peng et al. investigated the impact toughness evolution of 25Cr–20Ni–Nb–N stainless steel aged at 700 °C for 0, 500, 1000, 3000 and 5000 h [100]. The sharp decrease of the impact toughness after aging for 500 h was caused by the reduction of the bonding interface strength when the $M_{23}C_6$ carbides precipitated on grain boundaries. The weak $M_{23}C_6$/austenite interfaces of a novel austenitic stainless steel, where cracks preferentially initiated and propagated, were also observed by Zheng et al. in a tensile test [88].

Although the σ phase was not found to be the principal cause of the impact energy loss in our study, it is known for its embrittlement in the bulk materials. It is reported that the loss of ductility of two duplex stainless steels was caused by the increase of σ phase content precipitated during the heat treatments [81]. Pohl et al. observed the precipitation of the σ phase in a duplex stainless steel when heat treated between 750 and 950 °C [80]. The formation of the hard precipitates led to a detrimental loss of notch bar impact values. They also found that cracks first appeared in the σ phase during in-situ tensile tests. We believe the presence of the σ phase would also contribute to the decrease of the impact energy. The secondary cracks in the σ phase, observed in Figure 7.7c, d, e and f, corroborated its brittleness.

Though the $M_{23}C_6$ carbides in the interfacial layer were found to be the principal cause to degenerate the toughness by means of impact testing, the service conditions would be quite different from aging and impact testing. As proposed in our previous study, the σ phase played a more important role in hardness increase of the interfacial layer at lower temperatures than that at higher temperatures [94]. Namely, the σ phase contributed more at operation temperatures such as at 566 °C. Grain boundaries in the zones enriched with the lamellar σ phase were often observed [94]. The σ-phase-rich zone was also usually much thicker than the average thickness of the interfacial layer. The grain boundaries in the S21 served as easy pathways to form the σ phase. It is not hard to imagine that large amounts of σ phase might precipitate along grain boundaries in the S21 bulk material after years of service. Moreover, the σ phase might be distributed far away from the interface, deeply into the S21 bulk material. The hard σ phase could easily act as crack initiation sites. It should be emphasized that in addition to aging, there are also other factors during service, such as operation induced stresses (start-ups and shut-downs of plants and opening and closing of valves). They may also contribute to the failures. Thus, we can only conclude that the microstructural factors contributing to the delamination of high-temperature valves in service are the formation of hard and brittle $M_{23}C_6$ carbides and σ phase.

7.5 Conclusions

The effects of the F91/S21 interfacial microstructure on the mechanical properties of Stellite-hardfaced coating were explored using innovative Charpy U-notch specimens. At least 92% of the impact energy is lost for the specimens aged between 550 and 650 °C over durations ranging from 1008 to 8760 h. The impact energy loss increases with aging time and temperature.

Fractographic analysis revealed that the fracture of the as-tempered hardfacing specimens presents ductile, whereas the fracture of the aged hardfacing specimens is brittle. An interfacial layer formed during aging provides a brittle crack propagation pathway under the high-strain rate impact. The impact energy loss is mainly associated with the brittle $M_{23}C_6$ carbides in the interfacial layer. The more the equivalent diameter of the $M_{23}C_6$ carbides grows, the smaller the impact energy is. Although the σ phase was not found to be the principal cause of the impact energy loss, it would also contribute to the decrease of the impact energy.

The presence of the continuous interfacial layer containing the hard and brittle $M_{23}C_6$ carbides and σ phase severely damages the integrity of the Stellite-hardfaced coating after aging under the high-strain rate impact. Therefore, it is concluded that the microstructural factors contributing to the delamination of high-temperature valves in service are the formation of hard and brittle $M_{23}C_6$ carbides and σ phase. To meet this challenge and find a solution for industrial valves, other buffer layers for Stellite 6 hardfaing by PTA welding are being evaluated and the solution will be presented in our future article.

7.6 Acknowledgments

The authors acknowledge the financial support of the Natural Sciences and Engineering Research Council (NSERC) of Canada and of Velan Inc. though the NSERC Multisectorial Industrial Research Chair in Coatings and Surface Engineering (IRC 433808–11). We wish to thank Nabil Tarfa, Luc Vernhes, Gil Perez, and Réjean René from Velan for the valuable discussions. We also wish to thank Pascal Coté, Jonathan Delarosbil, and Nicolas Lévesque from Velan for their help and assistance in the welding process, machining of specimens and Charpy impact tests.

CHAPTER 8 ARTICLE 3: MICROSTRUCTURAL AND MECHANICAL CHARACTERIZATION OF STELLITE HARDFACING WITH TWO TYPES OF BUFFER LAYERS

Yuxiao Wu[a], Thomas Schmitt[a], Etienne Bousser[a, b], Luc Vernhes[c], Fadila Khelfaoui[c], Gil Perez[c], Jolanta Ewa Klemberg-Sapieha[a] and Myriam Brochu[a]

[a]Polytechnique Montréal, 2900 Boulevard Edouard-Montpetit, Montreal, Quebec H3T 1J4, Canada

[b]The University of Manchester, School of Materials, Manchester M13 9PY, United Kingdom

[c]Velan Inc., 7007 Côte-de-Liesse, Montreal, Quebec H4T 1G2, Canada

Submitted to the Journal of Manufacturing Processes

Abstract: In recent years, a major challenge facing the power generation industry is delamination of Stellite-hardfaced coatings from high-temperature valves. In order to meet this challenge, IN82 buffer layer was evaluated to replace the problematic S21 buffer layer. S6 and either S21 or IN82 hardfacing alloys were deposited onto F91 steel substrates using plasma-transferred arc welding. Aging was conducted at temperatures between 550 and 650 °C for three exposure durations within a one-year period. A comparative study was carried out on the microstructure and mechanical properties of IN82 and S21 hardfacing specimens. The F91/S21 interface is unstable during aging because a hard and brittle interfacial layer grows, which significantly reduces the impact energy of S21 hardfacing specimens. In contrast, the F91/IN82 interface is microstructurally much more stable than the F91/S21 interface; an interfacial band, part of the F91 steel, and some discrete $M_{23}C_6$ carbides along this band grow during aging at 650 °C for 8760 h. The impact energy loss of the IN82 specimens is much less significant than that of the S21 specimens. Moreover, the toughness degradation is not related to the F91/IN82 interface, but rather to coarsening and precipitation of the intergranular/interdendritic carbides in the IN82 bulk material during aging. To conclude, the IN82 buffer layer is a good alternative to replace the problematic S21 buffer layer, enhancing the durability of the S6 coating components. However, the hardness of the S6 top layer is compromised due to dilution of Fe and Ni. To maintain its hardness, more S6 layers can be deposited and process optimization can be undertaken to reduce dilution in the applications where wear resistance is critical.

Keywords: Stellite; Hardfacing; Inconel 82; Impact; Aging; Delamination.

8.1 Introduction

Delamination of Stellite-hardfaced coatings from valve seats or disks during service has presented itself as a major challenge in the power generation industry. These premature failures usually occur after a few years of service in power plant stations. Consequently, valve functions deteriorate. Valves, playing a vital role in power plant stations, are usually used to manage the flow of high-temperature and high-pressure steam. According to a technical update report, the high-temperature valves generally work in the temperature range of 540 to 600 °C (1000–1112 °F) [3]. Operation of valves such as opening and closing can cause wear of valve materials. In order to ensure durable valve function, hardfacing alloys are deposited onto the sealing surfaces to reduce friction and improve wear resistance at elevated temperatures.

Hardfacing alloys are a class of materials applied on the surface of a component for the primary purpose of reducing wear. They are normally classified as iron-based, nickel-based and cobalt-based alloys. With respect to the hardfacing alloys used in power generation industry, Stellite 6 (S6), a cobalt-based alloy, has been used for decades. Stellite 21 (S21), is often used as a buffer layer (also referred to as a butter layer) between the steel substrate and S6 to bridge the thermal expansion mismatch, as described in the Electric Power Research Institute's report [3].

Though nickel-based hardfacing alloys are not as prevalent as cobalt-based alloys, they also find their applications in the power generation industry. Several common nickel-based hardfacing alloys are Deloro 50, Deloro 60, Inconel 625 (IN625), and Inconel 82 (IN82) to name a few. They are generally hardened by borides, carbides and Laves phase. Chakraborty et al. studied the effects of IN625 as a buffer layer on the microstructure and hardness of alloy Deloro 50 over the modified 9Cr-1Mo steel [42]. They found that application of this buffer layer facilitated crack-free deposition due to bridging the thermal gap during the hardfacing process. In addition, the ductile IN625 buffer layer was found to prevent the increase in the Fe dilution in the top layer.

As this is a major industry challenge in power plants, several research teams have studied its damage mechanisms. Some researchers reported a hard interfacial layer containing deleterious phases such as the $M_{23}C_6$ carbides and the σ phase during natural or artificial aging. Leinenbach et al. reported a hard layer, composed of a $M_{23}C_6$-type carbide, a BCC α phase, and a Cr-rich α' phase, was formed between the steel and the S6 alloy after aging at 600 and 625 °C [39]. Lolla et al. studied the interfacial microstructure of an ex-service S21 hardfacing component [4]. In addition

to the α phase and the $M_{23}C_6$ carbides, they observed a Cr-rich σ phase at the fusion line, exhibiting the highest hardness among the studied phases, 11.7 GPa [4]. It was proposed to be the main cause for hardness increase of the interfacial layer. The Electric Power Research Institute concluded an agreement over this proposal in their report [3].

Nevertheless, Wu et al. concluded that both the $M_{23}C_6$ carbides and the σ phase contributed to the local hardening of the interfacial layer [94]. They investigated the interfacial microstructure between F91 (forged) and S21, artificially aged between 550 and 650 °C for durations up to 8760 h. The $M_{23}C_6$ carbides exhibited the highest hardness, 19.8 GPa; the σ phase exhibited the second highest hardness, 16.0 GPa. This team further validated this interfacial layer provided a brittle crack propagation pathway by studying the fractured Charpy specimens [22]. They concluded that the microstructural cause of delamination of high-temperature valves in service was the formation of hard and brittle $M_{23}C_6$ carbides and σ phase.

Since the damage mechanism is clear, this challenge should be met and a solution for industrial valves should be provided to enhance the durability of Stellite hardfaced coatings. The Electric Power Research Institute used thermodynamic simulations to predict possible phases formed at high temperature for potential multi-layered multi-layered coatings in a report [41]. Based on their thermodynamic simulations, it is proposed that the nickel-based IN82 alloy would be a good alternative to replace the cobalt-based S21 buffer layer. Namely, no deleterious σ phase was predicted to precipitate during aging. However, this option should be validated experimentally. Therefore, an IN82 buffer layer combined with S6 top layer deposited onto an F91 steel substrate using plasma-transferred arc (PTA) welding was characterized. For comparison, the S21 buffer layer combined with S6 top layer was deposited onto an F91 steel substrate as well. After fabrication of these hardfacing specimens, they were aged between 550 and 650 °C for exposure durations ranging from 1008 to 8760 h (1 year). Then, the microstructure and mechanical properties of the two types of hardfacing specimens were studied.

8.2 Experimental details

8.2.1 Sample preparation

Two blocks of the F91 steel with dimensions 356 mm × 57 mm × 38 mm were used as the substrate material. IN82 or S21 powders were deposited on each block separately as buffer layers. Then, top

layers of S6 were applied on the buffer layers. The chemical compositions of F91, IN82, S21, and S6, as per the material suppliers, are listed in Table 8.1. The deposition process was carried out by PTA welding with the conditions given in Table 8.2. During deposition, pure argon (100%) was chosen as the shielding, plasma and powder gas. The thickness of each layer was approximately 2 mm. A hardfaced-coating sample is illustrated in Figure 8.1b.

Table 8.1: Chemical compositions of F91, IN82, S21, and S6 (wt%).

	Cr	Mo	Fe	Co	Ni	W	Nb	Mn	C	Si	others
F91	8.39	0.90	Bal.	0.015	0.18	0.00	0.07	0.48	0.11	0.30	<1.00
IN82	20.07	0.00	0.06	0.00	Bal.	0.00	2.57	2.59	<0.01	0.39	<0.037
S21	27.45	5.37	1.44	Bal.	2.76	0.00	0.00	0.60	0.26	1.69	<0.50
S6	27.34	0.17	0.33	Bal.	1.78	4.22	0.00	0.33	1.63	1.09	<0.50

Table 8.2: Welding conditions used for IN82, S21 and S6 deposition.

Parameter	Value
Particle size of S21 and S6 (mesh)	80/325
Particle size of IN82 (mesh)	100/325
Current (A)	170 – 200
Voltage (V)	21.5 – 25.0
Preheat (°C for 1 h)	204
Interpass temperature (°C)	316 max

To evaluate the hardfaced-coating interfaces mechanically, two assemblies were designed. The process of manufacturing specimens for mechanical testing of the interfaces was presented in our previous work [22]. As shown in Figure 8.1, the S21/IN82 hardfacing samples (Figure 8.1b) were extended by welding another two blocks of F91 steel (Figure 8.1a) using IN625 as the filler material. Subsequently, the two new produced assemblies (Figure 8.1c) were cooled in air to room temperature, followed by a post-weld heat treatment conducted at 760 °C for 2 h under ambient

atmosphere. Later, wire electrical discharge machining was used to cut the two assemblies into bars from which two halves were extracted (Figure 8.1d).

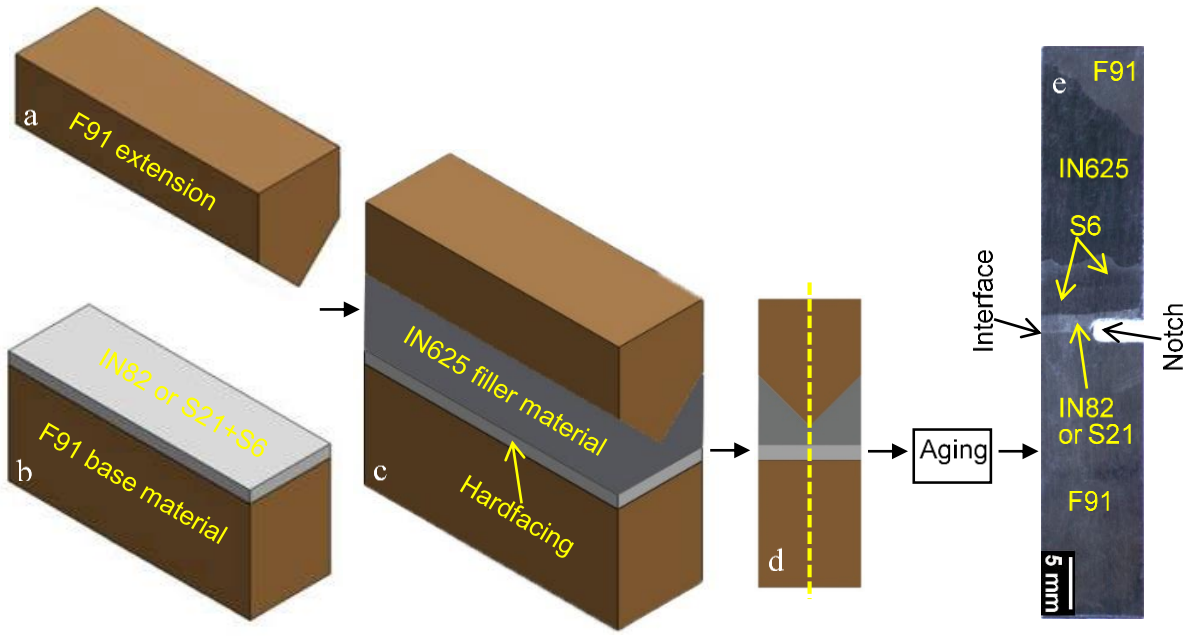

Figure 8.1: Charpy specimen manufacturing: (a) F91 extension, (b) hardfaced-coating sample with buffer layer of IN82 or S21 and top layer of S6, (c) assembly made by welding an F91 extension to the hardfaced-coating sample using IN625 as the filler material, (d) two halves cut from each bar, and (e) Charpy U-notch specimen machined from the half bars [22].

Some of these bars were aged under ambient atmosphere according to the temperatures and times given in Table 8.3. The three temperatures were selected either to simulate service temperatures (550 °C) or to accelerate the aging process (600 and 650 °C). The F91 steel is usually tempered at temperatures between 730 and 800 °C [43]. It is supposed that the selected aging temperatures did not significantly influence the microstructure and properties of F91 steel.

Table 8.3: Aging conditions.

Time (h)	1008	3600	8760
Temperature (°C)	550	550	550
	600	600	600
	650	650	650

Charpy U-notch specimens were machined from these aged bars and the as-tempered bars. In order to increase the probability of positioning the interface in the highly stressed area, U-notch was selected over V-notch, where the F91/IN82 and F91/S21 interfaces were centered (Figure 8.1e). The dimensions of Charpy U-notch specimens were 55 mm × 10 mm × 10 mm with a 5 mm deep notch having a 1 mm tip radius, according to ASTM E23 standard [44].

8.2.2 Mechanical characterization

An Instron pendulum impact testing machine (model SI-1C3) equipped with an 8 mm radius striker was used to perform Charpy impact tests at room temperature, following the ASTM E23 procedure [44]. This Charpy impact testing machine was calibrated through the Charpy machine verification program administered by the National Institute of Standards and Technology, in accordance with the ASTM E23 standard [44]. The energy absorbed by the specimen was calculated and recorded using Fracta software connected to the Charpy machine. Two to four measurements for each aging condition were used to obtain the averaged impact energy. For the small data set, the uncertainty thereof were obtained from the formula:

$$\Delta E_{\text{avg}} = \frac{E_{\max} - E_{\min}}{2\sqrt{N}} \qquad \text{Equation 8.1}$$

where ΔE_{avg} is the uncertainty in the mean value of the impact energy, $E_{\max}$ and $E_{\min}$ are the maximum and minimum impact energy respectively, and N is the number of measurements.

Micro-indentation measurements were performed on the entire cross-sections of the specimens (from F91 to S6) using an Anton-Paar Micro-Combi Tester equipped with a diamond pyramidal tip with a Vickers geometry. The tip area function was calibrated using a fused silica standard. The micro-hardness tests were carried out on the specimens aged at the most demanding temperature of 650 °C for 0 (as-tempered), 1008, 3600, and 8760 h. The indentations were spaced by an interval ranging from 250 to 650 μm depending on the materials to avoid interference from adjacent indentations. For each indentation, the applied load increased linearly over 30 s to reach a maximum of 5 N, kept constant for 15 s, and then decreased linearly over 30 s. The Oliver and Pharr method [46] was used to calculate the microhardness from each indentation.

To measure the hardness of phases at the F91/IN82 and F91/S21 interfaces, a Bruker Triboindenter 950 equipped with a Berkovich diamond tip was used to perform nano-indentation on the cross-sections of the hardfacing specimens. Prior to testing, the tip area function was calibrated

using a fused quartz standard. Matrices of 16 × 16 indentations evenly spaced by 2 μm were undertaken in accordance with a load function composed of a linearly increased loading section over 5 s, a constant section at a maximum of 2 mN for 2 s, and a linearly decreased loading section over 5 s. The hardness of each indentation from individual load-displacement curves was obtained using the Oliver and Pharr method [46]. Before the micro- and nano-indentation testing, the cross-sections of the specimens were mechanically ground using silicon carbide papers up to 1200 grade, and then followed by mechanical polishing using 6, 3 and 1 μm diamond suspensions.

8.2.3 Microstructural analysis

The microstructures and chemical compositions of the specimens were characterized from the cross-sections using a JSM-7600F field emission scanning electron microscopy (SEM) equipped with energy dispersive X-ray spectroscopy (EDS) operating at 15kV in high-current mode. The EDS analysis was performed using AZtec software with the built-in extended-quant standardizations (15 kV set). The EDS maps were collected with total size of 23.3 μm × 16.2 μm. The EDS line scans were all performed at 8 nA. Stereomicroscopy and SEM were both used to examine the fractured Charpy specimens.

Electron backscatter diffraction (EBSD) phase mapping was further applied to characterize the F91/IN82 interfacial microstructure using a Zeiss Sigma field emission SEM equipped with an Oxford Instruments Nordlys Max2 detector operating at 20kV in high-current mode. The maps were collected using step sizes of 0.05 μm with total size of 21 μm × 21 μm. AZtec software was used to collect and index Kikuchi patterns, taken at 4 × 4 binning at about 40 Hz. The HKL Channel 5 system was used to post-process the maps to identify the phases in the interfaces.

For SEM, EDS and EBSD characterization, in addition to the previously mentioned steps of grinding and polishing up to 1 μm surface finish, the cross-sections of the specimens were further polished with a mixed colloidal silica suspension to remove the final layer of surface deformation. After polishing, the cross-sections were ultrasonically cleaned in acetone and isopropanol. Some specimens were etched using Kalling's No. 2 reagent either for stereomicroscopy or for SEM observation in the secondary-electron mode.

8.3 Results

8.3.1 Charpy impact energy evolution

Figure 8.2 shows the Charpy impact energy measurements of the IN82 and S21 hardfacing specimens for all the aging conditions studied. The solid-line symbols represent the Charpy impact energy evolution of the IN82 hardfacing specimens and the dashed line symbols represent that of the S21 hardfacing specimens. Compared with the specimens in the as-tempered condition (aging time 0 h), the impact energy of the S21 hardfacing specimens decreased significantly after aging. At least 92% of the impact energy was lost for all the aging conditions. Compared with the as-tempered S21 hardfacing specimens, the impact energy of the as-tempered IN82 hardfacing specimens was initially lower. Nevertheless, the impact energy of the aged IN82 hardfacing specimens showed a smaller decrease with time, achieving a maximum energy loss of 38% when aged at 650 °C for 8760 h. The impact energy also decreased with temperature for a given aging time. However, after aging, they were all higher than those of specimens manufactured using S21 buffer layer.

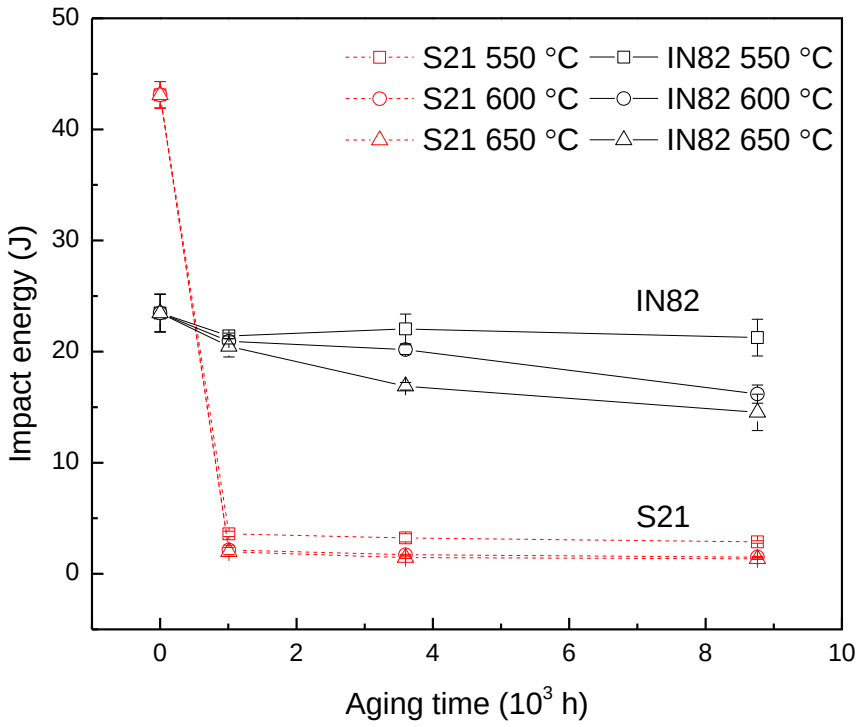

Figure 8.2: Charpy impact energy evolution of the IN82 and S21 hardfacing specimens.

8.3.2 Fracture analysis of the IN82 and S21 specimens

Following the impact energy evolution analysis, the fractured Charpy specimens were first examined by stereomicroscopy. The fracture occurred along the F91/S21 interface for all the aged S21 Charpy specimens. One example of an S21 specimen aged at 650 °C for 8760 h is shown in Figure 8.3a, c and e. In contrast, the fracture occurred in the IN82 bulk material for all the IN82 Charpy specimens, including those inspected in the as-tempered condition. One example of an IN82 specimen aged at 650 °C for 8760 h is shown in Figure 8.3b, d and f. From the macro-fractographic surfaces shown in Figure 8.3e and f, lateral expansion took place for the IN82 hardfacing Charpy specimens, which were characterized by impact energies above 14 J. On the other hand, no significant lateral expansion and smooth fracture surfaces were observed for the aged S21 Charpy specimens, which were characterized by impact energies below 4 J. This indicated that the fracture of the aged S21 hardfacing Charpy specimens was brittle compared with the IN82 specimens.

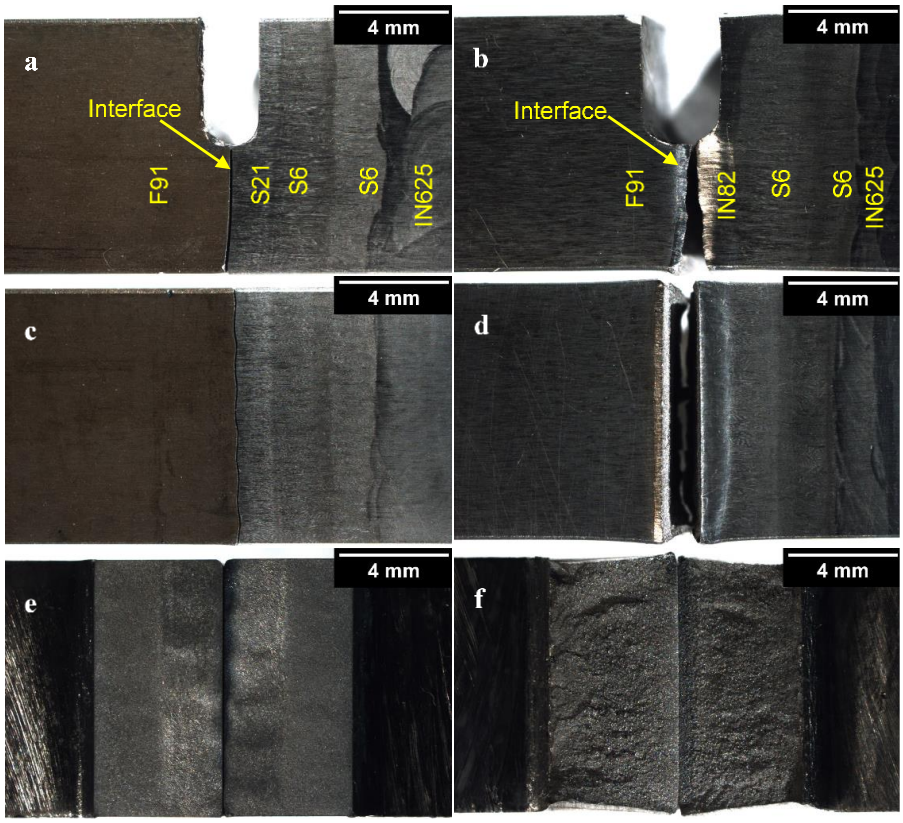

Figure 8.3: Fractured Charpy specimens after aging at 650 °C for 8760 h: representative cross-sections (a) S21 and (b) IN82; representative back-faces (c) S21 and (d) IN82; representative macro-fracture surfaces (e) S21 and (f) IN82.

SEM was used for further fractographical analysis. Figure 8.4 shows the fractographs of an S21 specimen aged at 650 °C for 8760 h. The fracture surfaces in Figure 8.4a, b and c revealed cleavage and quasi-cleavage features. Therefore, it is validated that the fracture of the S21 hardfacing Charpy specimens aged at 650 °C for 8760 h was brittle. The EDS map of Figure 8.4d exhibited a mixture of green $M_{23}C_6$ and purple Fe_xCo_y, which proved that the fracture was mainly along the interfacial layer between F91 and S21 [94].

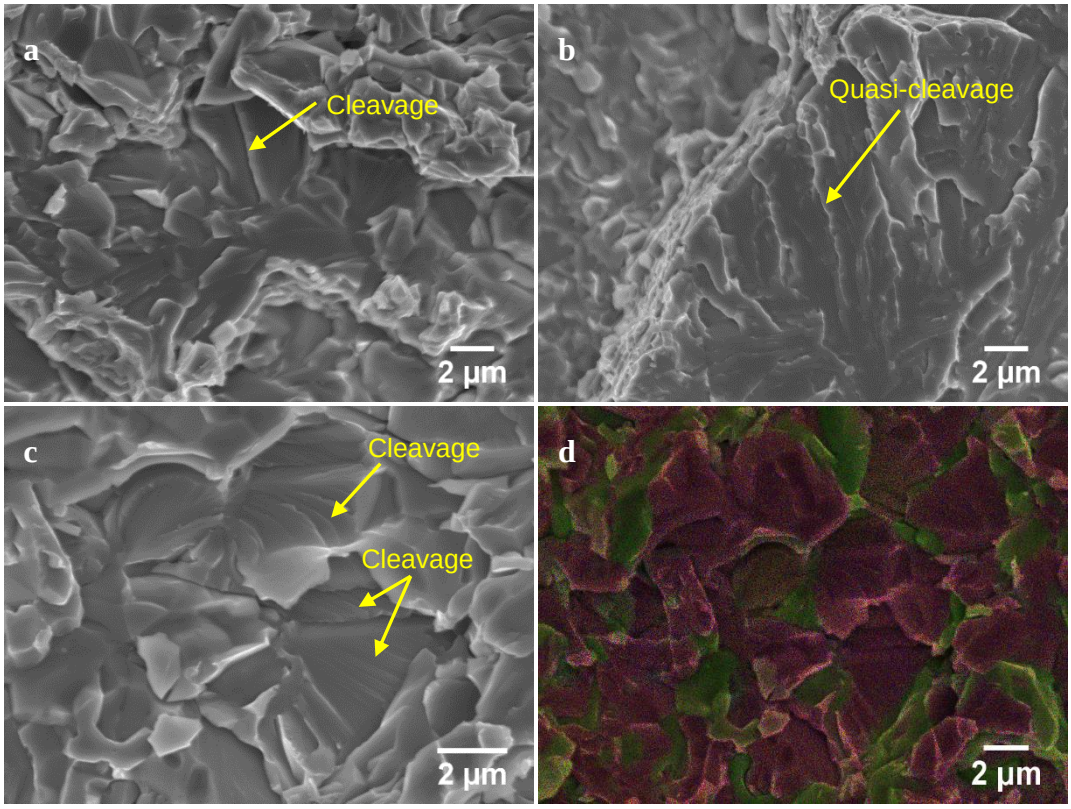

Figure 8.4: SEM fractographs of an S21 specimen aged at 650 °C for 8760 h: (a), (b) and (c) showing cleavage and quasi-cleavage; (d) EDS map obtained from the fracture surface ($M_{23}C_6$ in green and Fe_xCo_y in purple).

Since fracture occurred through IN82 bulk material for all the IN82 Charpy specimens, the impact energy loss recorded after aging was not related to the F91/IN82 interface. The IN82 dendritic microstructure formed during solidification is shown in Figure 8.5a. SEM fractographs of an IN82 hardfacing specimen aged at 650 °C for 8760 h are shown in Figure 8.5b, c and d. The rough fracture surface in Figure 8.5b exhibited intergranular/interdendritic cracks. As represented in Figure 8.5c and d, many microvoids surrounded by dimples were distributed along grain/dendrite boundaries. Hence, the fracture of the IN82 Charpy specimen aged at 650 °C for 8760 h was caused

by microvoid formation and coalescence in the interdendritic region.

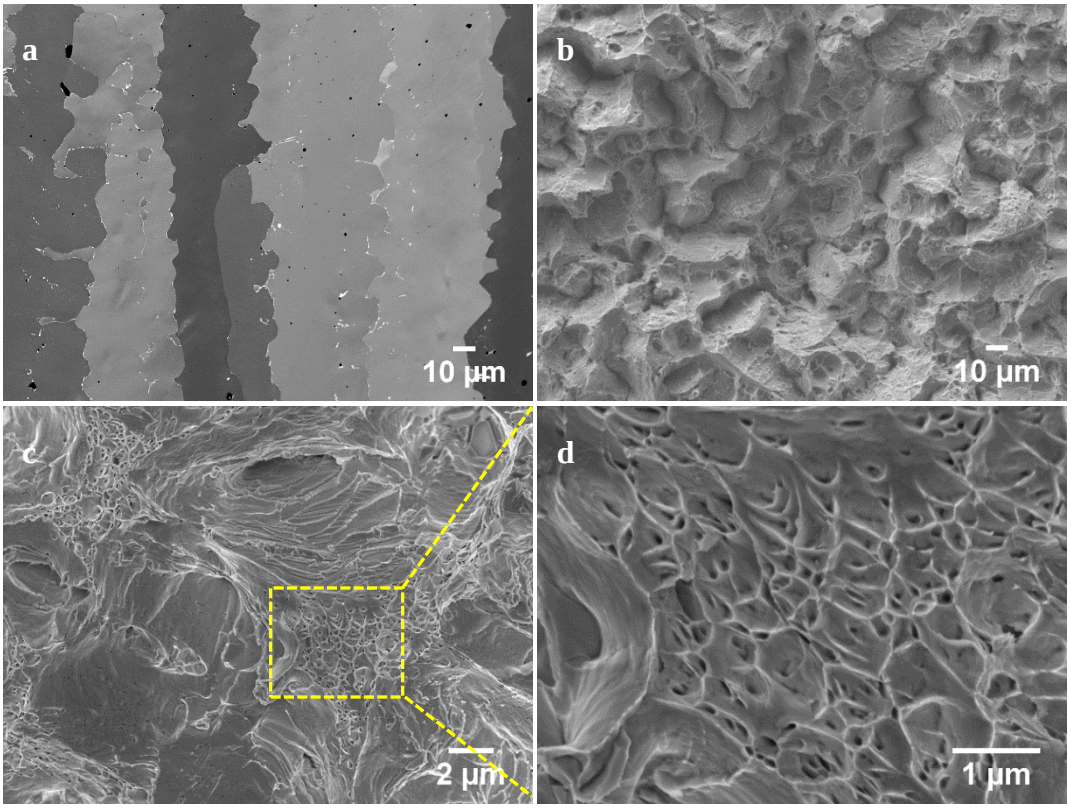

Figure 8.5: SEM micrographs of an IN82 specimen aged at 650 °C for 8760 h: (a) dendritic microstructure; (b) the intergranular/interdendritic cracks, (c) higher magnification view, and (d) the zone outlined by the rectangle showing the microvoids surrounded by dimples.

8.3.3 F91/IN82 and F91/S21 interfacial microstructure

In order to explain the difference in the impact energy evolution between the IN82 and S21 hardfacing specimens and the fractographical characteristics, an examination of the microstructure was performed. The F91/IN82 and F91/S21 interfacial microstructures were first investigated using SEM, as shown in Figure 8.6. Compared with the as-tempered F91/S21 interfacial microstructure, an interfacial layer was observed between the F91 and the S21 after aging at 650 °C for 8760 h. As reported in our previous study, this layer was composed of three main phases: a BCC-like Fe_xCo_y phase, a Cr-rich $M_{23}C_6$-type carbide and a Cr-rich σ phase, in decreasing order of proportion [94]. In contrast, no new phase was observed at the F91/IN82 interface after aging at 650 °C for 8760 h. Nevertheless, a band was growing along the interface, the width of which was of the order of 1-2 µm. This band was more clearly revealed in the upper-right inset image of Figure 8.6d due

to the effect of etching. It seemed that this band was part of the F91 steel. To validate this hypothesis, further analyses were performed.

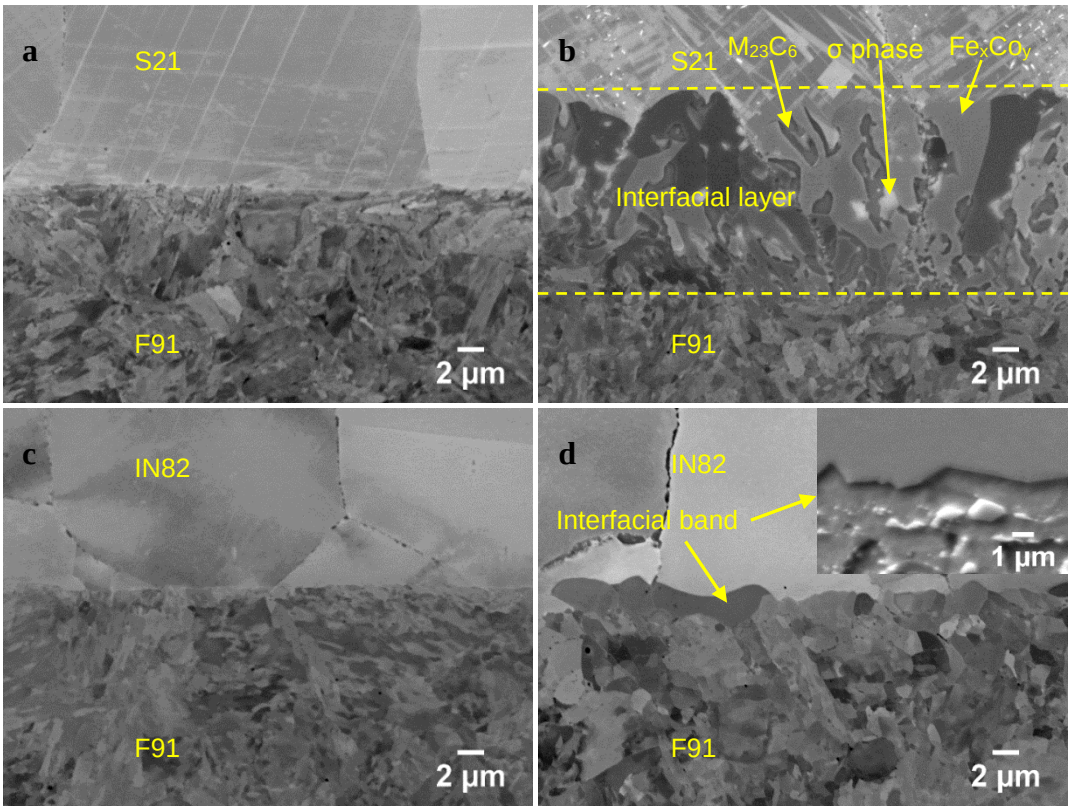

Figure 8.6: SEM images showing the interfacial microstructure: S21 (a) as-tempered and (b) aged at 650 °C 8760 h, IN82 (c) as-tempered and (d) aged at 650 °C 8760 h (the inset image in secondary-electron mode, others in backscattered-electron (BSE) mode).

EDS chemical elemental mapping was carried out on the F91/IN82 interface of a specimen aged at 650 °C for 8760 h. As shown in Figure 8.7, the chemical composition of this interfacial band was similar to that of the F91 steel from the EDS composite map and individual elemental maps. Some light green precipitates (A) in Figure 8.7a were observed just underneath the interfacial band. The precipitates A underneath the interfacial band and the precipitates along the grain boundary had comparable chemistries. They were rich in chromium, molybdenum and carbon, but depleted in iron and nickel. To appreciate better the chemistry of precipitate A, a spectrum was reconstructed from selecting an area inside A and the relative proportions of four elements obtained from this measurement were shown at the upper-right corner of Figure 8.7a. Based on the chemical compositions, the light green precipitates were expected to be a Cr-rich $M_{23}C_6$-type carbide, where the letter M represents metallic elements such as Cr, Fe, and Mo. The equivalent diameter of A was

of the order of 0.2-0.8 µm. It seems that the precipitates A were larger than the $M_{23}C_6$ precipitates from the F91 base material.

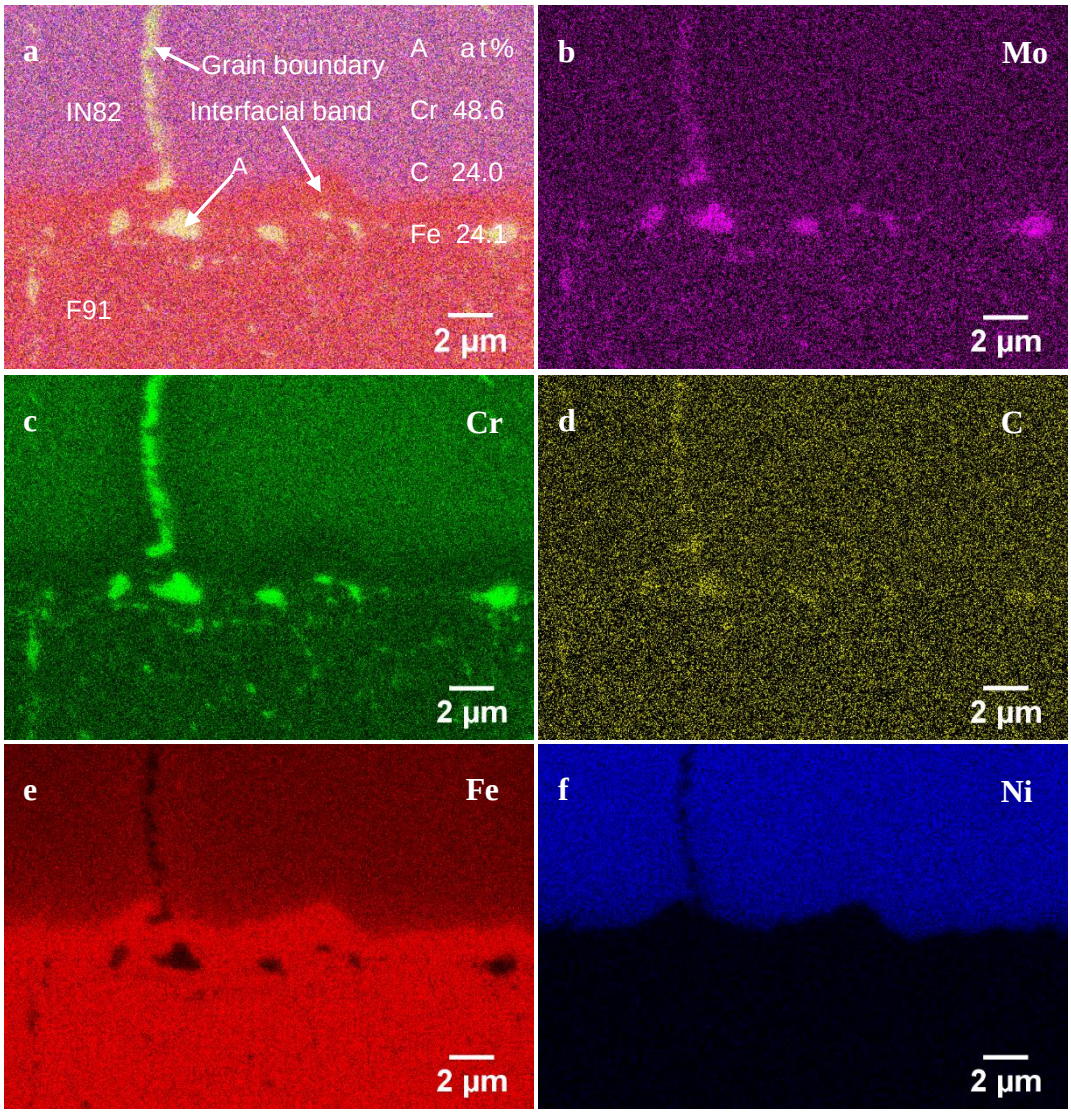

Figure 8.7: EDS elemental mapping on the F91/IN82 interface of a specimen aged at 650 °C for 8760 h: (a) EDS composite map; (b) Mo, (c) Cr, (d) C, (e) Fe, and (f) Ni elemental maps.

EBSD was further used to characterize the F91/IN82 interface of a specimen aged at 650 °C for 8760 h. In Figure 8.8, IN82 and F91 are located at the image top and bottom, respectively. This interfacial band was clearly revealed in the band contrast map, Figure 8.8a. From the corresponding EBSD phase map, Figure 8.8b, it is shown that the interfacial band (in blue) had the same crystalline structure as the F91 (in blue), namely body-centered cubic structure. Also, from the EDS composite map, Figure 8.8c, this interfacial band and the F91 steel had comparable chemistries (in

red). Therefore, this band was considered to be part of the F91 steel because of its comparable crystal structure and chemistry. Some $M_{23}C_6$ carbides precipitated along this band, as appreciated in Figure 8.8b and c. NbC carbides (color light blue in the EBSD phase map) were found close to the $M_{23}C_6$ carbides. The indexing of the $M_{23}C_6$ carbides in Figure 8.8b did not match the EDS map very well. That is, many regions of small green carbides dispersed in the F91 steel in Figure 8.8b. These errors in indexing most probably were due to grain distortion caused by the large strains during welding, or due to lattice distortion caused by solid solutions, defects, and so on.

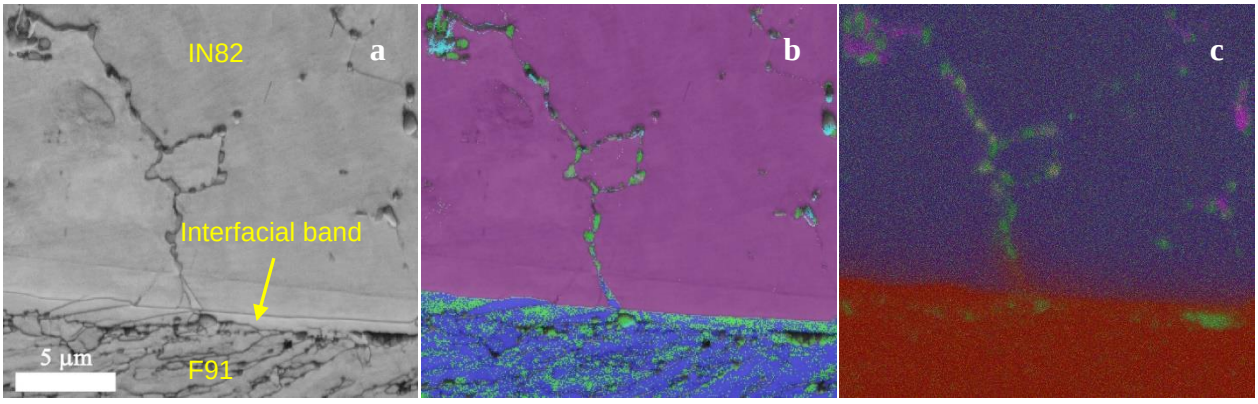

Figure 8.8: The F91/IN82 interface of a specimen aged at 650 °C for 8760 h (a) band contrast map, (b) the corresponding EBSD phase map (γ-Ni in purple, α-Fe in blue, $M_{23}C_6$ in green, and NbC in light blue), and (c) the corresponding EDS composite map.

After showing the microscopic morphology, EDS line scans were performed on the cross-sections of the IN82 and S21 specimens aged at 650 °C for 0 and 8760 h. One example (an as-tempered IN82 specimen) is presented in Figure 8.9. As observed in Table 8.1, there was only 0.06% Fe in IN82 before the hardfacing process. However, much higher content of Fe (above 20%) was measured in the IN82 after the hardfacing process. The change in the chemical composition of IN82 was caused by the admixture of the F91, since part of the steel was inevitably melted and diluted during hardfacing. Similarly, significant Ni also diluted from the IN82 to the S6 when using IN82 buffer layer. Based on the chemical composition profiles obtained from the as-tempered and aged IN82 and S21 specimens, a graph showing Fe concentration distribution is plotted in Figure 8.10. These Fe concentrations were averaged over a constant zone of the line scans, avoiding zones close to the interface. There was no considerable change in the Fe concentration after aging. However, more Fe was measured to dilute in the IN82 (around 25.8%) than in the S21 (19.1%). Correspondingly, the first layer of S6 in the IN82 specimen contained more Fe (10.2%) than that

in the S21 specimen (7.0%). The same was true of the second layer of S6 (3.8% versus 2.7%).

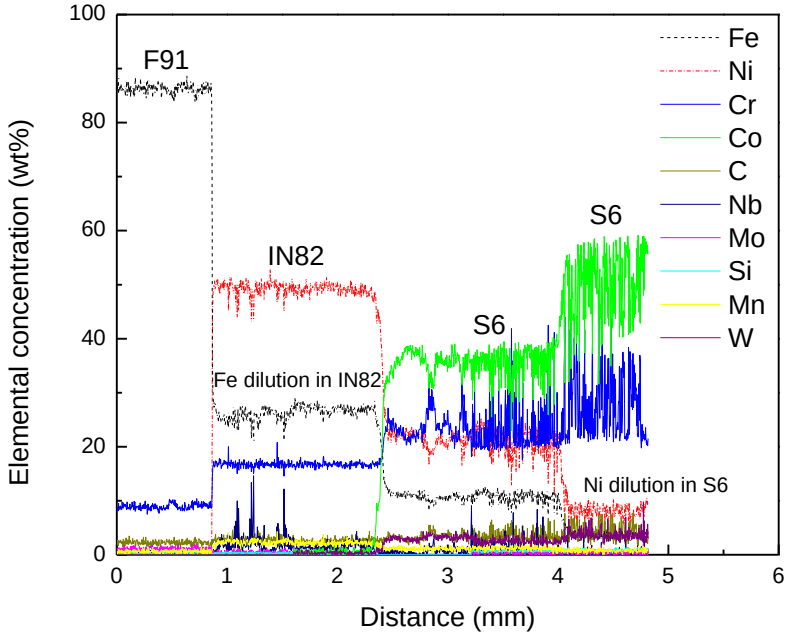

Figure 8.9: Elemental concentration profiles of the as-tempered IN82 hardfacing specimen.

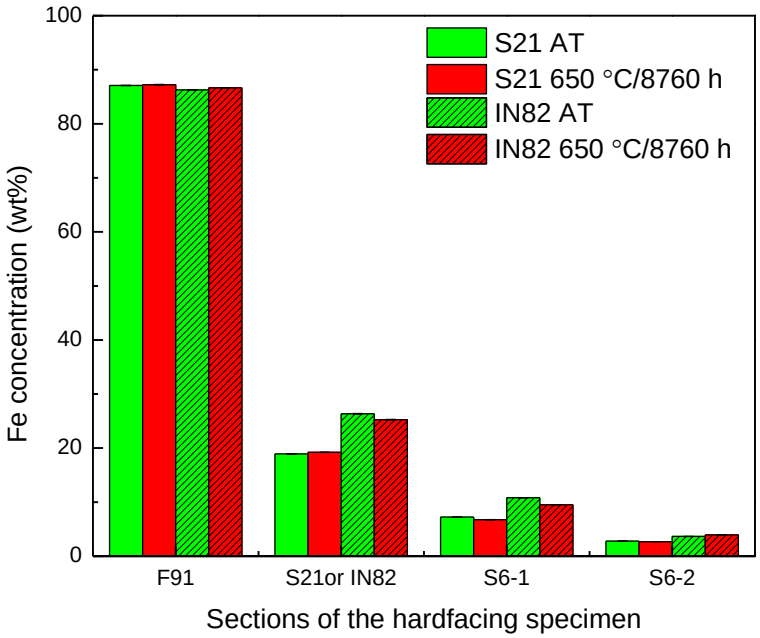

Figure 8.10: Fe concentrations measured in F91, buffer layer S21 or IN82, the first layer of S6 (S6-1), and the second layer of S6 (S6-2) in the as-tempered (AT) condition and after aging at 650 °C for 8760 h.

8.3.4 Microhardness and nanohardness testing

To show how dilution affected mechanical properties, micro-indentation measurements were carried out on the cross-sections of the IN82 and S21 hardfacing specimens aged at 650 °C for durations ranging from 0 to 8760 h. The results are presented in Figure 8.11. The open symbols represent the S21 specimens; the solid symbols represent the IN82 specimens. The hardness gradients were readily observed from the F91 to the second layer of S6. It is shown that the S21 and S6 were hardened after aging at 650 °C for 8760 h for the S21 specimens. However, there was no considerable change in hardness caused by aging for the IN82 specimens. When comparing the two types of specimens, the S21 buffer layer was harder than the IN82 buffer layer. The most notable difference was that the S6 deposited on the S21 buffer layer exhibited higher hardness than that deposited on the IN82 buffer, especially for the first layer of S6. The second layer of S6 was always harder than the first layer of S6 for the two types of specimens.

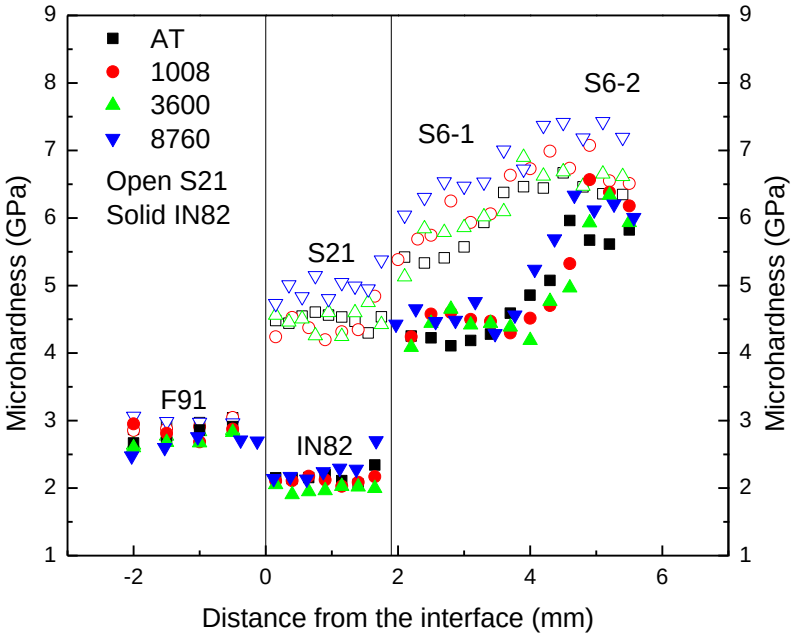

Figure 8.11: Microhardness profiles of the S21 and IN82 specimens aged at 650 °C for 0, 1008, 3600, and 8760 h.

To characterize the hardness of the interfacial microstructure, nano-indentation tests were performed on the IN82 and S21 specimens aged at 650 °C for 8760 h. BSE images and EDS maps

obtained from the indentation zones are shown in Figure 8.12. As shown in Figure 8.12a, b and c, the interfacial layer in the S21 sample after aging at 650 °C for 8760 h exhibited higher hardness than the F91 and S21. Two indents on the green $M_{23}C_6$ carbides outlined by circles in Figure 8.12c exhibited the highest hardness, in the range of 19 GPa. As presented previously, there were some $M_{23}C_6$ carbides underneath the interfacial band in the IN82 sample after aging. As shown in Figure 8.12d, e and f, two indents partially on the green $M_{23}C_6$ carbides outlined by triangles in Figure 8.12f exhibited the highest hardness, in the range of 8 GPa. Except the indents on or near the green $M_{23}C_6$ carbides, the hardness of other indents on the interfacial band was in the same range as that on the F91 base material. It was neither hardened nor softened. In addition, the F91 exhibited higher hardness than the IN82.

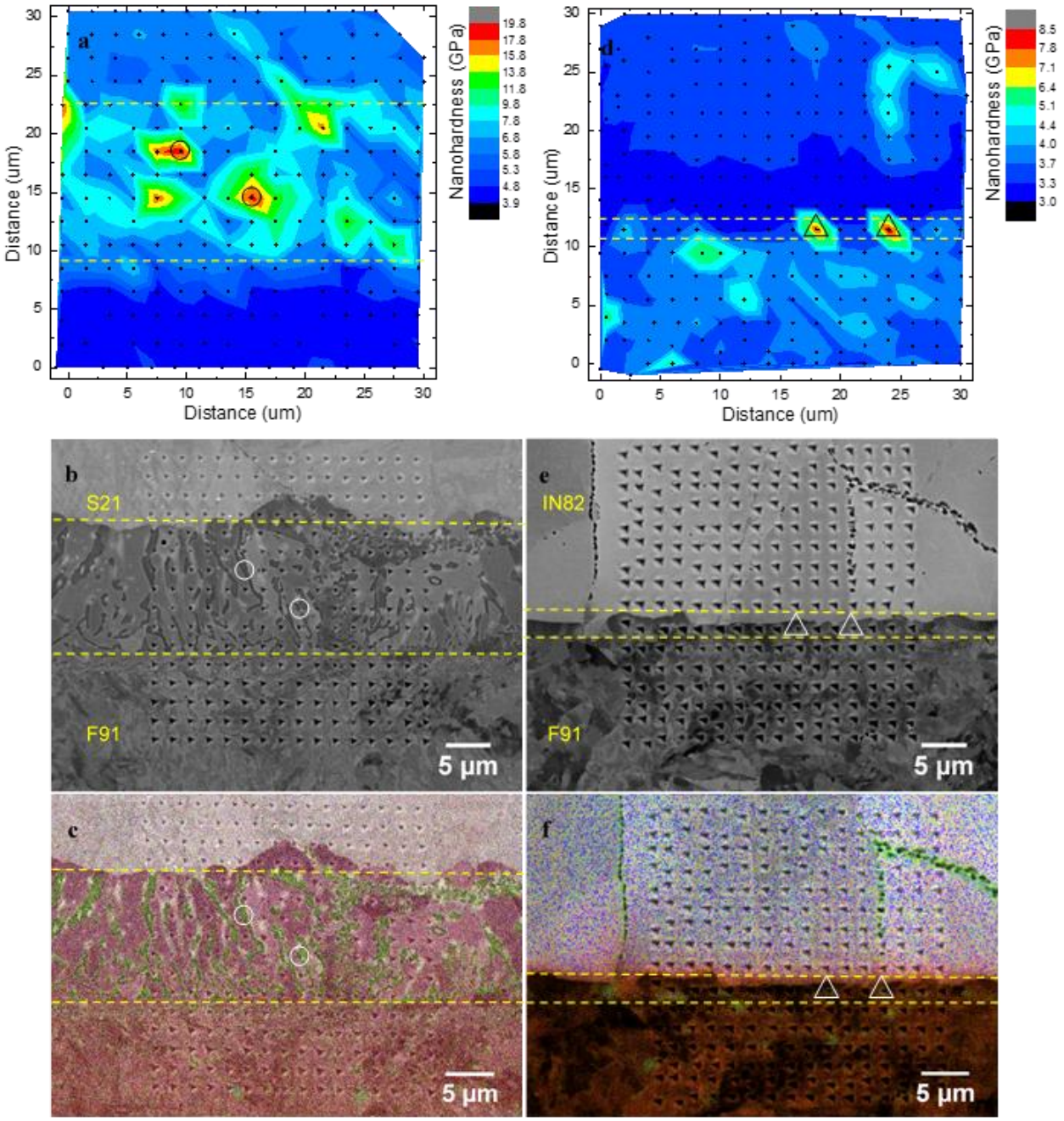

Figure 8.12: An S21 specimen aged at 650 °C for 8760 h (a) hardness map, (b) the corresponding BSE image and (c) the corresponding EDS composite map ($M_{23}C_6$ carbides in green); an IN82 specimen aged at 650 °C for 8760 h (d) hardness map, (e) the corresponding BSE image and (f) the corresponding EDS composite map ($M_{23}C_6$ carbides in green).

8.4 Discussion

In the present work, we studied the interfacial microstructure and mechanical properties of IN82 and S21 hardfacing specimens. For the S21 Charpy specimens, the impact energy decreased significantly (by at least 92%) when aged between 550 and 650 °C over durations ranging from 1008 to 8760 h. The fractographic analysis confirmed the brittle fracture of the aged S21 Charpy specimens. An interfacial layer provided a brittle crack propagation pathway under the high-strain rate impact due to the hard phases precipitated during aging, which are validated by nano-indentation.

For the IN82 Charpy specimens, the impact energy loss (at most 38%) was significantly less pronounced than that of the S21 specimens in the same aging conditions. The fracture occurred not along the F91/IN82 interface, but through the IN82 bulk material. Microvoid formation and coalescence in the interdendritic region was responsible for the fracture. As may be appreciated from Figure 8.6c and d, coarsening and precipitation of the $M_{23}C_6$ carbides along grain boundaries in IN82 bulk material occurred after aging at 650 °C for 8760 h, compared with the as-tempered IN82 specimen. As shown in the EBSD phase map, Figure 8.8b, NbC carbides were also identified along or close to grain boundaries. These intergranular/interdendritic carbides in the IN82 bulk material well explained the observed dimples and microvoids. They were associated with the aging-induced toughness degradation in IN82 specimens. Jiang et al. also reported that the secondary particles in the interdendritic region of Inconel 82/182 welds would have been the microvoid initiation sites [101]. Therefore, it is proposed that the impact energy loss of the IN82 specimens after aging was related to the coarsening and precipitation of the carbides such as $M_{23}C_6$ along grain/dendrite boundaries.

Though no new phase was observed along the F91/IN82 interface when aged at 650 °C for 8760 h, an interfacial band was found to grow from the F91 material. This band was actually part of the F91 steel based on the EDS and EBSD results. Nano-indentation confirmed that it was neither hardened nor softened. Some discrete $M_{23}C_6$ carbides of approximately 0.2-0.8 μm in equivalent diameter precipitated along this interfacial band.

The formation of the interfacial band at the weld fusion line between austenitic and ferritic materials has been reported by other authors. Nicholson observed a band of martensite between grade 22 steel (2.25Cr-1Mo, the zeroth generation of creep-resistant steels used in the power

generation industry) and nickel-based alloy Inconel 182 (an alloy very similar to IN82 in chemical composition) in the as-welded condition using manual metal arc welding [102]. The band was microstructurally different from the grade 22 steel. During the subsequent aging at 630 °C, two types of carbides ($M_{23}C_6$ and M_6C) precipitated on the edge of the martensite band in a single line parallel to the weld line. However, Laha et al. only observed a $M_{23}C_6$-type carbide in a weld system between 9Cr-1Mo steel and Inconel 182 alloy using shielded-metal arc welding [103]. The size of the $M_{23}C_6$ carbides was finer than the equivalent carbides in the 2.25Cr-1Mo steel joint after the same aging condition.

In our present study, an interfacial band along with some $M_{23}C_6$ carbides was also observed after aging at 650 °C for 8760 h. However, this band was not a martensitic band, but just part of the F91 (ferrite/tempered-martensite). Martensite is known for its high hardness. It is expected that this interfacial band would degenerate the hardfacing component if it is a martensitic band. Compared with the above reported literature, only one type of carbide ($M_{23}C_6$) was observed and these $M_{23}C_6$ carbides did not contribute to the failures during Charpy tests. This band along with the $M_{23}C_6$ carbides resulted from the chemical potential gradients between the austenitic (IN82) and ferritic (F91) materials during aging. We should mention that the term of band was used in the literature. It is quite different from the interfacial layer between F91 and S21 formed during aging.

The F91 interfacial band along with the precipitated carbides was observed after aging at 650 °C for 8760 h. Grade 91 steel is usually used within the temperature range of 538–593 °C (1000–1100 °F) in power plants [28]. In the present study, aging at 650 °C was selected to predict the long-term effects of service at lower temperatures. The Hollomon-Jaffe parameter, HP, can be used to determine the equivalent time and temperature for thermally activated processes performed under different time and temperature regimes. This parameter is given by the following equation:

$$HP = \frac{T(C+\log t)}{1000} \qquad \text{Equation 8.2}$$

where T is the temperature measured in kelvin, C is a constant related to the material used, and t is the time in h for an isothermal condition. For grade 91 steel, C was determined to be 22.3 [104]. According to this equation, aging at 650 °C for 8760 h is estimated to be equivalent to aging at 600 °C for 32 years and aging at 550 °C (within the service temperature range) for 1542 years. Therefore, the F91/IN82 interface is predicted not to embrittle even after aging at 550 °C for 1542 years. It should be noted that other factors in service such as operation-induced stresses are not

taken into account for experimentation. However, we do believe that the IN82 buffer layer in replacement of the problematic S21 would enhance the durability of the S6 coating components.

The microstructure and mechanical properties of the IN82 hardfacing specimens were more stable than those of the S21 specimens for the tested aging conditions. Nevertheless, the S6 deposited onto the S21 buffer layer exhibited higher hardness than that deposited over the IN82 buffer layer. The hardness of S6 correlates with dilution of elements. Mirshekari et al. deposited two layers of S6 on the AISI 420 martensitic stainless steel turbine blade using gas tungsten arc welding [105]. They also observed that a decrease in Fe dilution led to an increase in the hardness of the second layer of S6. The microstructure of S6 is composed of Co-based dendrites surrounded by eutectic carbides such as M_7C_3 and $M_{23}C_6$ (mainly Cr carbides). Mo [106] and W [96] elements are reported to form M_6C carbides. The hardness of S6 essentially depends on these carbides. During dissimilar metal welding, part of the base material is inevitably melted and subsequently inter-diffusion of elements can take place due to the chemical potential gradients. That is, the contents of Fe and Ni in S6 would increase, while the contents of Cr, W and C would decrease in our study, leading to a decrease in hardness due to lesser amount of carbides formed in the S6.

From our Fe dilution analysis, the first layer of S6 deposited on the IN82 buffer layer contained more Fe (10.2%) than that deposited on the S21 (7.0%). So did the second layer of S6 (3.8% versus 2.7%). Ni also diffused into the S6 from the IN82 buffer layer. This is a solid explanation for why the S6 deposited on the S21 buffer layer exhibited higher hardness than that deposited on the IN82. In addition, the difference in hardness between the first layers of S6 deposited on the S21 and the IN82 was observed larger than that between the second S6 layers. It is because the difference in concentration of Fe between the first layers of S6 (3.2%) was larger than that between the second S6 layers (1.1%). The second layers of S6 with less dilution of Fe and Ni were always harder than the first layers of S6. It can thus be proposed that Fe and Ni dilution could deteriorate the wear resistance of S6 when using the IN82 buffer layer in replacement of S21.

To maintain the hardness of S6, more layers of S6 can be deposited on the IN82 buffer layer. Moreover, the welding conditions used during the deposition process can be optimized to reduce the dilution. For example, after studying the effects of the processing parameters on the microstructure and mechanical properties of a Stellite F coating onto X45CrSi93 steel, Bharath et al. obtained the conclusion that current levels played a key role in dilution levels and further in

hardness values [14]. As demonstrated by D'Oliveira et al., compared with the constant direct current, the pulsed current was found to result in finer and more homogeneous coating microstructure, lower dilution, and thus higher coating hardness [15]. In addition to the current, heat input may also affect the dilution of deposited coatings. In short, process optimization could be considered to reduce the dilution levels, and thus to maintain the S6 hardness.

8.5 Conclusions

In the present work, we performed a comparative study on the microstructure evolution and mechanical properties of S6 coating components using the IN82 alloy as an alternative to the problematic S21 buffer layer. The F91/S21 interface was found to be unstable during aging. A hard and brittle interfacial layer grows, which significantly reduces the impact energy of the S21 specimens. The microstructure of the F91/IN82 interface was found to be much more stable than the F91/S21 interface after aging at 650 °C for 8760 h. The impact energy loss of the IN82 Charpy specimens is not related to the F91/IN82 interface, but rather to the aging of the IN82 bulk material. That is, coarsening and precipitation of the intergranular/interdendritic carbides contributes to the toughness degradation.

To meet the challenge of delamination of industrial valves, the IN82 buffer layer is recommended to replace the problematic S21 buffer layer, which can enhance the durability of S6 coating components. Nevertheless, compared with the S6 deposited over the S21 buffer layer, the hardness of S6 top layer deposited on the IN82 buffer layer is compromised due to the dilution of Fe and Ni. This downside could be mitigated by increasing the number of S6 layers and optimizing the processing conditions in the applications where wear resistance is critical.

8.6 Acknowledgments

The authors acknowledge the financial support of the Natural Sciences and Engineering Research Council of Canada (NSERC) and of Velan Inc. through the NSERC Multisectorial Industrial Research Chair in Coatings and Surface Engineering (IRC 433808–11). They would like to thank Nabile Tarfa, Réjean René, and Vahe Najarian from Velan for the valuable discussion. They would also like to thank Pascal Coté, Jonathan Delarosbil, and Nicolas Lévesque from Velan for their help and assistance in the welding process, machining of specimens and Charpy impact tests.

CHAPTER 9 EVALUATION OF THE IN625 HARDFACING COMPONENTS

As stated in chapter 8, the IN82 buffer layer is recommended to the replace problematic S21 to meet the challenge of high-temperature valve delamination. In this chapter, another nickel-based alloy IN625 is investigated as a buffer layer between the creep-resistant steel and S6 hardfacing. Though the analyses are not as thorough and elaborate as the previous three chapters, pertinent information can be extracted. In addition to the microstructural evolution, indentation testing, Charpy impact testing, and tensile testing coupled with DIC were used to study the IN625 hardfacing components.

9.1 Microstructural evolution

The F91/IN625 and F91/IN82 interfaces after aging at 650 °C for 8760 h are shown in Figure 9.1 Compared with the F91/IN82 interfacial microstructure, some white precipitates were observed close to the F91/IN625 interface in Figure 9.1a (yellow arrow). Many rod-like white precipitates were found in the IN625 bulk material. They precipitated within the grains. There were also white and grey precipitates along grain boundaries. No such white precipitates were observed in the IN82 specimen, but an interfacial band along the F91/IN82 interface was identified as part of F91 steel in chapter 8. For the IN625 specimen, a similar band was also observed.

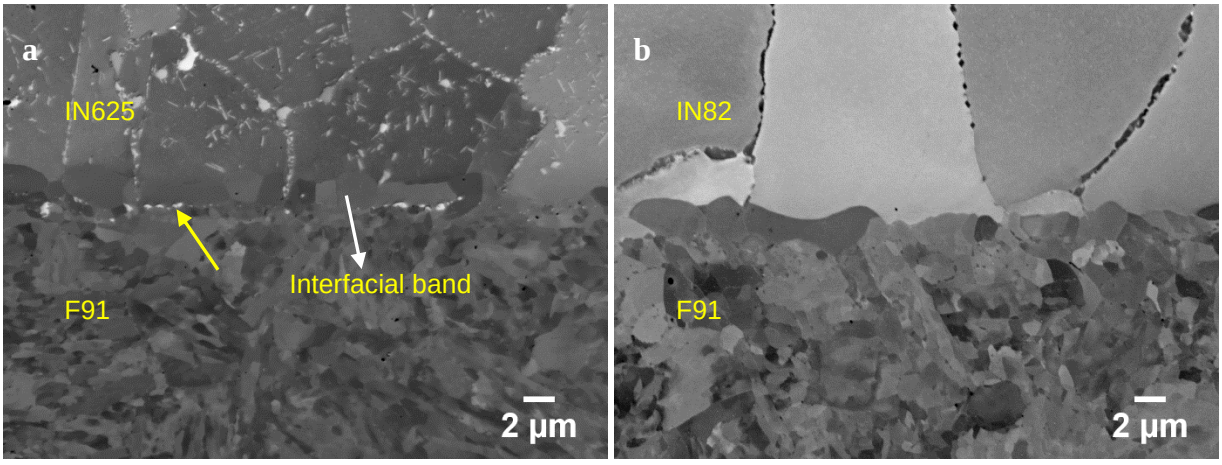

Figure 9.1: SEM images showing the interfacial microstructure (a) IN625 and (b) IN82 [22] aged at 650 °C for 8760 h.

The IN625 bulk material is shown in Figure 9.2. Many precipitates were found to be distributed within the dendrite/columnar structure and in the intergranular/interdendritic regions. A higher magnification view of the zone outlined by the rectangle is shown in Figure 9.2b, where a triple junction of grain boundaries was observed. There were three types of precipitates. Type A precipitate in color white exhibited bulky morphology. Type B precipitate in color grey was found to be smaller than the type A precipitate. They both precipitated close to the boundaries. In addition to the type A and B precipitates, many rod-like white precipitates were observed within the grains.

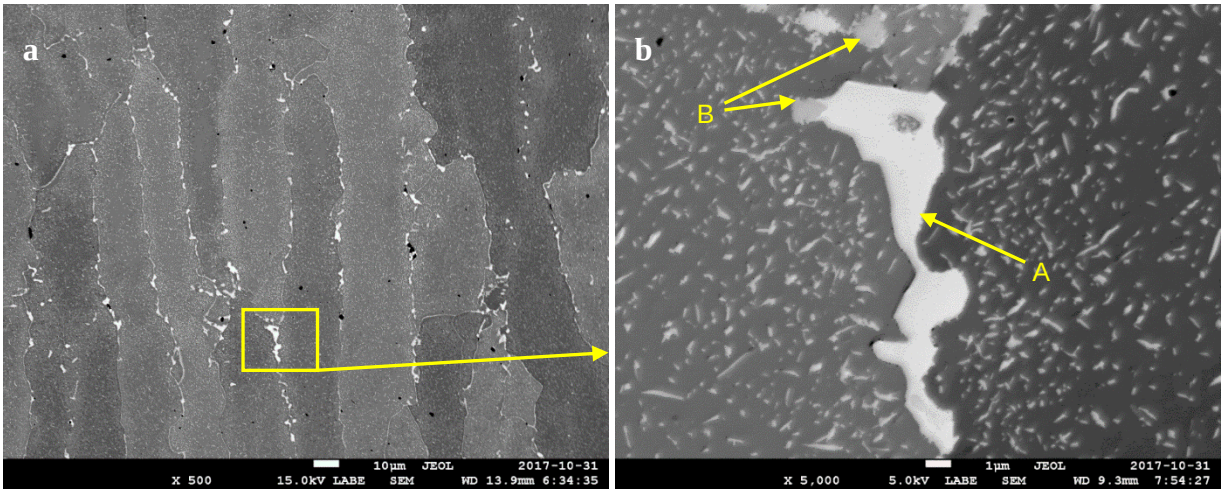

Figure 9.2: SEM images showing IN625 (a) dendrite microstructure and (b) the zone outlined by the rectangle after aging at 650 °C for 8760 h.

To identify these phases, EDS chemical elemental mapping was performed on this region. The EDS composite map and the corresponding individual elemental maps are shown in Figure 9.3. According to the corresponding individual elemental maps, type A precipitate was rich in niobium, silicon, and molybdenum, but depleted in iron, nickel and chromium. Type B precipitate was rich in carbon and niobium.

Following the EDS chemical elemental mapping, EDS spot measurements were performed on type A and B precipitates. The proportions of chemical elements obtained from the representative EDS spot measurements are shown in Figure 9.4b and c. According to the chemical compositions, type A precipitate was expected to be a M_6C-type carbide, where the letter M represents metallic elements such as Cr, Fe, Ni, Nb, and Mo. Type B precipitate was expected to be a Nb(C,N)-type carbide. However, EDS spot measurements performed on the rod-like precipitates were not shown

due to the relatively large size of interaction volume between the electron beam and the sample compared with the size of rod-like precipitate.

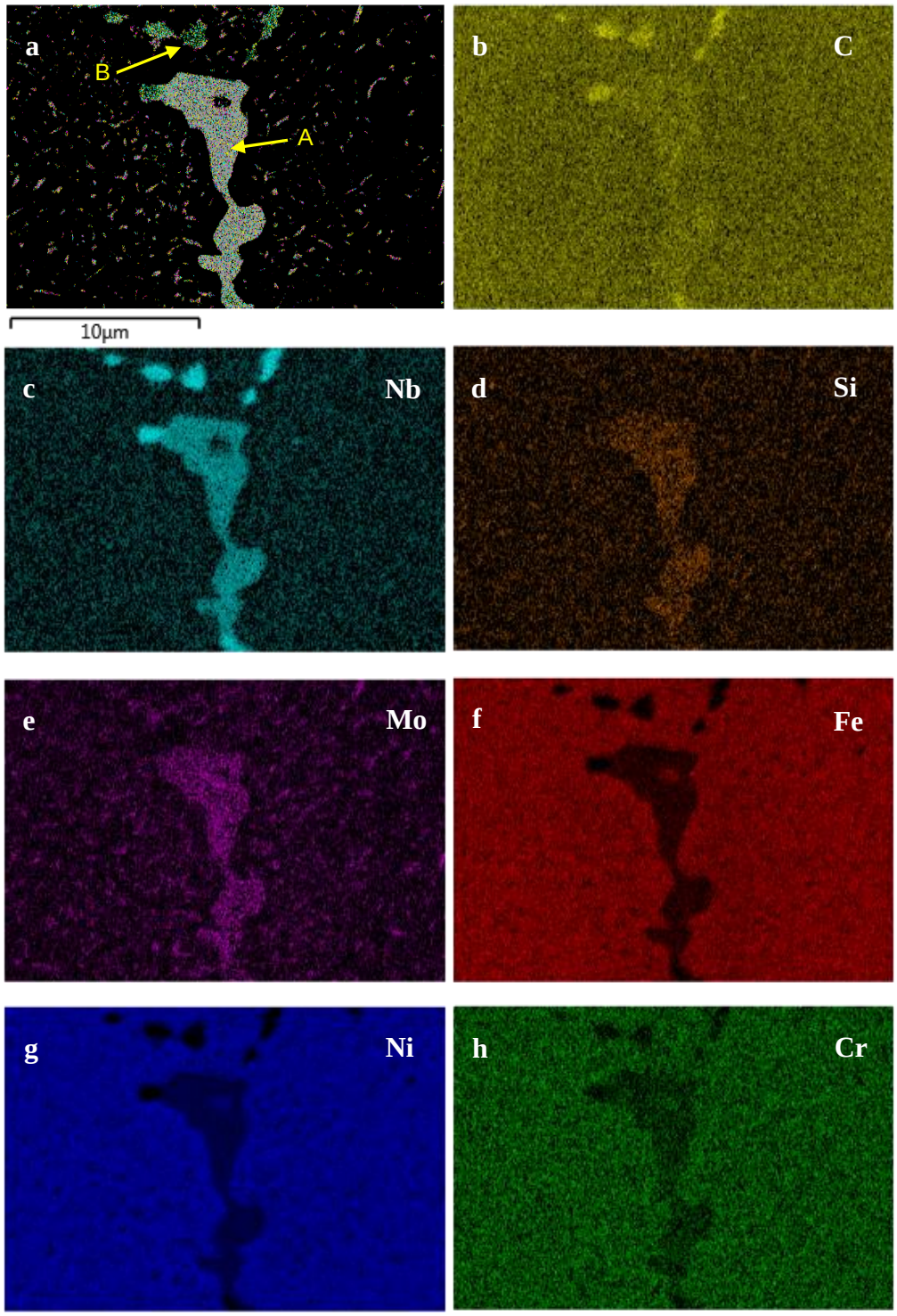

Figure 9.3: EDS elemental mapping on the IN625 bulk material after aging at 650 °C for 8760 h: (a) EDS composite map; (b) C, (c) Nb, (d) Si, (e) Mo, (f) Fe, (g) Ni, and (h) Cr elemental maps.

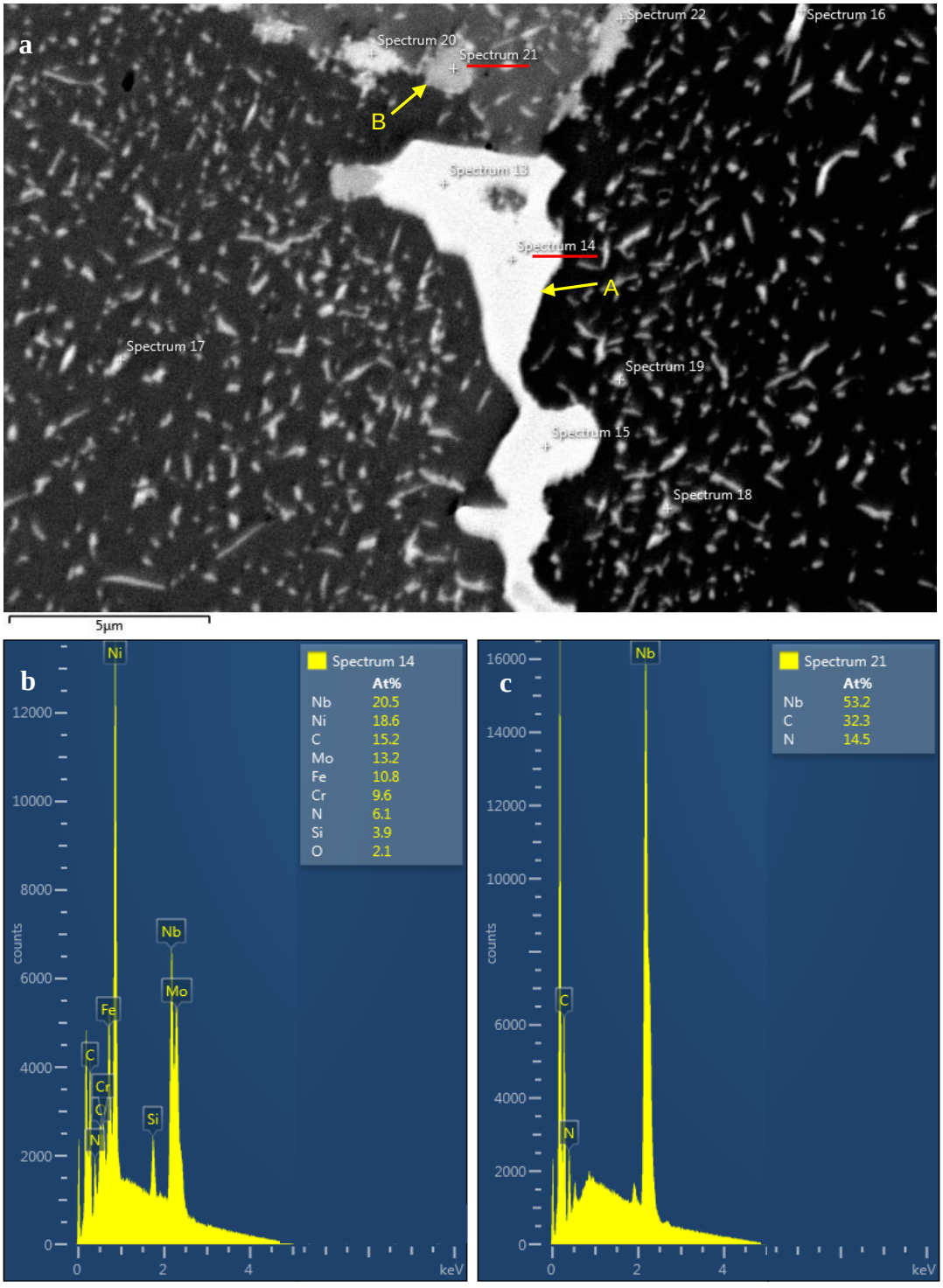

Figure 9.4: EDS spot measurements on type A and B precipitates: (a) BSE image; (b) a spectrum obtained from type B precipitate, and (c) a spectrum obtained from type A precipitate.

Figure 9.5 shows the XRD patterns of the F91/IN625 and F91/IN82 interfaces obtained from samples aged at 650 °C for 8760 h. The XRD patterns confirmed the major phases of γ-Ni and α-Fe

in both samples. The most intensive peaks for the IN625 and IN82 samples were observed Ni (200) and Ni (110) respectively, which may be caused by the directional growth of the dendrites or the columnar grains. Compared with the IN82 sample, some weak peaks were observed in the pattern of the IN625 sample. This indicated the presence of Nb(C,N) carbides and Ni_3Nb. As stated previously, the type A and B precipitates along grain boundaries in the bulk material were expected to be M_6C and Nb(C,N) respectively based on the chemical compositions. Therefore, it is inferred that the rod-like precipitates in the bulk IN625 may be Ni_3Nb, as shown in the XRD pattern. These abundant precipitates may affect the mechanical properties.

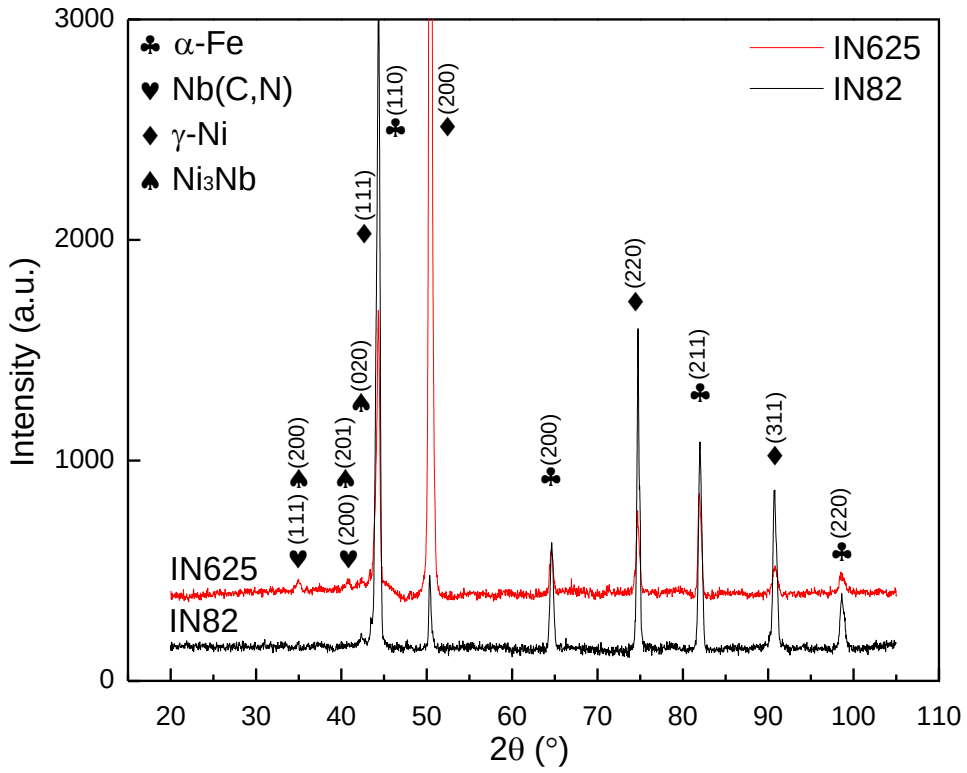

Figure 9.5: XRD patterns of the F91/IN625 and F91/IN82 interfaces after aging at 650 °C for 8760 h.

9.2 Mechanical testing

9.2.1 Indention testing

To show the effects of temperature on hardness of the IN625 hardfacing components, micro-indentation measurements were performed on the cross-sections of the IN625 hardfacing

samples in the as-tempered condition, and aged at 550, 600, 650, and 700 °C for 1008 h. The results are shown in Figure 9.6. One line measurements on the cross-section ranging from the steel substrate to the second layer of S6 are shown in Figure 9.6 as well. The hardness gradients observed in the IN625 hardfacing samples were quite similar as that in the IN82 and S21 samples shown in Figure 8.11. For the F91 steel, the first layer of S6 and the second layer of S6, there was no considerable change in hardness caused by temperature. However, the IN625 was found to harden with temperature. The second layer of S6 was observed always harder than the first layer of S6 due to Fe dilution, as explained in chapter 8.

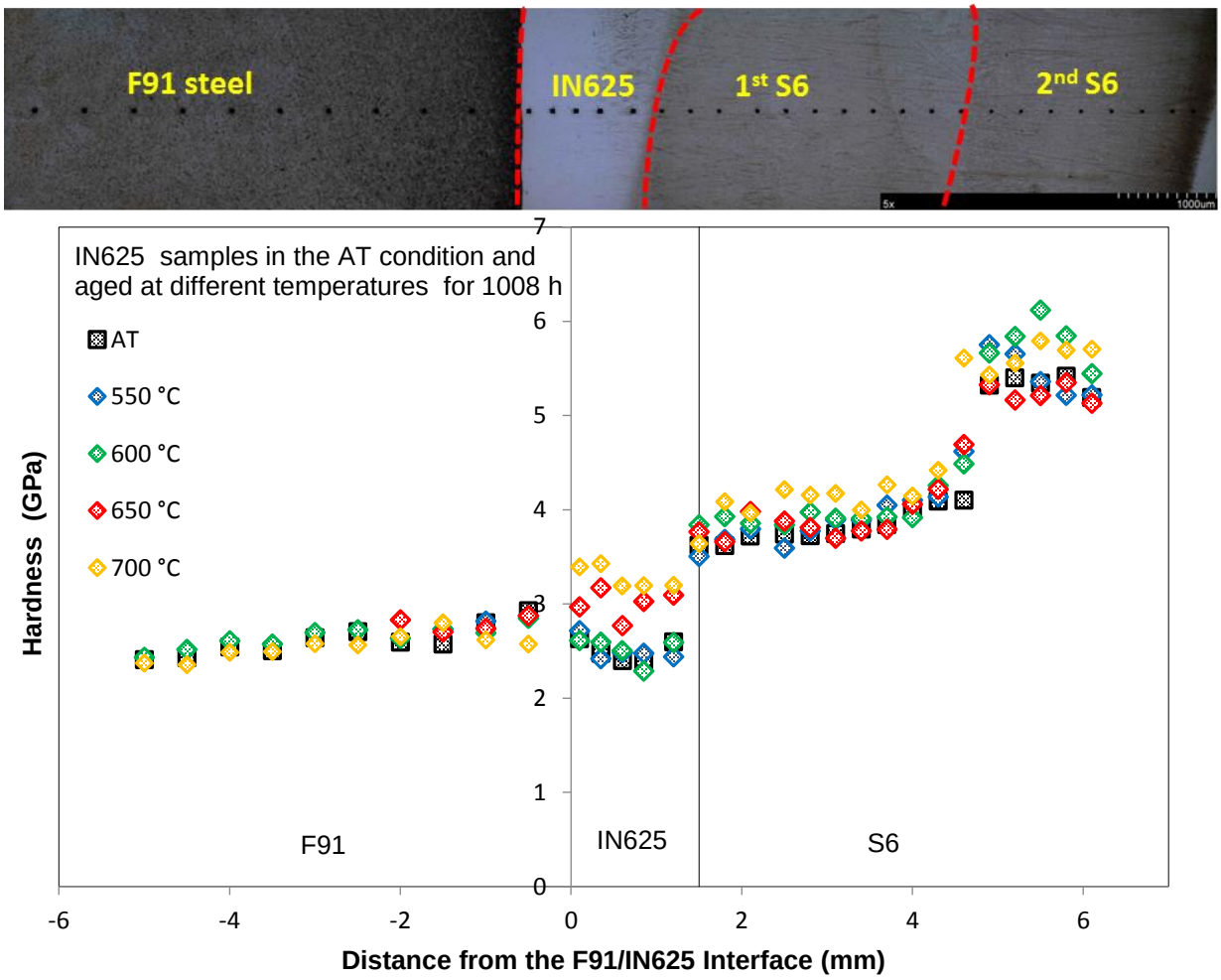

Figure 9.6: Microhardness profiles of the IN625 samples: (a) as-tempered condition; aged at 550, 600, 650, and 700 °C for 1008 h.

To show the effects of aging time on hardness of the IN625 hardfacing components, micro-indentation measurements were performed on the cross-sections of the IN625 hardfacing

samples in the as-tempered condition, and aged at 650 °C for 1008 and 3600 h. As shown in Figure 9.7, hardness gradients were also observed. There was no considerable change in hardness caused by aging time for the F91, the first layer of S6 and the second layer of S6. However, the IN625 was found to harden with aging time. The second layer of S6 was also harder than the first layer of S6.

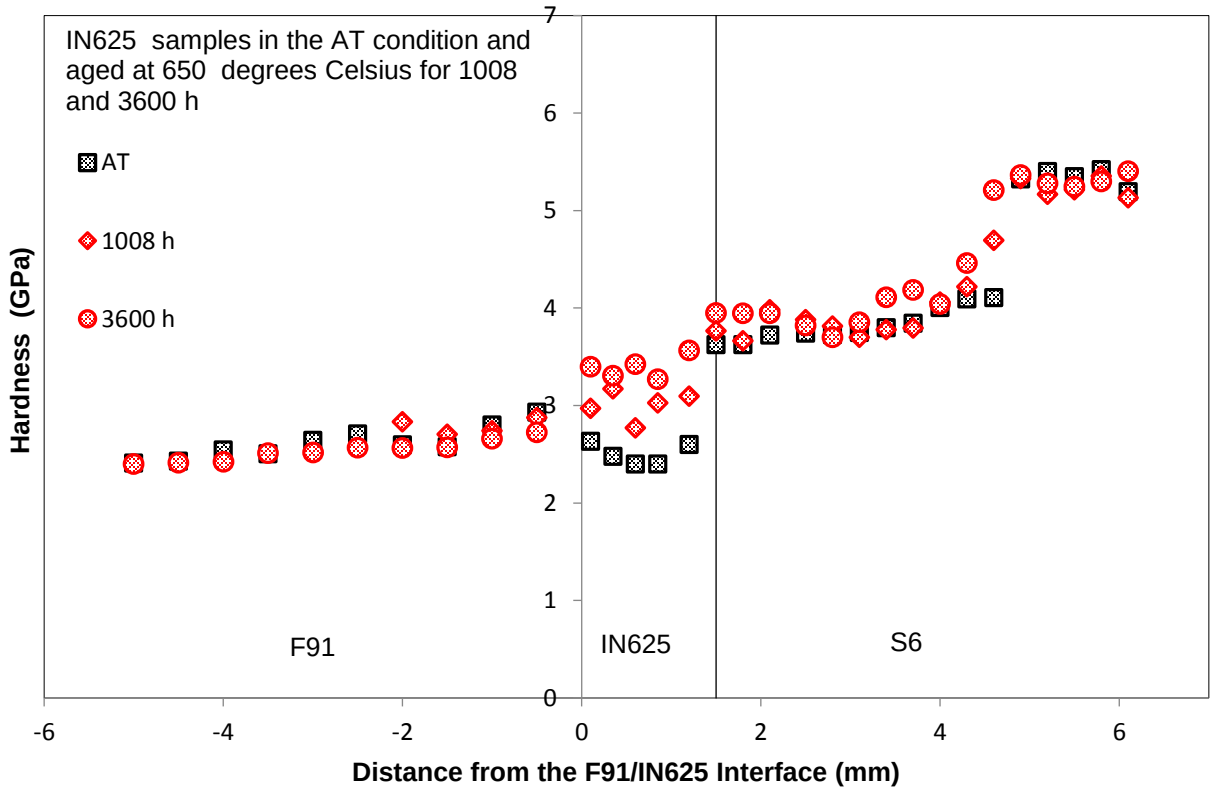

Figure 9.7: Microhardness profiles of the IN625 samples: as-tempered condition; aged at 650 °C for 1008 and 3600 h.

The IN625 bulk material was found to harden with aging time and temperature. It is reported that hardening of the IN625 occurred during aging due to the presence of precipitates. Shaikh et al. measured the hardness of IN625 after aging at 625, 700, and 760 °C for durations ranging from 1 to 335 h [107]. They found peak hardening occurred much earlier at 760 °C than at 700 °C. The hardening was caused by the precipitates. Electron probe microanalysis and transmission electron microscopy confirmed that those rod-like precipitates were $Ni_3(Nb,Mo)$ phase. In the present work, the rod-like precipitates in the bulk IN625 may be Ni_3Nb. These Ni_3Nb precipitates as well as the M_6C and Nb(C,N) along grain boundaries might be responsible for the hardening of bulk IN625 with aging time and temperature.

9.2.2 Charpy impact testing

The Charpy impact energy measurements of the IN625, IN82 and S21 hardfacing specimens aged at 650 °C for 0, 1008, 3600 and 8760 h are shown in Figure 9.8. Compared with the as-tempered S21 and IN82 hardfacing specimens, the impact energy of the as-tempered IN625 hardfacing specimens was initially the lowest. The impact energy of the aged IN625 hardfacing specimens decreased with time to reach a maximum energy loss of 88% after aging at 650 °C for 8760 h, which was significant. Its impact energy after aging at 650 °C for 8760 h was close to that of S21 in the same aging condition. The IN82 hardfacing specimens was found to be the most stable, achieving a maximum energy loss of 38% after aging at 650 °C for 8760 h.

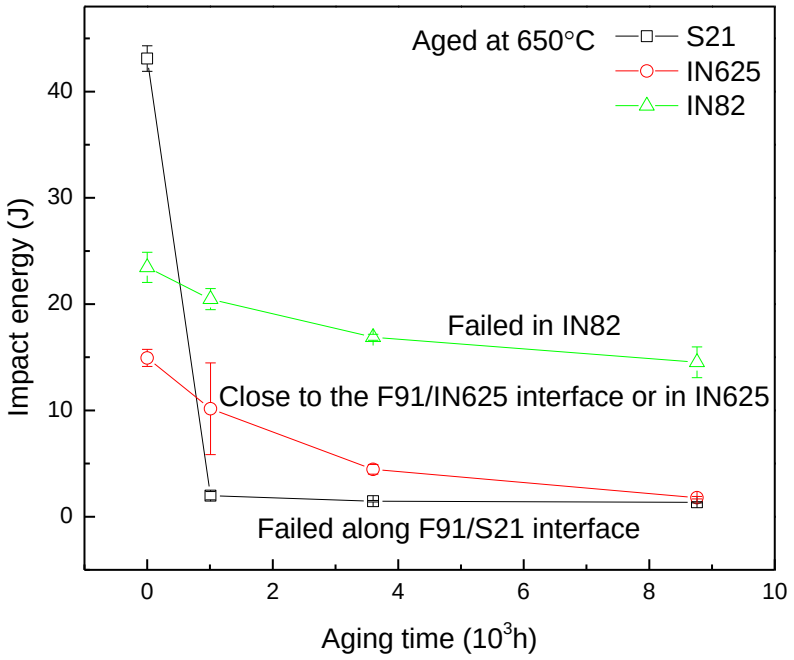

Figure 9.8: Impact energy evolution of the S21, IN625 and IN82 hardfacing specimens.

Stereomicroscopy was used to examine the IN625 Charpy specimens. Two types of fracture were observed, namely, fracture along the F91/IN625 interface and fracture in the IN625 bulk material. As shown in Figure 9.9a b and c, one type of fracture occurred along the F91/IN625 interface after aging at 650 °C for 8760 h, which may be resulted from the precipitates along the edge of the interfacial band shown in Figure 9.1a. As shown in Figure 9.9d e and f, the other type of fracture

occurred in the IN625 bulk material, which may be caused by the precipitates in the bulk material shown in Figure 9.2b. In addition, no significant plastic deformation was observed from cross-sections and back-faces of both types of specimens.

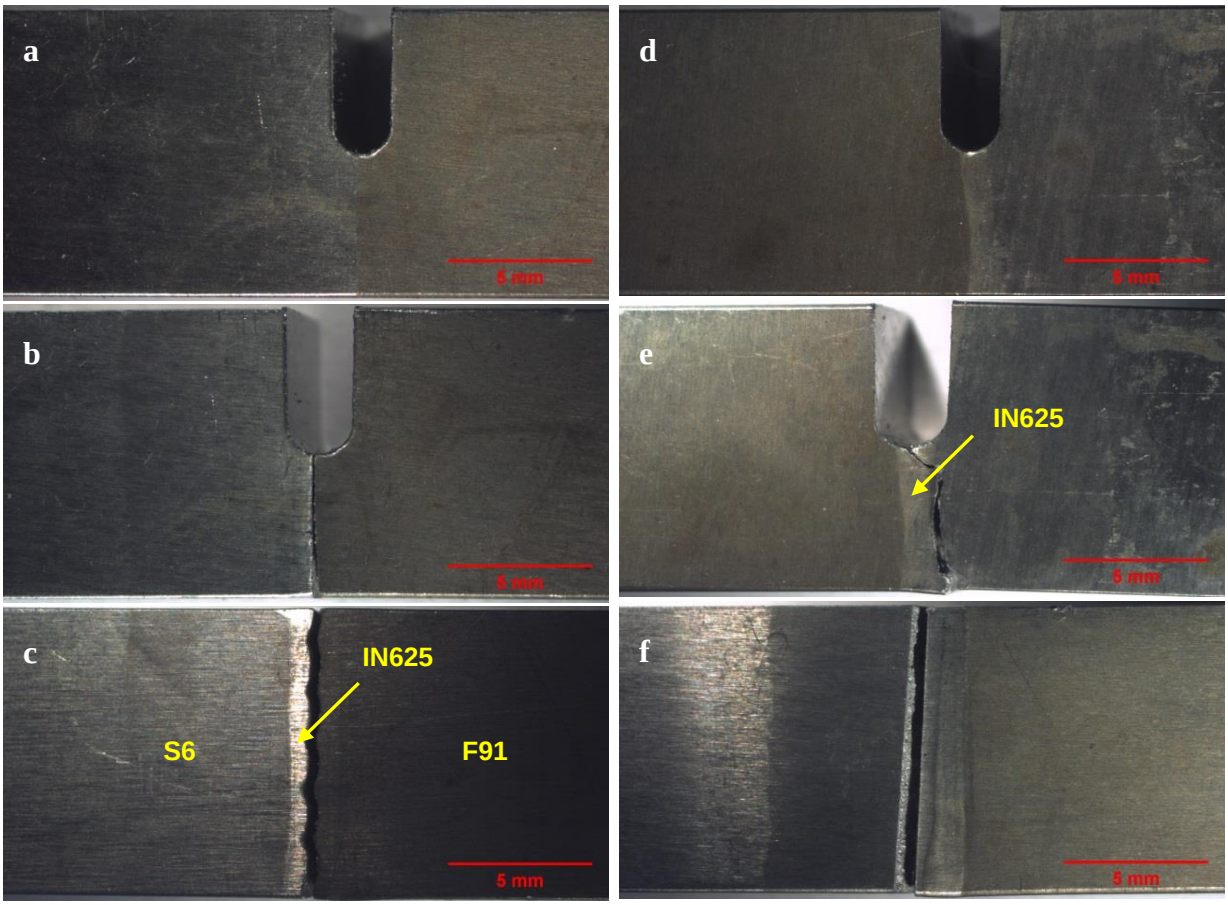

Figure 9.9: IN625 Charpy specimens after aging at 650 °C for 8760 h: showing fracture along the F91/IN625 interface (a) before fracture, (b) cross-section and (c) back-face after fracture; showing fracture in the IN625 (d) before fracture, (e) cross-section and (f) back-face after fracture.

9.2.3 Tensile testing coupled with DIC

9.2.3.1 Straight-shank specimen

The strain maps of an IN625 tensile specimen aged at 550 °C for 1008 h were analyzed using DIC. Figure 9.10 shows its principle strain maps just before and after fracture. The fracture occurred in the F91 steel. A reduction in cross-sectional area due to necking was observed. As seen in Figure 9.10b, it failed in a typical ductile fashion. From the strain maps, the maximum deformation was

observed in the F91 steel. Compared with the steel, a less extent of deformation was observed in the hardfacing including IN625 and S6 regions.

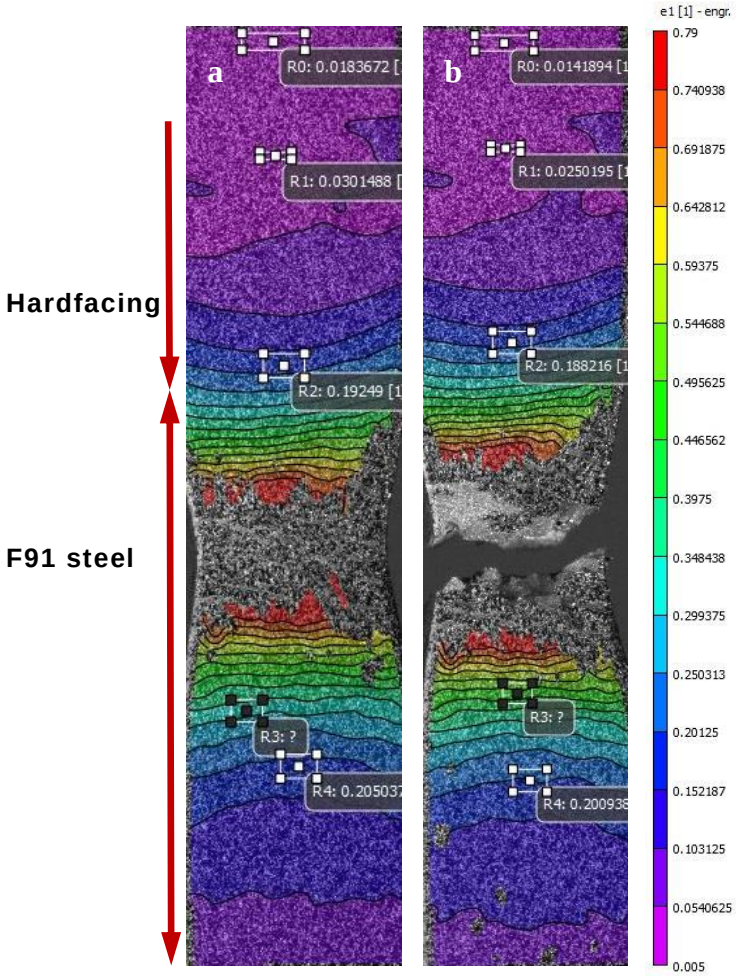

Figure 9.10: Principle strain maps of a tensile specimen aged at 550 °C for 1008 h: (a) before and (b) after fracture.

During the tensile testing, the stress obtained can be used to couple the local strain to obtain stress-strain curves for each region based on the DIC method. For example, rectangular areas from the F91, IN625 and S6 materials were selected as shown in Figure 9.10. Then, the local stress-strain curves for the F91, IN625 and S6 materials were extracted using VIC-3D software. The results obtained are as shown in Figure 9.11. The ultimate tensile stress of this IN625 hardfacing component was 647 MPa. The obtained yielding stresses of the F91, IN625 and S6 materials were 428, 482, and 490 MPa, respectively. The S6 showed the highest yielding stress while the F91 showed the lowest yielding stress. The stress-strain curves of IN625 and S6 were quite similar at

the beginning of the test. However, the S6 strength increased with strain more than the IN625 did. In addition, the S6 experienced the least amount of strain during the testing while the F91 underwent the most amount of strain. Since this IN625 hardfacing component failed in the F91 base material, the F91/IN625 interface was not the weakest link under monotonic normal stress for the straight-shank specimen.

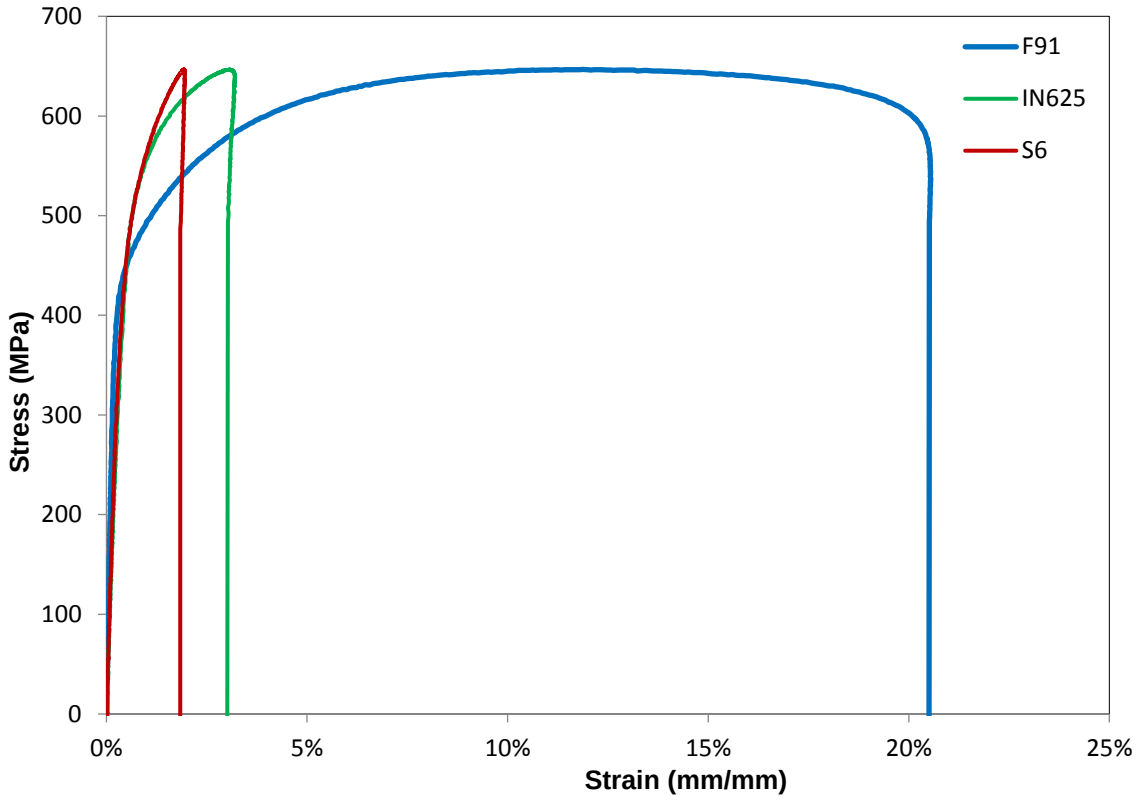

Figure 9.11: Local stress-strain curves obtained from F91, IN625 and S6.

9.2.3.2 Notched specimen

In addition to the straight-shank specimen geometry, some notched specimens with the F91/IN625 interface centered were manufactured for the purpose of forcing fracture in the notch, the highly stressed area. As shown in Figure 9.12, the fracture occurred in the IN625 for a notched specimen in the as-tempered condition. From the strain maps, the F91 steel experienced the most amount of strain before the fracture of specimen while the S6 experienced the least amount of strain. Due to stress concentration caused by the notch, large local strains close to the notch were also observed. Since this IN625 hardfacing component failed in the IN625 bulk material, the F91/IN625 interface

was not the weakest link under monotonic normal stress for the notched specimen in the as-tempered condition.

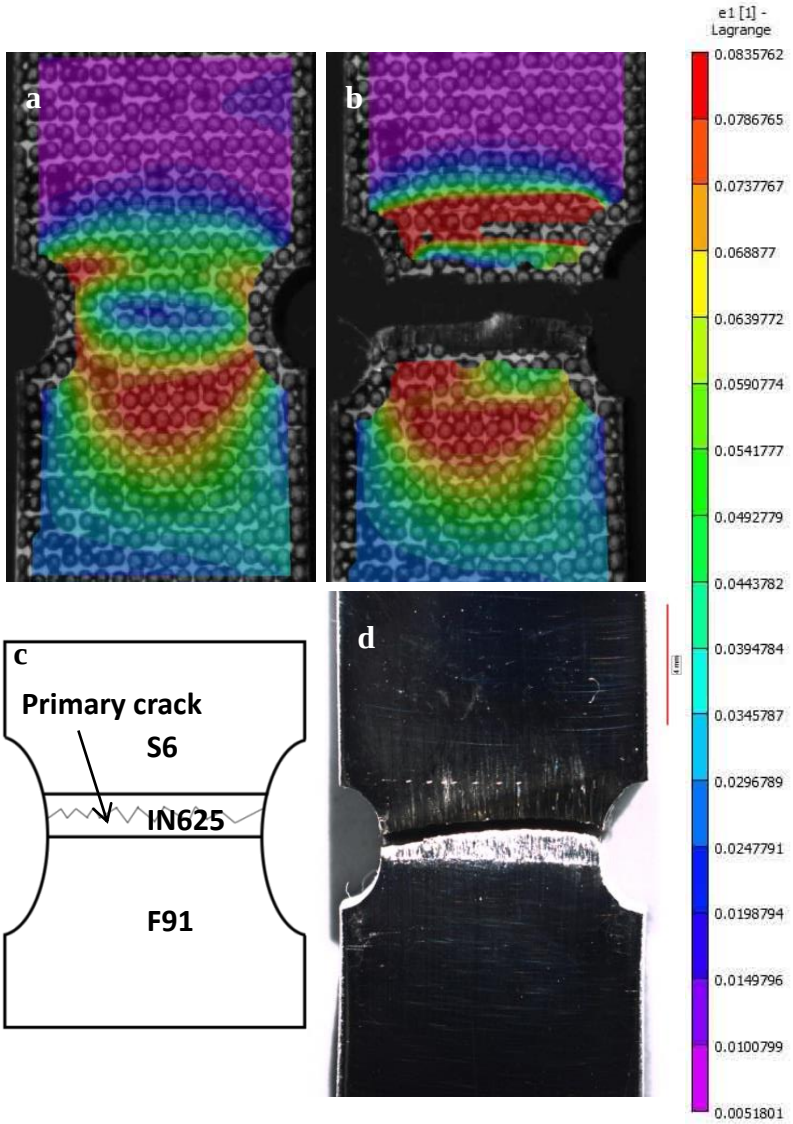

Figure 9.12: A notched specimen in the as-tempered condition: principle strain maps (a) before and (b) after fracture, (c) illustration showing the fracture, and (d) the other side of the fractured specimen.

The fracture analysis of this notched specimen in the as-tempered condition is shown in Figure 9.13. The EDS spot measurement on the fracture surface confirmed the primary crack in the nickel-based alloy, IN625. From its fractograph in Figure 9.13b, the interdendritic cracks were observed. The fracture of this notched specimen in the IN625 may be brittle. Not like the

straight-shank specimen, the stress-strain curves were not obtained for this notched specimen due to stress concentration caused by the notch.

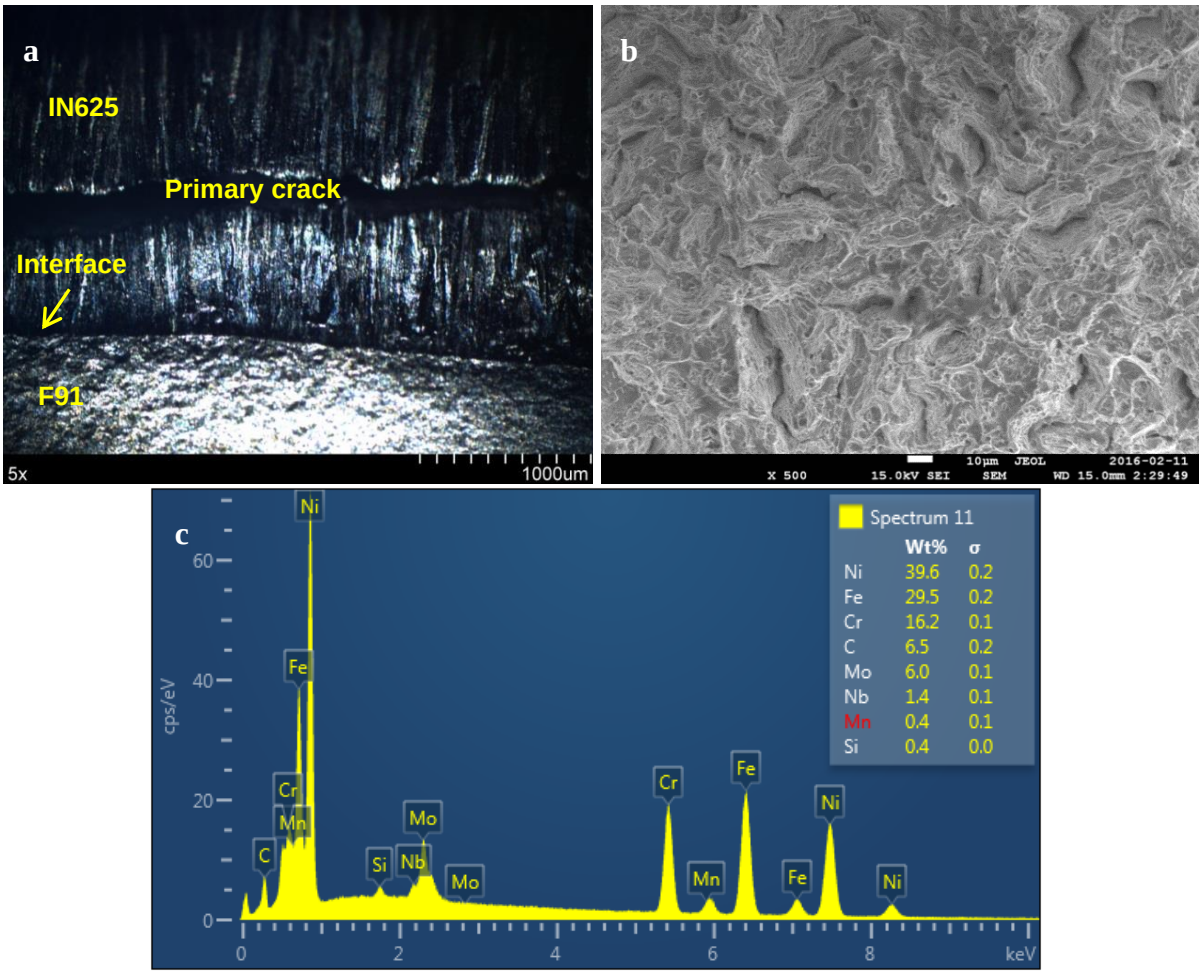

Figure 9.13: A fractured IN625 specimen in the as-tempered condition: (a) cross-section, (b) fractograph and (c) EDS spot measurement on the fracture surface.

The fracture occurred in the S6 for the notched specimens aged at 650 °C for 1008 h. One such example is shown in in Figure 9.14. The strain map before fracture presented similar distribution as the specimen in the as-tempered condition. Namely, the F91 steel experienced the most amount of strain while the S6 experienced the least amount of strain. Moreover, large local strains close to the notch were also observed. Since this IN625 hardfacing component failed in the S6, the F91/IN625 interface was also not the weakest link under monotonic normal stress for the notched specimen after aging at 650 °C for 1008 h.

Tensile testing of the IN82 and S21 hardfacing components are given in Appendix G.

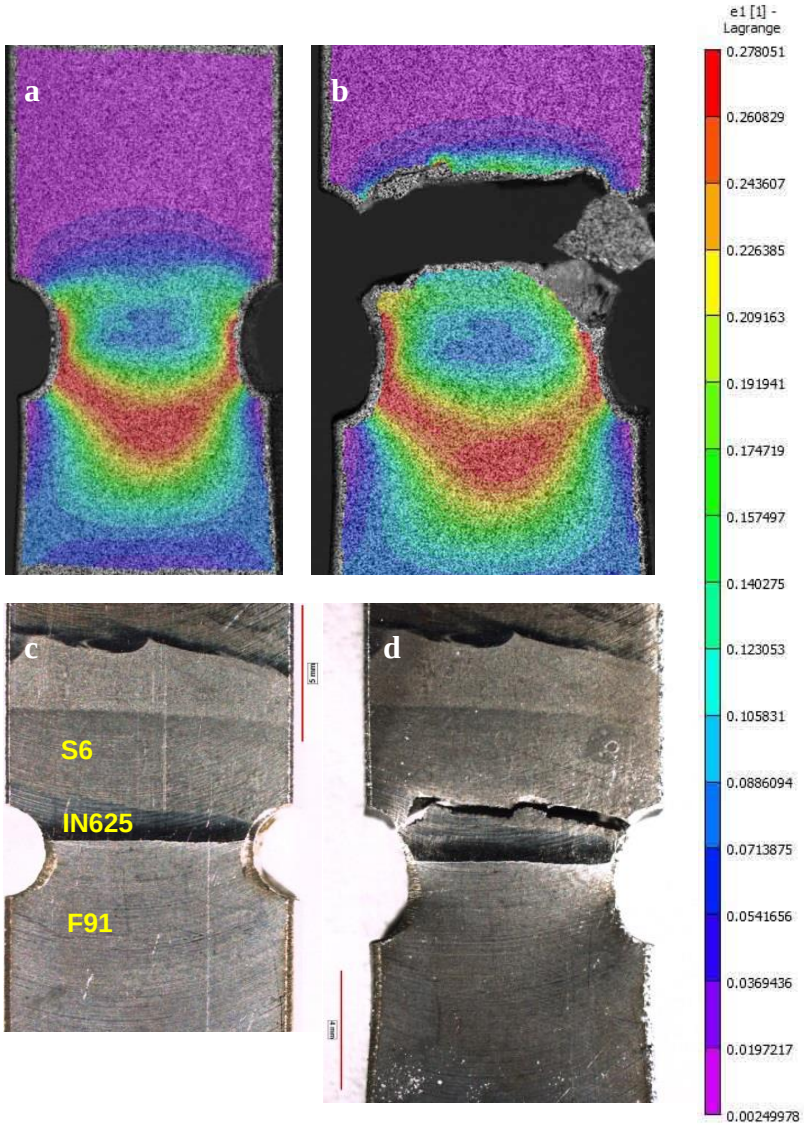

Figure 9.14: A notched specimen aged at 650 °C for 1008 h: principle strain maps (a) before and (b) after fracture, the other side of the specimen (c) before and (d) after fracture.

CHAPTER 10 AN EX-SERVICE WEDGE GATE VALVE STUDY

To transfer the knowledge obtained from the laboratory study to the industrial component, the delamination failure of an ex-service wedge gate valve, provided by a valve manufacturer, is investigated in this chapter. This ex-service wedge gate valve is shown in Figure 10.1. A part of this component was cut using wire electrical discharge machining. The sampling location is shown in Figure 10.2. A delamination crack was found in the sample, as shown in Figure 10.2.

Figure 10.1: An ex-service wedge gate valve.

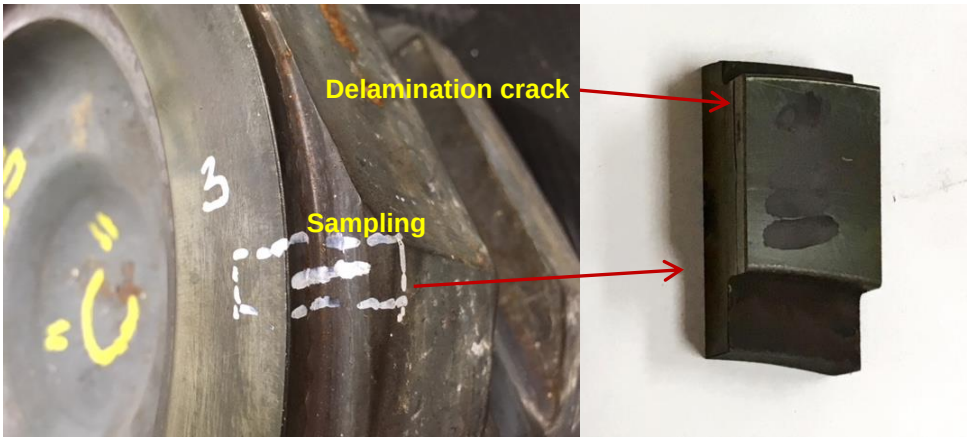

Figure 10.2: Sampling location and a sample after cutting.

The sample was ground and polished, in which this delamination crack was observed on the cross-section shown in Figure 10.3. Figure 10.4a shows a full cross-section of this ex-service component: base material grade 91, buffer layer S21 and top layer S6. The rectangular zones shown

in Figure 10.4a were further examined using SEM. The delamination crack went through the S21, not along the steel/S21 interface, as shown in Figure 10.4a. The S6 and S21 exhibited typical dendritic structure, as shown in Figure 10.4b, c, d and e. The most notable microstructural feature observed was the network of abundant veins starting at the steel/S21 interface, extending through the S21 bulk material, and stopping at the S21/S6 interface. These veins were up to nine µm in width. They appeared to follow grain boundaries.

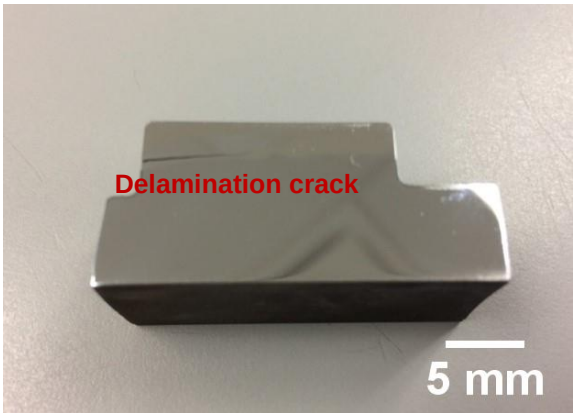

Figure 10.3: The cross-section of this sample after metallographic preparation.

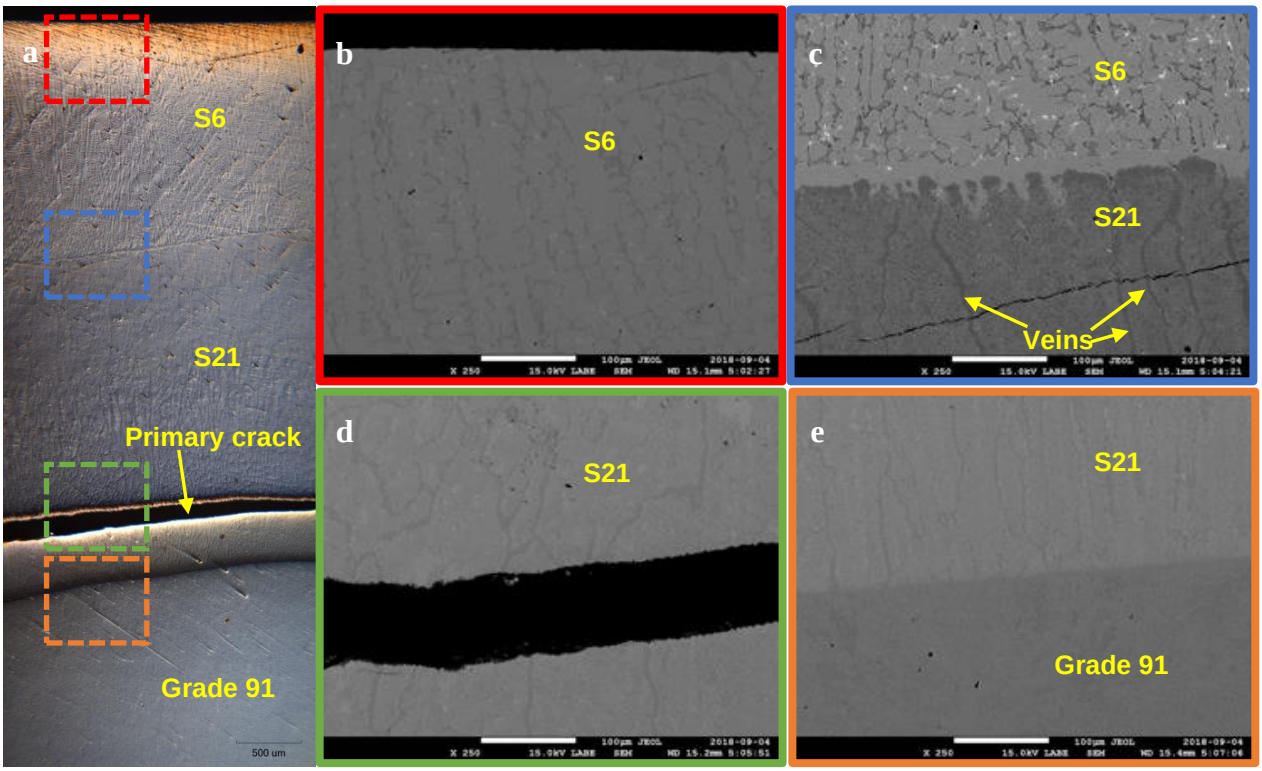

Figure 10.4: (a) OM micrographs showing the full cross-section; (b), (c), (d) and (e) higher SEM magnification views.

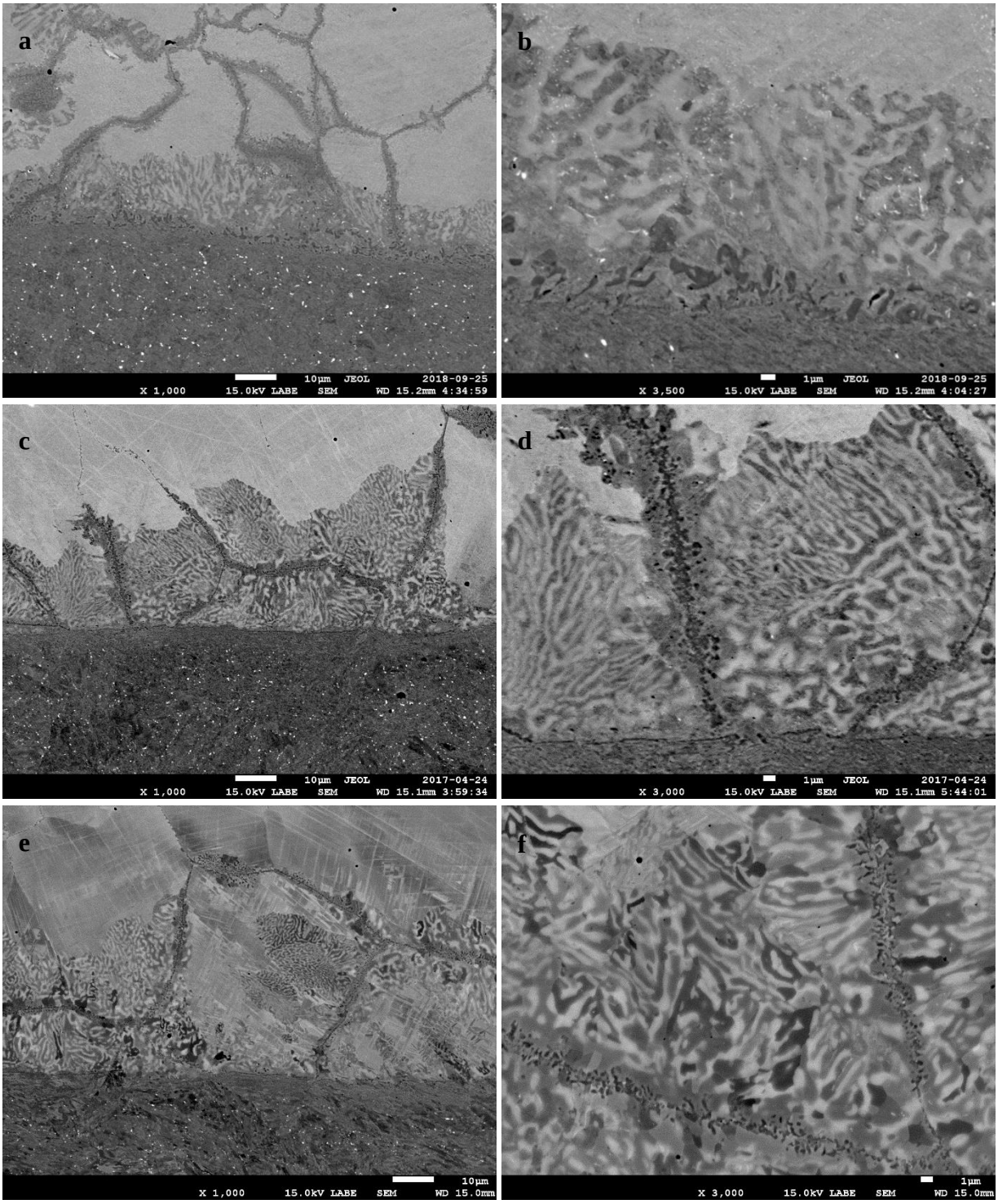

Figure 10.5: Steel/S21 interfacial microstructure: (a) and (b) from the ex-service component; from the laboratory sample aged at 550 °C for 8760 h (c) and (d) polished up to 1 µm, (e) and (f) further polished using a mixed colloidal silica suspension.

The steel/S21 interfacial microstructure from the ex-service component is shown in Figure 10.5a and b, while the corresponding interfacial microstructure from the sample aged at 550 °C for 8760 h is shown in Figure 10.5c, d, e and f. A great extent of similarity in microstructural appearance between the ex-service component and the laboratory sample (Figure 10.5c, d, e and f) was observed. However, the vein-like features at grain boundaries from the ex-service component were more abundant than those from the sample aged at 550 °C for 8760 h. Moreover, the veins observed from the ex-service component grew more deeply into the S21 bulk material until the S21/S6 interface. The veins observed from the sample aged at 550 °C for 8760 h were close to the F91/S21 interface, without extending through the S21 bulk material. The steel/S21 interfacial microstructure from the sample aged at 550 °C for 8760 h after further polishing using a mixed colloidal silica suspension is shown in Figure 10.5e and f. The two images showed a near-ideal microstructure due to the removal of the deformation layer. They were presented here since the SEM images in our article 1 were obtained using the same methodology.

EDS spot measurements were carried out on the ex-service component. The spot locations are shown in Figure 10.6. One representative measurement on each white, grey and dark grey phases was listed in Table 10.1. According to the obtained results and our article 1, the white phase was expected to be the σ phase; the grey phase was expected to be the intermetallic Fe_xCo_y phase; the dark grey phase was expected to be the $M_{23}C_6$-type carbide.

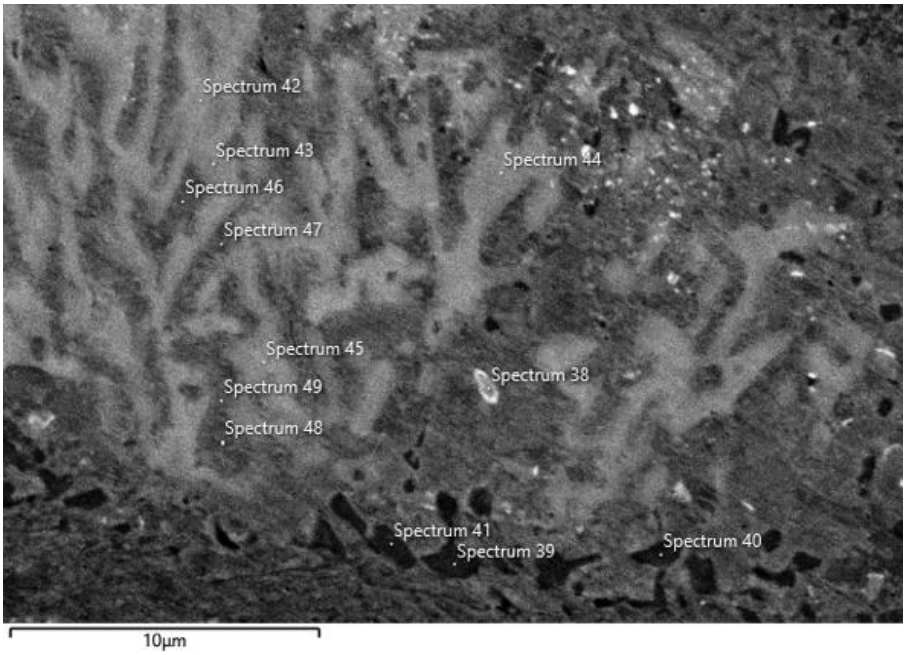

Figure 10.6: EDS spot measurements on the ex-service component.

Table 10.1: Representative EDS spot measurements on the three phases (wt%).

Element	Spectrum 40	Spectrum 45	Spectrum 48
Cr	69.0	36.8	2.6
Fe	9.7	29.6	54.8
Co	4.9	20.7	38.0
Mo	6.3	5.0	0.1
C	8.3	3.4	3.2
Si	0.3	1.8	0.2
Ni	1.4	1.7	0.8
Mn	0.0	1.1	0.4

After the exploration of the steel/S21 interfacial microstructure, the delamination crack located in the S21 was investigated using BSE imaging. As shown in Figure 10.7a, the primary delamination crack was observed propagating in the σ-phase-rich zone. Secondary cracks were observed in the σ phase, as seen in Figure 10.7b. Cracks in the σ phase, induced by Charpy impact testing, were also observed, as shown in Figure 7.7. Though the delamination of this ex-service component is not caused by impact testing, it is validated that the methodology we used (the U-notch impact specimen design with the interface centered) is able to examine the brittle phases effectively.

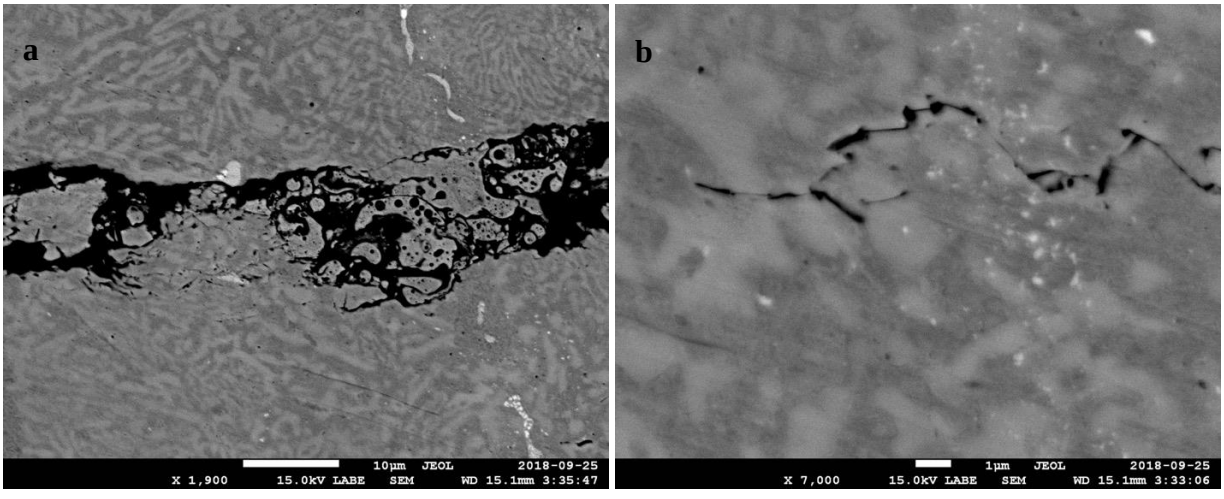

Figure 10.7: (a) Primary crack and (b) secondary cracks observed in the σ-phase-rich zones.

Based on all the above results, the failure mechanism of this ex-service wedge gate valve was clear. The σ phase played a deleterious role at the service temperature. The columnar grain boundaries in the S21 served as easy pathways for diffusion of elements necessary for the formation of σ phase. This resulted in the network of continuous and abundant vein-like features along grain boundaries after years of service. The σ phase was not only formed along the interface, but also precipitated deeply in to the S21 bulk material along grain boundaries. During service, the hard σ phase could easily act as crack initiation sites. Since large amounts of the σ phase grew into the S21 during the long-term service, once initiated, the crack could easily propagate in the S21 through the σ phase. This explained that the primary delamination crack was observed in the S21 bulk material rather than along the steel/S21 interface.

CHAPTER 11 GENERAL DISCUSSION

This chapter provides a general discussion of the results obtained during this PhD project. We discuss how the objectives defined in Chapter 1 have been fulfilled during this work. In addition, the limitations are presented.

As stated in Chapter 1, the first objective of this thesis is to explore the effects of the PWHT on the microstructure and properties of the hardfacing components to reduce the possible failures induced during manufacturing. The PWHT is one of the most important steps during the manufacturing process. We evaluated the PWHT used by our partner, 760 °C for 2 h, in terms of microstructure, hardness and residual stresses. It is found that the high-hardness HAZ was softened significantly after the PWHT due to the microstructure change. A uniform tempered-martensitic structure was formed after the PWHT. As seen in Figure 5.1, the hardness values of HAZ after the PWHT were comparable to the unaffected base material. In addition, the PWHT not only reduced the residual stresses in steel substantially, but also homogenized the lattice strains across the weld. The thickness of strained zone in steel was approximately 6 mm in Figure 5.3, which matched well with the thickness of high-hardness HAZ in Figure 5.1. The reduction in residual stresses of the steel after the PWHT was also caused by microstructure change. That is, the hard martensite was tempered after the PWHT. Thus, the PWHT is considered as a critical step right away after welding to reduce the risk of in-process and in-service failures. However, the measurements of residual stresses in the hardfacing layers were very challenging and most of the experiments did not give good results. In addition, we could not obtain conclusive results on the difference in residual stresses caused by the different thermal expansion mismatch values between the steel and the three types of buffer layers.

After manufacturing, the hardfacing components are used in service conditions. The second objective of this thesis is to investigate the effects of long-term aging on the microstructure evolution of the hardfacing components. Therefore, we performed aging experiments at temperatures between 550 and 650 °C for exposure durations ranging from 1008 to 8760 h on the Stellite hardfacing components. Compared with the studies reported in the literature, we characterized the samples aged in the widest temperature range from which two types of diffusion kinetics were observed according to Harrison's classification. In addition to the hard σ phase reported by Lolla et al. [4], we determined that the $M_{23}C_6$ phase was the hardest among the phases

studied. They both contributed to the increase of the interfacial layer's hardness. We also studied the growth kinetics of the interfacial layer between F91 and S21 from which the equivalent time and temperature can be determined by extrapolating the thickness of the interfacial layer and the area fraction of the $M_{23}C_6$ carbides, as shown in Figure 6.13. Similarly, the equivalent time and temperature can be obtained by extrapolating the equivalent diameter of the $M_{23}C_6$ carbides, which is of great significance. For example, we can predict the service time of an ex-service component after we examine the equivalent diameter of the $M_{23}C_6$ carbides and obtain its service temperature.

The third objective of this thesis is to establish a relationship between the microstructure evolution and the mechanical properties of the hardfacing components. As shown in Figure 6.11, the thickness of the interfacial layer grew up to 13 μm after aging at 650 °C for 8760 h [94]. How to test the toughness of such a local hard layer became a challenge. To accomplish the third objective, we welded an F91 extension to the original hardfacing components and designed an innovative Charpy U-notch geometry with the F91/S21 interface centered in the notch, where the novelty and originality lie. Therefore, it was feasible to investigate the effects of the interfacial microstructure on mechanical properties of hardfacing by means of impact testing.

The most important objective focuses on evaluating the alternative buffer layers on the durability of the hardfacing components. EPRI predicted that the nickel-based IN82 alloy would be a good alternative to replace the cobalt-based S21 buffer layer using thermodynamic simulations in a report [40]. Thus, we fabricated hardfacing components using the IN82 buffer layer. Then, we not only studied the microstructure evolution of IN82 hardfacing specimens during long-term aging, but also applied the same methodology as S21 to investigate the toughness degradation. Finally, we validated that by using the IN82 buffer layer, the durability of hardfacing components would be improved, which is promising and encouraging. According to the literature, it is the first time to validate the IN82 buffer layer deposited between F91 and S6 systematically and comprehensively.

The advantage of the IN625 buffer layer over the IN82 lies in its lower cost. We also investigated the IN625 buffer layer in chapter 9. The F91/IN625 interface after aging at 650 °C for 8760 h was not as stable as the F91/IN82 interface since the white precipitates were observed parallel to the interface. Clark studied an ex-service weld interface between P91 steel and IN625 after 40000 h of operation at 565 °C [108]. He observed a band of coarse carbides formed on the edge of the interfacial band in the steel. He also found that the edge of the interfacial band was nearly totally

covered by those carbides, which were identified as $M_{23}X_6$ and M_6X. In the present work, the white precipitates close to the F91/IN625 interface would not be expected to be $M_{23}C_6$ carbides based on their BSE imaging contrast. It is inferred that they may be M_6C carbides. The IN625 bulk material was found to harden from the indentation testing. The rod-like precipitates in the IN625 bulk material may be Ni_3Nb. They together with the M_6C and Nb(C,N) carbides along grain boundaries may cause the hardening of IN625 after aging.

As shown in Figure 9.9d, e and f, the fracture occurred in the IN625 bulk material during the Charpy impact testing. These precipitates in the bulk material may cause the failures. In addition, the fracture also occurred along the F91/IN625 interface, which may be resulted from the precipitates along the edge of the interfacial band. Clark reported the low-ductility creep failure of an ex-service weld [108]. The tip of the crack propagated through the carbon-denuded zone of the steel, next to the interface. This zone was characterized by decreased strength. It might be due to the dissolution of strengthening precipitates such as $M_{23}C_6$ and MX in the matrix, replaced by a band of continuous coarse carbides. Those continuous coarse carbides may act as stress concentrators and sites for void formation. As shown in Figure 9.8, the impact energy loss of IN625 hardfacing specimens (88%) was significant after aging at 650 °C for 8760 h (1 year). As reported in the literature, the application of IN625 buffer layer between alloy Deloro 50 and the modified 9Cr-1Mo steel was able to facilitate crack-free deposition [42]. However, the IN625 is not recommended as a buffer layer between steel and S6 in our study, which might also cause failures of valves.

Tough the fracture occurred along the F91/IN625 interface for some Charpy specimens during the impact testing, the interface was not the weakest link during the tensile testing. One reason may be that the tensile testing is not able to characterize brittleness effectively as the Chapry impact testing. As shown in Appendix G, the F91/IN82 interface was proved not to be the weakest link for all the IN82 tensile specimens studied, which further indicated the right choice of IN82 buffer layer. In addition to the straight-shank tensile specimens, there were notched specimens with the interface centered. As shown in Figures G.6 and G.8, the notch design was efficient to force fracture at the interface for the S21 tensile specimens after aging, which helped characterize the interface strength.

The DIC technique used in this work was able to extract local properties of the hardfacing components. For example, the yielding stresses obtained from the S6 increased with distance from

the IN82/S6 interface, and then decreased as it approached the interface between the second layer of S6 and the filler material IN625, as listed in Table G.1. The two layers of S6 differed each other in chemical compositions. As explained in chapter 8, the dilution of Fe and Ni would lead to the hardness difference in the two S6 layers. As evidenced in the DIC analysis, they also differed in the yielding stresses. The yielding stresses and hardness values of the two S6 layers correlated with the dilution of chemical elements.

The final study of the ex-service component validated our results and discussion in article 1. It was observed that more σ phase precipitated at lower temperatures. At lower temperatures such as service temperatures, grain boundary diffusion may dominate according to the diffusion regimes in Harrison's classification. The diffusion of the ex-service wedge fell into Type B regime. In addition to the grain boundary diffusion, there was bulk diffusion around grain boundaries. However, no overlap of bulk diffusion fields of neighboring grain boundaries occurred. We also discussed that grain boundaries served as easy pathways to form the σ phase. Therefore, larger amounts of σ phase may precipitate along grain boundaries in the S21 bulk material after long-term service, which would result in the vein-like features. However, the vein-like features in the sample aged at 550 °C for 8760 h were not as apparent as those in the ex-service component due to time.

The delamination crack of this ex-service component did not propagate along the F91/S21 interface, but some distance away from the interface, located in the S21bulk material. The cracks were observed in the σ-phase-rich zones. The σ phase precipitated in the S21 bulk material was responsible for the delamination crack in the S21. At service temperatures, the σ phase was the dominant factor for the failure. Thus, our knowledge obtained from the laboratory samples were successfully transferred to this ex-service component: σ-phase-forming elements mainly diffused along grain boundaries in the S21 at service temperatures and large amounts of σ phase in the S21 bulk material formed deteriorated the hardfacing component. The service conditions are quite complicated, not like just the impact testing and aging. However, the impact testing is sensitive to examine the toughness degradation. Cracks in the σ-phase-rich zones were also observed in our laboratory samples, as shown in Figure 7.7. These phenomena were in great accordance with this delaminated ex-service component.

As stated in paragraph 3 of this chapter, the equivalent service time and temperature of this ex-service wedge can be obtained by extrapolating the diameter of the $M_{23}C_6$ carbides. First, a

comparison of the morphology and distribution of the $M_{23}C_6$ carbides and σ phase between this ex-service component and our laboratory samples presented in chapter 6 was drew. Thus, it is proposed that this ex-service component was used at temperatures between 550 to 600 °C. According to the obtained field information, this ex-service component was exposed to 567–583 °C (1053–1082 °F) for about 6 years. The service temperature range of 567–583 °C fulfilled our expected temperature range of 550–600 °C. The equivalent diameter of the $M_{23}C_6$ carbides of this ex-service wedge was averaged over 41 carbides using using ImageJ software. The standard deviation of the mean was used to calculate the uncertainty of the equivalent diameter. The equivalent diameter was estimated to be 1.5 ± 0.5 μm. By extrapolation, the service time was estimated to be 7.4 ± 2.3 year at 567 °C and 4.7 ± 1.5 years at 583 °C. Therefore, the service exposure time of 6 years also fulfilled our expected time above.

On one hand, we successfully investigated the microstructural factors contributing to the delamination and validated that the durability of IN82 hardfacing components would be improved. On the other hand, there were limitations in our work. Ideally, all the hardfacing components under different conditions used for strain/stress measurements should come from the same hardfacing component. For example, after the strain measurements of an as-welded hardfacing component, the PWHT should have been performed on this component. Following the strain measurements of this as-tempered component, further aging should have been carried out on it. Then neutron diffraction measurements should have been undertaken on this aged component. However, each component represented each condition in this work. Moreover, we were not able to obtain conclusive residual stresses in the hardfacing layers.

There were also other limitations. Thermal cycle testing (start-ups and shut-downs of plants) was not taken into account for experimentation. We only performed aging at constant temperatures. It is because compared with the long-term operation at constant temperatures, the effects of thermal cycling on microstructural change and properties of the components might be not as significant as aging at constant temperatures does. We should also mention that other factors during service, such as operation induced stresses (opening and closing of valves) may also contribute to the failures. These stresses were also not taken into account by our experimentation. The aging experiments were conducted under ambient atmosphere while during service the valve components are in contact with media such as steam. In spite of these limitations, our laboratory experiments including aging, impact testing and microstructure characterization have successfully provided a

solid explanation for the failure mechanism of this delaminated ex-service component. In addition, its service time and temperature have been successfully predicted, which further validates the methodology we used.

CHAPTER 12 CONCLUSIONS AND PERSPECTIVES

12.1 Conclusions

In this PhD work, we studied the microstructure evolution and mechanical properties of the S6 hardfacing components produced using S21, IN82 or IN625 buffer layers comprehensively.

Evaluation of the PWHT

To reduce the risk of failures introduced during manufacturing, the effects of the PWHT on microstructure, hardness and residual stresses of the hardfacing components were studied. After the PWHT, the high-hardness HAZ in the as-welded condition is softened significantly due to the formation of tempered-martensitic structure. A significant decrease of the residual stresses in steel was observed. Moreover, the strains are also homogenized across the hardfacing component. Nevertheless, the measurements of residual stresses in the hardfacing layers were very challenging and thus the results obtained were not as good as those measured in the steel. It is highly recommended to perform the PWHT right away after welding to reduce the risk of potential failures.

Microstructural factors contributing to the delamination

For the problematic S21 hardfacing components, three phases including an (Fe,Co)(Cr,Mo)-type σ phase and a Cr-rich $M_{23}C_6$-type carbide were identified to precipitate in the F91/S21 interfacial layer during aging through the complementary characterization methods. By studying the growth kinetics, this interfacial layer was found to follow a parabolic rate of growth. Its activation energy was determined, which may be related to carbon diffusion. Due to the presence of the hard σ phase and $M_{23}C_6$ carbides, this interfacial layer is harder than the S21 and the F91 materials. More $M_{23}C_6$ carbides were observed with aging temperature and time. Nevertheless, lesser amount of the σ phase was found to precipitate at higher temperatures.

This interfacial layer formed during aging provides a brittle crack propagation pathway using high-strain rate impact testing for all the aged S21 hardfacing components. The impact energy decreases significantly with aging time and temperature. The aged S21 hardfacing specimens present brittle fracture, whereas the as-tempered S21 hardfacing specimens show ductile fracture. The formation of hard and brittle $M_{23}C_6$ carbides in the interfacial layer is mainly responsible for

the impact energy loss. In addition, the presence of the σ phase would also lead to the toughness degradation. Thus, we conclude that the hard and brittle $M_{23}C_6$ carbides and σ phase are the microstructural factors contributing to the delamination of high-temperature valves in service.

Evaluation of the IN82 hardfacing components

The F91/IN82 interface was found to be microstructurally much more stable than the F91/S21 interface after aging at 650 °C for 8760 h. Though the hard interfacial layer does not grow along the F91/IN82 interface as the S21 hardfacing components do, an interfacial band was observed. This band, neither softened nor hardened, is identified as part of the F91 steel through the complementary characterization methods. Though some discrete $M_{23}C_6$ carbides precipitate along this band, they do not contribute to embrittle the IN82 hardfacing components during the impact testing. The impact energy loss is associated with coarsening and precipitation of the intergranular/interdendritic carbides in the IN82 bulk material during aging, which is much less significant than that of the S21 components. We conclude that the IN82 buffer layer is a good alternative to replace the problematic S21 buffer layer, enhancing the durability of the S6 hardfacing components.

Evaluation of the IN625 hardfacing components

Compared with the F91/IN82 interface, some white precipitates (possibly M_6C) were observed close to the F91/IN625 interface during aging at 650 °C for 8760 h. Moreover, the rod-like precipitates (possibly Ni_3Nb), M_6C and Nb(C,N) carbides were observed in the IN625 bulk material, leading to the hardening of IN625 bulk material with temperature and time. The F91/IN625 interface was found not to be the weakest link under the monotonic normal stress for the studied tensile specimens. However, some Charpy specimens were found to fail along the F91/IN625 interface during the impact testing, which may be caused by the precipitates close to the F91/IN625 interface. For other specimens, the fracture was found to occur in the IN625 bulk material, which may be caused by the precipitates in the IN625 bulk material. The impact energy loss of IN625 specimens reached as high as 88% after aging at 650 °C for 8760 h. Therefore, the IN625 alloy is not recommended to be used as a buffer layer deposited between the creep-resistant steel and the S6 alloy.

Examination of an ex-service component

The examination of an ex-service component validates our laboratory study. At service temperatures, large amounts of σ phase precipitate along grain boundaries in S21 after long-term service. Thus, the hard σ phase is distributed deeply into the S21 bulk material. It acts as an easy delamination crack propagation pathway in the S21 bulk material. By extrapolating the diameter of the $M_{23}C_6$ carbides of this ex-service component, the equivalent service time and temperature obtained are in accordance with the operation time and temperature.

12.2 Perspectives

After the main conclusions, further ideas and interests in the research on Stellite hardfacing are proposed. As stated in the conclusions, the hardness of S6 deposited on the IN82 buffer layer decreases due to higher Fe and Ni dilution, which could compromise the wear resistance. It is proposed that more layers of S6 can be deposited to mitigate this downside. However, this may introduce more work and some changes to the manufacturing procedures when depositing more layers of S6. Therefore, we propose to carry out a comparative study on the wear properties of S6 deposited over the IN82 and S21 buffer layers. Then, appropriate measures will be taken in accordance with applications. The PTA welding parameters used during the manufacturing process such as current and heat input may also affect the dilution of deposited layer. Thus, process optimization could also be considered to reduce the dilution levels.

In addition to the IN82 buffer layer, nickel-based alloys such as EPRI P87 and Inco Weld A are also recommended by EPRI due to their stability over over a range of alloy combinations based on thermodynamic simulations [41]. However, as discussed in chapter 8, the decrease in S6 microhardness correlates with an increase in Fe content. EPRI P87 and Inco Weld A alloys contain around 40% and 12% Fe respectively [41], while IN82 only contains 0.06% Fe as shown in Table 8.1. Thus, when applying EPRI P87 or Inco Weld A as a buffer layer between the base material and the cobalt-based hardfacing alloy, it is expected that much higher Fe would dilute to the cobalt-based alloy such as S6. Consequently, the higher Fe content would deteriorate the wear resistance of S6 to a greater extent. This factor should be taken into account when choosing the two buffer layers.

As described in chapter 10, the vein-like features observed in our laboratory S21 hardfacing samples aged for 8760 h were not as notable as those observed in the ex-service component after operation of 6 years. We have some hardfacing samples aged for 30000 h (not within this PhD

work). It would be interesting to characterize the microstructure in the future further to validate the expected diffusion behavior. That is, the vein-like features are expected to extend more deeply into the S21 than those in the samples aged for 8760 h.

REFERENCES

[1] (July 3, 2019). *Sources of greenhouse gas emissions*. Available: https://www.epa.gov/ghgemissions/sources-greenhouse-gas-emissions

[2] N. S. Stoloff, "Wrought and P/M superalloys," in *ASM Handbook, Volume 01 - Properties and Selection: Irons, Steels, and High-Performance Alloys*: ASM International, 1990, pp. 962-968.

[3] D. Purdy, "Experiences in valve hardfacing disbonding," Electric Power Research Institute, Palo Alto, California, April 2015.

[4] T. Lolla, J. Siefert, S. S. Babu, and D. Gandy, "Delamination failures of Stellite hardfacing in power plants: a microstructural characterisation study," *Science and Technology of Welding and Joining*, vol. 19 (6), pp. 476-486, 2014.

[5] (Aug. 7, 2013). headsUP: Stellite delamination in HP, HRH steam valves. *Combined Cycle Journal*. Available: http://www.ccj-online.com/headsup-stellite-delamination-in-hp-hrh-steam-valves/

[6] K. Bezzant. (August 7, 2013) Inspect steam valves for stellite delamination. *Combined Cycle Journal*. 106-113. Available: http://www.ccj-online.com/1q-2013/steam-valves/

[7] R. C. Tucker Jr, "Comparison of Major Coating Methods," in *ASM Handbook, Volume 05A - Thermal Spray Technology*: ASM International, p. 28.

[8] R. Shanmugam and N. Murugan, "Effect of gas tungsten arc welding process variables on dilution and bead geometry of Stellite 6 hardfaced valve seat rings," *Surface Engineering*, vol. 22 (5), pp. 375-383, 2006.

[9] R. C. Tucker Jr, "Comparison of Major Coating Methods," in *ASM Handbook, Volume 05A - Thermal Spray Technology*: ASM International, p. 29.

[10] K. Marimuthu and N. Murugan, "Sensitivity analysis of process parameters in PTA hardfacing of valve seats using response surface methodology," *Materials Science and Technology*, vol. 21 (8), pp. 941-947, 2005.

[11] K. Marimuthu and N. Murugan, "Prediction and Optimisation of Weld Bead Geometry of Plasma Transferred Arc Hardfaced Valve Seat Rings," *Surface Engineering*, vol. 19 (2), pp. 143-149, 2003.

[12] S.-Y. Tu, M.-D. Jean, J.-T. Wang, and C.-S. Wu, ""A robust design in hardfacing using a plasma transfer arc," *The International Journal of Advanced Manufacturing Technology*, vol. 27 (9-10), pp. 889-896, 2006.

[13] E. H. Takano, D. de Queiroz, and A. S. C. M. D'Oliveira, "Evaluation of processing parameters on PTA hardfacing surfaces," *Welding International*, vol. 24 (3), pp. 241-248, 2010.

[14] R. R. Bharath, R. Ramanathan, B. Sundararajan, and P. B. Srinivasan, "Optimization of process parameters for deposition of Stellite on X45CrSi93 steel by plasma transferred arc technique," *Materials & Design*, vol. 29 (9), pp. 1725-1731, 2008.

[15] A. S. C. M. D'Oliveira, R. S. C. Paredes, and R. L. C. Santos, "Pulsed current plasma transferred arc hardfacing," *Journal of Materials Processing Technology*, vol. 171 (2), pp. 167-174, 2006.

[16] J. R. Davis, "Hardfacing, weld cladding, and dissimilar metal joining," in *ASM Handbook, Volume 06 - Welding, Brazing, and Soldering*: ASM International, 1993, p. 802.

[17] J. R. Davis, "Hardfacing, weld cladding, and dissimilar metal joining," in *ASM Handbook, Volume 06 - Welding, Brazing, and Soldering*: ASM International, 1993, pp. 796-800.

[18] J. R. Davis, "Hardfacing, weld cladding, and dissimilar metal joining," in *ASM Handbook, Volume 06 - Welding, Brazing, and Soldering*: ASM International, 1993, pp. 789-796.

[19] (May 6, 2019). *Kennametal*. Available: http://www.stellite.com/content/dam/kennametal/kennametal/common/Resources/Catalogs-Literature/Stellite/B-18-05723_KMT_Stellite_Alloys_Brochure_Direct_update_LR.pdf

[20] (May 7, 2019). *Kennametal*. Available: http://www.interweld.com.au/images/Stellite%20Alloys%20Brochure.pdf

[21] (May 8, 2019). *Special metals*. Available: http://www.specialmetals.com/divisions/welding-products/products/tradenames/inconel.html

[22] Y. Wu, T. Schmitt, E. Bousser, F. Khelfaoui, V. Najarian, J.-E. Klemberg-Sapieha, *et al.*, "Effect of interfacial microstructure on mechanical properties of cobalt-based hardfacing during long-term aging," *Submitted*.

[23] M. Alimardani, V. Fallah, A. Khajepour, and E. Toyserkani, "The effect of localized dynamic surface preheating in laser cladding of Stellite 1," *Surface and Coatings Technology*, vol. 204 (23), pp. 3911-3919, 2010.

[24] H.-X. Deng, H.-J. Shi, S. Tsuruoka, H.-C. Yu, and B. Zhong, "Influence of Heat Treatment on Characteristic Behavior of Co-Based Alloy Hardfacing Coatings Deposited by Plasma Transferred Arc Welding," *Key Engineering Materials* vol. 462 - 463, pp. 593-598, 2011.

[25] R. L. Klueh, "Elevated-Temperature Ferritic and Martensitic Steels and their Application to Future Nuclear Reactors," Oak Ridge National Laboratoy ORNL/TM-2004/176, 2004.

[26] W. Bendick, L. Cipolla, J. Gabrel, and J. Hald, "New ECCC assessment of creep rupture strength for steel grade X10CrMoVNb9-1 (Grade 91)," *International Journal of Pressure Vessels and Piping*, vol. 87 (6), pp. 304-309, 2010.

[27] M. K. Booker, V. K. Sikka, and B. L. P. Booker, "COMPARISON OF THE MECHANICAL STRENGTH PROPERTIES OF SEVERAL HIGH-CHROMIUM FERRITIC STEELS," in *Ferritic Steels for High-Temperature Applications, Proceedings of an ASM International Conference on Production, Fabrication, Properties and Application.*, Warren, PA, USA, 1983, pp. 257-273.

[28] J. P. Dobson. (2006, October 12, 2017) Why new U.S. supercritical units should consider T/P92 piping. *Power*. Available: https://www.powermag.com/why-new-u-s-supercritical-units-should-consider-tp92-piping/

[29] P. J. Ennis and A. Czyrska-Filemonowicz, "Recent advances in creep-resistant steels for power plant applications," *Sadhana*, vol. 28 (3-4), pp. 709-730, 2003.

[30] "A335/A335M-11 Standard Specification for Seamless Ferritic Alloy-Steel Pipe for High-Temperature Service," West Conshohocken, PA, United States: ASTM International.

[31] F. Abe, "Effect of boron on creep deformation behavior and microstructure evolution in 9 % Cr steel at 650C," *International Journal of Materials Research,* vol. 99 (4), pp. 387-94, 2008.

[32] I. Holzer, "Modelling and Simulation of Strengthening in Complex Martensitic 9-12% Cr Steel and a Binary Fe-Cu Alloy," Doctor, Graz University of Technology, 2010.

[33] A. Aghajani, F. Richter, C. Somsen, S. G. Fries, I. Steinbach, and G. Eggeler, "On the formation and growth of Mo-rich Laves phase particles during long-term creep of a 12% chromium tempered martensite ferritic steel," *Scripta Materialia,* vol. 61 (11), pp. 1068-1071, 2009.

[34] L. Cipolla, "Conversion of MX Nitrides to Modified Z-phase in 9-12%Cr Ferritic Steels," Technical University of Denmark Kongens Lyngby, 2010.

[35] L. Cipolla, A. Di Gianfrancesco, D. Venditti, G. Cumino, and S. Caminada, "Microstructural evolution during long term creep tests of 9%Cr steel grades," in *2007 ASME Pressure Vessels and Piping Conference - 8th International Conference on Creep and Fatigue at Elevated Temperatures, PVP-2007/CREEP8, July 22, 2007 - July 26, 2007*, San Antonio, TX, United states, 2008, pp. 445-459.

[36] H. K. Danielsen and J. Hald, "Behaviour of Z phase in 9-12%Cr steels," *Energy Materials,* vol. 1 (1), pp. 49-57, 2006.

[37] D. R. Jara, "9-12% Cr heat resistant steels: alloy design, TEM characterisation of microstructure evolution and creep response at 650°C " Doctor, Ruhr University Bochum, Bochum, 2011.

[38] J. H. Hattel, "Integrated multiphysics modeling in materials and manufacturing processes," *International Review of Chemical Engineering,* vol. 2 (1), pp. 52-62, 2010.

[39] C. Leinenbach, A. Al-Badri, and M. Roth, "Interface microstructure of Stellite-6 coatings on a 12%Cr steel after long term thermal exposure," *Materials Science & Engineering Technology,* vol. 41 (10), pp. 861-868, 2010.

[40] D. Purdy, "Proposed solutions for hardfacing disbonding in high-temperature valves," Electric Power Research Institute, Palo Alto, California, December 2015.

[41] D. Purdy, "Guidelines and specifications for high-reliability fossil power plants," Electric Power Research Institute, Palo Alto, California, March 2015.

[42] G. Chakraborty, C. R. Das, S. K. Albert, A. K. Bhaduri, S. Murugesan, and A. Dasgupta, "Effect of Alloy 625 Buffer Layer on Hardfacing of Modified 9Cr-1Mo Steel Using Nickel Base Hardfacing Alloy," *Journal of Materials Engineering and Performance,* vol. 25 (4), pp. 1663-1672, 2016.

[43] "ASTM A182/A182M-18 Standard Specification for Forged or Rolled Alloy and Stainless Steel Pipe Flanges, Forged Fittings, and Valves and Parts for High-Temperature Service," West Conshohocken, Pennsylvania: ASTM International, 2018.

[44] "ASTM E23-16b Standard Test Methods for Notched Bar Impact Testing of Metallic Materials," West Conshohocken, Pennsylvania: ASTM International, 2016.

[45] "ASTM E8/E8M-16a Standard Test Methods for Tension Testing of Metallic Materials," West Conshohocken, Pennsylvania: ASTM International, 2016.

[46] W. C. Oliver and G. M. Pharr, "An improved technique for determining hardness and elastic modulus using load and displacement sensing indentation experiments," *Journal of Materials Research,* vol. 7 (06), pp. 1564-1583, 1992.

[47] A. C. Fischer-Cripps, *Nanoindentation*: Springer New York, 2011.

[48] "ISO 14577-1:2002 Metallic materials -- Instrumented indentation test for hardness and materials parameters -- Part 1: Test method," Geneva: International Organization for Standardization, 2002.

[49] A. J. Schwartz, M. Kumar, B. L. Adams, and D. P. Field, *Electron backscatter diffraction in materials science*: Springer US, 2009.

[50] M. T. Hutchings, P. J. Withers, T. M. Holden, and T. Lorentzen, *Introduction to the characterization of residual stress by neutron diffraction*. Boca Raton: CRC press, 2005.

[51] P. Mayr, "Evolution of microstructure and mechanical properties of the heat affected zone in B-containing 9% chromium steels," Doctor, Graz University of Technology, Graz, 2007.

[52] S. Sulaiman, "Structure of properties of the heat affected zone of P91 creep resistant steel," PhD, University of Wollongong, 2007.

[53] R. L. Klueh, "Elevated temperature ferritic and martensitic steels and their application to future nuclear reactors," *International Materials Reviews,* vol. 50 (5), pp. 287-310, 2005.

[54] R. L. Klueh and A. T. Nelson, "Ferritic/martensitic steels for next-generation reactors," *Journal of Nuclear Materials,* vol. 371 (1-3), pp. 37-52, 2007.

[55] Y. Birol, "High temperature sliding wear behaviour of Inconel 617 and Stellite 6 alloys," *Wear,* vol. 269 (9-10), pp. 664-671, 2010.

[56] A. V. Narlikar, *Superconductors*: OUP Oxford, 2014.

[57] T. Ohmura, K. Tsuzaki, K. Sawada, and K. Kimura, "Inhomogeneous nano-mechanical properties in the multi-phase microstructure of long-term aged type 316 stainless steel," *Journal of Materials Research,* vol. 21 (5), pp. 1229-1236, 2006.

[58] L. Xu, D. Zhang, Y. Liu, B. Ning, Z. Qiao, Z. Yan, *et al.*, "Precipitation kinetics of $M_{23}C_6$ in T/P92 heat-resistant steel by applying soft-impingement correction," *Journal of Materials Research,* vol. 28 (11), pp. 1529-1537, 2013.

[59] W. F. Hosford, *Physical Metallurgy, Second Edition*: Taylor & Francis, 2010.

[60] H. U. Rehman, "Solid Solution Strengthening and Diffusion in Nickel- and Cobalt-based Superalloys," Doctoral dissertation, Friedrich-Alexander-University of Erlangen-Nürnberg, 2016.

[61] T. Ustad and H. Sørum, "Interdiffusion in the Fe-Ni, Ni-Co, and Fe-Co systems," *Physica Status Solidi (a),* vol. 20 (1), pp. 285-294, 1973.

[62] A. M. Brown and M. F. Ashby, "Correlations for diffusion constants," *Acta Metallurgica,* vol. 28 (8), pp. 1085-1101, 1980.

[63] Y. Iijima, F. Makuta, R. P. Agarwala, and K. Hirano, "Diffusion of Carbon in Cobalt," *Materials Transactions Jim,* vol. 30 (12), pp. 984-990, 1989.

[64] B. Li, Q. Zhang, L. Chen, P. Cui, and X. Pan, "Vacancy-mediated diffusion of carbon in cobalt and its influence on CO activation," *Physical Chemistry Chemical Physics,* vol. 12 (28), pp. 7848-55, 2010.

[65] F. Johnson, P. Hughes, R. Gallagher, D. E. Laughlin, M. E. McHenry, M. A. Willard, *et al.*, "Structure and thermomagnetic properties of new FeCo-based nanocrystalline ferromagnets," *IEEE Transactions on Magnetics,* vol. 37 (4), pp. 2261-2263, 2001.

[66] R. H. Yu, S. Basu, Y. Zhang, A. Parvizi-Majidi, and J. Q. Xiao, "Pinning effect of the grain boundaries on magnetic domain wall in FeCo-based magnetic alloys," *Journal of Applied Physics,* vol. 85 (9), pp. 6655-6659, 1999.

[67] J. W. Elmer, T. A. Palmer, and E. D. Specht, "Direct observations of sigma phase formation in duplex stainless steels using in-situ synchrotron X-ray diffraction," *Metallurgical and Materials Transactions a-Physical Metallurgy and Materials Science,* vol. 38a (3), pp. 464-475, 2007.

[68] R. Magnabosco, "Kinetics of Sigma Phase Formation In a Duplex Stainless Steel," *Materials Research-Ibero-American Journal of Materials,* vol. 12 (3), pp. 321-327, 2009.

[69] F. B. Waanders, S. W. Vorster, and H. Pollak, "The influence of temperature on σ-phase formation and the resulting hardening of Fe–Cr–Mo-alloys," *Hyperfine Interactions,* vol. 120/121 (1/8), pp. 751-755, 1999.

[70] T. Yamada, K. Miura, M. Kajihara, N. Kurokawa, and K. Sakamoto, "Kinetics of reactive diffusion between Au and Sn during annealing at solid-state temperatures," *Materials Science and Engineering: A,* vol. 390 (1), pp. 118-126, 2005.

[71] S. Sasaki and M. Kajihara, "Reactive diffusion between Ag-5Pt alloy and Sn at solid-state temperatures," *Materials Transactions,* vol. 48 (10), pp. 2642-9, 2007.

[72] P. Heitjans and J. Karger, *Diffusion in condensed matter: Methods, materials, models*: Springer Berlin Heidelberg, 2005.

[73] R. J. Gray, V. K. Sikka, and R. T. King, "Detecting transformation of delta-ferrite to sigma-phase in stainless steels by advanced metallographic techniques," *Journal of Metals,* vol. 30 (11), pp. 18-26, 1978.

[74] D. M. E. Villanueva, F. C. P. Junior, R. L. Plaut, and A. F. Padilha, "Comparative study on sigma phase precipitation of three types of stainless steels: austenitic, superferritic and duplex," *Materials Science and Technology,* vol. 22 (9), pp. 1098-1104, 2006.

[75] F. B. Waanders and S. W. Vorster, "The Influence of Mo on the Formation of the σ-Phase in Fe-Cr Alloys," *Hyperfine Interactions,* vol. 112 (1/4), pp. 139-142, 1998.

[76] G. Sasikala, S. K. Ray, and S. L. Mannan, "Kinetics of transformation of delta ferrite during creep in a type 316(N) stainless steel weld metal," *Materials Science and Engineering a-Structural Materials Properties Microstructure and Processing,* vol. 359 (1-2), pp. 86-90, 2003.

[77] C. Lee, S. Roh, C. Lee, and S. Hong, "Influence of Si on sigma phase precipitation and pitting corrosion in superaustenitic stainless steel weld metal," *Materials Chemistry and Physics,* vol. 207, pp. 91-97, 2018.

[78] A. K. Sinha, "Topologically close-packed structures of transition metal alloys," *Progress in Materials Science,* vol. 15 (2), pp. 81-185, 1972.

[79] J. A. Lee, I. Kim, and A. Kimura, "Application of small punch test to evaluate sigma-phase embrittlement of pressure vessel cladding material," *Journal of Nuclear Science and Technology,* vol. 40 (9), pp. 664-671, 2003.

[80] M. Pohl, O. Storz, and T. Glogowski, "Effect of intermetallic precipitations on the properties of duplex stainless steel," *Materials Characterization,* vol. 58 (1), pp. 65-71, 2007.

[81] N. Lopez, M. Cid, and M. Puiggali, "Influence of σ-phase on mechanical properties and corrosion resistance of duplex stainless steels," *Corrosion Science,* vol. 41 (8), pp. 1615-1631, 1999.

[82] I. Radu, D. Y. Li, and R. Llewellyn, "Tribological behavior of Stellite 21 modified with yttrium," *Wear,* vol. 257 (11), pp. 1154-1166, 2004.

[83] A. Gholipour, M. Shamanian, and F. Ashrafizadeh, "Microstructure and wear behavior of stellite 6 cladding on 17-4 PH stainless steel," *Journal of Alloys and Compounds,* vol. 509 (14), pp. 4905-4909, 2011.

[84] K. Maruyama, K. Sawada, and J. Koike, "Strengthening mechanisms of creep resistant tempered martensitic steel," *ISIJ International,* vol. 41 (6), pp. 641-653, 2001.

[85] F. Abe, "Precipitate design for creep strengthening of 9% Cr tempered martensitic steel for ultra-supercritical power plants," *Science and Technology of Advanced Materials,* vol. 9 (1), pp. 1-15, 2008.

[86] F. Abe, "Analysis of creep rates of tempered martensitic 9%Cr steel based on microstructure evolution," *Materials Science and Engineering: A,* vol. 510-11 (0), pp. 64-69, 2009.

[87] K. Guguloth and N. Roy, "Creep deformation behavior of 9Cr1MoVNb (ASME Grade 91) steel," *Materials Science and Engineering: A,* vol. 680, pp. 388-404, 2017.

[88] L. Zheng, X. Hu, X. Kang, and D. Li, "Precipitation of $M_{23}C_6$ and its effect on tensile properties of 0.3C–20Cr–11Mn–1Mo–0.35N steel," *Materials & Design,* vol. 78 (Supplement C), pp. 42-50, 2015.

[89] T. Lee, Y.-J. Lee, S.-H. Joo, H. Nersisyan, K.-T. Park, and J. H. Lee, *Intergranular $M_{23}C_6$ Carbide Precipitation Behavior and Its Effect on Mechanical Properties of Inconel 690 Tubes* vol. 46, 2015.

[90] L. J. Wang, L. Y. Sheng, and C. M. Hong, "Influence of grain boundary carbides on mechanical properties of high nitrogen austenitic stainless steel," *Materials & Design,* vol. 37 (Supplement C), pp. 349-355, 2012.

[91] L. Z. He, Q. Zheng, X. F. Sun, G. C. Hou, H. R. Guan, and Z. Q. Hu, "$M_{23}C_6$ precipitation behavior in a Ni-base superalloy M963," *Journal of Materials Science,* vol. 40 (11), pp. 2959-2964, 2005.

[92] Å. Gustafson and M. Hättestrand, "Coarsening of precipitates in an advanced creep resistant 9% chromium steel—quantitative microscopy and simulations," *Materials Science and Engineering: A,* vol. 333 (1-2), pp. 279-286, 2002.

[93] J. R. Davis, "Hardfacing, weld cladding, and dissimilar metal joining," in *ASM Handbook, Volume 06 - Welding, Brazing, and Soldering*: ASM International, 1993, pp. 789-829.

[94] Y. Wu, E. Bousser, T. Schmitt, N. Tarfa, F. Khelfaoui, R. René, *et al.*, "Thermal stability of a Stellite/steel hardfacing interface during long-term aging," *Materials Characterization,* vol. 154, pp. 181-192, 2019.

[95] C. M. Hong, J. Shi, L. Y. Sheng, W. C. Cao, W. J. Hui, and H. Dong, "Effects of hot-working parameters on microstructural evolution of high nitrogen austenitic stainless steel," *Materials & Design,* vol. 32 (7), pp. 3711-3717, 2011.

[96] V. Fallah, M. Alimardani, S. F. Corbin, and A. Khajepour, "Impact of localized surface preheating on the microstructure and crack formation in laser direct deposition of Stellite 1 on AISI 4340 steel," *Applied Surface Science,* vol. 257 (5), pp. 1716-1723, 2010.

[97] L. Wei, W. Hao, Y. Cheng, and S. Tan, "Isothermal aging embrittlement in an Fe-22Cr-25Ni alloy," *Materials Science and Engineering: A,* vol. 737, pp. 40-46, 2018.

[98] O. H. Ibrahim, I. S. Ibrahim, and T. A. F. Khalifa, "Effect of Aging on the Toughness of Austenitic and Duplex Stainless Steel Weldments," *Journal of Materials Science & Technology,* vol. 26 (9), pp. 810-816, 2010.

[99] "ASTM C633 Standard Test Method for Adhesion or Cohesion Strength of Thermal Spray Coatings," West Conshohocken, PA: ASTM International, 2017.

[100] B. Peng, H. Zhang, J. Hong, J. Gao, Q. Wang, and H. Zhang, "Effect of aging on the impact toughness of 25Cr–20Ni–Nb–N steel," *Materials Science and Engineering: A,* vol. 527 (7), pp. 1957-1961, 2010.

[101] C. Jang, J. Lee, J. Sung Kim, and T. Eun Jin, "Mechanical property variation within Inconel 82/182 dissimilar metal weld between low alloy steel and 316 stainless steel," *International Journal of Pressure Vessels and Piping,* vol. 85 (9), pp. 635-646, 2008.

[102] R. D. Nicholson, "Effect of aging on interfacial structures of nickel-based transition joints," *Metals Technology,* vol. 11 (1), pp. 115-124, 1984.

[103] K. Laha, K. S. Chandravathi, P. Parameswaran, S. Goyal, and M. D. Mathew, "A Comparison of Creep Rupture Strength of Ferritic/Austenitic Dissimilar Weld Joints of Different Grades of Cr-Mo Ferritic Steels," *Metallurgical and Materials Transactions A,* vol. 43 (4), pp. 1174-1186, 2012.

[104] V. K. Sikka, "Development of modified 9 Cr-1 Mo steel for elevated-temperature service," in *Proceedings of Topical Conference on Ferritic Alloys for Use in Nuclear Energy Technologies.*, Snowbird, UT, USA, 1984, pp. 317-327.

[105] G. R. Mirshekari, S. Daee, S. F. Bonabi, M. R. Tavakoli, A. Shafyei, and M. Safaei, "Effect of interlayers on the microstructure and wear resistance of Stellite 6 coatings deposited on

AISI 420 stainless steel by GTAW technique," *Surfaces and Interfaces*, vol. 9, pp. 79-92, 2017.

[106] J. C. Shin, J. M. Doh, J. K. Yoon, D. Y. Lee, and J. S. Kim, "Effect of molybdenum on the microstructure and wear resistance of cobalt-base Stellite hardfacing alloys," *Surface & Coatings Technology*, vol. 166 (2-3), pp. 117-126, 2003.

[107] M. A. Shaikh, M. Ahmad, K. A. Shoaib, J. I. Akhter, and M. Iqbal, "Precipitation hardening in Inconel* 625," *Materials Science and Technology*, vol. 16 (2), pp. 129-132, 2000.

[108] J. W. G. Clark, "Investigating chemical and microstructural evolution at dissimilar metal welds " Doctor University of Nottingham, 2015.

APPENDIX A – DRAWING OF A POCKET MACHINED FROM THE SAMPLE

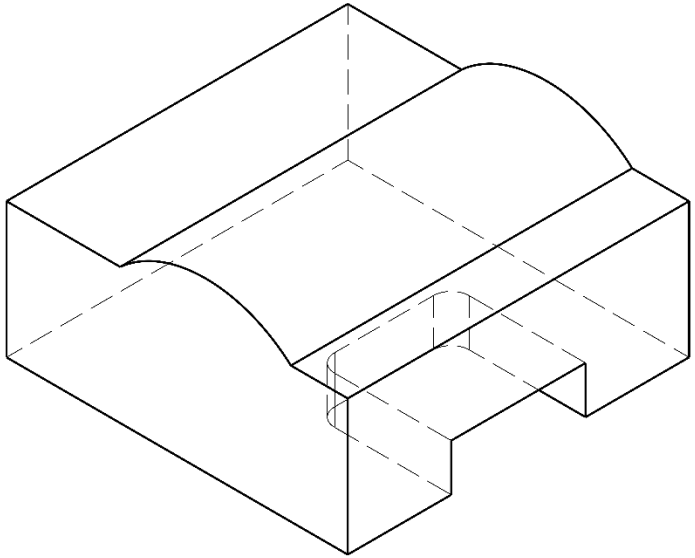

Isometric view
Scale: 1:1

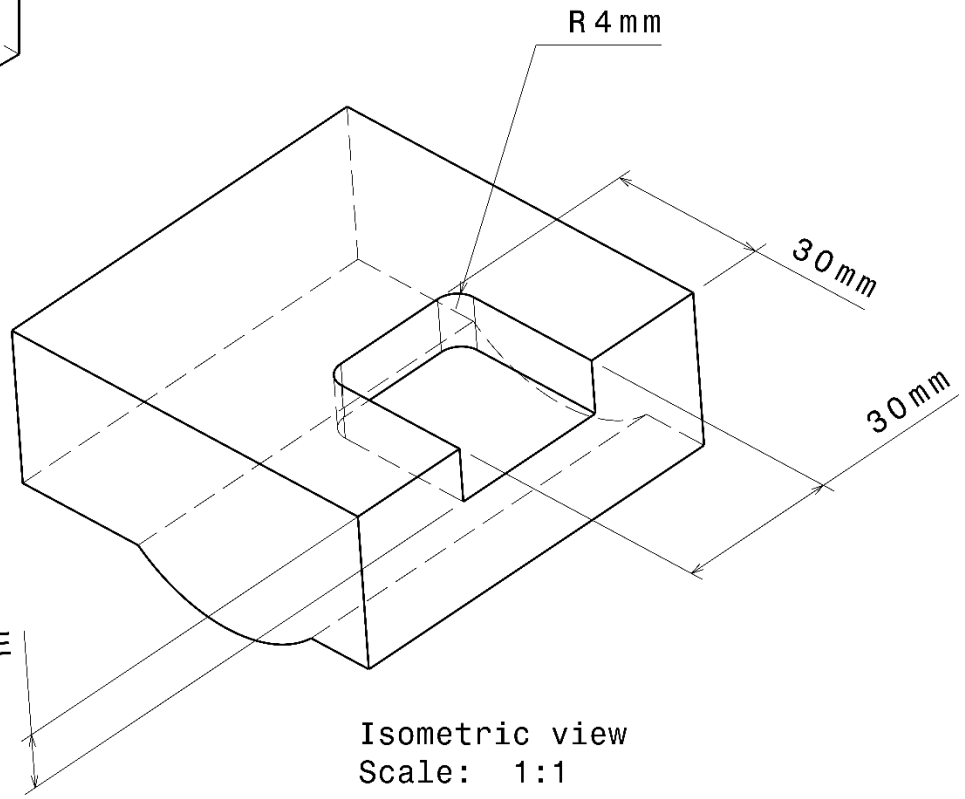

Isometric view
Scale: 1:1

NOTES:

POCKET TO BE CENTERED
TOP DEPOSIT TO GROOVE BOTTOM = 27mm

APPENDIX B – DRAWINGS OF REFERENCE SAMPLES

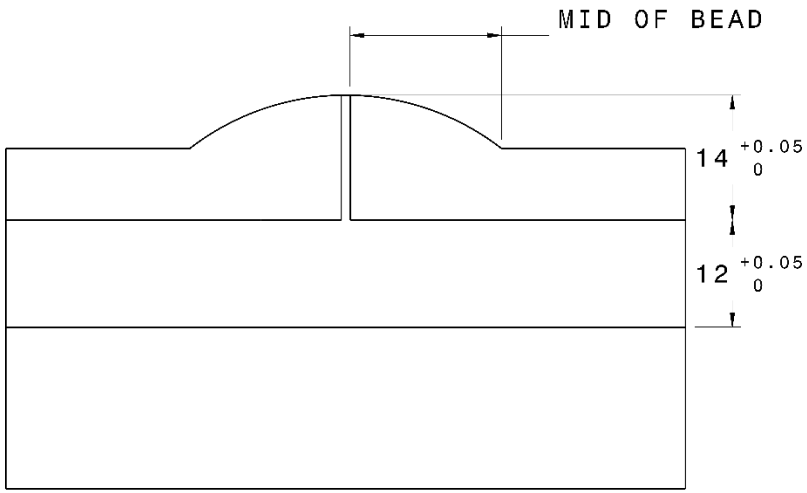

Front view
Scale: 2:1

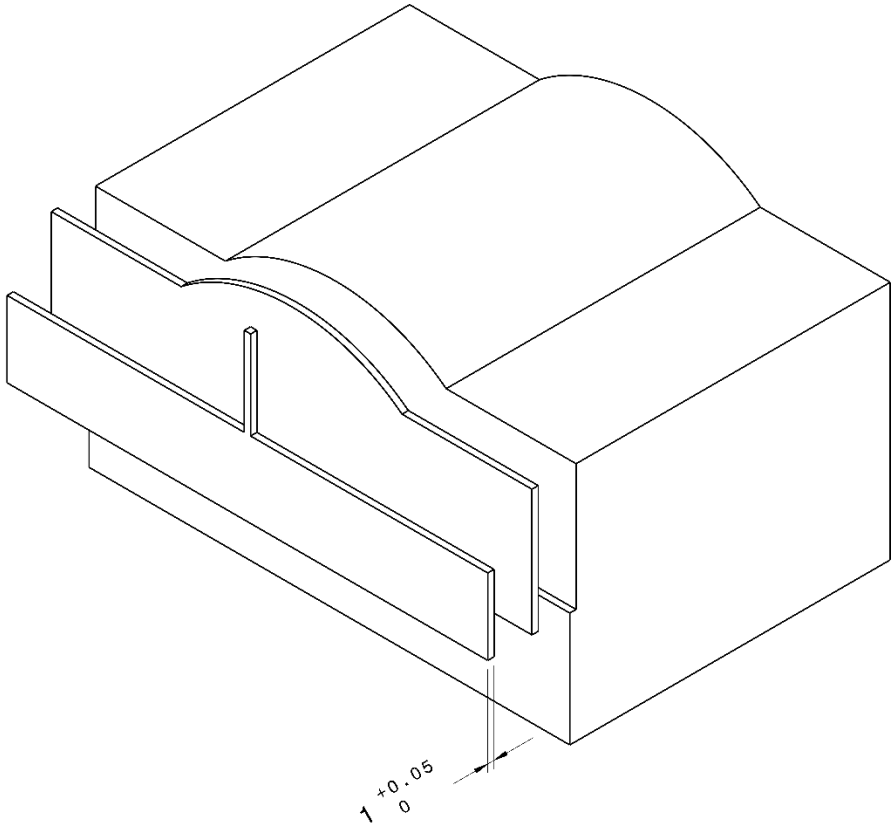

Isometric view
Scale: 2:1

NOTES:

ALL DIMENSION ARE MM

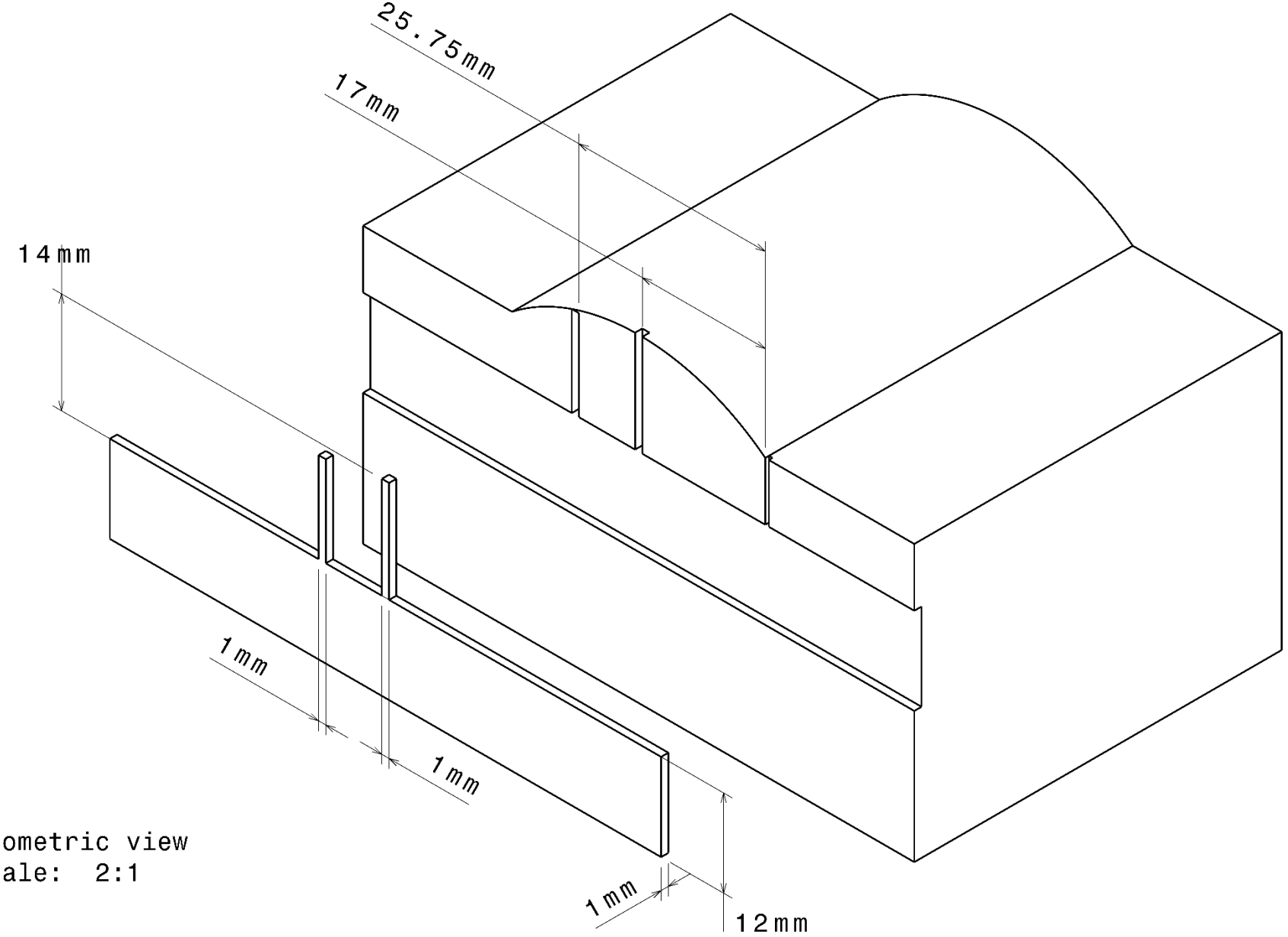

Isometric view
Scale: 2:1

APPENDIX C – DRAWINGS OF THE ASSEMBLIES

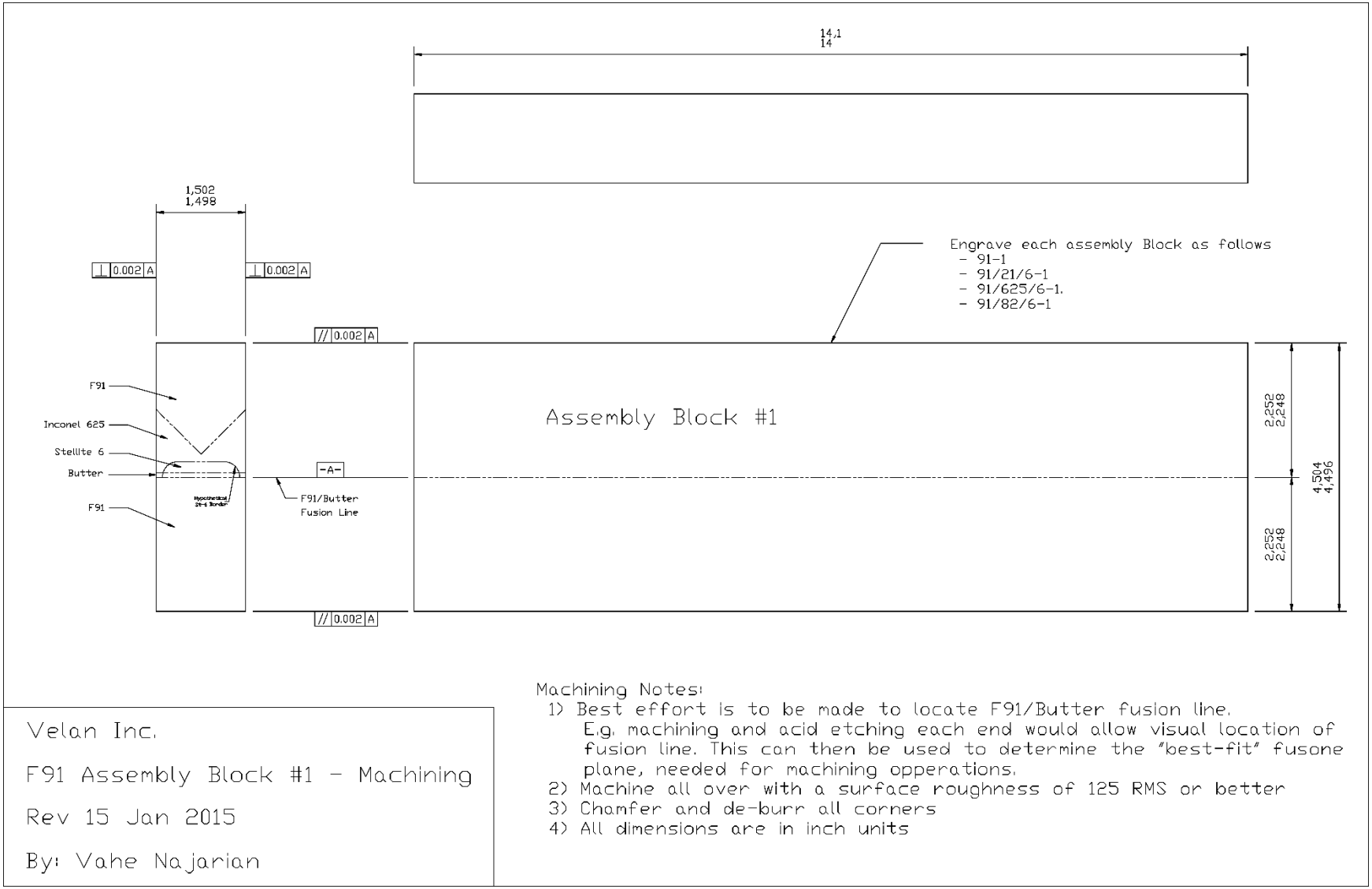

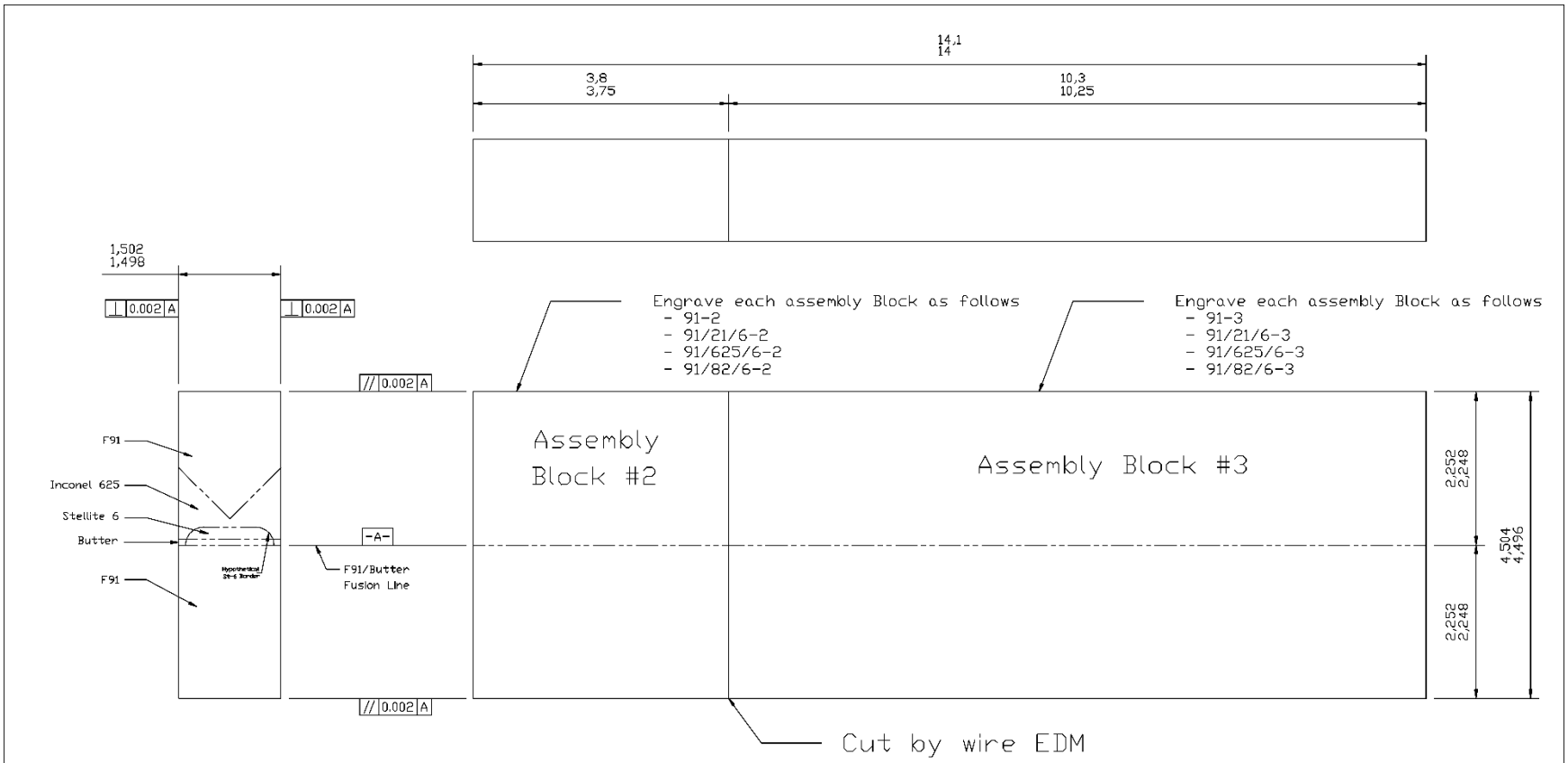

Velan Inc.

F91 Assembly Block #2&3 - Machining

Rev 15 Jan 2015

By: Vahe Najarian

Machining Notes:

1) Best effort is to be made to locate F91/Butter fusion line. E.g. machining and acid etching each end would allow visual location of fusion line. This can then be used to determine the "best-fit" fusone plane, needed for machining opperations.
2) Machine all over with a surface roughness of 125 RMS or better
3) Chamfer and de-burr all corners
4) All dimensions are in inch units

APPENDIX D – DRAWING OF THE CHARPY U-NOTCH SPECIMEN

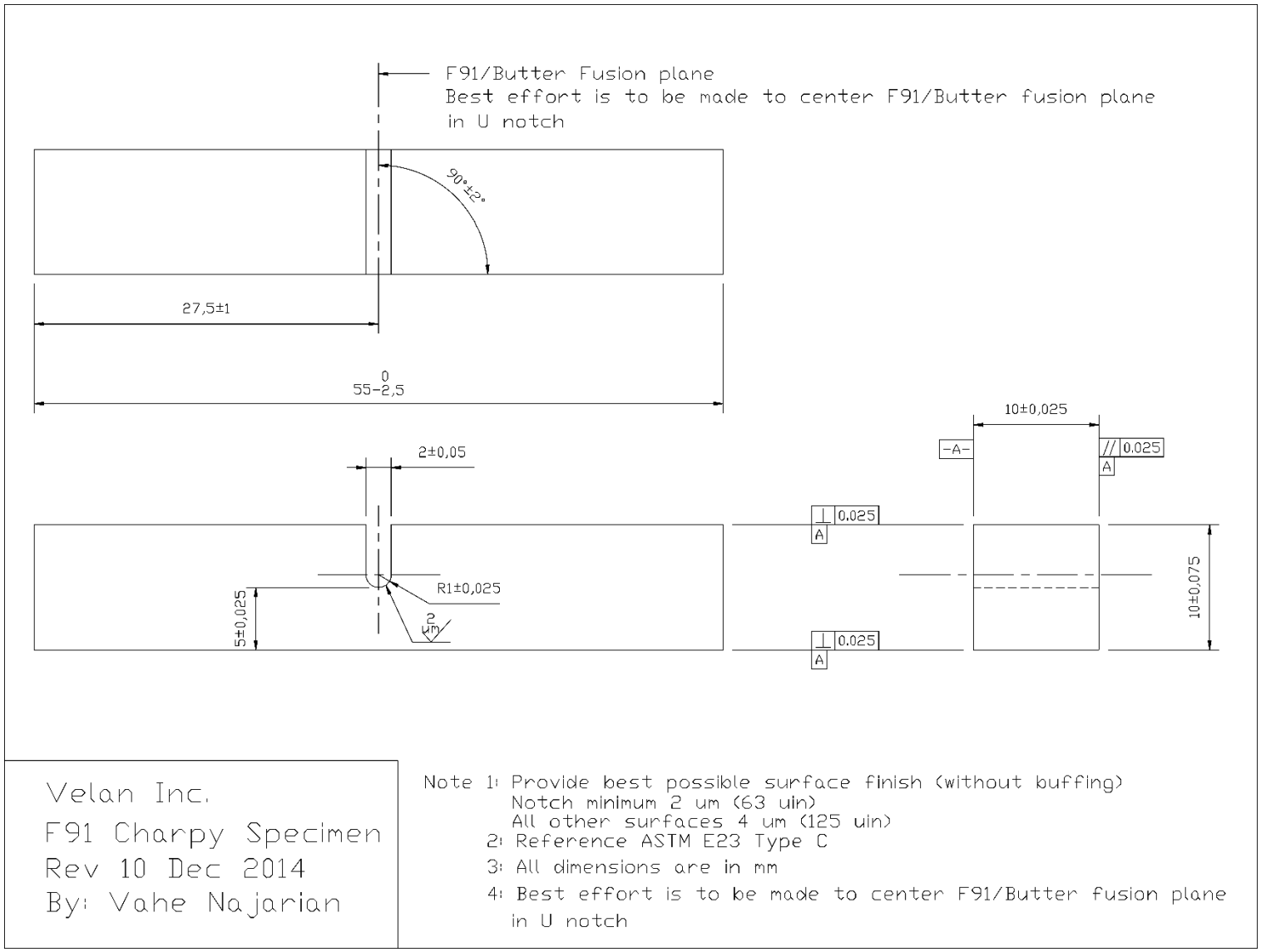

APPENDIX E – DRAWINGS OF THE TENSILE SPECIMENS

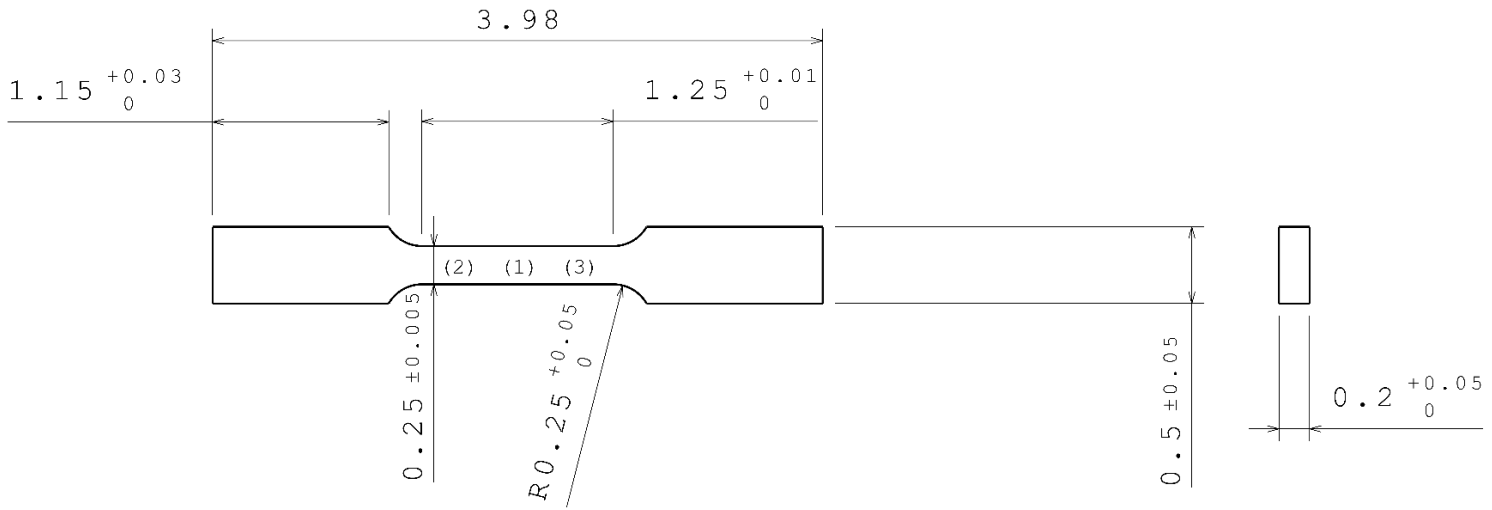

ALL THE DIMENSIONS ARE IN INCHES

- All the surface finish must be at 63µin or better.

- The ends of the reduced section,(2) & (3), must not differ by more than 0.001in.

- There may be a decrease in the width from the ends, (2) & (3), to the center (1), but the width at each end, (2) & (3), shall not be more than 1% larger than the width at the center (1).

- The reduced sections of prepared specimens should be free of cold work, notches, chatter marks, grooves, gouges, burrs, rough surfaces or edges, overheating.

ECOLE POLYTECHNIQUE	
Tensile Test ASTM E8	
Designer: Thierry KLOTZ and Yuxiao WU	
Manager: Myriam BROCHU	
Date: 23/06/2016	Scale: 1:1

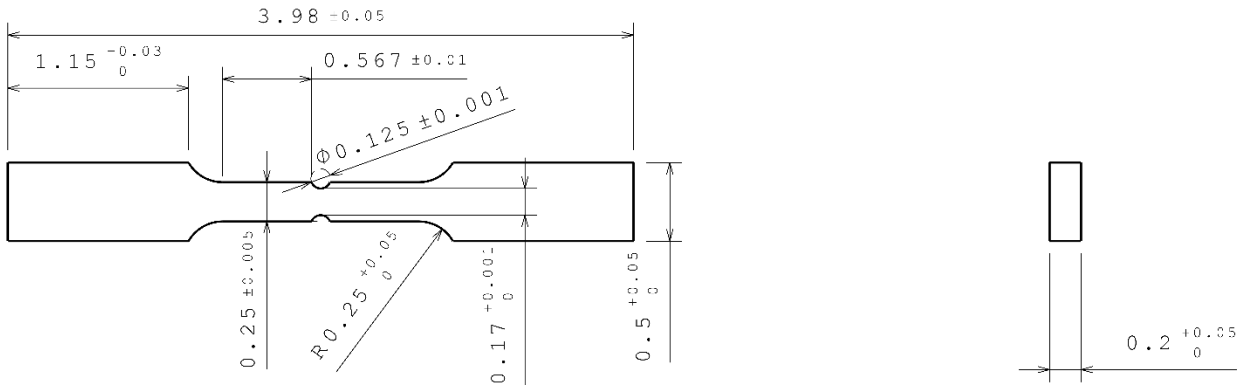

ALL THE DIMENSIONS ARE IN INCHES

- Provide the best machined surface finish possible without polishing (Ra=32µin or better). There is no surface finish requirement for the grip section.

- The reduced sections of prepared specimens should be free of cold work, notches, chatter marks, grooves, gouges, burrs, rough surfaces or edges, overheating.

ECOLE POLYTECHNIQUE	
Tensile U notch Test	
Designer: Thierry Klotz and Yuxiao Wu	
Manager: Myriam BROCHU	
Date: 01/20/2017	Scale: 1:1

APPENDIX F – RESIDUAL STRESS/STRAIN DISTRIBUTIONS

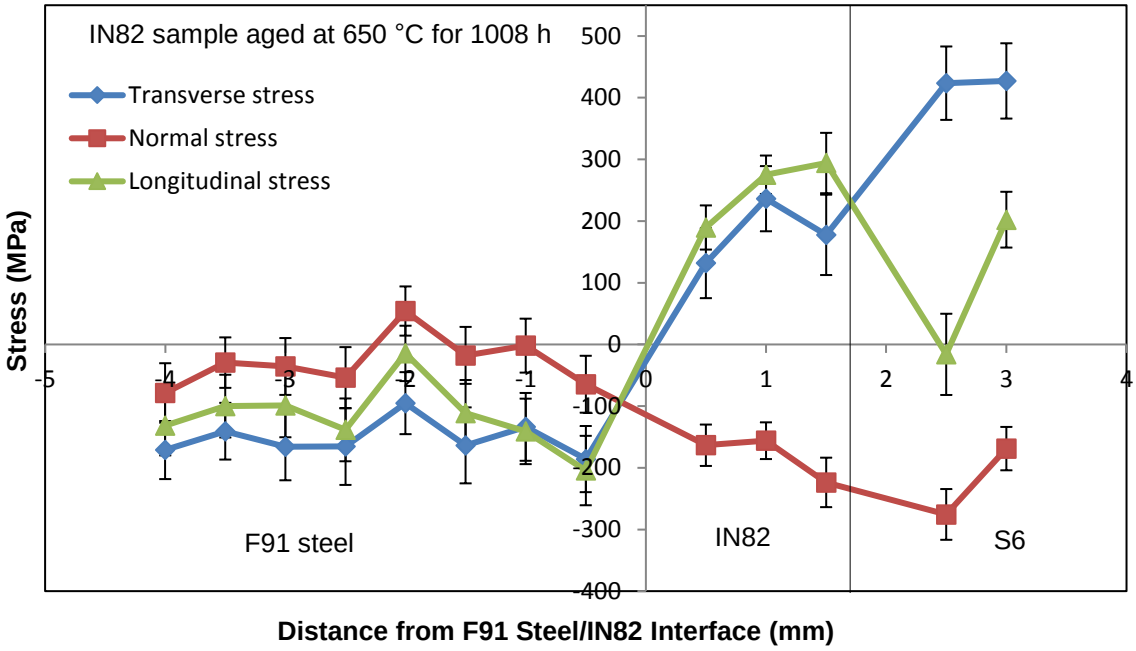

Figure F.1: Residual stress along three directions of an IN82 hardfacing component aged at 650 °C for 1008 h.

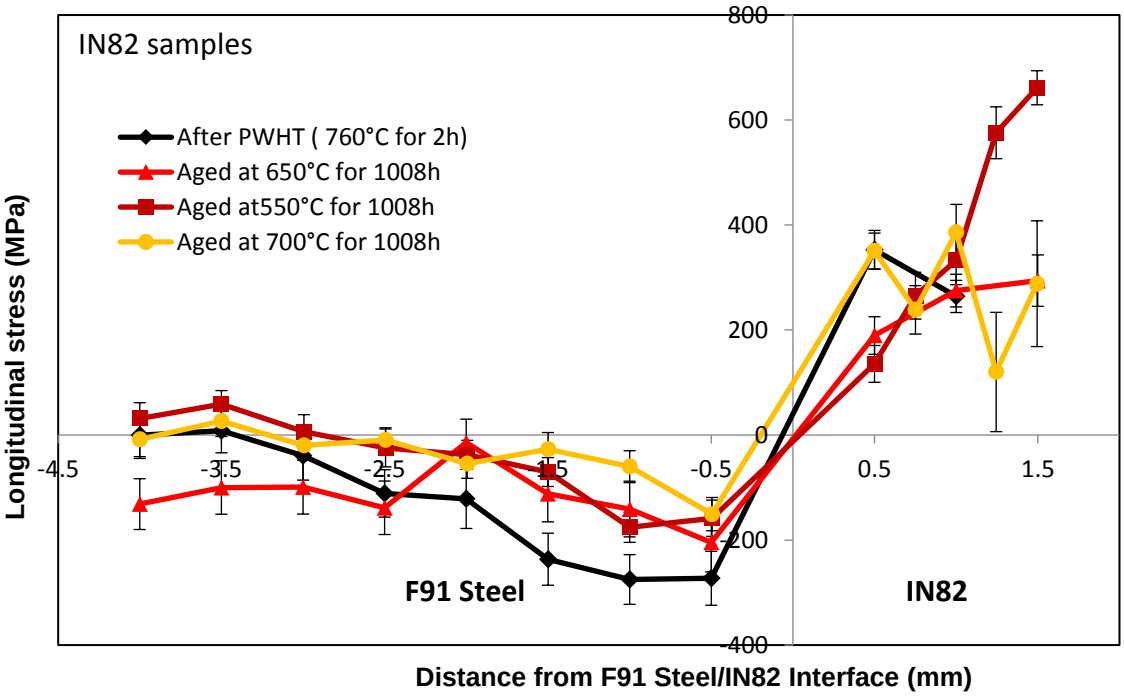

Figure F.2: Longitudinal stress of the IN82 hardfacing components in different aging conditions.

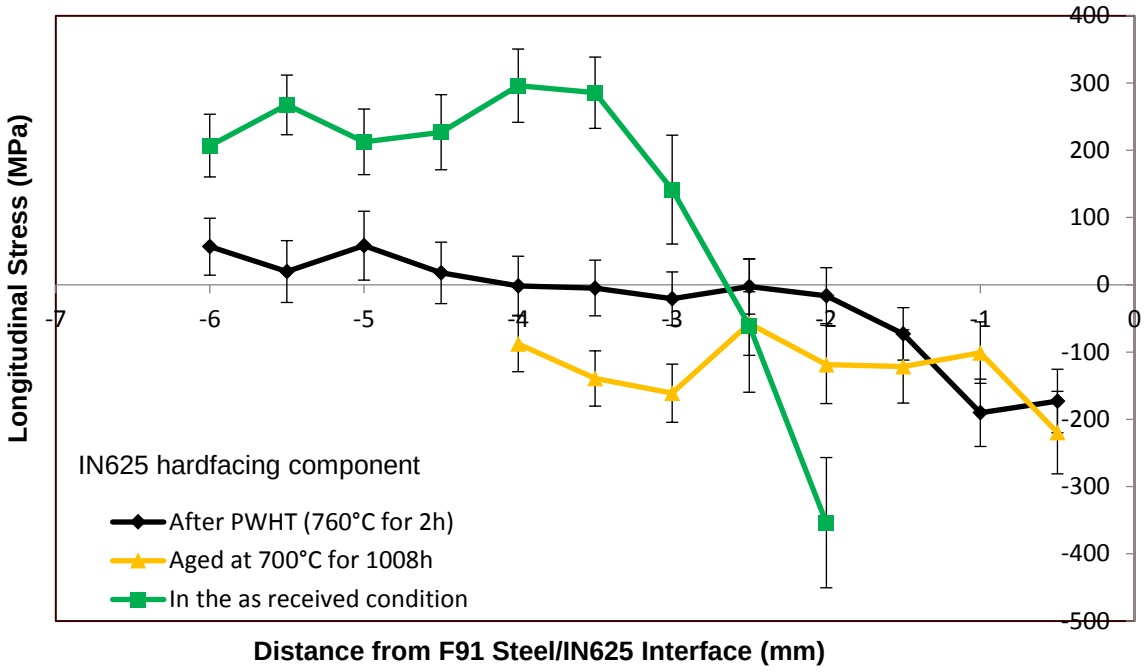

Figure F.3: Longitudinal stress of the IN625 hardfacing components in three conditions.

APPENDIX G – TENSILE TESING OF THE IN82 AND S21 SPECIMENS

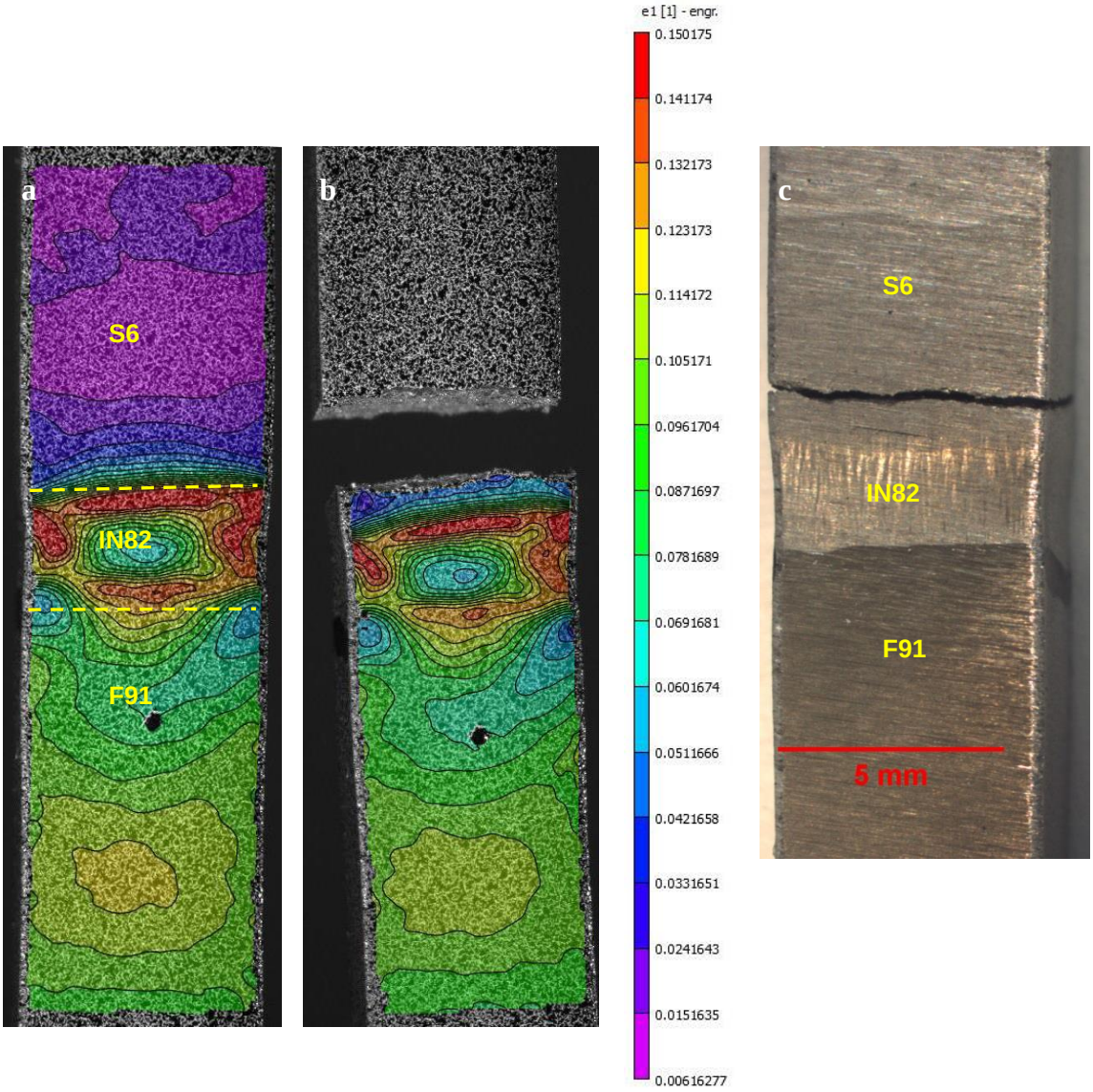

Figure G.1: A straight-shank IN82 specimen aged at 550 °C for 1008 h: principle strain maps (a) before and (b) after fracture, and (c) the other side of the fractured specimen.

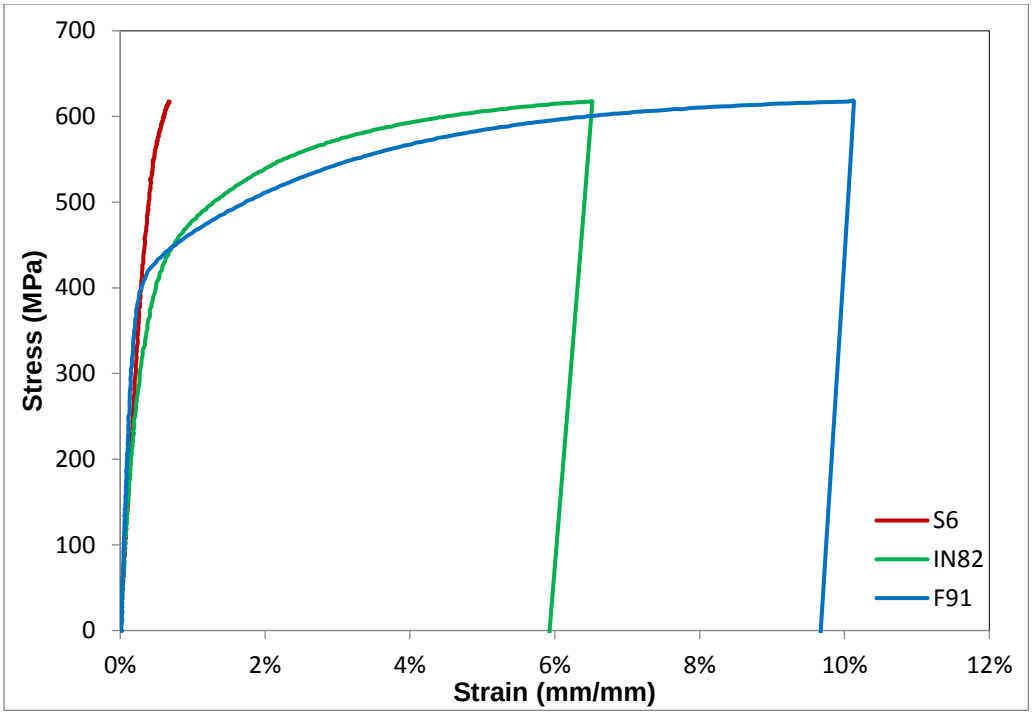

Figure G.2: Local stress-strain curves obtained from the F91, IN86 and S6.

Table G.1: Extracted yielding stresses from different locations of the specimen aged at 550 °C for 1008 h (S6-1, S6-2, S6-3, and S6-4 were selected around 0.5, 1.5, 2.5, and 3.5 mm from the IN82/S6 interface, respectively).

Material	F91	IN82	S6-1	S6-2	S6-3	S6-4
Yielding stress (MPa)	418	398	483	566	606	574

Table G.2: Tensile stresses for specimens aged at 550, 600 and 700 °C for 1008 h (MPa).

Temperature	550	600	700
Tensile stress	618	624	595

Table G.3: Extracted yielding stresses (MPa) from specimens aged at 550, 600 and 700 °C for 1008 h.

Temperature (°C)	F91	IN82	S6
550	418	398	606
600	418	397	626
700	393	432	601

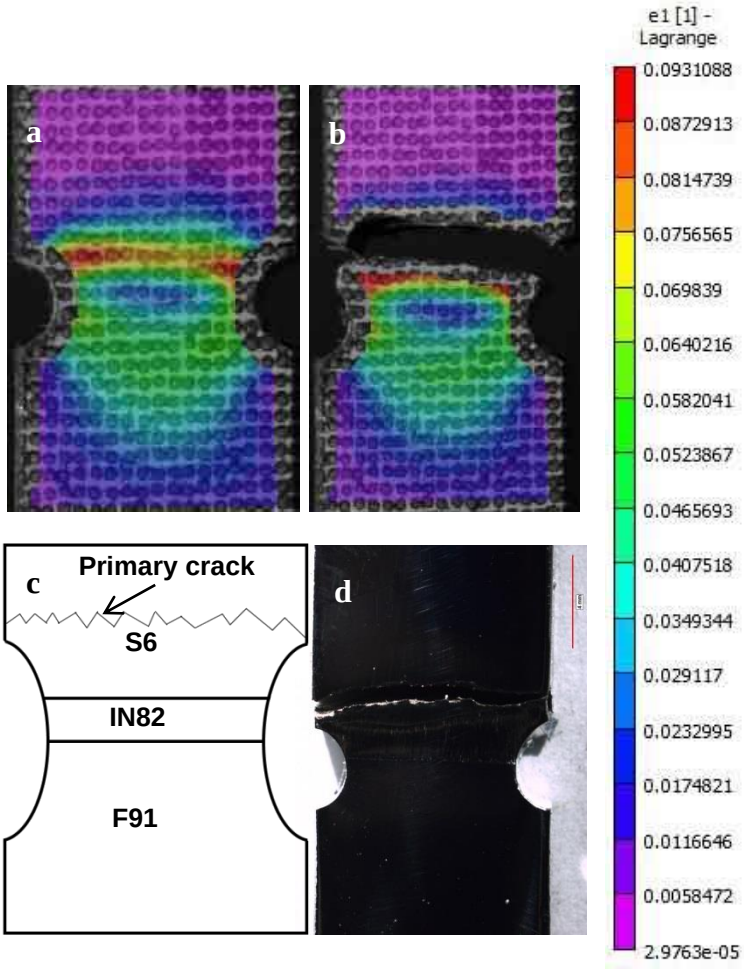

Figure G.3: A notched IN82 specimen in the as-tempered condition: principle strain maps (a) before and (b) after failure, (c) illustration showing the fracture in the S6, and (d) the other side of the fractured specimen.

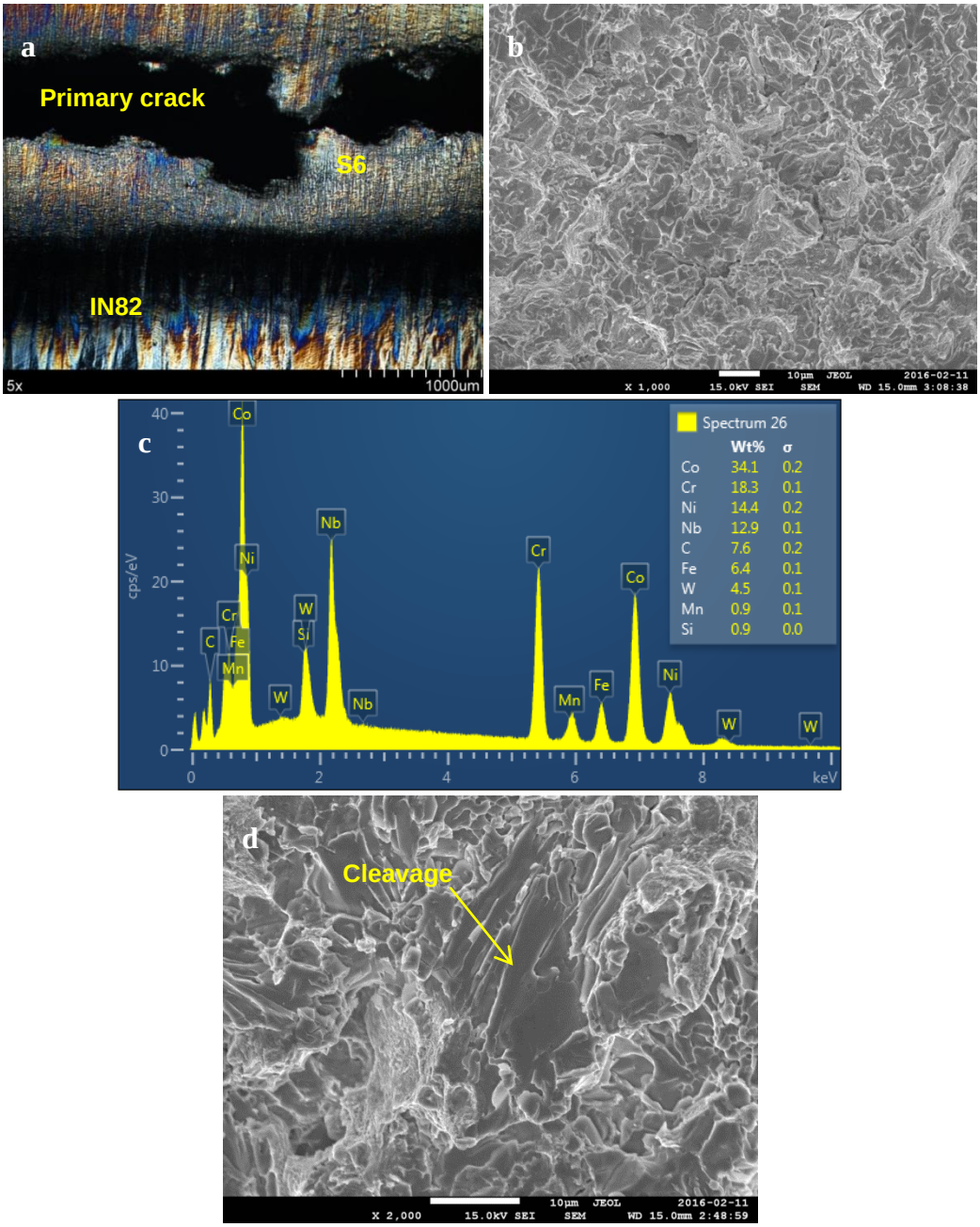

Figure G.4: A fractured IN82 specimen in the as-tempered condition: (a) cross-section, (b) fractograph showing the interdendritic cracks, (c) EDS spot measurement on the fracture surface, and (d) cleavage areas.

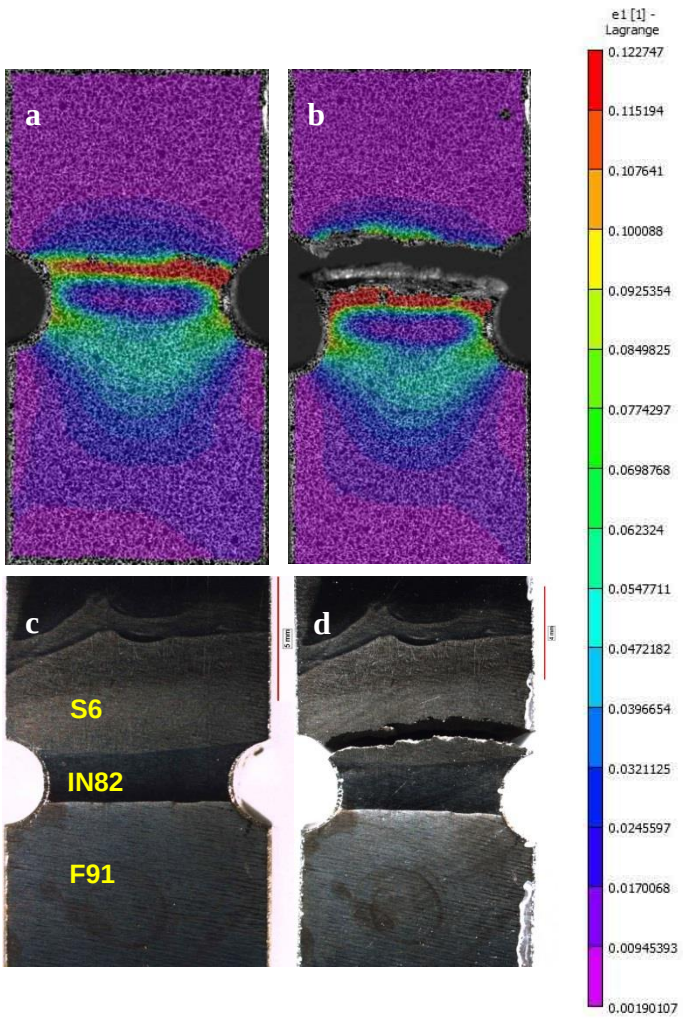

Figure G.5: A notched IN82 specimen aged at 650 °C for 1008 h: principle strain maps (a) before and (b) after fracture, and the other side of the specimen (c) before and (d) after fracture.

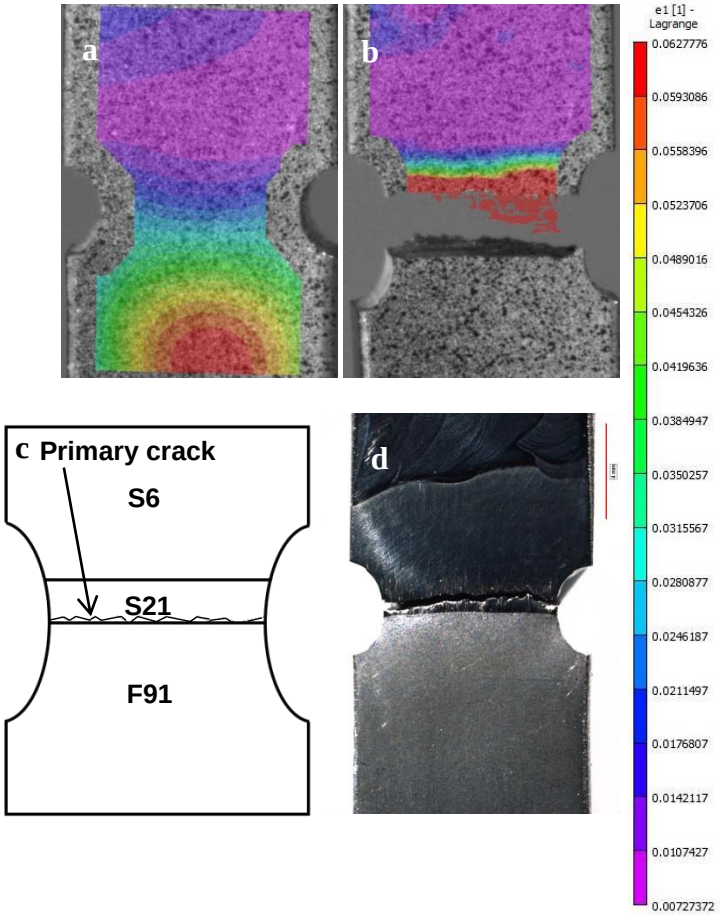

Figure G.6: A notched S21 specimen in the as-tempered condition: principle strain maps (a) before and (b) after fracture, (c) illustration showing the fracture in the S21 bulk material, and (d) the other side of the fractured specimen.

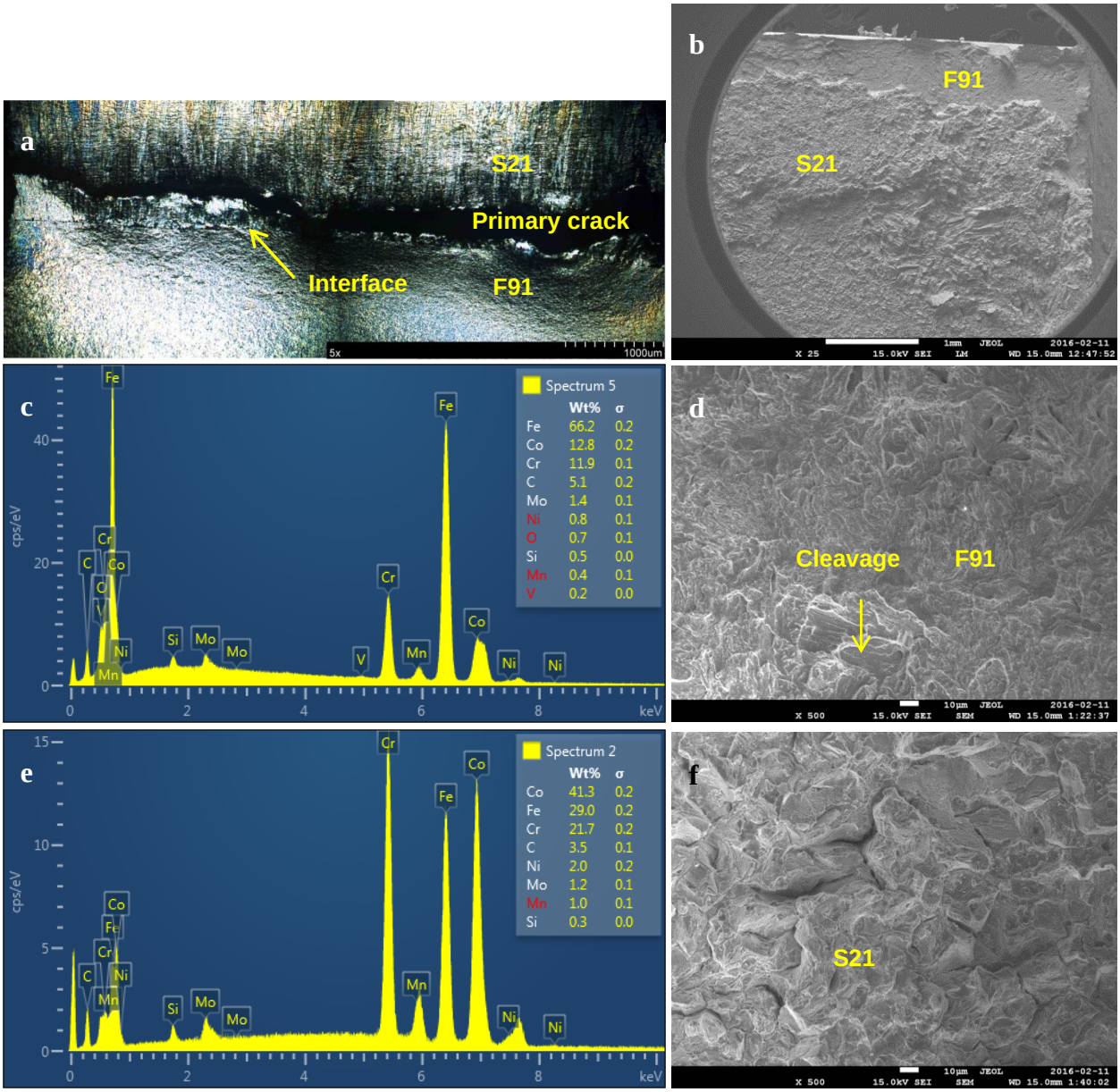

Figure G.7: A fractured S21 specimen in the as-tempered condition: (a) cross-section, (b) macro-fractograph, (c) EDS spot measurement on the F91 region, (d) fractograph showing cleavage in the F91, (e) EDS spot measurement on the S21 region, (f) fractograph showing the interdendritic cracks.

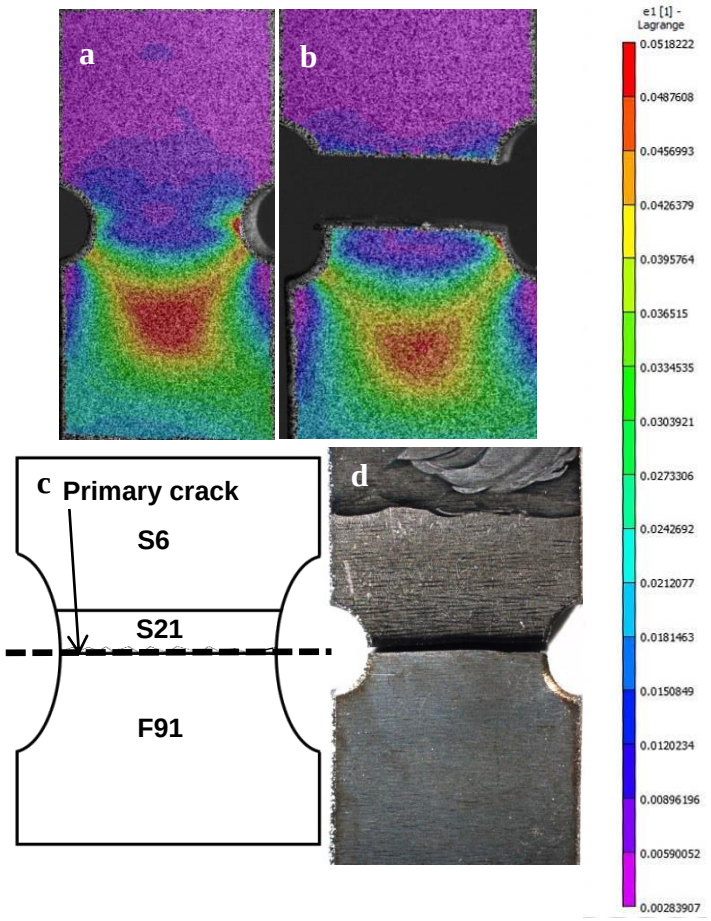

Figure G.8: A notched S21 specimen aged at 650 °C for 1008 h: principle strain maps (a) before and (b) after fracture, (c) illustration showing the fracture along the F91/S21 interface, and (d) the other side of the fractured specimen.